

**CONTRACTION HEAT TRANSFER COEFFICIENT
CORRELATION FOR RECTANGULAR PIN FIN HEAT SINKS**

by

Stephan Schmitt

Submitted in partial fulfilment of the requirements for the degree

MASTER OF ENGINEERING (Mechanical Engineering)

in the

Faculty of Engineering, the Built Environment and Information Technology

UNIVERSITY OF PRETORIA

Pretoria

Supervisors: Dr. D.J. de Kock and Prof. J.P. Meyer

June 2010



ABSTRACT

Title: Contraction heat transfer coefficient correlation for rectangular pin fin heat sinks

Author: Stephan Schmitt

Supervisors: Dr. D.J. de Kock and Prof. J.P. Meyer

Department: Mechanical and Aeronautical Engineering

University: University of Pretoria

Degree: Master of Engineering (Mechanical Engineering)

The demand for smaller but more powerful electronic components is ever increasing. This demand puts a strain on engineers to produce optimal cooling designs for these electronic components. One method for cooling these electronic components is with heat sinks which effectively increase the surface area available for extracting the heat from the electronic components. Computational Fluid Dynamics (CFD) software is sometimes used to aid in the design process, but CFD simulations are computationally expensive and take long to complete. This causes the design engineer to test only a few proposed designs based on his/her experience and select the design that performs the best out of the tested designs, which might not be the optimum.

The temperature distribution inside the heat sink can be solved relatively quickly with the diffusion equation, but the flow around the heat sink complicates the CFD simulation and increases the solving time significantly. Therefore, applications have been developed where the interaction between the heat sink and the flow around the heat sink is replaced by heat transfer coefficients. These coefficients are calculated from correlated equations which contain the flow properties. The flow properties are extracted from a flow network solver, which solves the flow around the heat sink. This procedure results in less expensive simulations, which can be used together with an optimisation procedure to develop an optimum cooling design.



In this dissertation, a correlation for the contraction heat transfer coefficients of rectangular pin fin heat sinks was developed. A methodology was developed where consecutive regression lines were fitted to a large set of data extracted from numerous CFD simulations. The combination of these regression lines formed the basis of the correlation, which was divided into two correlations; one for laminar flow and another for turbulent flow. The correlations were tested against CFD simulations as well as experimental data. The results indicate that these correlations can be effectively used to calculate the contraction heat transfer coefficients on pin fin heat sinks.

Key words: *heat sink, pin fin, heat transfer, correlation, mathematical optimisation, Computational Fluid Dynamics, correlation methodology*



SAMEVATTING

Titel:	Vernouingswarmte-oordragkoëffisiënt korrelasie vir reghoekige penvinhitteputte
Outeur:	Stephan Schmitt
Promotor:	Dr. D.J. de Kock en prof. J.P. Meyer
Departement:	Meganiese en Lugvaartkundige Ingenieurswese
Universiteit:	Universiteit van Pretoria
Graad:	Magister in die Ingenieurswese (Meganiese Ingenieurswese)

Die vraag na kleiner maar kragtiger elektroniese komponente styg voortdurend. Dié vraag plaas druk op ingenieurs om optimale verkoelingsontwerpe vir dié elektroniese komponente te produseer. Een metode om hierdie komponente te verkoel is met hitteputte wat effektiewelik die oppervlak wat beskikbaar is vir verkoeling verhoog. Sageware vir Berekeningsvloedinamika (BVD) word soms in die ontwerpproses gebruik, maar BVD-simulasies is berekeningsintensief en vat lank om te voltooi. Dit veroorsaak dat die ontwerpingenieur net 'n paar voorgestelde ontwerpe, gegrond op sy/haar ondervinding, toets en dan die beste een kies, wat nie noodwendig die optimum is nie.

Die temperatuurverspreiding binne-in die hitteput kan redelik vinnig opgelos word met die diffusievergelyking, maar die vloei om die hitteput bemoeilik die BVD-simulasie en verhoog die oplostyd noemenswaardig. Programmatuur is daarom ontwikkel waar die interaksie tussen die hitteput en die vloei om die hitteput vervang word deur warmte-oordragkoëffisiënte. Hierdie koëffisiënte word bereken uit gekorreleerde vergelykings wat die vloei-eienskappe bevat. Die vloei-eienskappe word afgelei van 'n vloei-netwerk-oplossingspakket wat die vloei om die hitteput oplos. Hierdie prosedure is minder berekeningsintensief en kan dus saam met 'n optimeringsprosedure gebruik word om 'n optimum verkoelingsontwerp te ontwikkel.



In hierdie verhandeling is 'n korrelasie vir die vernouingswarmte-oordragkoeffisiënt van reghoekige penvinhitteputte ontwikkel. 'n Metodiek is ontwikkel waar opeenvolgende regressielyne gepas word op 'n groot datastel wat afgelei is van verskillende BVD-simulasies. Die kombinasie van hierdie regressielyne het die basis gevorm van die korrelasie wat in twee verdeel is; naamlik, een korrelasie vir laminêre vloei en 'n ander een vir turbulente vloei. Die korrelasies is teen BVD-simulasies en eksperimentele data getoets. Die resultate toon dat hierdie korrelasies doeltreffend gebruik kan word om die vernouingswarmte-oordragkoeffisiënt vir penvinhitteputte te bereken.

Sleutelwoorde: hitteput, penvin, warmte-oordrag, korrelasie, wiskundige optimering, Berekeningsvloeidinamika, korrelasiemetodiek



ACKNOWLEDGEMENTS

I would like to express my heartfelt appreciation to the following people for their contribution to this dissertation:

- Dr. Danie de Kock, for the opportunity to conduct this study, and for his support and guidance.
- Dr. Jan Visser and Frank Conradie from Qfinsoft, for their support and guidance.
- Prof. Jan Snyman from the University of Pretoria, for his advice on the optimisation.
- My fellow masters students, Bronwyn Meyers, Gerard Scheepers and Marius Botha, for their friendship.
- My family, friends and other Qfinsoft employees, for their interest and support, especially near the end of the study.



TABLE OF CONTENTS

ABSTRACT	II
SAMEVATTING.....	IV
ACKNOWLEDGEMENTS	VI
LIST OF TABLES.....	X
LIST OF FIGURES	XI
NOMENCLATURE	XVII
CHAPTER 1: INRODUCTION	1
1.1 BACKGROUND	1
1.2 EXISTING KNOWLEDGE	3
1.3 RESEARCH OBJECTIVES	4
1.4 SCOPE OF THE STUDY	4
1.5 ORGANISATION OF THE DISSERTATION	5
CHAPTER 2: LITERATURE STUDY.....	6
2.1 INTRODUCTION.....	6
2.2 EXISTING MODELS.....	6
2.2.1 Governing equations and exact solutions.....	6
2.2.2 Compact models.....	10
2.2.3 Software-incorporated models	13
2.2.4 Flow characterisation	14
2.3 CURRENT HEAT SINK DESIGN OPTIMISATION PROCEDURES	19
2.4 THE THEORY BEHIND QFIN	21
2.5 NUMERICAL MODELLING.....	24



2.5.1	Mesh generation.....	25
2.5.2	Navier-Stokes equations	25
2.5.3	Conservation of mass	26
2.5.4	Conservation of momentum.....	26
2.5.5	Conservation of energy	27
2.5.6	Turbulence modelling	28
2.5.7	Solving the equations	32
2.6	MATHEMATICAL OPTIMISATION	34
2.6.1	Optimisation algorithms.....	35
2.6.2	LFOPC	36
2.6.3	Dynamic-Q.....	37
2.6.4	Zero-order method	42
2.7	CONCLUSION.....	44
CHAPTER 3: EQUATION FORMULATION METHODOLOGY.....		45
3.1	INTRODUCTION.....	45
3.2	VALIDATION OF CFD MODEL	45
3.3	METHODOLOGY.....	57
3.4	LAMINAR FLOW	73
3.5	LAMINAR FACE EQUATION.....	90
3.6	TURBULENT FLOW.....	103
3.7	TURBULENT FACE EQUATION	115
3.8	COMBINATION OF EQUATIONS.....	127
3.9	CONCLUSION.....	134
CHAPTER 4: APPLICATION OF THE EQUATIONS IN CASE STUDIES..		135
4.1	INTRODUCTION.....	135
4.2	CORRELATION APPLIED TO DIFFERENT REGIONS	135
4.3	CORRELATION COMPARED WITH CFD DATA.....	141
4.3.1	Heat sink configuration: $L_{fin}=0.002$, $L_{gap}=0.004$, $W_{fin} = 0.006$, $W_{gap} = 0.008$	142
4.3.2	Heat sink configuration: $L_{fin}=0.004$, $L_{gap}=0.004$, $W_{fin} = 0.004$, $W_{gap} = 0.006$	145



4.3.3 Heat sink configuration: $L_{fin}=0.002$, $L_{gap}=0.008$, $W_{fin} = 0.004$, $W_{gap} = 0.008$	148
4.4 CORRELATION COMPARED WITH LITERATURE DATA.....	151
4.5 CONCLUSION.....	153
CHAPTER 5: CONCLUSION AND RECOMMENDATIONS	154
5.1 CONCLUSION.....	154
5.2 RECOMMENDATIONS AND FUTURE WORK	157
5.2.1 Refining the mesh	157
5.2.2 Extending the correlation to the transitional flow region	157
5.2.3 Including additional terms for fluids other than air	157
5.2.4 Applying the correlation generation methodology to other areas	158
REFERENCES	159
APPENDIX A.....	165



LIST OF TABLES

Table 3-1: Test heat sink dimensions.....	47
Table 3-2: Parameter ranges	63
Table 3-3: Reynolds number ranges	68
Table 3-4: Optimised constants for the final equation.....	87
Table 3-5: Optimised constants for the laminar fraction equation	101
Table 3-6: Constants X_1 to X_{16} for the turbulent edge Nusselt number equation.....	112
Table 3-7: Constants for the turbulent face equation.....	124
Table 3-8: Coefficients for the complete laminar correlation.....	133
Table 3-9: Coefficients for the complete turbulent correlation	134
Table 4-1: Thermal resistance comparisons for different combinations of faces with correlations applied to them	137
Table 4-2: Thermal resistance comparisons for heat sink, Configuration 1	142
Table 4-3: Thermal resistance comparisons for heat sink, Configuration 2	145
Table 4-4: Thermal resistance comparisons for heat sink, Configuration 3	148



LIST OF FIGURES

Figure 1-1: Contraction heat transfer coefficient faces.....	3
Figure 2-1: Energy balance on a pin fin element.....	8
Figure 2-2: Image of a compact model.....	10
Figure 2-3: Compact resistor model or Delphi model.....	12
Figure 2-4: Typical heat sink and fan combination in Q_{fin}	22
Figure 2-5: Post-processing data in Q_{fin}	23
Figure 2-6: Mean and fluctuating turbulent velocities.....	29
Figure 2-7: Graphical representation of the different turbulence layers.....	31
Figure 2-8: Difference between Wall function and Near-wall approaches.....	32
Figure 2-9: The iterative CFD process.....	34
Figure 2-10: The Dynamic-Q method.....	41
Figure 2-11: Zero-order optimisation example.....	43
Figure 3-1: Heat sink dimensions.....	47
Figure 3-2: Measured thermal resistance data from literature, Comparison 1.....	48
Figure 3-3: Measured thermal resistance data from literature, Comparison 2.....	48
Figure 3-4: Measured thermal resistance data from literature, Comparison 3.....	49
Figure 3-5: Measured thermal resistance data from literature, Comparison 4.....	49
Figure 3-6: Combination of all literature data.....	50
Figure 3-7: Laminar thermal resistance comparison with Lei and Ortega [59].....	51
Figure 3-8: Laminar thermal resistance comparison with Dogruoz et al. [27].....	51
Figure 3-9: Laminar thermal resistance comparison with Shaukatullah et al. [33].....	51
Figure 3-10: Laminar thermal resistance comparison with Dogruoz et al. [27].....	52
Figure 3-11: Turbulent thermal resistance comparison with Lei and Ortega [59], k- ϵ models.....	53
Figure 3-12: Turbulent thermal resistance comparison with Lei and Ortega [59], k- ω models.....	53
Figure 3-13: Turbulent thermal resistance comparison with Dogruoz et al. [27], k- ϵ models.....	54
Figure 3-14: Turbulent thermal resistance comparison with Dogruoz et al. [27], k- ω models.....	54



Figure 3-15: Turbulent thermal resistance comparison with Shaukatullah et al. [33], k- ϵ models	55
Figure 3-16: Turbulent thermal resistance comparison with Shaukatullah et al. [33], k- ω models	55
Figure 3-17: Turbulent thermal resistance comparison with Dogruoz et al. [27], k- ϵ models	56
Figure 3-18: Turbulent thermal resistance comparison with Dogruoz et al. [27], k- ω models	56
Figure 3-19: Top view of heat sink displaying selected parameters.....	61
Figure 3-20: An example of the CFD model used in the study	62
Figure 3-21: Close-up of the heat sink from Figure 3-20	62
Figure 3-22: Representative section of the mesh.....	63
Figure 3-23: Thermal conductivity of air (k_f)	65
Figure 3-24: Density of air (ρ)	66
Figure 3-25: Dynamic viscosity of air (μ).....	66
Figure 3-26: Difference between the approach and fin velocities	67
Figure 3-27: Non-dimensional heat transfer profile along the width of a pin	70
Figure 3-28: Edges on which the edge Nusselt number is calculated.....	73
Figure 3-29: The influence of W_{fin}/L_{gap} on the Nusselt number	74
Figure 3-30: The influence of L_{fin}/W_{gap} on the Nusselt number	74
Figure 3-31: The influence of L_{fin}/L_{gap} on the Nusselt number	75
Figure 3-32: The influence of W_{fin}/W_{gap} on the Nusselt number	75
Figure 3-33: The influence of Reynolds number on the Nusselt number.....	75
Figure 3-34: The effect of W_{fin}/L_{gap} on the Reynolds-Nusselt function	76
Figure 3-35: The effect of L_{fin}/W_{gap} on the Reynolds-Nusselt function	76
Figure 3-36: The effect of L_{fin}/L_{gap} on the Reynolds-Nusselt function.....	77
Figure 3-37: The effect of W_{fin}/W_{gap} on the Reynolds-Nusselt function	77
Figure 3-38: The Nusselt number as a function of Reynolds number with constants L_{fin} , L_{gap} and W_{fin} , but variable W_{gap}	78
Figure 3-39: The effect of W_{fin}/L_{gap} on the Nusselt numbers	78
Figure 3-40: Constants a and b as a function of W_{fin}/L_{gap}	79
Figure 3-41: Constants c_1 and c_3 as a function of L_{fin}/L_{gap}	80
Figure 3-42: Constants c_2 and c_4 as a function of L_{fin}/L_{gap}	80
Figure 3-43: Comparison of the preliminary equation values with CFD values	81



Figure 3-44: Differences between the preliminary equation and the CFD values in Figure 3-43.....	82
Figure 3-45: Preliminary equation Nusselt numbers as a function of CFD Nusselt numbers.....	82
Figure 3-46: Comparison between CFD values and initial correlation	84
Figure 3-47: Percentage differences between CFD and initial correlation.....	85
Figure 3-48: Equation Nusselt numbers as a function of CFD Nusselt numbers	85
Figure 3-49: Convergence history of the objective function	86
Figure 3-50: Percentage differences between CFD values and correlated equation before and after optimisation.....	88
Figure 3-51: Equation Nusselt numbers as a function of CFD Nusselt number before and after optimisation	89
Figure 3-52: Comparison between CFD Nusselt numbers and the final laminar edge correlation.....	89
Figure 3-53: Contraction heat transfer coefficient faces.....	90
Figure 3-54: Nusselt number across the pin face.....	90
Figure 3-55: Hyperbolic tangent curve fit	91
Figure 3-56: Combination of a hyperbolic tangent and first-order curve fit	92
Figure 3-57: Normalised heat transfer on a single pin with different Reynolds numbers.....	93
Figure 3-58: Pin centre Nusselt number as a function of L_{gap}/W_{gap}	94
Figure 3-59: Constants d_1 and d_2 as functions of W_{fin}/W_{gap}	95
Figure 3-60: Parameter a for $L_{fin}/L_{gap}=1$	96
Figure 3-61: Comparison between CFD values and the correlation for a	97
Figure 3-62: Correlation for a as a function of the CFD values for a	97
Figure 3-63: The effect of L_{fin}/L_{gap} on the pin heat transfer coefficient	98
Figure 3-64: The effect of L_{gap}/W_{gap} on the pin heat transfer coefficient	98
Figure 3-65: The effect of W_{fin}/W_{gap} on the pin heat transfer coefficient.....	99
Figure 3-66: Percentage differences between CFD and integrated laminar pin width correlation Nusselt numbers	101
Figure 3-67: Comparison between integrated pin width correlation and the integrated CFD normalised Nusselt numbers	102
Figure 3-68: Correlation Nusselt numbers as a function of CFD Nusselt number.....	102
Figure 3-69: The influence of W_{fin}/L_{gap} on the Nusselt number	103



Figure 3-70: The influence of L_{fin}/W_{gap} on the Nusselt number	104
Figure 3-71: The influence of L_{fin}/L_{gap} on the Nusselt number	104
Figure 3-72: The influence of W_{fin}/W_{gap} on the Nusselt number	104
Figure 3-73: The influence of the Reynolds number on the Nusselt number	105
Figure 3-74: Nusselt as a function of Reynolds number for different values of W_{fin}/L_{gap}	105
Figure 3-75: Nusselt as a function of Reynolds number for different values of L_{fin}/W_{gap}	106
Figure 3-76: Nusselt as a function of Reynolds number for different values of L_{fin}/L_{gap}	106
Figure 3-77: Nusselt as a function of Reynolds number for different values of W_{fin}/W_{gap}	106
Figure 3-78: The effect of W_{fin}/W_{gap} and the Reynolds number on the Nusselt number	107
Figure 3-79: Constants a and b as functions of W_{fin}/W_{gap}	108
Figure 3-80: Constant c_1 as a function of L_{fin}/L_{gap}	109
Figure 3-81: Constant c_2 as a function of L_{fin}/L_{gap}	109
Figure 3-82: Constant c_3 as a function of L_{fin}/L_{gap}	109
Figure 3-83: Constant c_4 as a function of L_{fin}/L_{gap}	110
Figure 3-84: Percentage difference before and after optimisation	113
Figure 3-85: Equation Nusselt numbers relative to CFD Nusselt numbers	114
Figure 3-86: Comparison between CFD Nusselt numbers and the optimised equation	114
Figure 3-87: Normalised Nusselt numbers as a function of L_{fin}/L_{gap}	116
Figure 3-88: Normalised Nusselt numbers as a function of L_{gap}/W_{gap}	116
Figure 3-89: Pin centre normalised Nusselt numbers as a function of L_{gap}/W_{gap}	117
Figure 3-90: Coefficient m as a function of W_{fin}/W_{gap}	117
Figure 3-91: Pin centre normalised Nusselt numbers	118
Figure 3-92: Pin width normalised Nusselt numbers as a function of L_{gap}/W_{gap}	119
Figure 3-93: Hyperbolic tangent gradient offset as a function of L_{gap}/W_{gap}	120
Figure 3-94: Hyperbolic tangent gradient offset (c) as a function of $\ln(L_{gap}/W_{gap})$	120
Figure 3-95: Coefficient d_1 as a function of W_{fin}/W_{gap}	121
Figure 3-96: Coefficient d_3 as a function of W_{fin}/W_{gap}	121



Figure 3-97: Coefficient d_3 as a function of $\ln(W_{fin}/W_{gap})$	122
Figure 3-98: Coefficient b as a function of W_{fin}/W_{gap}	123
Figure 3-99: Coefficient b as a function of $\ln(W_{fin}/W_{gap})$	123
Figure 3-100: Percentage difference between the Nusselt number face correlation and the CFD values.....	125
Figure 3-101: Equation Nusselt numbers compared with CFD Nusselt numbers.....	125
Figure 3-102: Comparison between the integrated CFD pin Nusselt numbers and the integrated optimised pin equation Nusselt numbers.....	126
Figure 3-103: Comparison between the integrated complete laminar correlation values and the integrated CFD Nusselt numbers.....	129
Figure 3-104: Comparison between the integrated complete turbulent correlation values and the integrated CFD Nusselt numbers.....	130
Figure 3-105: Example of the laminar correlation together with the relevant CFD data, on a single heat sink configuration.....	131
Figure 3-106: Example of the turbulent correlation together with the relevant CFD data, on a single heat sink configuration.....	131
Figure 3-107: Percentage difference between CFD and complete laminar correlation Nusselt numbers.....	132
Figure 3-108: Percentage difference between CFD and complete turbulent correlation Nusselt numbers.....	132
Figure 4-1: Faces to which the correlation has been applied.....	136
Figure 4-2: Thermal resistance for different cases of contraction faces used [K/W].....	137
Figure 4-3: Thermal resistance where the correlation has been applied to front and rear of pins [K/W].....	138
Figure 4-4: Temperature distribution for an original CFD simulation (3 m/s) [K]....	139
Figure 4-5: Temperature distribution for a case where the correlation has been applied to the faces used for data extraction (3 m/s) [K].....	139
Figure 4-6: Temperature distribution for a case where the correlation has been applied to all the contraction faces (3 m/s) [K].....	140
Figure 4-7: Temperature distribution for a case where the correlation has been applied to the contraction and expansion faces (3 m/s) [K].....	140
Figure 4-8: Heat sink configurations.....	141
Figure 4-9: Thermal resistance as a function of velocity, Configuration 1 [K/W].....	143



Figure 4-10: Differences in thermal resistance as a function of velocity, Configuration 1 [%]	143
Figure 4-11: Temperature distribution for the CFD simulation (4 m/s), Configuration 1 [K].....	144
Figure 4-12: Temperature distribution for the correlated simulation (4 m/s), Configuration 1 [K].....	144
Figure 4-13: Thermal resistance as a function of velocity, Configuration 2 [K/W]...	146
Figure 4-14: Differences in thermal resistance as a function of velocity, Configuration 2 [%]	146
Figure 4-15: Temperature distribution for the CFD simulation (4 m/s), Configuration 2 [K].....	147
Figure 4-16: Temperature distribution for the correlated simulation (4 m/s), Configuration 2 [K].....	147
Figure 4-17: Thermal resistance as a function of velocity, Configuration 3 [K/W]...	149
Figure 4-18: Differences in thermal resistance as a function of velocity, Configuration 3 [%]	149
Figure 4-19: Temperature distribution for the CFD simulation (4 m/s), Configuration 3 [K].....	150
Figure 4-20: Temperature distribution for the correlated simulation (4 m/s), Configuration 3 [K].....	150
Figure 4-21: Heat sink geometry from literature [27]	151
Figure 4-22: Correlation comparison with literature data.....	152

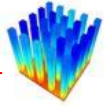


NOMENCLATURE

Symbols:

Variable	Description	Units
A	Hessian matrix	-
A_c	Cross-sectional area	m^2
a	Acceleration vector	m/s^2
a	Correlation constant	-
	Fin width	m
	Curvature	♦
	Vertical offset of hyperbolic function	-
B_j	Hessian matrix	-
b	Correlation constant	-
	Distance between fins	m
	Slope of hyperbolic function	-
b_j	Curvature	♦
C_k	Hessian matrix	-
C_p	Specific heat capacity	J/kg
c	Correlation constant	-
	Horizontal offset of centre of slope of hyperbolic function	-
c_1, c_2, c_3, c_4	Correlation constants	-
c_k	Curvature	♦
c_p	Specific heat capacity	J/kg
D_i	Difference between CFD and correlation Nusselt numbers	-
$\frac{D}{Dt}$	Total derivative	-

♦ Problem dependent

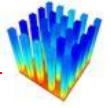


d	Characteristic length	m
$d_1, d_2 \dots d_8$	Correlation constants	-
E_i	Difference percentage between CFD and correlation	
	Nusselt numbers	-
$F(\mathbf{x})$	Objective function	♦
$F(Z)$	Objective function	♦
$f(x)$	Objective function	♦
$g(x)$	Equality constraint	♦
\mathbf{g}	Gravitational acceleration	m/s ²
g_1, g_2, g_3, g_4	Correlation constants	-
H	Fin height	m
h	Fluid enthalpy	J/kg
h_c	Convection heat transfer coefficient	W/m ² .K
$h(x)$	Inequality constraint	♦
h_1, h_2, h_3	Correlation constants	-
\mathbf{I}	Identity matrix	-
i	Data point	-
	Index	-
j	Index	-
k	Thermal conductivity	W/m.K
k_f	Fluid thermal conductivity	W/m.K
k_s	Solid thermal conductivity	W/m.K
L	Pin length	m
	Characteristic length	m
L_{fin}	Fin length	m
L_{gap}	Gap length	m
m	Linear gradient	♦
Nu	Nusselt number	-
Nu_{CFD}	Nusselt number from CFD simulation	-
$Nu_{CFD,i}$	Discrete Nusselt value from CFD simulation	-
Nu_{eq}	Calculated Nusselt number from correlation	-
$Nu_{eq}(\mathbf{x}, i)$	Calculated Nusselt value	-

♦ Problem dependent

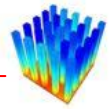


Nu_{pre}	Preliminary Nusselt number	-
Nu_s	Nusselt number modification equation	-
n	Number in the data set	-
	Number of fins	-
nNu	Normalised Nusselt number	-
nNu_p	Part of the normalised Nusselt number	-
\mathcal{P}	Perimeter	m
P_L	Longitudinal pitch	-
Pr	Prandtl number	-
p	Pressure	Pa
\overline{p}	Time-averaged pressure	Pa
Q	Heat input	W
q	Heat flux	W/m ²
Re	Reynolds number	-
R_{th}	Thermal resistance	K/W
S_m	Mass source	kg/m ³
T	Temperature	K
	Kinetic energy	J
T_B	Base temperature	K
T_e	Fluid temperature	K
T_{ref}	Reference temperature	K
T_s	Surface temperature	K
t	Time	s
U_i	Mean velocity	m/s
u	Velocity component	m/s
u_i	Velocity component	m/s
u_i'	Fluctuating velocity	m/s
V	Velocity	m/s
\mathbf{V}	Velocity vector	m/s
$\overline{\mathbf{V}}$	Time-averaged velocity vector	m/s
v	Velocity component	m/s
W_{fin}	Fin width	m
W_{gap}	Gap width	m

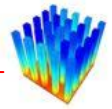


w	Velocity component	m/s
$X_1, X_2 \dots X_{24}$	Correlation constants	-
x	Spatial coordinate	m
	Optimisation parameter	♦
\mathbf{x}	Design point	♦
\mathbf{x}^*	Optimum	♦
\mathbf{x}^i	Successive approximations	♦
y	Direction normal to surface	m
	Spatial coordinate	m
$Z_1, Z_2 \dots Z_{21}$	Correlation constants	-
z	Spatial coordinate	m
β	Heat transfer area per unit volume	1/m
	Inequality value	-
δ_{ij}	Kronecker Delta function	-
λ	Coefficient of bulk viscosity	m/s ²
$\boldsymbol{\mu}$	Penalty vector	-
μ	Viscosity	Pa.s
	Penalty value	-
$\boldsymbol{\rho}$	Penalty vector	-
ρ	Density	kg/m ³
	Penalty value	-
Φ	Viscous dissipation	W/m ³

♦ Problem dependent

**Abbreviations:**

CFD	Computational Fluid Dynamics
CSV	Comma-separated values
FEA	Finite Element Analysis
FNM	Flow Network Modelling
LES	Large-Eddy simulation
LFOPC	Leap-frog optimisation procedure for constrained minimisation
PCB	Printed circuit board
RANS	Reynolds-averaged Navier-Stokes equation
rke	Realizable k- ϵ
RMS	Root mean square
RNG	Renormalisation group
RSM	Reynolds stress model
RSS	Root sum square
ske	Standard k- ϵ
skw	Standard k- ω
SST	Shear stress transport
TDO	Toolkit for Design Optimisation

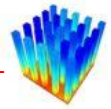


CHAPTER 1: INTRODUCTION

1.1 BACKGROUND

The information technology community is continuously in search of smaller but more powerful electronic devices. Therefore, the packaging industry is constantly in the process of shrinking electronic package sizes and increasing the heat dissipation levels in the packages. This results in soaring power densities in electronic products. The increase in power densities results in an increase in temperatures [1]. The lifetime of the electronic components in these products is limited by the maximum temperatures in these components. In most products, where the temperatures of the components need to be reduced, aluminium heat sinks are attached to the packages to cool them down. The heat sinks provide more heat transfer surface area for the dissipation of the heat, effectively decreasing the thermal resistance of the package. Unfortunately, heat sinks take up space resulting in an increased overall package size. They also add extra weight and cost to the products, and the occupied space can be seen as wasted space. For these reasons, optimal heat sinks are required, which, in turn, creates a need for an effective design tool or method to design such heat sinks.

In most thermal design problems on the cooling of packages, mainly one of two methods is used. The two methods will be discussed in more detail in the next chapter, but a short description will be given here. The first method is compact modelling where a single heat transfer coefficient is calculated for the entire package [2]. This method is computationally inexpensive, but very general. Optimisation of a heat sink can easily be done with this method, but the answers are very crude. The other method is Computational Fluid Dynamics (CFD), which is computationally very expensive, and optimisation is rarely done. For the majority of problems, the designer solves a few heat sinks with selected properties and geometry, and picks the one with the lowest thermal resistance as the final design [3]. Charts are available showing the characteristics of commercially available heat sinks. From these charts, the designer



can determine the influences certain parameters might have on the thermal resistance [4]. The performance of the design is entirely a function of the knowledge and expertise of the designer and might not even be close to the optimum design.

There is a third method, which uses the strengths of both previously mentioned methods. This method sets up flow paths through the geometry and calculates the flow first by making use of a flow network solver [5]. Then from the calculated flow field; derived equations, empirical formulas or curve fits are used to determine the heat transfer coefficients on the faces of the heat sinks. After the heat transfer coefficients have been obtained, the temperature distribution is then numerically modelled with a curvilinear form of the discretised diffusion equation.

The heat sink design tool, Qfin [6], uses this method to solve the fluid flow and the temperature distribution in heat transfer problems. The next chapter will provide a more in-depth description of the workings of Qfin, but a short introduction follows. Qfin has built-in heat sink and fan models with which a cooling design can be modelled and solved. Qfin also has the option of optimising the design for any specified objective function by selecting certain parameters as variables in the optimisation procedure. The results from Qfin are relatively accurate, but the main attraction of this method is the speed at which one can design a feasible solution. With Qfin, it is therefore possible to design near optimal cooling solutions in very little time, which, in turn, decreases the actual and computational cost of the design process.

This study looks at improving the contraction heat transfer coefficient correlation for rectangular pin fin heat sinks in Qfin. The contraction heat transfer coefficient is defined as the heat transfer coefficient on the rear faces on the pins looking in the flow direction. Figure 1-1 displays a graphical representation of the contraction heat transfer coefficient faces. A new heat transfer correlation is needed to increase the accuracy and expand the parameter window in which the correlation is valid.

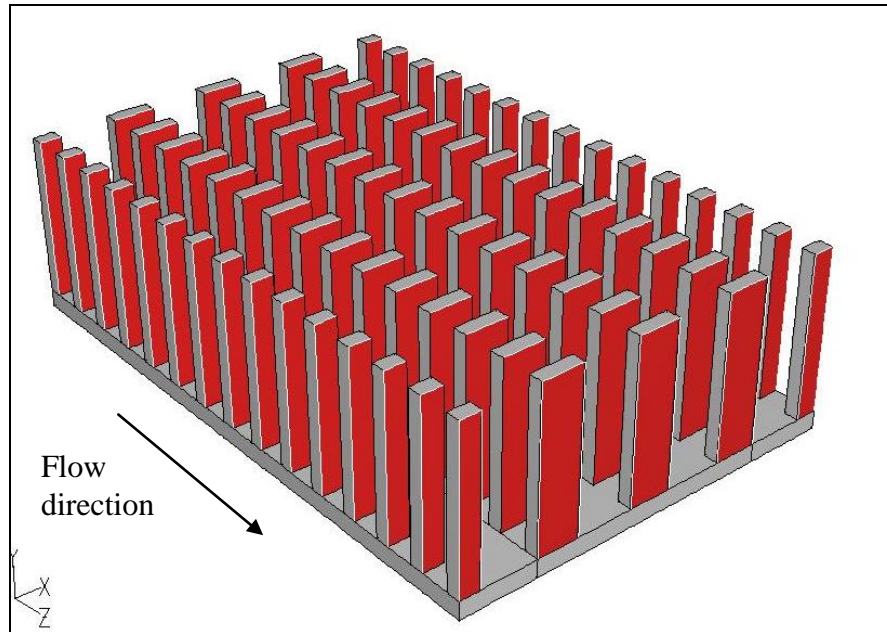


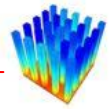
Figure 1-1: Contraction heat transfer coefficient faces

1.2 EXISTING KNOWLEDGE

For some simple flow configurations, exact solutions for the heat transfer coefficient can be derived from the governing differential equations for fluid flow and energy transfer to yield analytical formulas. In most practical configurations, this is unfortunately not the case and one has to turn to experimental work to obtain correlations for the heat transfer coefficients.

Usually, correlations for heat transfer coefficients are generated by doing physical experiments on the different geometries and then fitting curves to the data extracted from these experiments. These formulas generally correlate only the global heat transfer coefficients of different geometries and flow characteristics due to the difficulty of measuring the data. Only where the geometry is very simple, such as flat plates or cylinders, can local heat transfer coefficients be correlated. The fluid flow and heat transfer characteristics of pin fin heat sinks are much too complex and do not lend itself to simple analytical methods [7].

Recently, engineers have started using CFD to create numerical experiments that yield results which resemble the data obtained from physical experiments. CFD has become



a powerful research tool in examining the characteristics of different fluid flow and heat transfer configurations.

1.3 RESEARCH OBJECTIVES

The objectives of this study are:

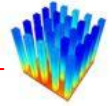
- to create a correlation for the contraction heat transfer coefficients of rectangular pin fin heat sinks in laminar and turbulent flow conditions;
- to optimise the coefficients in the correlated equation in order to minimise errors;
- to compare the final equation with experimental data and CFD solutions.

1.4 SCOPE OF THE STUDY

This study focuses on constructing an empirical formula that correlates the contraction heat transfer coefficients of ducted rectangular pin fin heat sinks with no flow bypass. The methodology generated in this study to create such a formula can also be used to correlate other heat transfer coefficients on pin fin heat sinks as well as on other similar geometries.

Wirtz and Mathur [8] showed that it is possible to determine detailed heat transfer coefficient data on small components such as electronic packages and heat sinks by means of experimentation. They determined local heat transfer coefficients on each face of an electronic package. Although this is possible, it is not a feasible option for this research due to the amount of data needed. CFD supplies data more rapidly than this experimental method.

Due to the number of variables that has an influence on the contraction heat transfer coefficient, the number of experiments needed to get adequate results for creating and testing the correlation is extremely high. Therefore, CFD, instead of experiments, is used as an analysis tool to rapidly generate sufficient data for the creation and testing of the correlation. The CFD data also give more detailed results than actual



experiments. Barrett and Obinelo [9] experimented with CFD to determine if the use of commercial CFD packages is a feasible option to effectively gather vast amounts of experimental data in order to quantify the characteristics of all the involved parameters on the heat transfer and pressure drop of extruded fin heat sinks in ducted flow. They concluded that CFD is definitely a practical and effective tool in gathering a large amount of data for the characterisation of heat sinks.

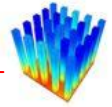
For an equation that correlates data with the number of variables looked at in this study, many coefficients will have to be estimated. An optimisation procedure is used to optimise the estimated coefficients in the correlated equation for higher accuracy.

The generated formula for the contraction heat transfer coefficient is tested by implementing it into Q_{fin} and solving a few selected cases to compare with CFD results and experimental data.

1.5 ORGANISATION OF THE DISSERTATION

The dissertation consists of the following chapters:

- Chapter 2 discusses the appropriate literature relevant to the study of heat transfer coefficients for pin fin heat sinks. It also contains discussions on current trends in industry and research. Furthermore, the basics of CFD and mathematical optimisation are also discussed.
- Chapter 3 develops new correlations for the contraction heat transfer coefficient of pin fin heat sinks in laminar and turbulent flow. It includes data on the optimisation of the coefficients in the developed correlations.
- Chapter 4 compares the developed correlations with different CFD simulations as well as with experiments from literature. This chapter also shows that these correlations are very effective in replacing complex CFD simulations with simple temperature distribution calculations.
- Chapter 5 provides the conclusions drawn from this study as well as recommendations and possible future work that can flow from this research.



CHAPTER 2: LITERATURE STUDY

2.1 INTRODUCTION

This chapter describes the literature relevant to the study. It is divided into five parts, each considering a different aspect of the study. The first part discusses the different modelling strategies and the current heat sink models available in each of these strategies. The second part gives examples of how heat sink optimisation is done currently. After this, a brief discussion follows on the theory behind Qfin and why it is a useful tool for optimising heat sinks. The fourth part describes numerical modelling of fluid flow and heat transfer. It explains the theory behind CFD and how it is solved. The last part considers the theory of optimisation and also gives discussions on the procedures used in this study.

2.2 EXISTING MODELS

2.2.1 Governing equations and exact solutions

The governing equations for fluid flow and heat transfer inside a fluid are given by Equations 1 to 3 below [10]. These equations represent the conservation of mass, conservation of momentum and the conservation of energy respectively.

$$\frac{\partial \rho}{\partial t} + \text{div} \rho \mathbf{V} = S_m \quad (1)$$

$$\rho \frac{D\mathbf{V}}{Dt} = \rho \mathbf{g} - \nabla p + \frac{\partial}{\partial x_j} \left[\mu \left(\frac{\partial v_i}{\partial x_j} + \frac{\partial v_j}{\partial x_i} \right) + \delta_{ij} \lambda \text{div} \mathbf{V} \right] \quad (2)$$

$$\rho \frac{Dh}{Dt} = \frac{Dp}{Dt} + \text{div}(k \nabla T) + \Phi \quad (3)$$



where

ρ : Density [kg/m^3]

t : Time [s]

\mathbf{V} : Velocity vector [m/s]

v : Velocity component [m/s]

S_m : Mass source [kg/m^3]

$\frac{D}{Dt}$: Total derivative

\mathbf{g} : Gravitation vector [m/s^2]

p : Pressure [Pa]

x : Spatial coordinate [m]

μ : Coefficient of viscosity [Pa.s]

δ_{ij} : Kronecker Delta function ($\delta_{ij} : 1$ if $i=j$ and $\delta_{ij} : 0$ if $i \neq j$)

λ : Coefficient of bulk viscosity [m/s^2]

h : Fluid enthalpy [J/kg]

k : Thermal conductivity [W/m.K]

T : Temperature [K]

Φ : Viscous dissipation [W/m^3]

Heat transfer in a solid is governed by Fourier's law of heat conduction [10], which states that in a homogeneous substance, the local heat flux is proportional to the negative of the local temperature gradient. Introducing a constant of proportionality, this law can be written as

$$q = k \frac{dT}{dx} \quad (4)$$

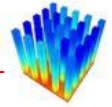
where

q : Heat flux [W/m^2]

k : Thermal conductivity [W/m.K]

T : Temperature [K]

x : Spatial coordinate [m]



Mills [11] showed how to derive solutions for the temperature distribution in several different shapes, including fins and pins that can be used to simulate heat sinks. Figure 2-1 shows a pin fin and the energy balance on an element of the pin fin.

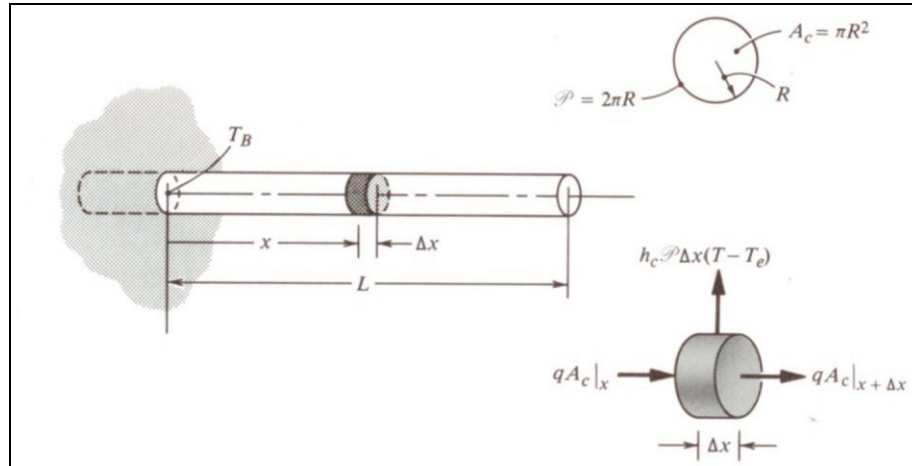


Figure 2-1: Energy balance on a pin fin element

Source: Mills [11]

Looking at an infinitesimal pin element, the energy balance is given by

$$qA_c|_x - qA_c|_{x+\Delta x} - h_c P \Delta x (T - T_e) = 0 \quad (5)$$

where

q : Heat flux [W/m^2]

A_c : Cross-sectional area [m^2]

h_c : Convection heat transfer coefficient [$\text{W}/\text{m}^2 \cdot \text{K}$]

P : Perimeter [m]

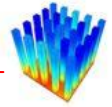
x : Spatial coordinate [m]

T : Temperature [K]

T_e : Fluid temperature [K]

By making use of Fourier's law, and assuming that the fluid temperature is fairly constant, the base temperature is fixed and there is no heat loss at the tip of the pin, Equation 5 can be manipulated to represent the temperature distribution in a pin as

$$\frac{T - T_e}{T_B - T_e} = \frac{\cosh \beta(L - x)}{\cosh \beta L} \quad (6)$$



where

T_B : Base temperature [K]

L : Pin length [m]

$$\beta = \left(\frac{h_c \mathcal{P}}{kA_c} \right)^{1/2} \quad [1/m]$$

Although an image of a circular pin fin is shown, this equation can be used with any pin with constant cross-section. The only variable that is still needed is the convection heat transfer coefficient.

Fluid in contact with a wall is stationary due to friction. Therefore the local heat transfer between a solid and a fluid at the interface is due to conduction only

$$q = -k \frac{\partial T}{\partial y} \Big|_{y=0} \quad (7)$$

where y is the coordinate direction normal to the surface and k is the fluid thermal conductivity. Newton's law of cooling defines the convective heat transfer coefficient as

$$q = h_c (T_s - T_e) \quad (8)$$

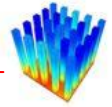
where T_s is the surface temperature and T_e is the fluid temperature. Combining these two equations, gives an equation for the convection heat transfer coefficient.

$$h_c = \frac{-k(\partial T / \partial y) \Big|_{y=0}}{T_s - T_e} \quad (9)$$

For generalisation, the convection heat transfer coefficient can be written in a non-dimensional form, called the Nusselt number

$$Nu = \frac{h_c L}{k} \quad (10)$$

where L is a characteristic length and k is the fluid conductivity.



In most engineering applications, the Nusselt number is correlated to experimental data. For certain simple geometries like flow between parallel plates and flow inside ducts, an exact formula for the Nusselt number can be derived. For example, fully developed laminar flow in a circular duct with a constant wall temperature has an exact formula for the Nusselt number:

$$Nu = 3.66 \quad (11)$$

2.2.2 Compact models

The term compact model describes the method where a heat sink is replaced by simplified geometric shapes or a resistance model. The most common method is to replace the heat sink with a porous fluid block with fluid properties giving the same heat transfer the heat sink would have given. Figure 2-2 displays the simplification. This model is very effective where a large number of heat sinks exist in a single design, because of its little computational expense.

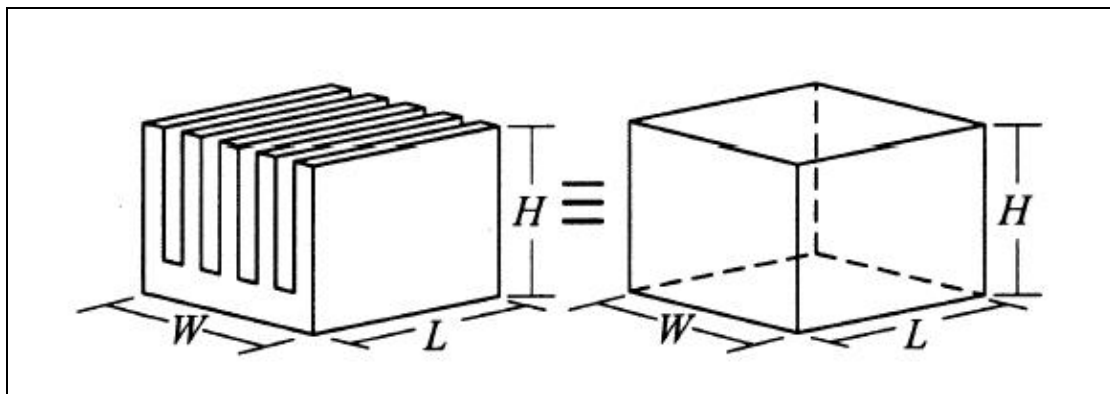
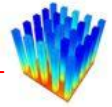


Figure 2-2: Image of a compact model

Source: Brucker and Majdalani [2]

Brucker and Majdalani [2] described a method to determine the effective conductivity of the fluid block of the compact model based on the flat-plate Nusselt number correlation of Churchill and Chu. This method can also be applied to other Nusselt



number correlations. Usually, the calculation of the effective conduction coefficient for the fluid block contains an iterative process, but this method does not make use of an iterative process, which makes it much more attractive to use.

Narasimhan and Majdalani [12] used CFD to determine the thermal conductivity value for compact models of a pin fin heat sink and an extruded heat sink under natural convection cooling. The thermal resistance was determined from the CFD and converted to an overall heat transfer coefficient representative of the heat sink. Correlations were used to relate the heat transfer coefficient to the conduction coefficient. To determine the actual value of the effective conductivity from the correlations, they used an iterative scheme.

Krishnan [13] developed a numerical code based on the governing equations of fluid flow and heat transfer to replace a plate fin or pin fin heat sink with a compact model consisting of a porous fluid block. Although this is a numerical code and numerical codes are computationally expensive, this one is not as costly. A great deal of computation is saved in the simplification of the heat sink geometry into a fluid block.

Kim et al. [14] created a compact model for the Nusselt number and pressure drop across pin fin heat sinks in cross-flow conditions based on the volume-averaging technique. The pin fins are modelled as a porous medium.

Another type of compact model, not usually applied to heat sinks but to packages, is the resistor model. Instead of solving the heat transfer in the components, the components are replaced by resistors. A specific method was developed to create a universal standard for this type of compact model, called the Delphi method [15]. Figure 2-3 displays an example of a common compact resistor model.

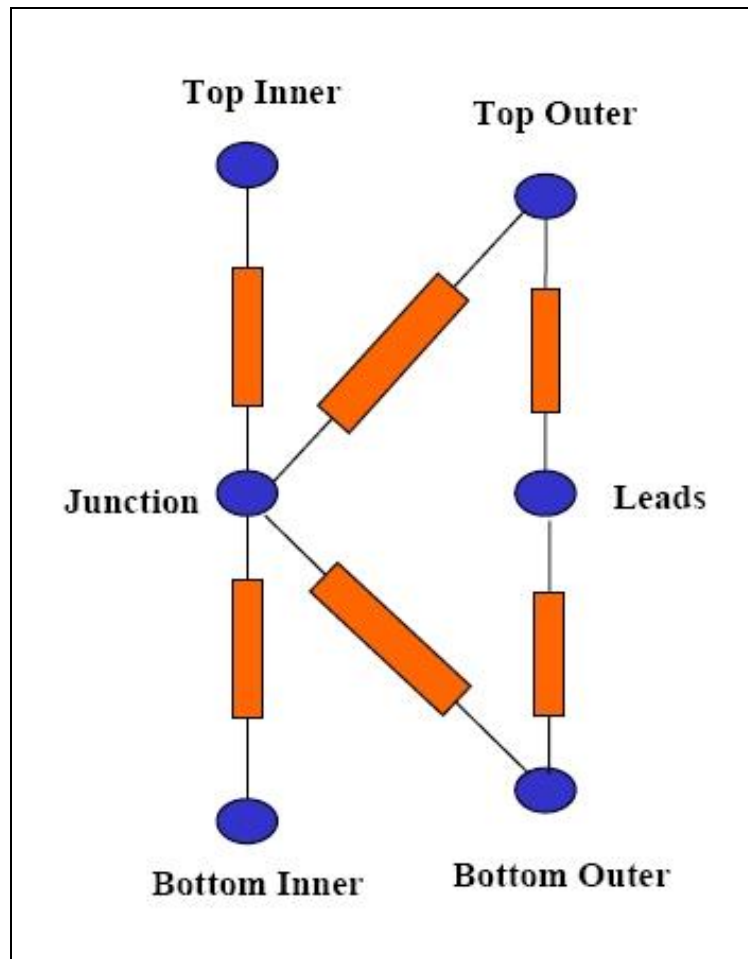
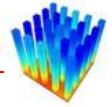
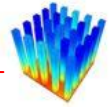


Figure 2-3: Compact resistor model or Delphi model

Source: Shidore and Sahrapour [16]

The Delphi method is described in detail by Malhammar [17] in a series of articles in the online Coolingzone magazine. This model uses an electrical analogy to thermal flow. A node is put at each point of the design where the temperature needs to be calculated. All the nodes are then connected to each other by means of resistors. The values of the resistors depend on the fluid flow and geometry around the heat sink. Usually, one will have three or four resistors, but an indefinite number can be used. The values of the resistors are calculated by experimental procedures. In general, this method has very small parameter windows where the accuracy is acceptable; the models are only valid for small parameter changes. Although this method is not really designed to be applied to heat sinks, it is possible to implement it on heat sinks.



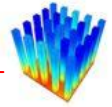
2.2.3 Software-incorporated models

There exist several software programs that can be used to model fluid flow and heat transfer by means of empirical correlations. The use of programs that incorporate empirical correlations rather than solving the governing fluid flow equations has several advantages:

- The time needed to design cooling solutions is only a fraction of the time needed by CFD programs.
- One does not need high-end computers to run these programs.
- It is more feasible to do optimisation on the cooling design.

This is done by decoupling the convection and conduction parts of the problem and replacing the convection coefficients with empirical equations. The conduction in the solid regions is then solved with the discretised heat transfer equations. Culham et al. [18] demonstrated the simulation software called META by means of a comparison between the META results, experimental results and correlation equations of a rectangular heat sink cooled by natural convection. META uses empirically correlated equations to determine the heat transfer coefficients on the heat sink surface areas. The temperatures in the heat sink are calculated by assuming the plates can be modelled as uniform heat flux plates.

Another way of minimising the time needed for the design of cooling solutions and still make use of CFD is described next. Conduction heat transfer in solids does not need such a high cell count as convection cooling and flow in fluid regions. If one can therefore use two meshes with different densities, one can save cells in the solid regions. The problem is that usually the solid and fluid regions are coupled to each other and therefore need the same cell sizes. Agonafer and Free [19] presented a methodology to solve the heat transfer and fluid flow over pin fin heat sinks with fewer control volumes than normally needed. They did numerical experimentation on round and square pin fins with impingement flow and parallel flow. As described above, most models consist of decoupling the conduction heat transfer and the convection heat transfer by solving for the heat transfer coefficients on the faces of the heat sink by means of correlations or CFD computation, and then solving the



conduction in the solids afterwards. The presented method solves the coupled solution by making use of different size meshes for the fluid flow and the conduction. The interface values between the two meshes, namely between convection and conduction, are mapped onto each other.

2.2.4 Flow characterisation

Several different strategies exist to examine the influences of parameter changes on the heat transfer and pressure drop characteristics of heat sinks. Each of these has their own advantages and problems. The easiest method to determine the characteristics of certain parameters on a heat sink design is to use an existing correlation or model and plot the equation for different parameter values. Numerical experiments in the form of CFD solutions, and physical experiments can also be conducted on a set of heat sinks with different sizes and in different flow configurations to determine the influences.

These three methods can also be used to create correlations for the heat transfer coefficient and pressure drop of heat sinks in different configurations. Most researchers combine analytical studies with experimentation to come up with a correlation that fits the data. By combining two methods, the validity of the selected methods can also be determined.

Analytical

The following section describes some analytical studies done on heat sinks.

Pin fins with cross-flow

Ahmed and Yovanovich [20] did an analytical study to develop a general method for predicting forced convection heat transfer from isothermal volumes such as flat plates, circular cylinders and spheres. The solutions are valid for a large range of Reynolds and Prandtl numbers and compare very well with existing solutions. The only



drawback of this study is that the equations are still area-averaged heat transfer values.

Kahn et al. [21] determined analytical models for the heat transfer from in-line and staggered round pin fin heat sinks. Their correlations are in good agreement with current numerical and experimental data. They plotted the pressure drop and Nusselt number for different parameters to determine the influence of each parameter on these values. They also did the same study on elliptical cylinders.

A physics-based analytical model is presented by Kang and Holahan [22] to predict the thermal behaviour of pin fin heat sinks in transverse flow conditions. This model was developed by using both CFD and experimental data. The model is based on the adiabatic heat transfer coefficient and a thermal wake function, which includes the effect of upstream pins on the adiabatic temperature.

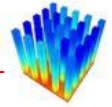
Pin fins with impingement flow

Kobus and Oshio [23] did a theoretical and experimental study to determine the effect of radiation on the heat transfer characteristics of staggered vertical pin fin heat sinks with impingement flow. The influence of radiation on the thermal performance of a pin fin heat sink was accounted for by introducing an effective radiation heat transfer coefficient that was added to the convective heat transfer coefficient.

Extruded fins with cross-flow

Figliola and Thomas [24] presented an approximate method to determine the heat transfer coefficient between parallel flat plates with imbedded heat sources and laminar flow characteristics. They used theoretical analyses to derive an equation for the Nusselt number. The results were compared with experimental results.

Najafi and Scott [25] created correlations for the average heat transfer coefficients on flat, partially heated plates for laminar and turbulent flow. They used an analytical



approach to integrate correlations that determine local heat transfer coefficients on plates.

Experimental

There is much more experimental work in this field. Many researchers tried to determine the effects of different parameters on heat sinks and characterise them to make the design of cooling solutions easier. The next section describes some of these studies.

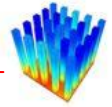
Pin fins with cross-flow

Yeh and Chyu [26] studied the heat transfer coefficients of staggered pin fin arrays used to cool turbine blades. They tested the pin fin arrays in a high Reynolds number range corresponding to turbulent flow and compared their data with previous studies. They discovered that the general row-resolved Nusselt number is the highest on the third row of pins. The Nusselt number of the rows after that becomes slightly less.

Dogruoz et al. [27] experimented with flow bypass on in-line square pin fin heat sinks. They compared their experimental results with the two-branch bypass model and correlations for heat transfer for infinitely long tube bundles. For high Reynolds numbers and tall fins, the comparison is relatively good but there is a discrepancy between the experimental data and the computations when the approach velocity and fin height are decreased. They also determined the optimum pin spacing as a function of the clearance ratio.

Zapach et al. [28] analysed the pressure drop and heat transfer characteristics of in-line and staggered round pin fin heat sinks. The heat transfer correlations were verified with experimental results. The correlations were based on tube bank heat exchanger correlations. Some modifications were made to the correlations to fit the experimental data better.

Ahmed and Yovanovich [29] determined correlations for an area-averaged Nusselt number for circular and square cylinders and toroids by means of experiments. These



equations were compared with previous correlations from other authors. It was found that these correlations were valid for a large range of Reynolds numbers. Unlike many of the previous correlations, these correlations are independent of the geometric dimensions (L/D).

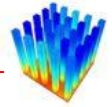
Chapman et al. [30] compared the heat transfer performance of elliptical pin fin heat sinks with square pin fin heat sinks and extruded heat sinks in a forced convection configuration. The idea behind elliptical pins is to minimise the pressure drop over the heat sink due to vortices behind the fins. They also tested the influence of flow bypass over all three types of heat sinks.

Maudgal and Sunderland [31] investigated forced convection and radiation from round in-line pin fin heat sinks. The parameters that they studied were inclination angle, tip clearance, fin diameter, fin spacing and fluid flow rate. Measurements of flow velocity, pressure and temperatures were taken from their experimental set-up. The radiation heat transfer component was determined analytically. The experimental values were used to generate an empirical correlation for the area-averaged Nusselt number.

Ryu et al. [32] also did experimental testing of square in-line pin fin heat sinks with no flow bypass. They characterised the heat sinks by plotting the thermal resistance and pressure drop data against different parameters.

Shaukatullah et al. [33] did a study to determine the best compromised square pin fin heat sink for low velocity flow configurations. They did experiments on several fabricated pin fin heat sink designs and commercially available heat sinks. The goal of the study was to maximise the heat sink thermal performance. The parameters involved were base size, pin size, pin height, fin count and channel velocity. There was a large amount of space around the heat sink for the flow to bypass when the pressure drop over the heat sink was high. The influences of flow direction and surface finish on the heat sinks were also tested.

Dogruoz et al. [27] did an experimental and modelling study on in-line square pin fin heat sinks with bypass flow. They compared pressure drop characteristics and thermal



resistance. They found good agreement between their bypass model and the experiments conducted with high flow velocities and long fins.

An experimental study on round pin fin heat sinks was carried out by Rizzi and Catton [34] to support the development of optimisation studies by supplying more detailed data for the heat transfer coefficients of the pin fin heat sinks.

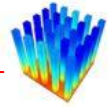
Pin fins with impingement flow

Reddy and Hammoud [35] did some experiments on high Reynolds number impingement cooling of pin fin heat sinks. They compared their experiment with the numerical CFD code called Icepak as well as Qfin. They determined that the thermal resistance of the experimental data was lower than that of the commercial packages' solutions, but that the trends were correct.

Zheng and Wirtz [36] created new correlations for the friction factor and average heat transfer coefficient in cylindrical pin fin heat sinks with impingement flow. They also determined that the fan-driven impingement cooling configuration resulted in lower pressure drop and heat transfer rates than the jet-driven impingement flow configuration.

Jung and Maveety [37] performed numerical experiments to investigate the turbulent fluid flow and heat transfer from pin fin heat sinks with impingement cooling at high Reynolds numbers. The k-epsilon turbulence model was used in the numerical experiments. The numerical values compared favourably with available experimental data.

Kobus and Oshio [38] carried out an experimental study on pin fin heat sinks with impingement flow, by investigating the thermal performance and overall convective heat transfer coefficients of the heat sinks. A theoretical model was correlated to the experimental data to predict the pin fin characteristics.



2.3 CURRENT HEAT SINK DESIGN OPTIMISATION PROCEDURES

The optimisation of heat sink designs is a very complicated procedure. First, one has to select the variable or combination of variables to optimise. Then one has to select the parameters that will have an influence on the optimisation and select the boundaries of these parameters. To include all the effects of all the parameters is a daring task, and consequently, in most optimisation procedures less than three parameters are chosen for the optimisation.

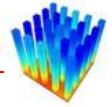
Usually, heat sink designers adjust the different parameters manually and select a set of parameters that gives a lower thermal resistance than their original design to be the optimal design. This method is very crude and depends on the experience of the designer to interpret the results and change the parameters in order to obtain an improved design.

The following paragraphs describe a few attempts at optimising heat sink designs. There are many more, but the ones selected provide an overall indication of how most optimisation is done.

Shah et al. [39] optimised the fin shapes on an extruded fin heat sink by using a fixed number of designs and solving them in the numerical code called Flotherm. The optimum design is selected to be the design with the lowest thermal resistance and pressure drop.

Shi et al. [3] optimised the cooling design of an optical transponder. They tested several heat sink designs with different parameter values by making use of a CFD code. Their optimum design was selected to be the heat sink with the lowest junction temperature.

Enertron Inc [40] published a research paper describing a method to determine the optimum channel width/length ratio for an extruded fin heat sink by using an experimental method and a theoretical method. In the experimental method, several heat sinks were tested and the thermal resistance of each was calculated and plotted.



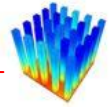
The theoretical method used convection and fin conduction theory to calculate the thermal resistance.

Arik et al. [41] used numerical and analytical approaches to solve and optimise the thermal performance of power electronics. They optimised two parameters by first optimising for the one and keeping the other one fixed, and then when the first one was optimised, the other one was optimised. For simple problems, this method might produce the overall optimum, but in general one has to optimise both parameters at the same time since the optimum can be an intricate function where the variables can be in the same terms and not necessarily separate from each other. The optimum is therefore not the global optimum but rather a local optimum design, which is still better than the initial design.

Lee [42] created an analytical model to determine the thermal resistance of extruded heat sinks. This model was based on a correlation for the overall heat transfer coefficient of plates heated on one end. He validated it against experimental data, and also plotted the thermal resistance against each of the selected parameters separately to determine their effect on the thermal resistance. As mentioned previously, this does not necessarily provide the overall optimum set of parameter values. An overview of different design parameters that can be selected as optimisation parameters is also given.

Biber and Fijol [43] also plotted the influence of each selected parameter on the thermal resistance of extruded heat sinks. They used a fan curve to determine the flow characteristics from the pressure drop through the heat sink. The heat transfer was solved by making use of a correlation for forced convection between parallel plates. Fin efficiencies and the air temperature were also taken into account.

None of these methods can prove that the selected heat sink design is actually the global optimum, or even a strong local optimum. The methods where equations are available to calculate the thermal resistance or base temperature, for example, an empirical correlation or fin conduction theory, have a huge advantage when one looks at optimising designs. An optimisation procedure to determine the global or strong local optimum can be applied to these methods with relative ease. One significant



problem with these methods is the fact that only average values for the entire heat sink are calculated and not detailed values, as available from CFD solutions.

The thermal design tool, Qfin, uses heat transfer theory and correlations to determine the heat transfer coefficients and solve the temperatures in the solids with a curvilinear form of the discretised diffusion equation. This method results in detailed solutions of the design problem. The next section describes how Qfin works.

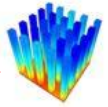
2.4 THE THEORY BEHIND QFIN

Qfin [6] is a fluid flow and heat transfer calculation software tool. It is mostly used by thermal engineers as a quick cooling design tool for electronic systems. Qfin can be used to solve component, board or system-level problems.

One starts by adding components to the design domain. Several standard pre-defined components exist, which can be added directly to the design. Complex three-dimensional shapes can be obtained by adding several basic shapes together.

The list of standard components includes:

- Heat sinks
- Heat sources
- Packages
- Fans
- Openings
- Blocks
- Flow resistance blocks
- Plates
- Local boundaries
- Printed circuit boards (PCBs)



Each standard component is defined by a list of parameters. The values of the parameters can be modified to set up the design problem.

Figure 2-4 shows a screen shot of a typical heat sink and fan simulation inside Qfin.

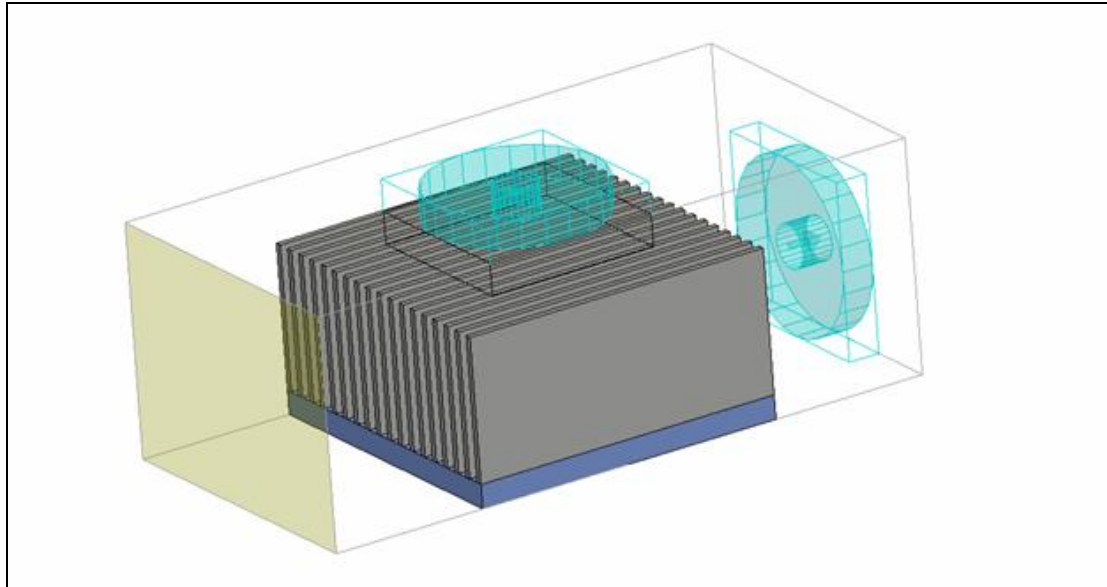


Figure 2-4: Typical heat sink and fan combination in Qfin

Source: Qfinsoft Technologies [44]

After the design has been created, a mesh is automatically generated with some user control. The solutions are calculated in two steps. First, the flow field is solved by using a system solver. After this, the boundary conditions for the energy equation are calculated by using the values from the flow solution. The energy equation is then solved by using a full three-dimensional conduction solver.

Post-processing can be done by plotting temperature curves and velocity fields in the domain. Reports can also be printed out with detailed information on the solution. Figure 2-5 displays an example of the post-processing capabilities of Qfin.

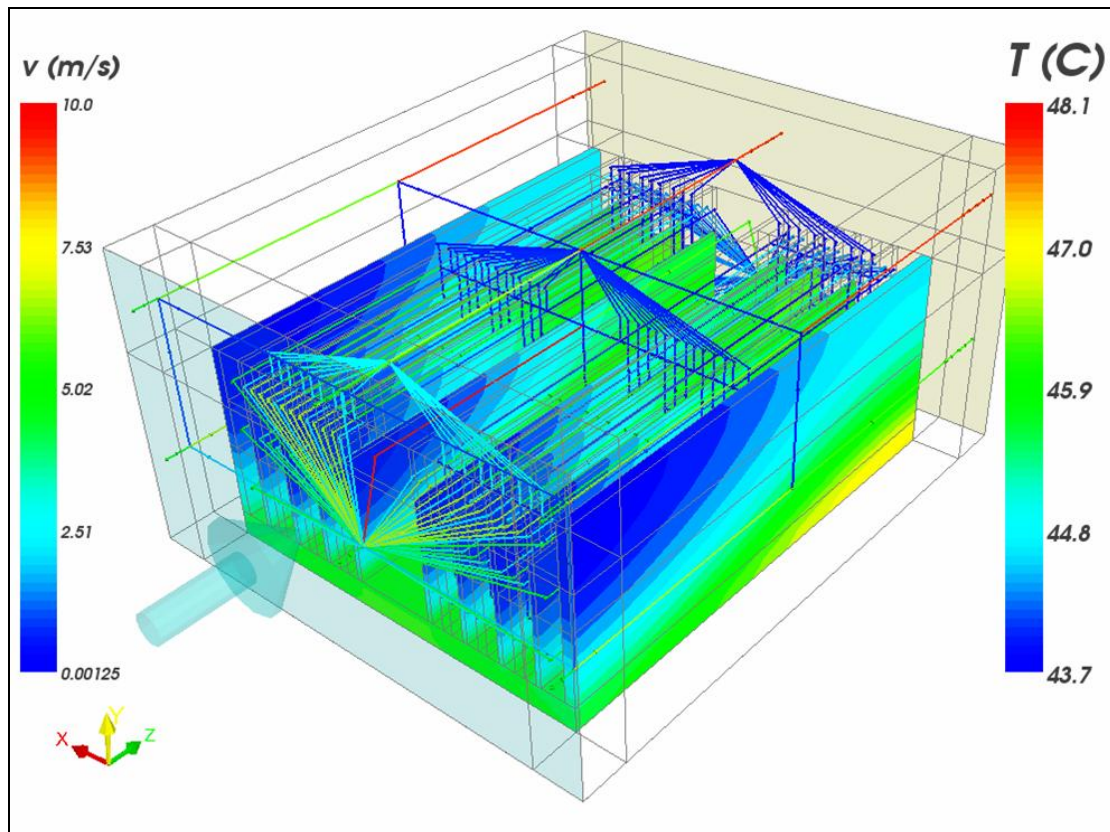
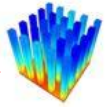
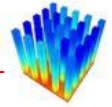


Figure 2-5: Post-processing data in Qfin

Source: Qfinsoft Technologies [44]

Qfin has a built-in optimisation algorithm that can be used to optimise a design for a specific application. One simply selects the function to optimise as well as the parameters and their limits to use in the optimisation, and an optimised solution will be calculated. This optimisation procedure is based on the Dynamic-Q optimisation procedure developed by Snyman [45].

The outcome of this study will be incorporated into Qfin in the form of an equation calculating the boundary conditions of pin fin heat sinks before solving the energy equation by making use of the flow solution and geometric parameters of the heat sink.



2.5 NUMERICAL MODELLING

The governing equations of fluid flow, called the Navier-Stokes equations, are a set of complex non-linear partial differential equations describing mass and momentum conservation in a fluid.

CFD is a modelling method for solving these non-linear equations by means of a discretised domain of the fluid region by enforcing certain boundary conditions on the fluid. Together with these Navier-Stokes equations, one can also solve additional conservation equations like energy, combustion and multiphase flow.

A CFD analysis consists of setting up the problem (pre-processing), solving the problem (discrete solver), and examining the results (post-processing).

The pre-processing step consists of the following:

- Defining the necessary outputs
- Determining the domain that will be solved
- Modelling the domain
- Generating the mesh

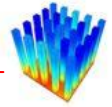
Solving consists of the following steps:

- Setting up the model to solve all the necessary equations
- Defining the boundary equations
- Running the solver and checking for convergence

Post-processing consists of the following steps:

- Examining the results
- Retrieving the relevant data
- Determining if the solution is adequate or needs revision

Further discussion on some of these points follows.



2.5.1 Mesh generation

Mesh generation is the process of dividing the domain that needs to be solved into small blocks, called control volumes. The discretised governing equations will be solved on each of these blocks. Usually mesh generation takes up a large percentage of the overall time of a CFD solution and therefore several mesh generation packages are available and are being developed for automatic mesh generation.

In this study, the pre-processor Icepak [46] was used to create all the meshes needed. Icepak was developed especially for electronics cooling applications and is therefore perfectly suited for this study. Icepak has predefined components representing common objects in electronics cooling applications, for example, heat sinks, grilles, printed circuit boards, heat sources and fans. One can then add any number of these components to a project and change the values of the parameters of each component to represent the problem under consideration. After the geometry has been built, a mesh can be generated automatically. The available meshing schemes are hexahedral unstructured, hexahedral Cartesian and tetrahedral. Icepak uses the Fluent solver to solve the problem at hand directly in Icepak.

The components in Icepak are parameterised, so one can define an array of values for each parameter and Icepak can then be used to solve each possible combination of parameter values as a different problem. This feature makes Icepak a very attractive program to use as a tool in automating the data generation process of this particular study.

2.5.2 Navier-Stokes equations

The Navier-Stokes equations are a set of non-linear partial differential equations describing a fluid field. These equations are derived from the conservation of momentum and mass.



2.5.3 Conservation of mass

The conservation of mass, also called the continuity equation, in its general form for fluid flow is given as follows:

$$\frac{\partial \rho}{\partial t} + \text{div} \rho \mathbf{V} = S_m \quad (12)$$

where ρ is the density, t is the time, \mathbf{V} is the velocity vector, and S_m is the mass source. In this particular application, there is no mass source. In a low velocity flow field, with small temperature differences, it can be assumed that the density of air is constant. With this assumption, the continuity equation simplifies to

$$\text{div} \mathbf{V} = 0 \quad (13)$$

2.5.4 Conservation of momentum

The conservation of momentum, also known as Newton's second law, is used to derive the Navier-Stokes equations. From an Eulerian view, in indicial notation, the set of equations can be written as:

$$\rho \frac{D\mathbf{V}}{Dt} = \rho \mathbf{g} - \nabla p + \frac{\partial}{\partial x_j} \left[\mu \left(\frac{\partial v_i}{\partial x_j} + \frac{\partial v_j}{\partial x_i} \right) + \delta_{ij} \lambda \text{div} \mathbf{V} \right] \quad (14)$$

where

\mathbf{g} : Gravitation vector [m/s²]

x : Spatial coordinate [m]

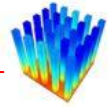
\mathbf{V} : Velocity vector [m/s]

μ : Coefficient of viscosity [Pa.s]

λ : Coefficient of bulk viscosity [m/s²]

δ_{ij} : Kronecker Delta function ($\delta_{ij} : 1$ if $i=j$ and $\delta_{ij} : 0$ if $i \neq j$)

$\frac{D}{Dt}$: Total derivative



For low velocity applications, incompressible flow can be assumed, which reduces Equation 14 to the following:

$$\rho \frac{DV}{Dt} = \rho \mathbf{g} - \nabla p + \mu \nabla^2 \mathbf{V} \quad (15)$$

For special cases with steady-state flow conditions, where the velocities do not change in time, and small vertical dimension with a low density fluid, the equation can be reduced to the following:

$$\rho = -\nabla p + \mu \nabla^2 \mathbf{V} \quad (16)$$

2.5.5 Conservation of energy

The first law of thermodynamics is used to derive an equation for the conservation of energy in Eulerian terms. Conduction heat flux is assumed to follow Fourier's law, and radiation is neglected due to relative low temperature conditions.

$$\rho \frac{Dh}{Dt} = \frac{Dp}{Dt} + \text{div}(k\nabla T) + \Phi \quad (17)$$

where

$\frac{D}{Dt}$: Total derivative

h : Fluid enthalpy [J/kg]

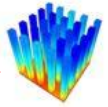
p : Pressure [Pa]

k : Thermal conductivity [W/m.K]

T : Temperature [K]

Φ : Viscous dissipation [W/m³], defined as

$$\Phi = \mu \left[2 \left(\frac{\partial u}{\partial x} \right)^2 + 2 \left(\frac{\partial v}{\partial y} \right)^2 + 2 \left(\frac{\partial w}{\partial z} \right)^2 + \left(\frac{\partial v}{\partial x} + \frac{\partial u}{\partial y} \right)^2 + \left(\frac{\partial w}{\partial y} + \frac{\partial v}{\partial z} \right)^2 + \left(\frac{\partial u}{\partial z} + \frac{\partial w}{\partial x} \right)^2 \right] + \lambda \left(\frac{\partial u}{\partial x} + \frac{\partial v}{\partial y} + \frac{\partial w}{\partial z} \right)^2$$



When incompressible flow, constant thermal conductivity and low-velocity flow are assumed, Equation 17 reduces to:

$$\rho c_p \frac{DT}{Dt} = k \nabla^2 T \quad (18)$$

The viscous dissipation is insignificant at low velocity flow conditions.

2.5.6 Turbulence modelling

In turbulent flow, there are small-scale fluctuations in the flow field. Due to computational constraints, these small-scale fluctuations cannot be resolved in the standard Navier-Stokes equations on a normal-sized grid. To take these fluctuations into account, the standard Navier-Stokes equations have to be changed. Every quantity in the Navier-Stokes equations is written as a quantity consisting of a mean part and a fluctuating part. This is called the Reynolds-Averaged Navier-Stokes equations (RANS). For example, the velocity component will look like this:

$$u_i(\vec{x}, t) = U_i(\vec{x}, t) + u_i'(\vec{x}, t) \quad (19)$$

where

U_i : Mean velocity [m/s]

u_i' : Fluctuating velocity [m/s]

Figure 2-6 shows how the turbulence is divided into mean and fluctuating velocities.

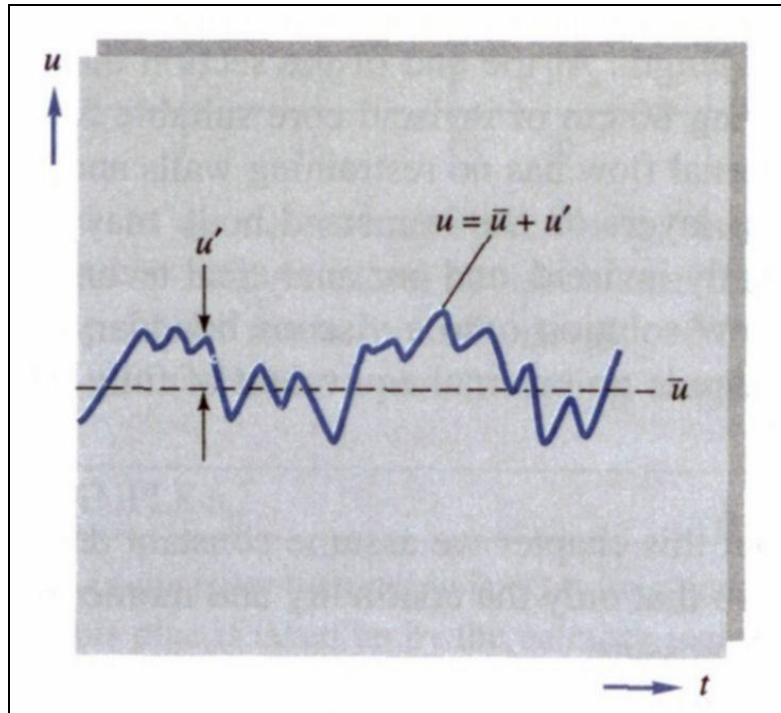
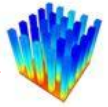


Figure 2-6: Mean and fluctuating turbulent velocities

Source: White [47]

The RANS equations for incompressible flow with constant viscosity are given as:

$$\rho \frac{D\bar{V}}{Dt} + \rho \frac{\partial}{\partial x_j} \left(\overline{u_i u_j} \right) = \rho \bar{g} - \nabla \bar{p} + \mu \nabla^2 \bar{V} \quad (20)$$

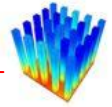
where

u_i' : Small fluctuations in the velocity field [m/s]

\bar{V} : Time-averaged velocity vector [m/s]

\bar{p} : Time-averaged pressure [Pa]

In this equation, the term $\left(\overline{u_i u_j} \right)$ is called the Reynolds stress term, or the turbulent inertia tensor. This term is not known when starting a solution and can therefore not be calculated. Instead, this term is replaced with a turbulence model, which simulates the turbulent inertia tensor. Instead of calculating the turbulent inertia tensor, the dynamic viscosity term is modified to contain the sum of the fluid viscosity and the



turbulent viscosity. The turbulent viscosity is directly calculated from the turbulence model equations. Several different turbulence models are available and can be divided into groups, depending on the complexity of the models.

Zero-equation models

The zero-equation models are computationally very inexpensive, but not very accurate. They only model local flow behaviour with a simple algebraic equation and do not use information from the surrounding flow field. The most common model in this category is the Mixing-length model.

One-equation models

The second group of turbulence models are based on the turbulent kinetic energy equation. These models use algebraic equations to correlate the length scales. The models are only slightly better than the zero-equation models, but are computationally more expensive and are therefore not used very often. The Spalart-Allmaras [48] model is the most common model, and is specifically developed for high velocity flows in an external configuration.

Two-equation models

These models are the most popular models. They are accurate enough to give usable solutions and are not too computationally expensive. The turbulent kinetic energy equation from the one-equation models is expanded with a second equation which models the rate of change of a selected variable. There are mainly two families of models in this category; the $k-\varepsilon$ models [49][50][51] and the $k-\omega$ models [52][53].

Other models

There exist other methods that cannot be placed in one of these categories. Most of them are more accurate, but also more computationally expensive. The Reynolds stress model (RSM) [54] models the Reynolds stresses by using partial differential equations. The RSM model has a big advantage over the two-equation models and has



the potential to be more accurate because the turbulence in the RSM model is not assumed to be isotropic. All the previous models are based on the assumption that the turbulence is isotropic. The Large-Eddy simulation (LES) tries to solve all but the very small fluctuations in the flow field. For these very small fluctuations, one of the two-equation models is used. To be able to solve small fluctuations, a very fine mesh is needed and the solution needs to be unsteady. This makes the LES model computationally very expensive. The most accurate method available is Direct Numerical solution. This method solves even the very small fluctuations in the flow field, and no modelling of turbulence is used. Because of the extreme fine mesh and small time step, this method is impractical for most applications.

Turbulence models are usually only valid from a certain distance from a wall. The distance close to a wall is divided into layers, consisting of the viscous sublayer, buffer layer, fully turbulence layer and the outer layer. Figure 2-7 displays these layers graphically.

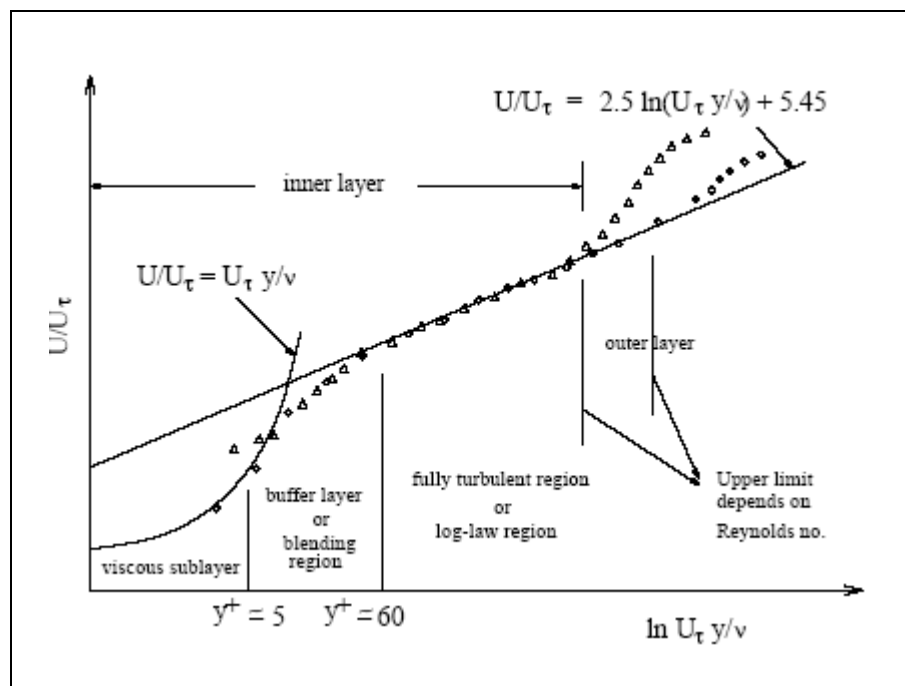
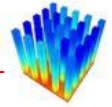


Figure 2-7: Graphical representation of the different turbulence layers

Source: Fluent manual [55]

Turbulence models are usually only valid from the fully turbulent region. There are basically two methods for dealing with the region between the wall and the start of the



turbulence model. For high Reynolds turbulence models, wall functions are used between the wall and the start of the turbulence models. Wall functions are semi-empirical equations and functions, which model the variables like velocity, turbulence and other scalars in the region between the wall and the turbulence model.

A second method for calculating turbulence at low Reynolds numbers is to modify the turbulence models to be valid up to the wall. This is called the near-wall approach. To use this approach, the mesh close to the wall needs to be very fine in order to model this correctly. This is shown in Figure 2-8.

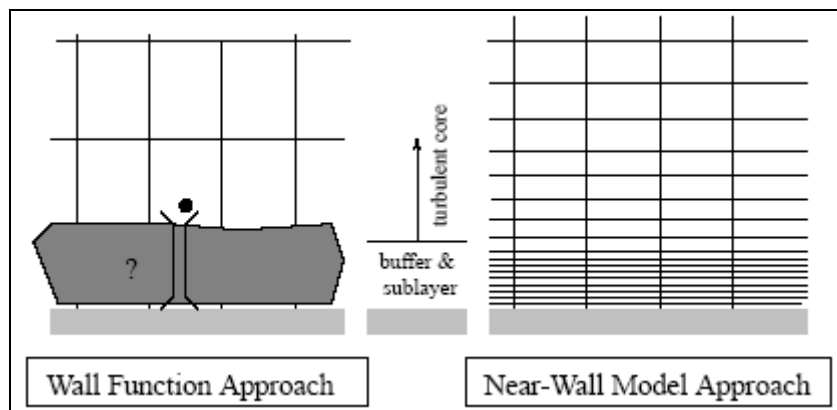
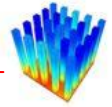


Figure 2-8: Difference between Wall function and Near-wall approaches

Source: Fluent manual [55]

2.5.7 Solving the equations

In this study, the commercial CFD solver, Fluent [55], was used to solve the heat transfer and fluid flow through heat sinks. Fluent uses the finite volume approach, based on control volumes. In the finite volume approach, the governing equations are integrated over each control volume in the pre-generated mesh. Algebraic equations for all the dependent variables are constructed through the integration process. The algebraic equations are then linearised to simplify the solutions process. This yields a system of linear equations, which can be solved by adding boundary conditions to constrain the problem.



A direct matrix inversion to solve this set of linear equations is not feasible due to the size and amount of variables in the problem. Instead, the matrix is solved in an iterative method. The segregated method of Fluent was used in this study, which means that the governing equations are solved one after the other instead of simultaneously. The governing fluid flow equations are in fact coupled, which means they are dependent on each other, and for this reason numerous iterations have to be performed to get a converged solution. Before starting the solution, one has to define an initial value for every variable in each control volume in the mesh. Each iteration consists of the following steps:

1. Fluid properties are updated based on the current variable values.
2. The velocity fields in all three directions (momentum equations) are solved one after another by using the current pressure and face mass fluxes.
3. The velocities solved in the previous step might not satisfy the continuity equation. Therefore, a Poisson-type equation is derived from the continuity equation and the momentum equations to calculate a pressure correction. This equation is then solved to obtain corrections for the pressure, velocity field and face mass fluxes. This ensures that continuity is satisfied.
4. The scalar equations such as energy and turbulence are then solved using the updated values of the other variables.
5. A convergence check is made. If the convergence criteria are not met, go to step one, otherwise stop.

These steps are also illustrated in Figure 2-9.

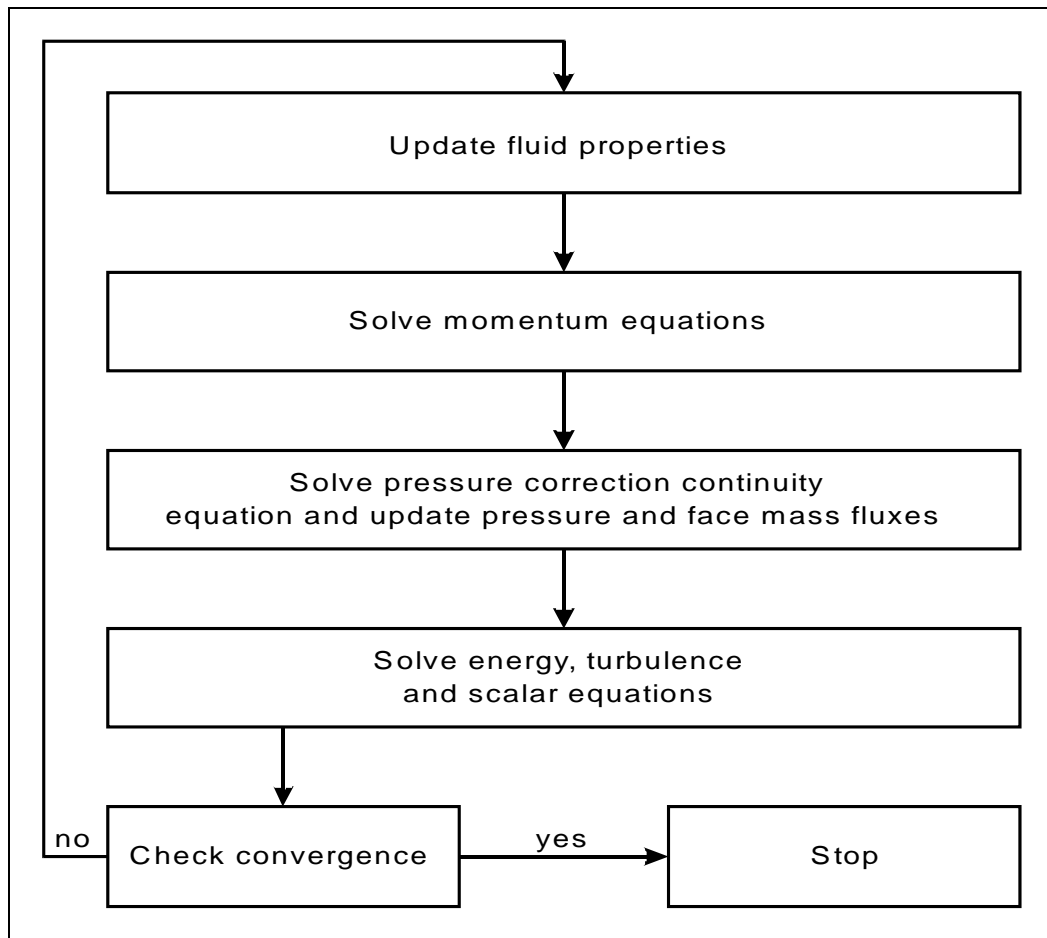
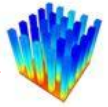


Figure 2-9: The iterative CFD process

2.6 MATHEMATICAL OPTIMISATION

Mathematical optimisation is the process of finding the minimum or maximum of a specific function, subject to a set of constraints.

A constrained optimisation problem can be defined in general as follows:

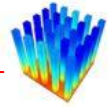
$$\text{Minimise } f(\mathbf{x}), \mathbf{x} = [x_1, x_2, \dots, x_n]^T \in \mathbb{R}^n \quad (21)$$

Subject to the constraints

$$g_j(\mathbf{x}) \leq 0, j = 1, 2, \dots, m$$

$$h_j(\mathbf{x}) = 0, j = 1, 2, \dots, r$$

Where $f(\mathbf{x})$, $g(\mathbf{x})$ and $h(\mathbf{x})$ are functions of the vector \mathbf{x}



The function $f(\mathbf{x})$ is called the objective or cost function, $g(\mathbf{x})$ and $h(\mathbf{x})$ denote the inequality and equality constraint functions respectively. The vector \mathbf{x} is called the variable vector, or in engineering terms, the design variables. The variable n denotes the number of design variables in the optimisation problem. The solution to the problem, or the optimum vector, is denoted by \mathbf{x}^*

$$\mathbf{x}^* = [x_1^*, x_2^*, \dots, x_n^*]^T \quad (22)$$

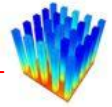
and gives the lowest value for the function $f(\mathbf{x})$ subject to the constraint functions.

Throughout the years, many optimisation procedures have been developed. It must be noted that there is no single optimisation procedure that will work for any optimisation problem. Every optimisation procedure is tailored to a specific type of problem and it is the user's responsibility to find an appropriate procedure for the particular problem at hand. This is an important choice and will determine the convergence rate and, in some cases, even whether an optimum set of design variables will indeed be found.

This chapter will only describe the optimisation methods used in this study. More information on state-of-the-art optimisation procedures can be found in mathematical optimisation literature [45].

2.6.1 Optimisation algorithms

In this study, four different optimisation algorithms were used to determine the optimum values for the constants in the correlated equation for the contraction heat transfer coefficient. The first method that will be discussed is the LFOPC method of Snyman [45]. The LFOPC method is the primary optimisation code used in this study due to the simplicity of setting up the problem. The LFOPC method was used as a Matlab [56] script. A second method, the Dynamic-Q method [45], was also used in this study for smaller optimisation tests. The program, Toolkit for Design Optimisation (TDO) [57], was used because of its simple implementation of the



Dynamic-Q method, although it has a limit of five optimisation variables. An extremely simple one-dimensional minimisation method was also used to determine the effect of a change in variable values on the correlations created. A non-linear optimisation algorithm from the Matlab Optimization Toolbox [58] was used to validate the optimised coefficients from the LFOPC algorithm.

2.6.2 LFOPC

The LFOPC (Leap-frog optimisation procedure for constrained minimisation) optimisation method by Snyman [45], also called the Dynamic Trajectory method, is an extension of the LFOP (Leap-frog optimisation procedure) to handle constrained optimisation problems.

The outstanding characteristics of the LFOP procedure are:

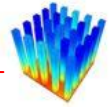
1. It only uses function gradient information.
2. No explicit line searches are performed.
3. It is extremely robust, handling steep gradients, noise and discontinuities with relative ease.
4. The algorithm seeks relative low local minima and can therefore be used as the basic component in global optimisation.
5. It can handle a lot of variables with no difficulty.

The basic model on which this procedure is based is the dynamic movement of a particle in a conservative force field. The particle with unit mass with potential energy at \mathbf{x} given by $f(\mathbf{x})$ is subject to an acceleration force (\mathbf{a}) given by:

$$\mathbf{a} = \ddot{\mathbf{x}} = -\nabla f(\mathbf{x}) \quad (23)$$

The motion of the particle of the time interval $[0, t]$ can be described in terms of energy as:

$$\frac{1}{2} \|\dot{\mathbf{x}}(t)\|^2 - \frac{1}{2} \|\dot{\mathbf{x}}(0)\|^2 = f(\mathbf{x}(0)) - f(\mathbf{x}(t)) \quad (24)$$



or

$$T(t) - T(0) = f(0) - f(t) \quad (25)$$

Where $T(t)$ represents the kinetic energy of the particle at time t . For the conservation of energy, it follows that

$$f(t) + T(t) = \text{constant} \quad (26)$$

And therefore, as long as T increases, f needs to decrease. This is the underlying principle on which the dynamic leap-frog optimisation procedure is based.

The extension to constrained optimisation is done by adding a penalty function formulation to the original optimisation equation. The penalty function formulation is given by:

Minimise $P(\mathbf{x})$ where

$$P(\mathbf{x}, \boldsymbol{\rho}, \boldsymbol{\mu}) = f(\mathbf{x}) + \sum_{j=1}^r \rho_j h_j^2(\mathbf{x}) + \sum_{j=1}^m \beta_j g_j^2(\mathbf{x}) \quad (27)$$

where the components of the penalty vectors $\boldsymbol{\rho}$ and $\boldsymbol{\mu}$ are given by:

$$\rho_j \gg 0$$

$$\beta_j = \begin{cases} 0 & \text{if } g_j(\mathbf{x}) \leq 0 \\ \mu_j \gg 0 & \text{if } g_j(\mathbf{x}) > 0 \end{cases}$$

2.6.3 Dynamic-Q

The Dynamic-Q optimisation method is an efficient and robust method of solving constrained optimisation problems. This method solves successive quadratic approximations to the actual optimisation problem. This approach of creating approximations, and the fact that it uses very few function evaluations, makes this method ideal for optimisation problems where the function evaluations are computationally expensive. These types of problems are common in engineering



applications, for example, CFD, Finite Element Analysis (FEA) or multibody dynamic systems.

The successive subproblems ($P[i]$, $i=0,1,2,\dots$) are created at successive approximations \mathbf{x}^i to the solution \mathbf{x}^* , by constructing spherical quadratic approximations ($\tilde{f}(\mathbf{x}), \tilde{g}_j(\mathbf{x}), \tilde{h}_k(\mathbf{x})$) to the optimisation problem ($f(\mathbf{x})$) and the constraint functions ($g_j(\mathbf{x}), h_k(\mathbf{x})$). These approximation functions are as follows:

$$\begin{aligned}
 \tilde{f}(\mathbf{x}) &= f(\mathbf{x}^i) + \nabla^T f(\mathbf{x}^i)(\mathbf{x} - \mathbf{x}^i) + \frac{1}{2}(\mathbf{x} - \mathbf{x}^i)^T \mathbf{A}(\mathbf{x} - \mathbf{x}^i) \\
 \tilde{g}_j(\mathbf{x}) &= g_j(\mathbf{x}^i) + \nabla^T g_j(\mathbf{x}^i)(\mathbf{x} - \mathbf{x}^i) + \frac{1}{2}(\mathbf{x} - \mathbf{x}^i)^T \mathbf{B}_j(\mathbf{x} - \mathbf{x}^i), \quad j = 1, \dots, p \\
 \tilde{h}_k(\mathbf{x}) &= h_k(\mathbf{x}^i) + \nabla^T h_k(\mathbf{x}^i)(\mathbf{x} - \mathbf{x}^i) + \frac{1}{2}(\mathbf{x} - \mathbf{x}^i)^T \mathbf{C}_k(\mathbf{x} - \mathbf{x}^i), \quad k = 1, \dots, q
 \end{aligned} \tag{28}$$

with the Hessian matrices \mathbf{A} , \mathbf{B}_j and \mathbf{C}_k :

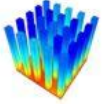
$$\begin{aligned}
 \mathbf{A} &= a\mathbf{I} \\
 \mathbf{B}_j &= b_j\mathbf{I} \\
 \mathbf{C}_k &= c_k\mathbf{I}
 \end{aligned} \tag{29}$$

and

$$\mathbf{I} = \text{diag}(1, 1, \dots, 1) \tag{30}$$

For the first subproblem, a , b_j and c_k are set to zero. From the second subproblem onwards, the curvatures are calculated so that the approximated function interpolates the actual function values at \mathbf{x}^i and \mathbf{x}^{i-1} . This implies that

$$\begin{aligned}
 a &= \frac{2[f(\mathbf{x}^{i-1}) - f(\mathbf{x}^i) - \nabla f(\mathbf{x}^i)(\mathbf{x}^{i-1} - \mathbf{x}^i)]}{\|\mathbf{x}^{i-1} - \mathbf{x}^i\|^2} \\
 b_j &= \frac{2[g_j(\mathbf{x}^{i-1}) - g_j(\mathbf{x}^i) - \nabla g_j(\mathbf{x}^i)(\mathbf{x}^{i-1} - \mathbf{x}^i)]}{\|\mathbf{x}^{i-1} - \mathbf{x}^i\|^2}, \quad j = 1, \dots, p \\
 c_k &= \frac{2[h_k(\mathbf{x}^{i-1}) - h_k(\mathbf{x}^i) - \nabla h_k(\mathbf{x}^i)(\mathbf{x}^{i-1} - \mathbf{x}^i)]}{\|\mathbf{x}^{i-1} - \mathbf{x}^i\|^2}, \quad k = 1, \dots, q
 \end{aligned} \tag{31}$$



If analytical formulae for the gradient vectors ($\nabla^T f, \nabla^T g_j, \nabla^T h_k$) are not known, they can be approximated by first-order differences.

The Dynamic-Q method also allows for lower and upper bounds on the variables. These bounds are implemented as first-order inequality constraints. These lower and upper limits are respectively of the form

$$\begin{aligned}\widehat{g}_l(\mathbf{x}) &= \widehat{k}_{vl} - x_{vl} \leq 0, \quad l = 1, 2, \dots, r \leq n \\ \widetilde{g}_m(\mathbf{x}) &= x_{wm} - \widetilde{k}_{wm} \leq 0, \quad m = 1, 2, \dots, s \leq n\end{aligned}\quad (32)$$

To keep the Dynamic-Q algorithm stable, move limits are placed on the variables. These move limits limit the amount the variable may change from one subproblem to the next. They are implemented as another inequality constraint

$$g_\rho(\mathbf{x}) = \|\mathbf{x} - \mathbf{x}^{i-1}\|^2 - \rho^2 \leq 0 \quad (33)$$

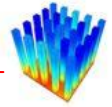
where ρ is an appropriately chosen step limit.

Together with all these limits, the approximated subproblem to the optimisation problem becomes

$$P[i] = \min_{\mathbf{x}} \widetilde{f}(\mathbf{x}), \quad \mathbf{x} = [x_1, x_2, \dots, x_n]^T \in \mathbf{R}^n \quad (34)$$

subject to

$$\begin{aligned}\widetilde{g}_j(\mathbf{x}) &\leq 0, \quad j = 1, 2, \dots, p \\ \widetilde{h}_k(\mathbf{x}) &= 0, \quad k = 1, 2, \dots, q \\ \widehat{g}_l(\mathbf{x}) &\leq 0, \quad l = 1, 2, \dots, r \\ \widetilde{g}_m(\mathbf{x}) &\leq 0, \quad m = 1, 2, \dots, s \\ g_\rho(\mathbf{x}) &= \|\mathbf{x} - \mathbf{x}^{i-1}\|^2 - \rho^2 \leq 0, \quad j = 1, 2, \dots, p\end{aligned}$$



These approximated subproblems are then solved with the LFOPC method described in Section 2.6.2 above.

Figure 2-10 summarises the Dynamic-Q procedure. In (1), an initial function value is calculated with initial guess x^0 . Together with the gradient vectors, or first-order finite difference function value (dx), the first approximated subproblem is set up in (2). The optimum (x^1) of the subproblem is calculated in (3). The actual function is then calculated at x^1 (4). Again the gradient vectors or another function value at x^1 is used to set up the second approximated subproblem (5). The optimum (x^2) of the second subproblem is calculated and used to calculate the actual function value (6). This procedure is then repeated until the convergence criteria have been reached.

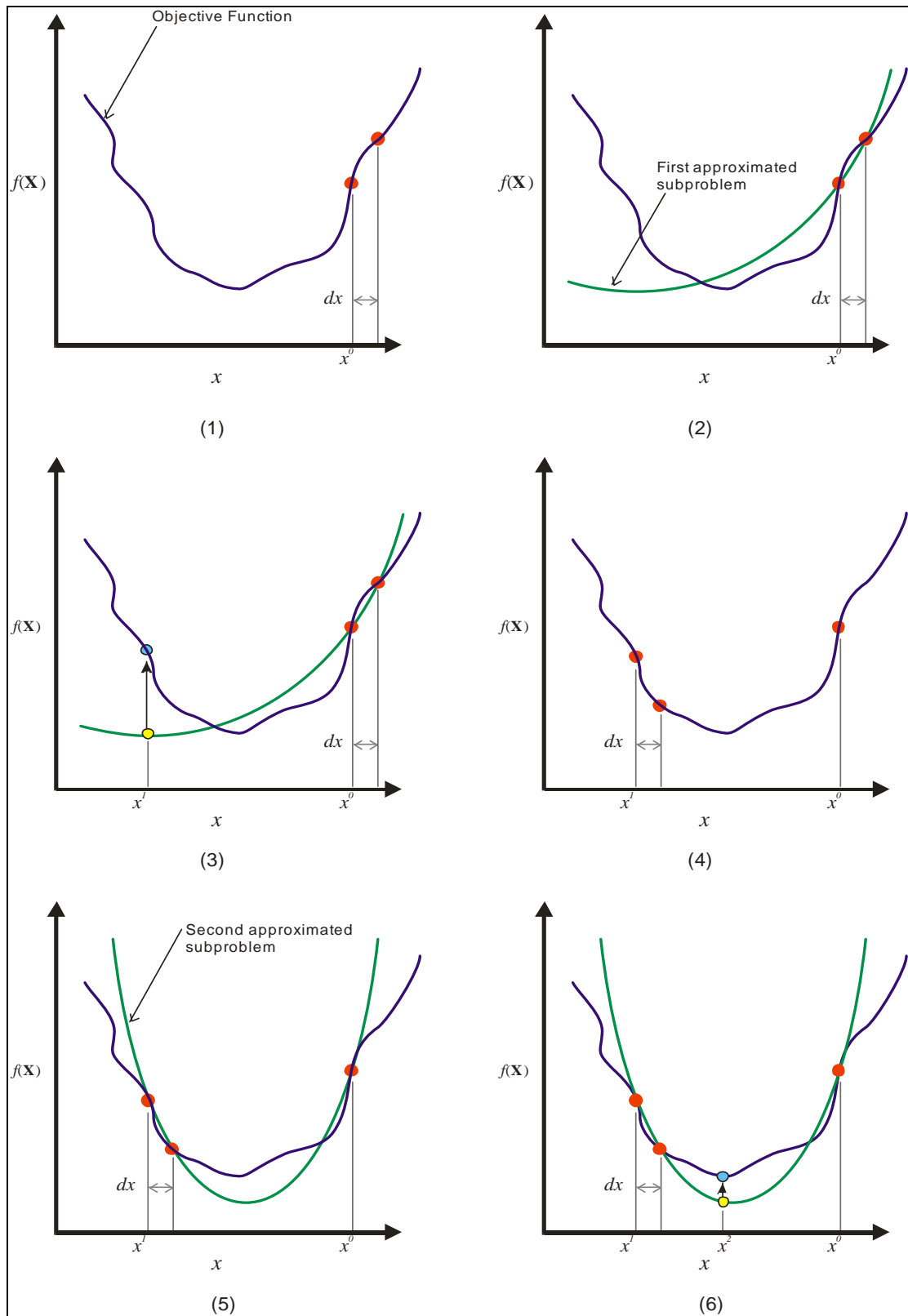
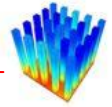


Figure 2-10: The Dynamic-Q method



2.6.4 Zero-order method

This quick and easy method can be described as a multivariable one-dimensional minimum search method based on discrete function values. This method seeks the lowest function value in a grid of orthogonal values calculated at discrete points along the variable axes. The minimum function value is selected as the local optimum and a new search is done around the selected local minimum. This continues until all the function values around the local minimum are higher than the local minimum.

A description of the method follows:

1. Select initial values (\mathbf{x}^0) for every variable in the function.
2. Choose a value for the discrete distance between search points (dx).
3. Loop until minimum is reached and dx is below a pre-defined value.
4. Calculate the function values at $[x_i - 2dx; x_i - dx; x_i; x_i + dx; x_i + 2dx]$ for $x_i = x_1, x_2, \dots, x_n$
5. Select the set of variables with the lowest function value as the new local minimum value.
6. If the original value is the lowest, decrease dx .
7. Go to step 3.

Figure 2-11 indicates an optimisation loop. In (1), the function value is calculated with the initial variable values. The function values around the initial value are calculated (2) and the minimum function value is selected as starting point for next iteration (yellow dot). Again the function values around the lowest point are calculated and a new minimum is chosen (3, 4). In step (5), the minimum function value corresponds to the initial function value. This results in a decrease in dx in (6).

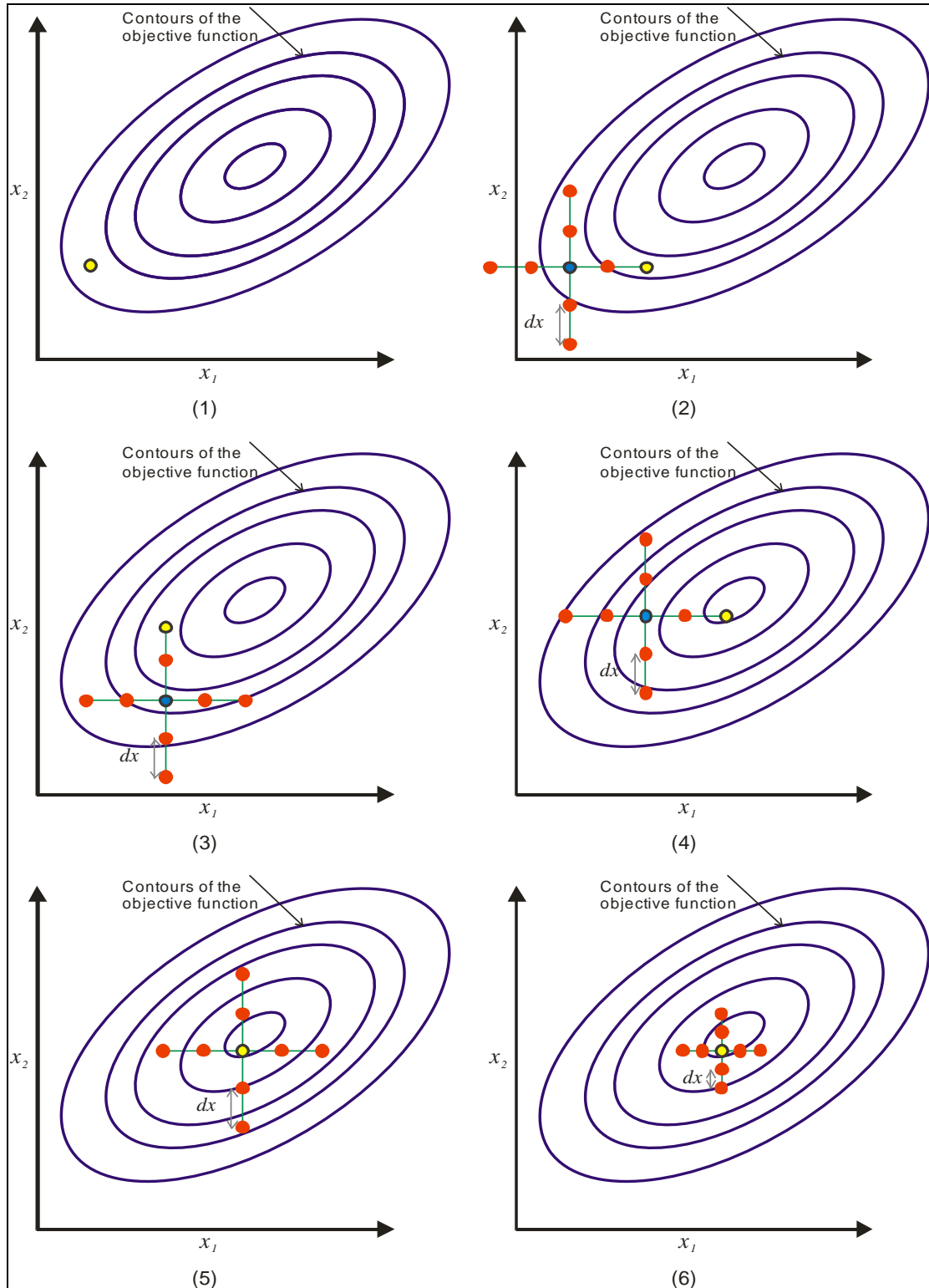
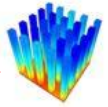


Figure 2-11: Zero-order optimisation example



2.7 CONCLUSION

This chapter looked at the literature and theory pertaining to this dissertation. The first part looked at current heat sink models available in the literature. This was followed by a discussion of current heat sink optimisation procedures, showing their inadequacies. A short description of the Qfin electronics cooling software, to which the formulae in this dissertation will be added, is given with a description of the modelling and optimisation methods used by Qfin.

The fourth part described the theory behind Computation Fluid Dynamics. It also discussed the different turbulence modelling techniques available. A discussion on all the different optimisation procedures used in this study concluded the chapter.



CHAPTER 3: EQUATION FORMULATION METHODOLOGY

3.1 INTRODUCTION

This chapter describes the methodology followed in obtaining optimised equations for the convection heat transfer coefficient of rectangular pin fin heat sinks. It is divided into four main parts.

The first part discusses the validation of CFD as a tool in the selected methodology. Since no physical experiments were done in this study, this step is very important in accepting the outcome of the study as applicable to physical heat sinks.

The second part gives an outline of the methodology developed in this study for generating the equations, and also describes in detail all the steps taken to get to the equations formulated in this study.

Sections 3 and 4, and Sections 5 and 6 of this chapter present the equations for laminar flow and turbulent flow respectively. These sections also discuss the accuracy and complexities in these equations and why they are different from each other. Section 7 summarises the correlations.

3.2 VALIDATION OF CFD MODEL

Before CFD could be used as a tool in generating data for this project, the CFD models and methodology had to be validated and compared with physical data. A set of heat sinks, which is often used in experimental research on pin fin heat sinks, was chosen. Data on this set of heat sinks were extracted from several papers from different authors [59] [33] [27] [32]. This set of heat sinks was modelled using Icepak [46] and Fluent. Afterwards, the data sets from the literature were compared with the CFD models of the heat sinks.



The main problem with modelling this particular set of heat sinks was the transitional Reynolds number range. It was decided to start with laminar flow and increase the Reynolds number for each heat sink until the CFD values and literature data did not compare satisfactory any more. From this point onwards, with increasing Reynolds numbers, turbulence modelling was used in the CFD models. Several different turbulence models were tested to select the model that fits the data best. A point was determined along the Reynolds number range where the CFD values were close enough to the literature values to be considered accurate enough for use in this study. The range between this point and the end of the laminar region was considered to be the transitional area. No calculations or comparisons were done in this region.

Two different mesh sizes were used in comparing the data. A coarser mesh was used in the laminar solutions than in the turbulent solutions. The y^+ values in the turbulent solutions were kept below five. This was done to make use of enhanced wall functions on the sides of the heat sink pins and increase the heat transfer accuracy. The mesh did not need to be as fine in the laminar flow cases since no wall functions were used.

The heat sink set that was selected for comparison consisted of relatively long pins and a variety of gap sizes and fin widths and lengths. The long fin heat sinks were chosen because this project needed average heat transfer coefficient data along the length of the pins, as it was decided to neglect base and tip influences. The longer the pins are, the less the top shroud and heat sink base will influence the heat transfer. The papers discussing the common pin fin data set give graphical representations of the average heat sink thermal resistances for several heat sinks in the selected data set. The average thermal resistance quantity was therefore chosen as the main criterion for comparing the literature and CFD data. The thermal resistance is defined as

$$R_{th} = \frac{\Delta T}{Q} = \frac{T_B - T_e}{Q} \quad (35)$$

where

T_B : Heat sink base temperature [K]

T_e : Fluid bulk temperature [K]

Q : Heat input [W]



Table 3-1 lists the set of heat sinks used to validate the CFD models and their dimensions. All the heat sinks had a base size of 25 x 25 mm with a height of 2.5 mm. Figure 3-1 shows the dimensions graphically.

Table 3-1: Test heat sink dimensions

Heat sink number	a [mm] Fin width	b [mm] Distance between fins	H [mm] Fin height	n Number of fins	$P_L=(a+b)/a$ Longitudinal pitch
1	1.5	6.333	22.5	4 x 4	5.222
2	1.5	4.375	22.5	5 x 5	3.917
3	1.5	3.200	22.5	6 x 6	3.133
4	1.5	2.417	22.5	7 x 7	2.611
5	1.5	1.857	22.5	8 x 8	2.238

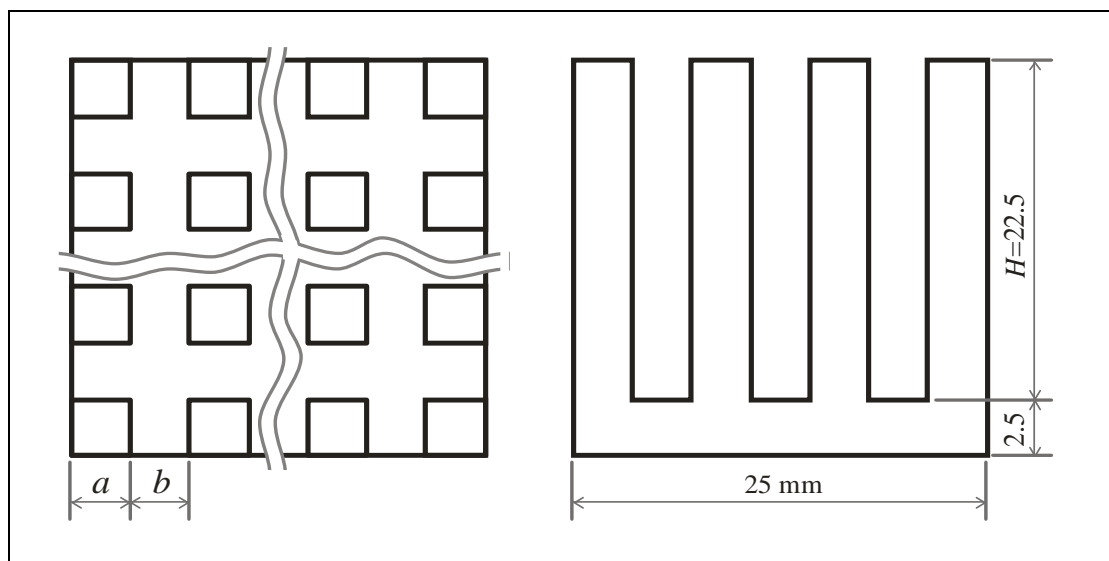


Figure 3-1: Heat sink dimensions

Figure 3-2 to Figure 3-5 display the graphs from the literature with which the CFD simulations have been compared.

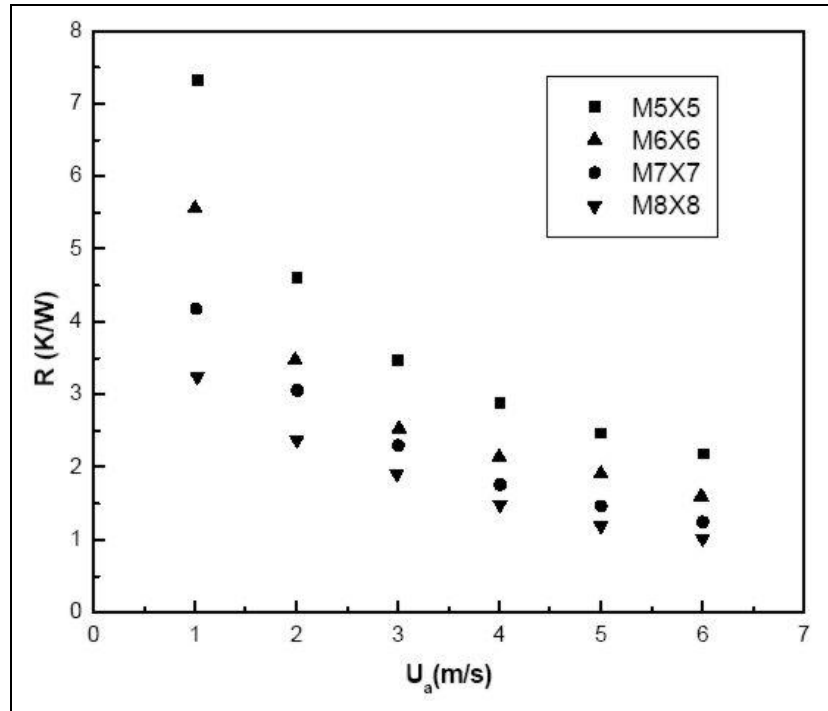


Figure 3-2: Measured thermal resistance data from literature, Comparison 1

Source: Lei and Ortega [59]

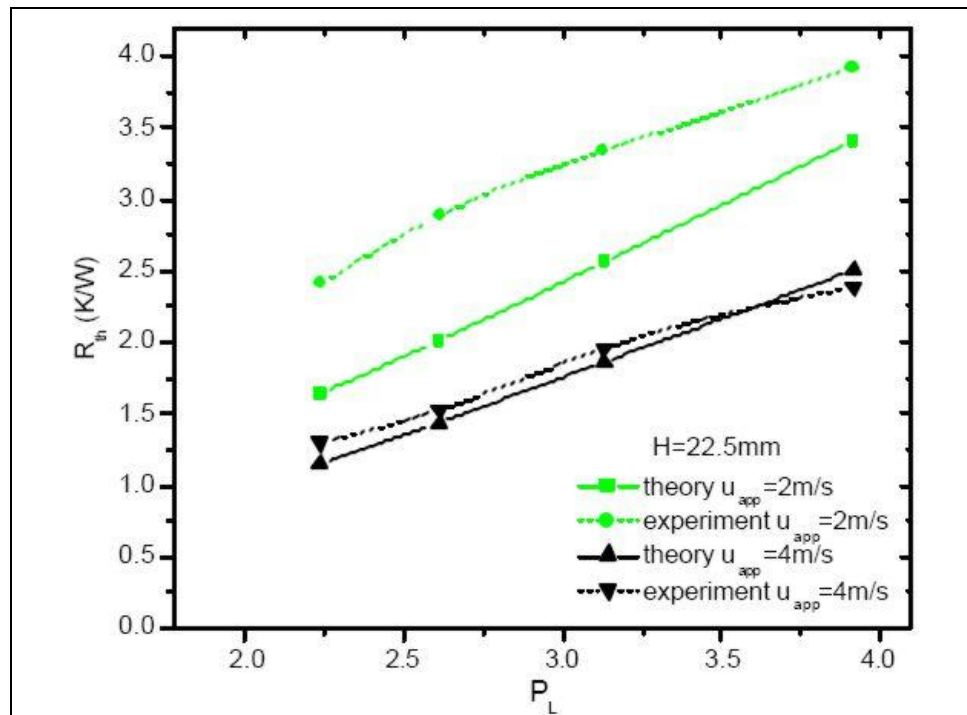


Figure 3-3: Measured thermal resistance data from literature, Comparison 2

Source: Dogruoz et al. [27]

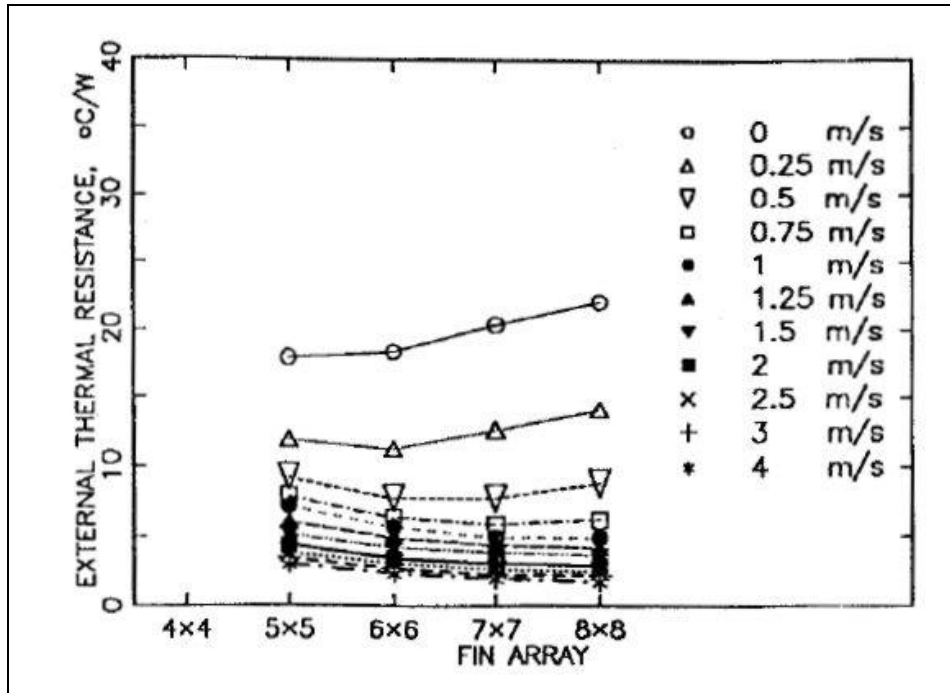


Figure 3-4: Measured thermal resistance data from literature, Comparison 3
Source: Shaukatullah et al. [33]

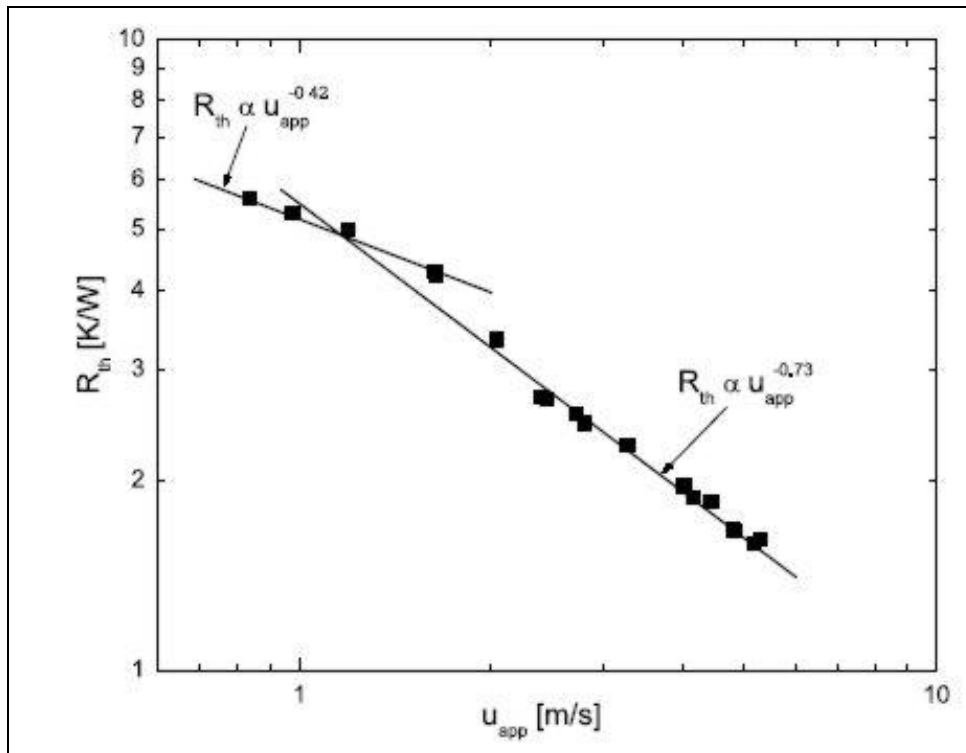


Figure 3-5: Measured thermal resistance data from literature, Comparison 4
Source: Dogruoz et al. [27]

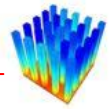


Figure 3-6 displays the literature data in Figure 3-2 to Figure 3-5 on a single graph. Each colour represents a heat sink from the selected set. Ideally, the series with the same colours should lie on top of each other, but there are some discrepancies in the literature data. This is probably due to differences in experimental set-ups, measuring equipment, external conditions and measuring accuracy.

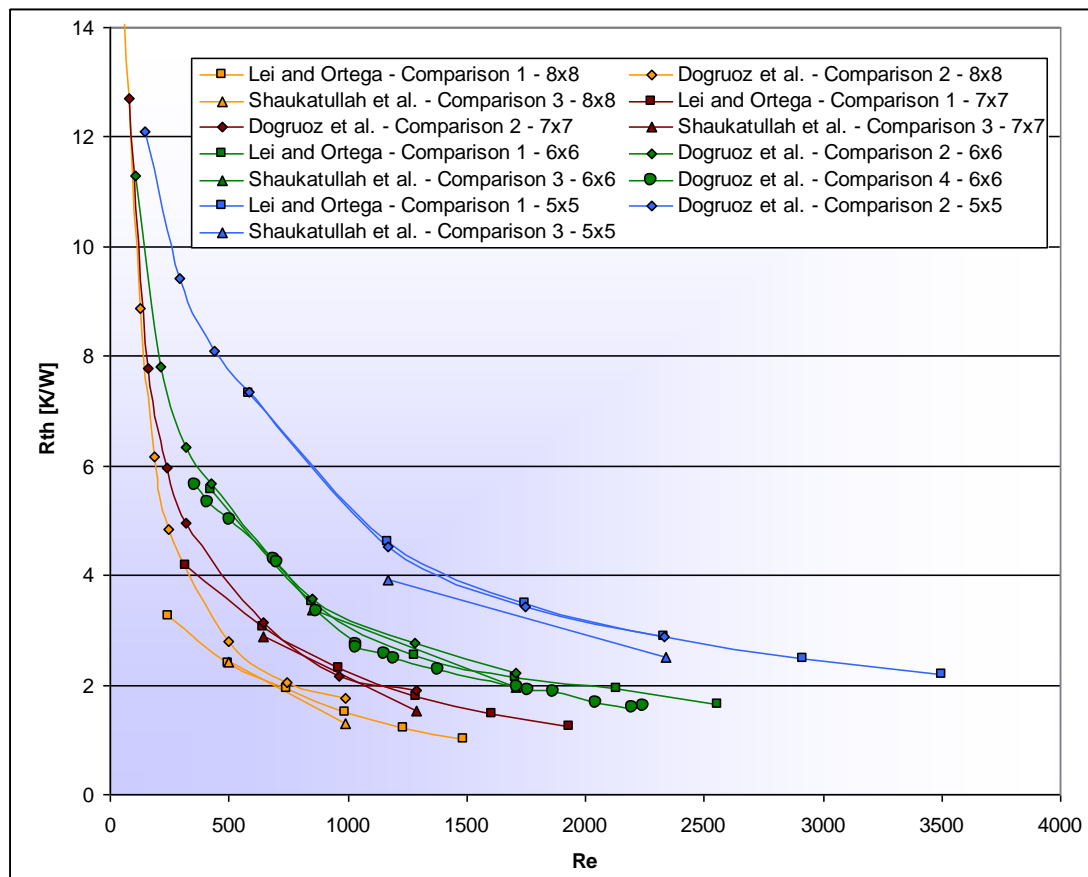


Figure 3-6: Combination of all literature data

Figure 3-7 to Figure 3-10 display comparisons of the literature data, shown in Figure 3-2 to Figure 3-5, with the CFD simulations using the laminar viscous model. The differences between the simulated laminar models and the literature data varies from 0% to 22%. In the Reynolds number range of 200 to 700, the data varies between 0% and 10% with 15 out of 21 data points below 5%. Since the Reynolds numbers between the CFD simulations and the literature data differ, the percentage differences for the data in Figure 3-10 were calculated using interpolated data based on a regression line through the CFD data. This was done to estimate the CFD thermal resistances at the Reynolds numbers used in the literature data.

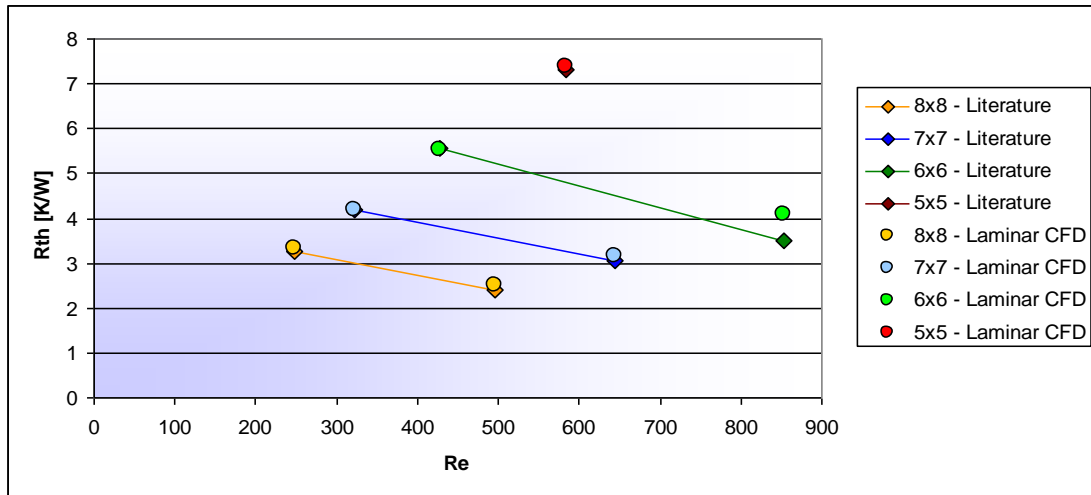


Figure 3-7: Laminar thermal resistance comparison with Lei and Ortega [59]

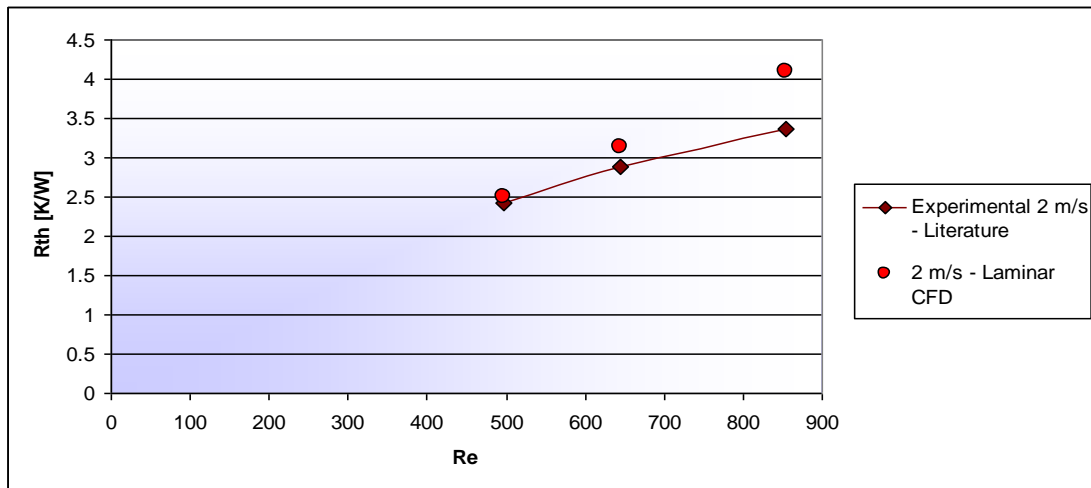


Figure 3-8: Laminar thermal resistance comparison with Dogruoz et al. [27]

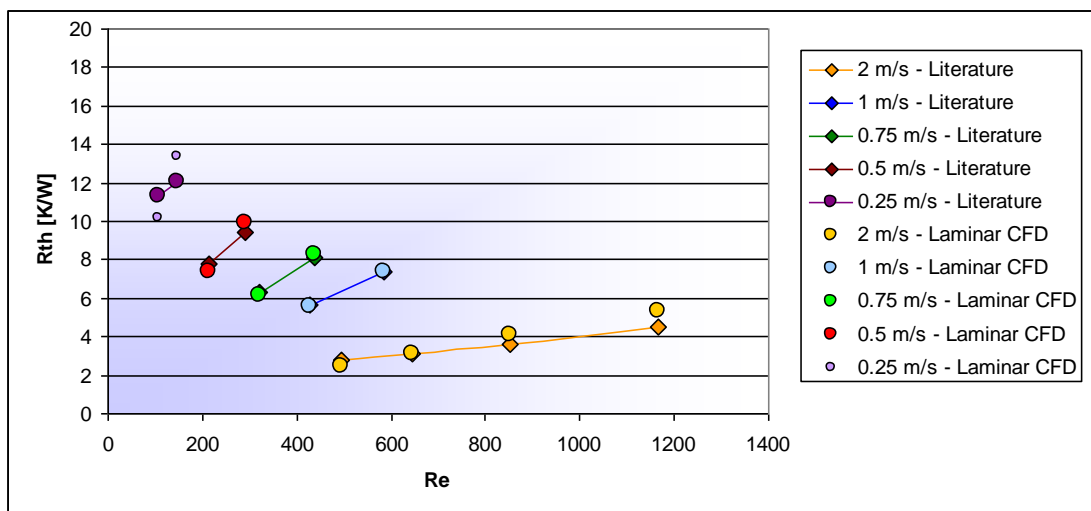


Figure 3-9: Laminar thermal resistance comparison with Shaukatullah et al. [33]

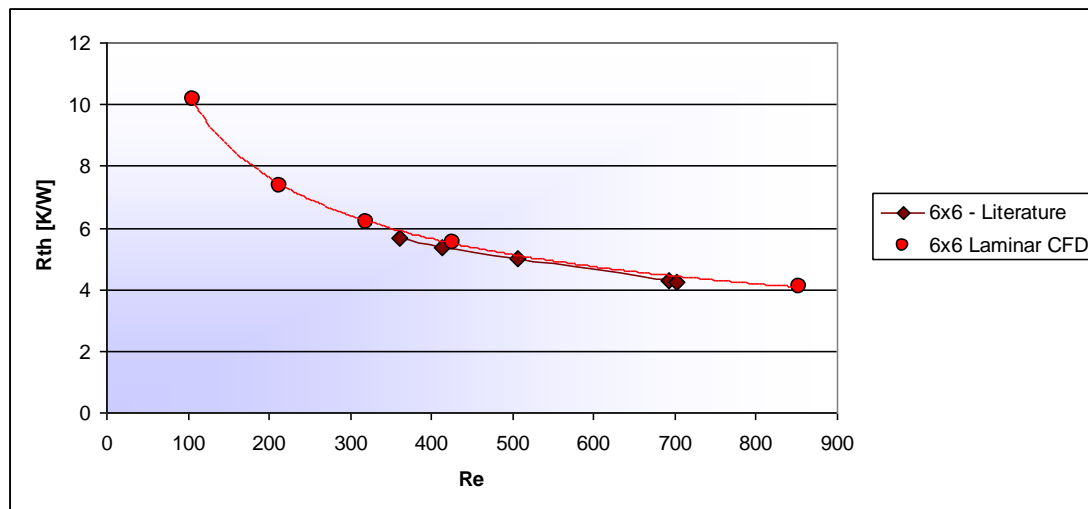


Figure 3-10: Laminar thermal resistance comparison with Dogruoz et al. [27]

The turbulence models tested were the following:

- Standard $k-\varepsilon$ with enhanced wall treatment
- Realisable $k-\varepsilon$ with enhanced wall treatment
- RNG $k-\varepsilon$ with enhanced wall treatment
- Standard $k-\omega$ with transition parameters
- SST $k-\omega$ with transition parameters

Figure 3-11 to Figure 3-18 display the thermal resistances of the simulated CFD models with the different turbulence models listed above compared with the data from the literature as shown in Figure 3-2 to Figure 3-5. The thermal resistances from the three $k-\varepsilon$ models are very close to each other in all the simulated cases. The differences in the thermal resistance values vary between 0% and 30% with large differences in the low Reynolds number range. Between the Reynolds numbers of 1 000 and 4 000, the percentage differences are below 20%. The $k-\varepsilon$ models underpredict the bulk of the experimental thermal resistances, but fit the data in Figure 3-9 very well. The standard $k-\omega$ thermal resistances are lower than the SST $k-\omega$ thermal resistances, but both models overpredict the data from the literature. The $k-\omega$ models are closer to the data from the literature at lower Reynolds numbers, but at higher Reynolds numbers, the $k-\varepsilon$ models perform better. At high Reynolds numbers, the thermal resistances of the $k-\omega$ models and the literature data vary up to 40%.

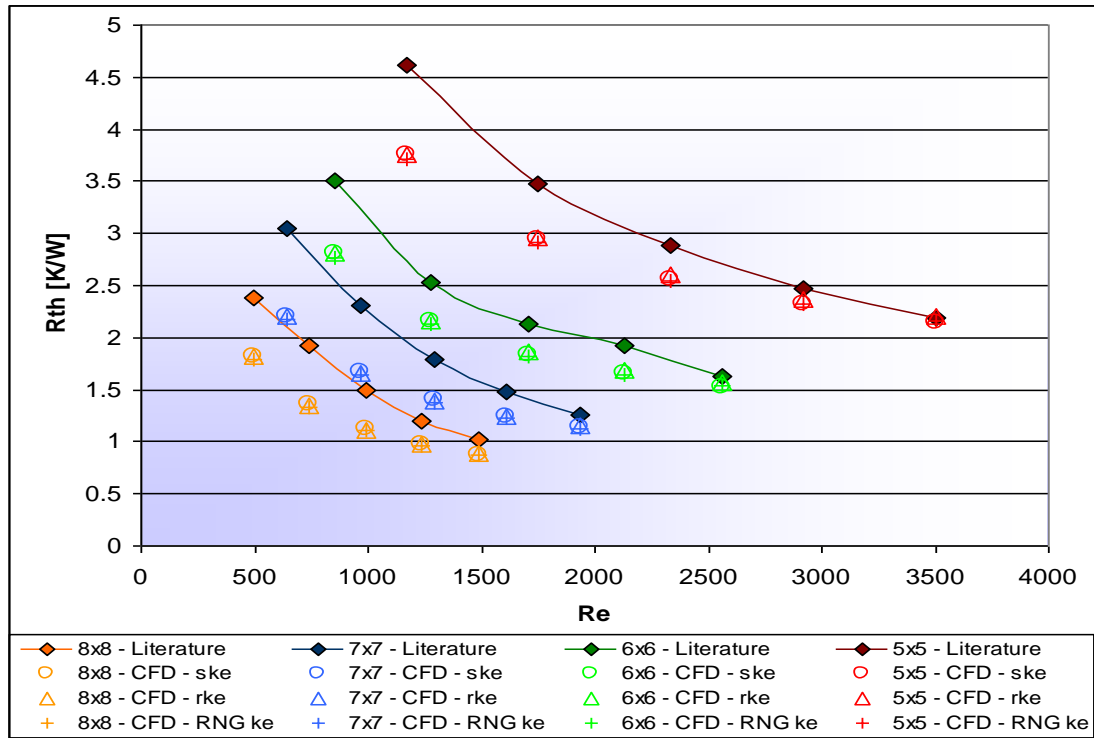
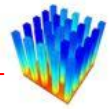


Figure 3-11: Turbulent thermal resistance comparison with Lei and Ortega [59], $k-\epsilon$ models

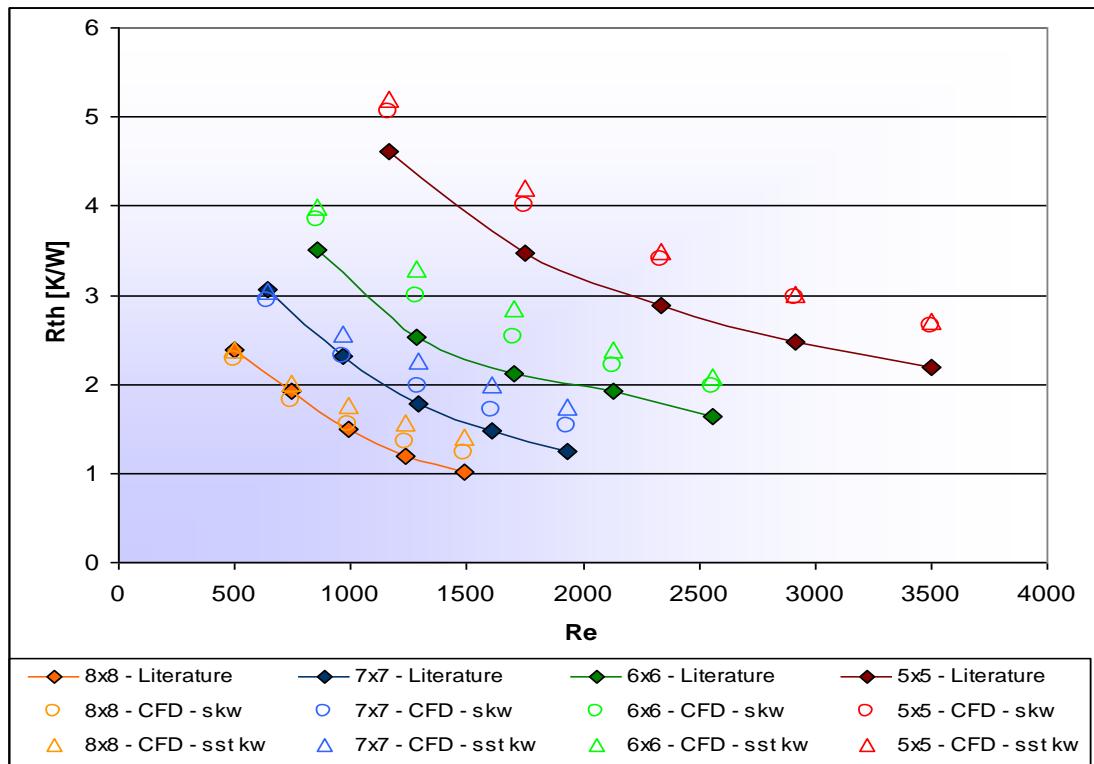


Figure 3-12: Turbulent thermal resistance comparison with Lei and Ortega [59], $k-\omega$ models

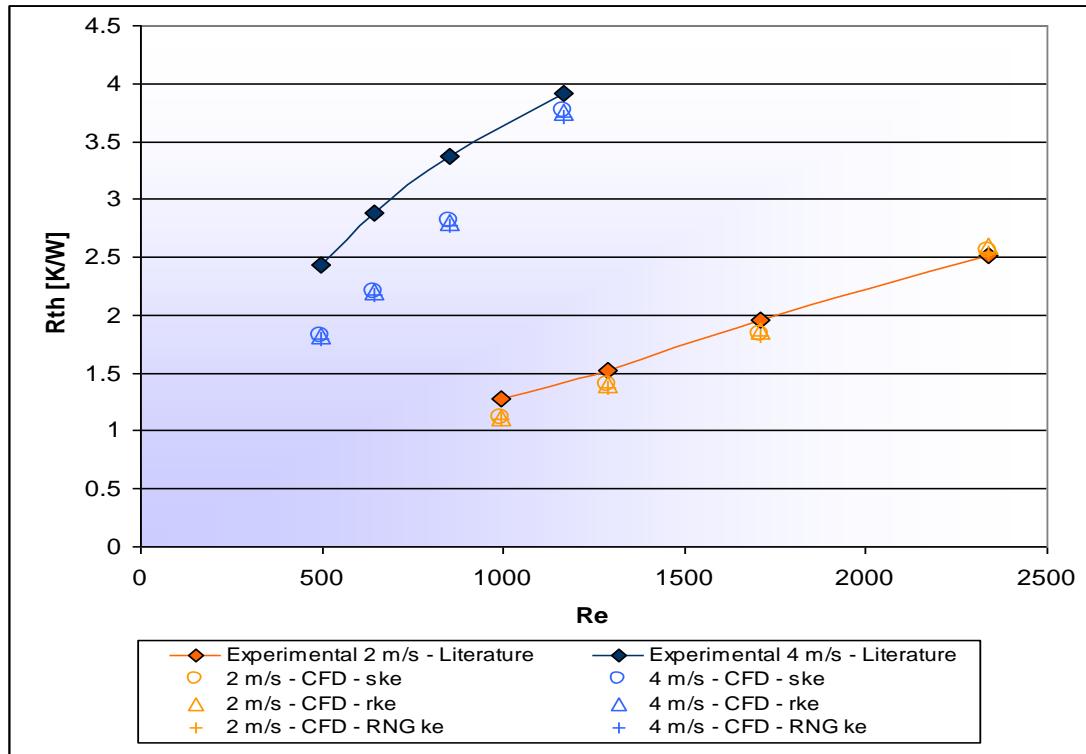
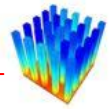


Figure 3-13: Turbulent thermal resistance comparison with Dogruoz et al. [27], $k-\epsilon$ models

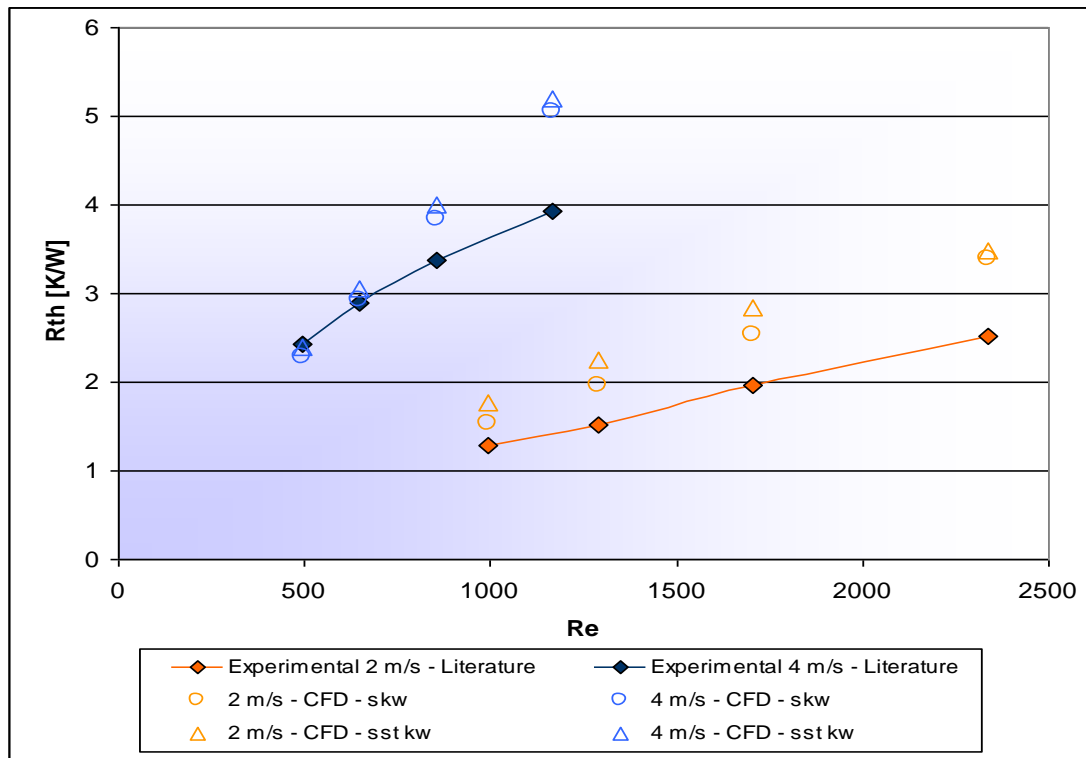


Figure 3-14: Turbulent thermal resistance comparison with Dogruoz et al. [27], $k-\omega$ models

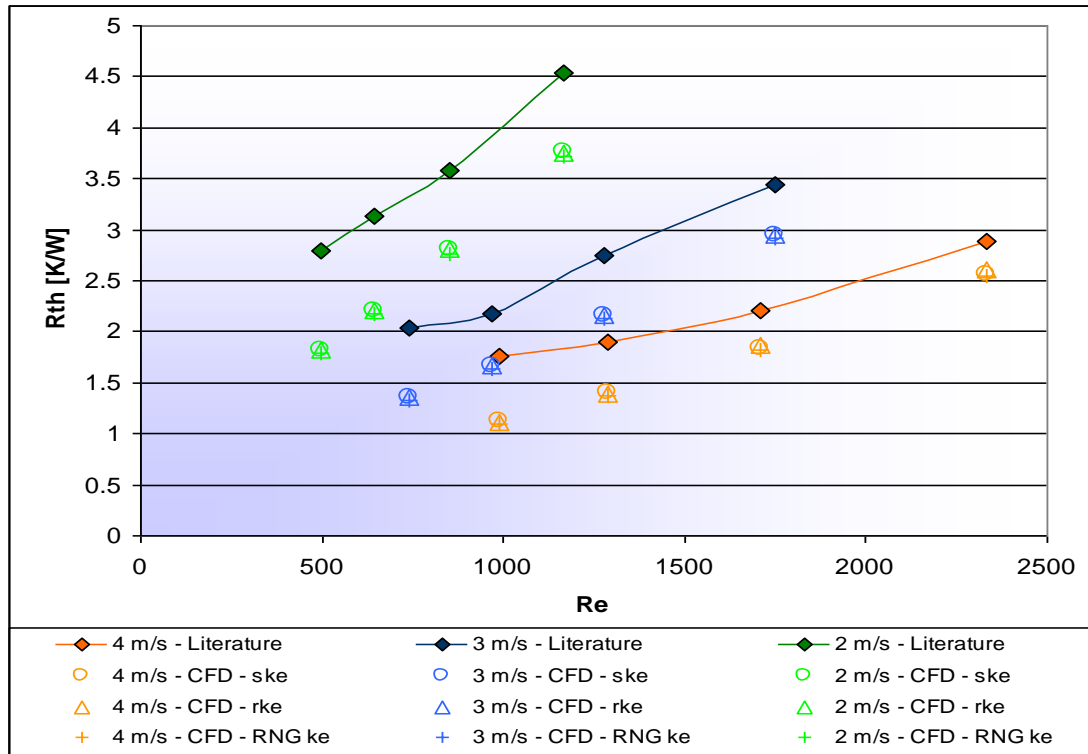


Figure 3-15: Turbulent thermal resistance comparison with Shaukatullah et al. [33], k-ε models

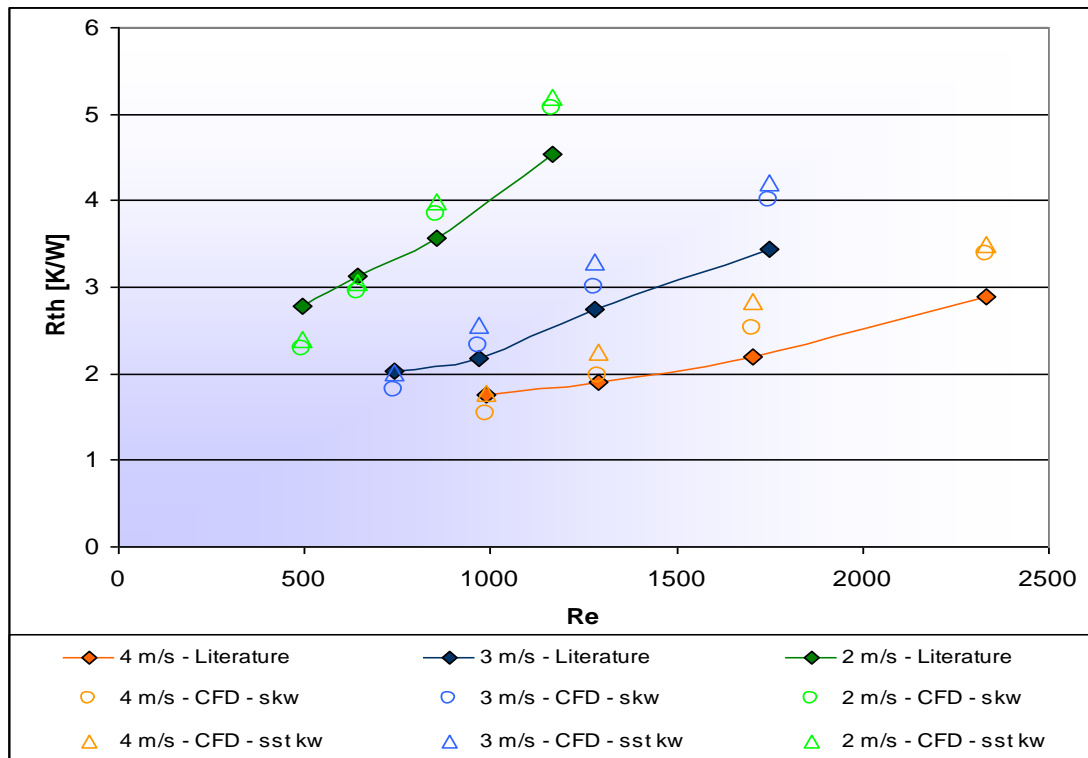


Figure 3-16: Turbulent thermal resistance comparison with Shaukatullah et al. [33], k-ω models

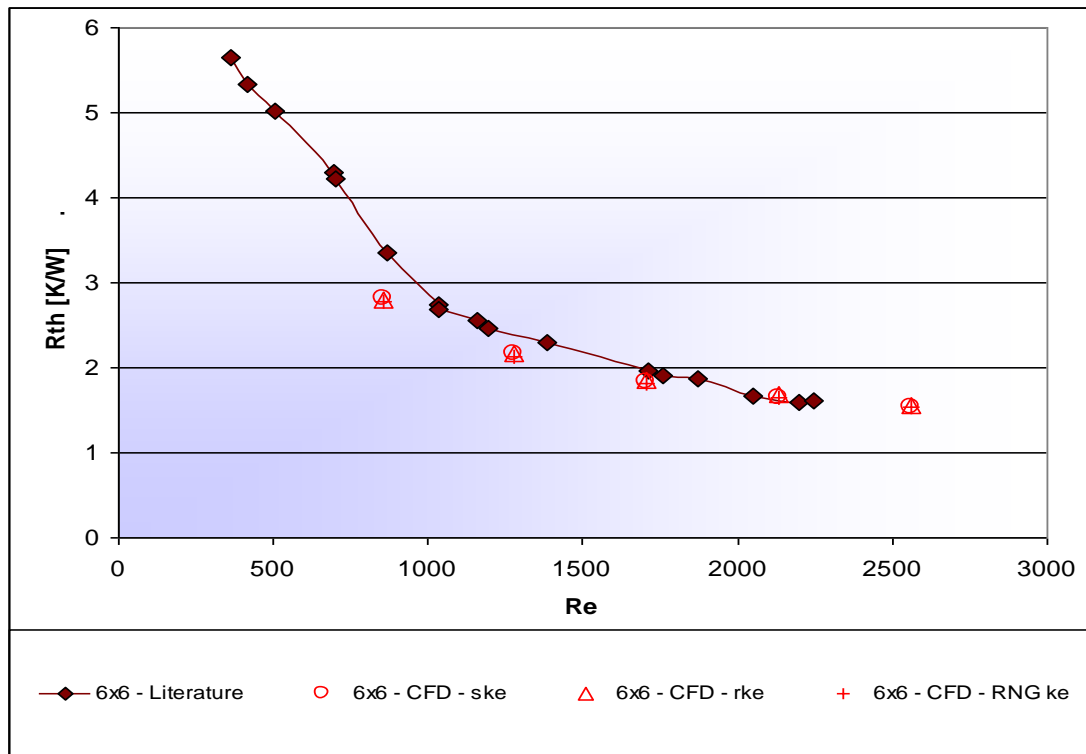
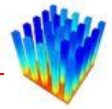


Figure 3-17: Turbulent thermal resistance comparison with Dogruoz et al. [27], k-ε models

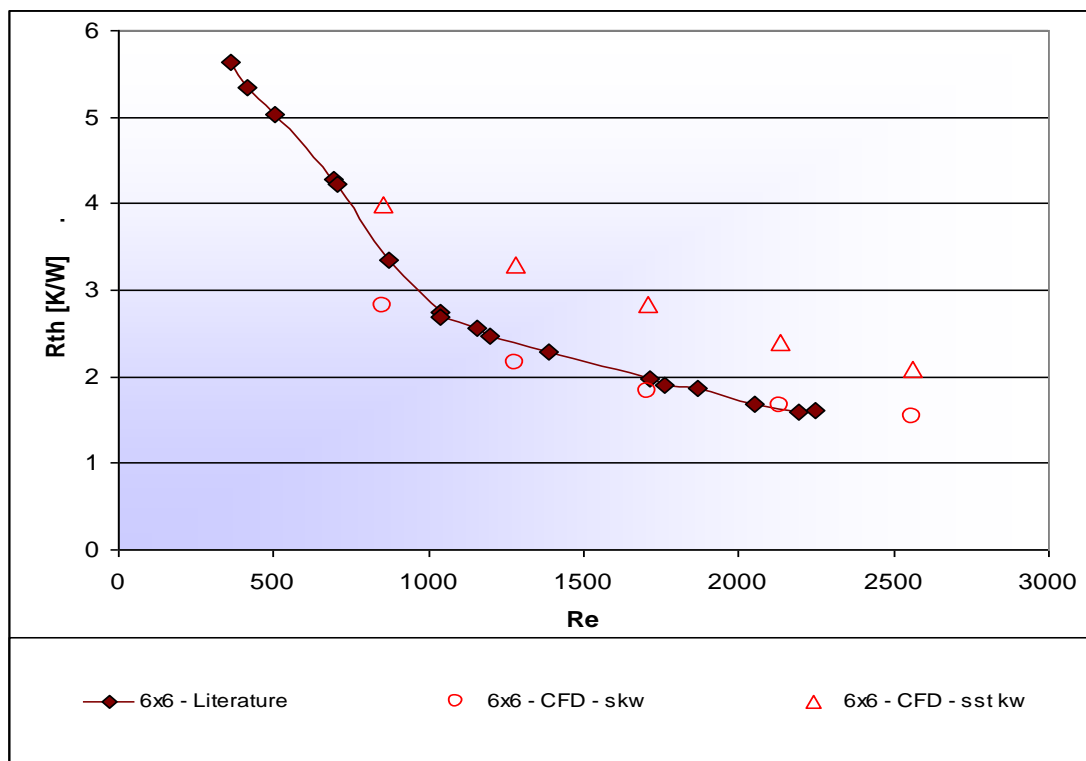


Figure 3-18: Turbulent thermal resistance comparison with Dogruoz et al. [27], k-ω models

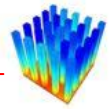


From the laminar comparison graphs, it follows that the laminar flow region ends around a Reynolds number of 650. The transitional flow region lies between Reynolds numbers 650 and 1 000. The laminar flow region used for calculations is between Reynolds numbers of 100 to 650, based on the gap width between the fins. This range is very low and is due to the short sides of the pins tripping the flow through the heat sink into the turbulent region. The selected turbulent range lies between the Reynolds numbers of 1 000 to 7 000. It was decided to use the Realisable $k-\varepsilon$ (rke) turbulence model for this study since these values compare more favourably with the data from the literature. The percentage differences between the Realisable $k-\varepsilon$ model and the literature lie within a 20% error band. For CFD solutions, this is generally considered as acceptable values. Since the errors are acceptably small, the CFD set-up procedure for this range of pin fin heat sinks is confirmed to be valid. It can therefore be used to generate data for this study in the tested range.

3.3 METHODOLOGY

The methodology in creating the equations will be described next. The following list summarises the steps in this methodology. Each of these steps is described in more detail in the subsequent sections. The steps in the methodology are:

- Determining applicable parameters;
- Setting up an Icepak model and creating case files for Fluent;
- Creating a script for setting up the environment and boundaries, and creating reporting faces;
- Running the Fluent model with a range of velocities and exporting the data to a comma-separated values (csv) text file for post-processing;
- Tidying up csv file by extracting only the relevant data and averaging the values for each heat sink;
- Non-dimensionalising the parameters for a wider application range, using correlated property equations;
- Plotting parameters against each other to determine the effects on heat transfer;



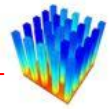
- Calculating regression lines on the plots;
- Combining regression lines with constants to form one large equation;
- Optimising the equation.

First, the parameters have to be selected. To do this, the heat transfer coefficients on some test runs were plotted on the faces and inspected to determine the effects they have on the heat transfer coefficients. The parameters that make up an in-line square pin fin heat sink can be summed up as follows:

- Pin width
- Pin length
- Pin height
- Gap width
- Gap length
- Base height
- Pin count in length direction
- Pin count in width direction

The base width is a function of the gap width, pin width and pin count in the width direction. Similarly, the base length is a function of the gap length, pin length and the pin count in the length direction. It was decided not to take flow bypass into account because it introduces extra geometric parameters and complicates the solution to a great extent. Other properties that influence the heat transfer are material and fluid properties, and are as follows:

- Fluid velocity (V)
- Fluid density (ρ)
- Fluid viscosity (μ)
- Fluid thermal conductivity (k_f)
- Fluid heat capacity (C_p)
- Solid thermal conductivity (k_s)



From these properties, one can define the following non-dimensional parameters:

$$Re = \frac{\rho V d}{\mu} \quad (36)$$

$$Nu = \frac{h_c d}{k_f} \quad (37)$$

$$Pr = \frac{C_p \mu}{k_f} \quad (38)$$

where

d : Characteristic length [m]

h_c : Convection coefficient [W/m²K]

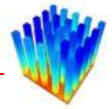
Re : Reynolds number

Nu : Nusselt number

Pr : Prandtl number

Since most heat sinks are cooled with air, it was decided not to take the effect of the Prandtl number into account as the Prandtl number changes with less than 2% over the inlet and outlet temperature ranges considered in this study. There exists a method of incorporating the Prandtl number into the non-dimensional heat transfer coefficient, but it will not be discussed here.

From several CFD runs, it can be seen that the height of the base of the heat sink has very little effect on the pins' heat transfer coefficients. The influence of the height of the pins on the heat transfer coefficients decreases as the pin height increases. The heat transfer coefficients can be assumed to be constant for a pin height larger than a certain fraction of the heat sink width. At the base and the tip of the heat sink, there exist small portions where the heat transfer coefficients are lower than on the rest of the pin height. This is due to friction on the base and the shroud at the tip of the heat sink. The pin height parameter is discarded and the heat transfer coefficient is averaged from a certain distance above the base up to a certain distance below the tips of the pins.



The number of pins on the heat sinks in both the length and width direction is also kept constant. It is also determined that in a very dense heat sink, the pins in the width direction have more or less the same heat transfer coefficient distribution. The heat transfer coefficients on consecutive pins in the flow direction changes, but to simplify the model and minimise the amount of tests to be carried out, average heat transfer coefficients are calculated. All the heat sinks tested had 15 pins in the flow direction. The average heat transfer coefficient from the third row up to the second last row is used. The heat transfer coefficients on the first two rows and the last row vary significantly from the rest of the pins due to entrance and exit effects. Even though a single row of pins could have been modelled, five pins in the width direction were used to calculate average values and minimise some numerical error from the simulations. This leaves only four geometric parameters and the Reynolds number to correlate to the Nusselt number. The four geometric parameters are as follows:

- Pin width (W_{pin})
- Pin length (L_{pin})
- Gap width (W_{gap})
- Gap length (L_{gap})

Figure 3-19 shows a graphical representation of a heat sink with the selected parameters.

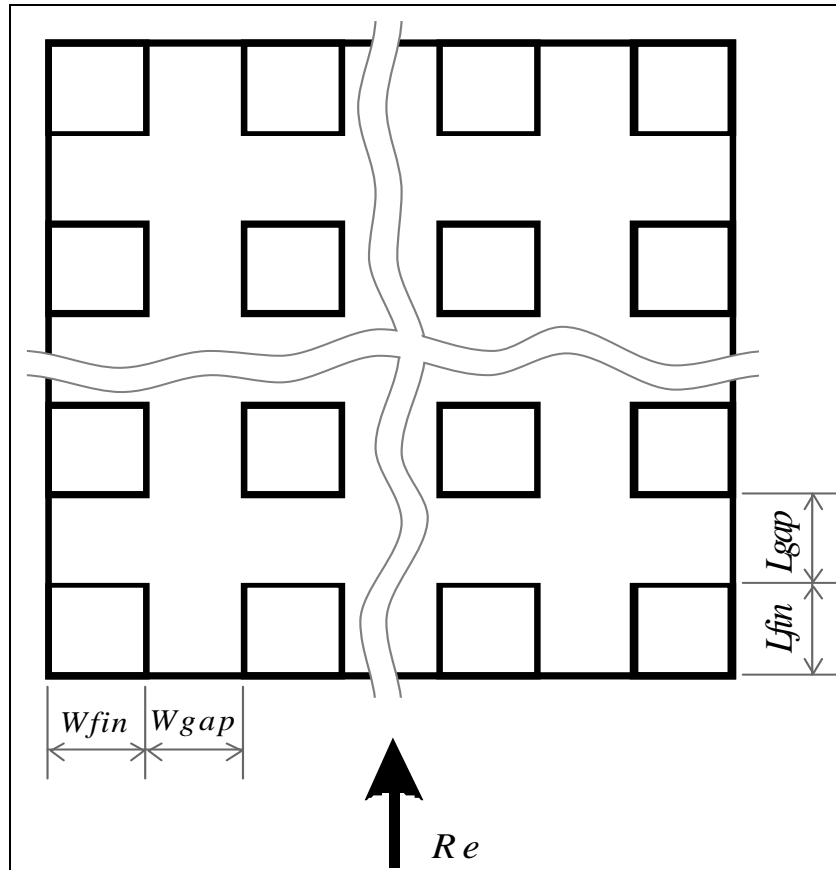


Figure 3-19: Top view of heat sink displaying selected parameters

A parameterised Icepak project was created with the parameters in Figure 3-19 as variables. Five pins in the width direction and 15 pins in the length direction were modelled. The first and last pins in the width direction were modelled as half-size pins. This was done to make use of symmetry boundaries on the sides of the heat sink. By doing this, one eliminates the effect of friction on the walls of the bounding box. The top surface of the bounding box was also selected to be frictionless. Channels were extruded upstream and downstream of the heat sink to allow the fluid to develop completely. The top surface of the base of the heat sink was in line with the bottom surface of the channel. This ensures that there is no step or vertical geometric change in the flow, which will influence the heat transfer from the heat sink. The heat source was applied to the entire bottom surface of the heat sink.

A Cartesian hexahedral mesh was used as the meshing scheme. For turbulent flow, the parameters were selected to maintain a y^+ value of less than 5. The number of cells was kept to a minimum. Since numerous CFD cases were needed, the models



needed to be relatively computationally inexpensive. For the laminar flow heat sinks, meshes with larger cells were used. Figure 3-20 shows a representation of the model used. The blue face depicts the velocity inlet and the red face depicts the pressure outlet. The yellow faces are the symmetry planes on the sides of the heat sink. Figure 3-21 displays a close-up of the heat sink and Figure 3-22 displays a representative section of the mesh. The turbulent mesh size is in the order of 1 million cells and the laminar mesh size is 270 thousand cells.

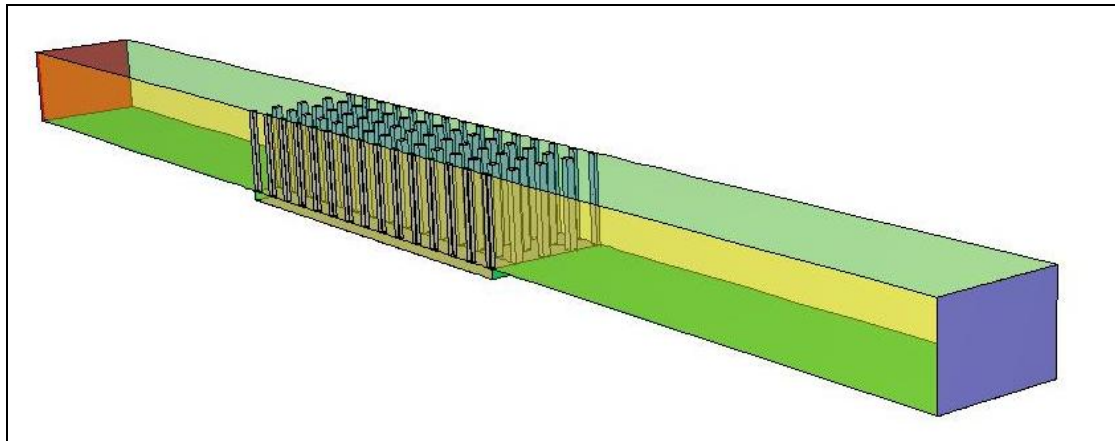


Figure 3-20: An example of the CFD model used in the study

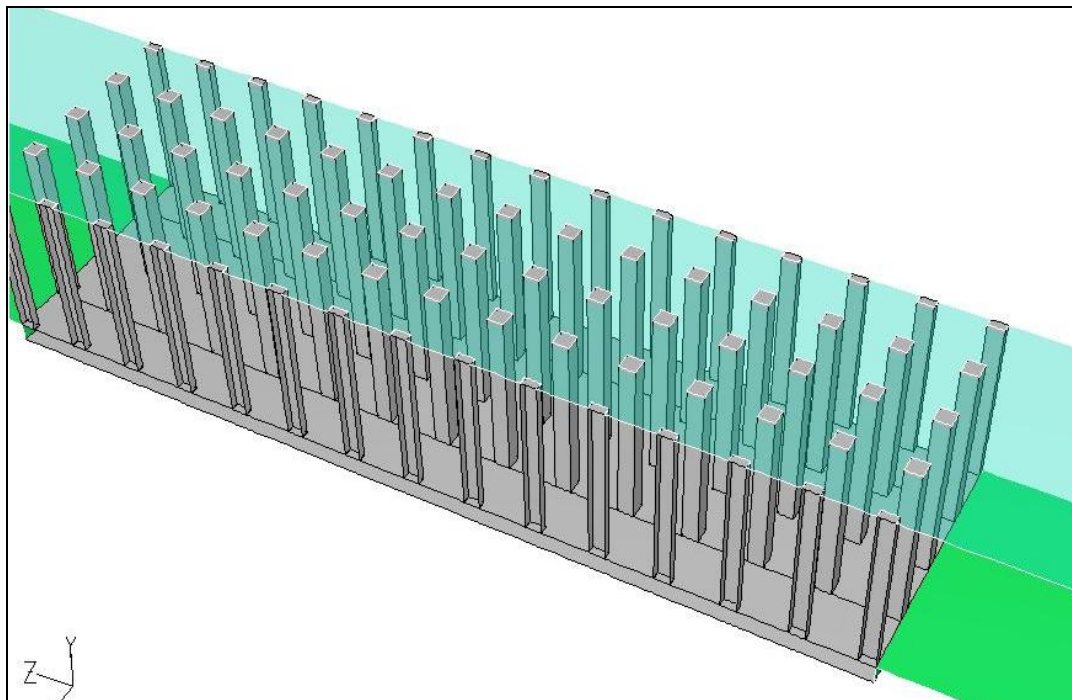


Figure 3-21: Close-up of the heat sink from Figure 3-20

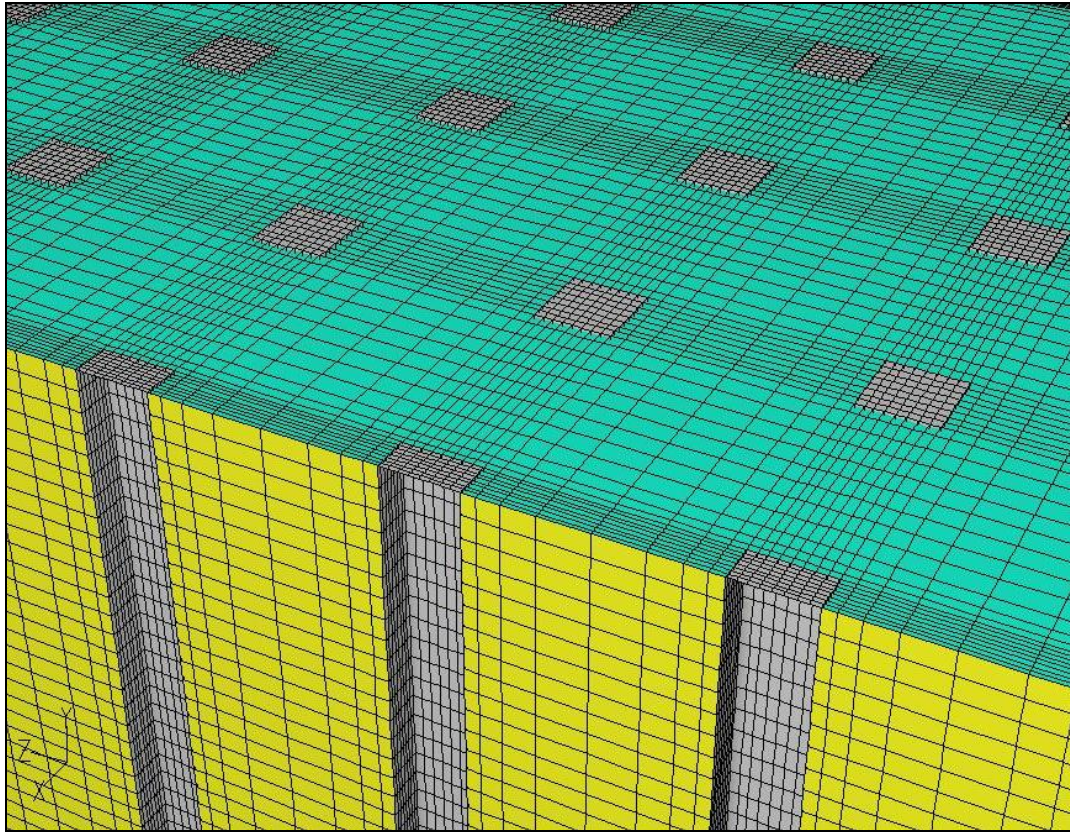


Figure 3-22: Representative section of the mesh

Since the laminar flow models run quicker than the turbulent ones, due to a smaller mesh size and amount of equations to solve, more laminar runs were carried out. Table 3-2 displays the ranges of the parameters used in the simulations.

Table 3-2: Parameter ranges

Parameter	Values
Laminar flow	
Pin length (L_{fin}) [m]	0.002, 0.004, 0.006, 0.008
Pin width (W_{fin}) [m]	0.002, 0.004, 0.006, 0.008
Gap length (L_{gap}) [m]	0.002, 0.003, 0.004, 0.005, 0.006, 0.007, 0.008
Gap width (W_{gap}) [m]	0.002, 0.003, 0.004, 0.005, 0.006, 0.007, 0.008
Velocity (V) [m/s]	0.1 0.2, 0.3, 0.4, 0.5, 0.6
Turbulent flow	
Pin length (L_{fin}) [m]	0.002, 0.004, 0.006, 0.008
Pin width (W_{fin}) [m]	0.002, 0.004, 0.006, 0.008



Gap length (L_{gap}) [m]	0.002, 0.004, 0.006, 0.008
Gap width (W_{gap}) [m]	0.002, 0.004, 0.006, 0.008
Velocity (V) [m/s]	2, 3, 4, 5, 6

This gives a total of 4 704 laminar flow cases and 1 280 turbulent flow cases. All 5 984 cases were solved using Fluent. Scilab [60] scripts, one for laminar flow and one for turbulent flow, were written to generate Fluent journal files for running the cases and exporting the data. See Appendix A for the script file. The script file writes Fluent commands to a journal file to perform the following for each case:

1. Read in the case file.
2. Create faces as thin strips on either side of the leading face of each pin on the pin fin heat sink, which is used for post-processing. This was done because initially only the heat transfer coefficients on the edges of the leading faces were examined.
3. Set the boundary conditions and solution parameters.
4. Initialise the data.
5. Solve the case.
6. Save the data file.
7. Export a transcript file with the average temperatures and heat fluxes of each face created in Step 2. Also write out the average outlet temperature.
8. Repeat from Step 3 with a new velocity boundary condition until all velocity values have been solved.
9. Repeat from Step 1 with new case file until all the case files have been solved.

See Appendix A for an example journal file and transcript file.

The average simulation time was in the order of two hours for laminar cases and four hours for turbulent cases. The hardware ranged from 2 GHz single-core machines with 2 GB RAM, to 3 GHz dual core machines with 4 GB RAM. The total space requirement for the compressed data set of all the simulations together is in the order of 200 GB.



Another script was written to extract the relevant data from the transcript files and combine it to generate the non-dimensional numbers previously mentioned. The geometric parameters were also non-dimensionalised. The following equations were used for the properties of air flowing through the heat sink:

$$k_f = 6 \times 10^{-5} T_{ref} + 0.0085 \quad (39)$$

$$\rho = \frac{352}{T_{ref}} \quad (40)$$

$$\mu = 3 \times 10^{-7} T_{ref}^{0.7054} \quad (41)$$

These equations are regression lines fitted on the data in Mills [11]. Figure 3-23 to Figure 3-25 display the equations together with the data from the reference.

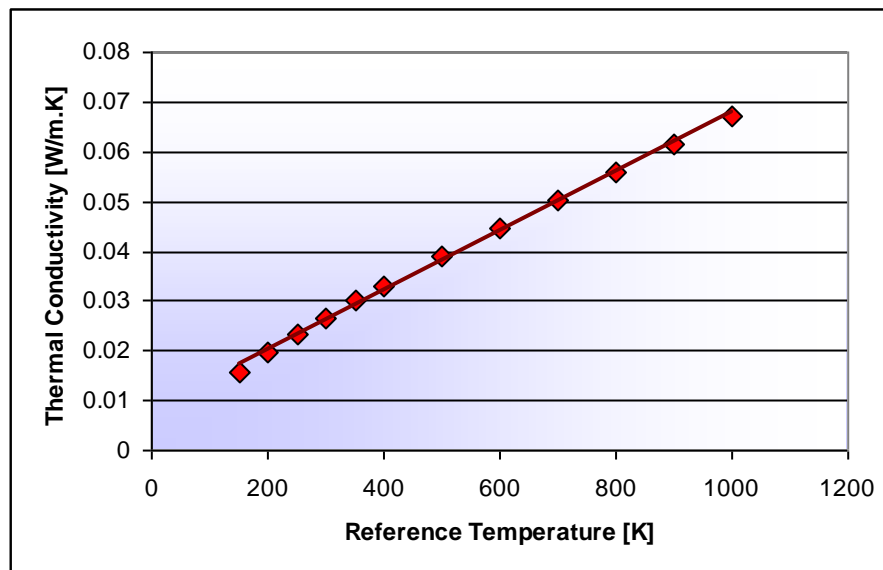


Figure 3-23: Thermal conductivity of air (k_f)

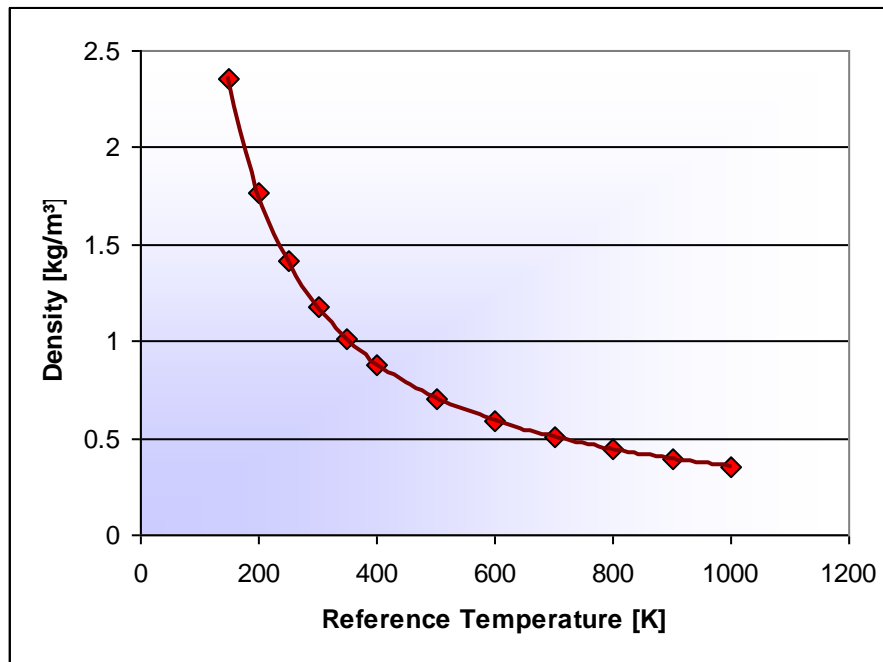
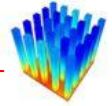


Figure 3-24: Density of air (ρ)

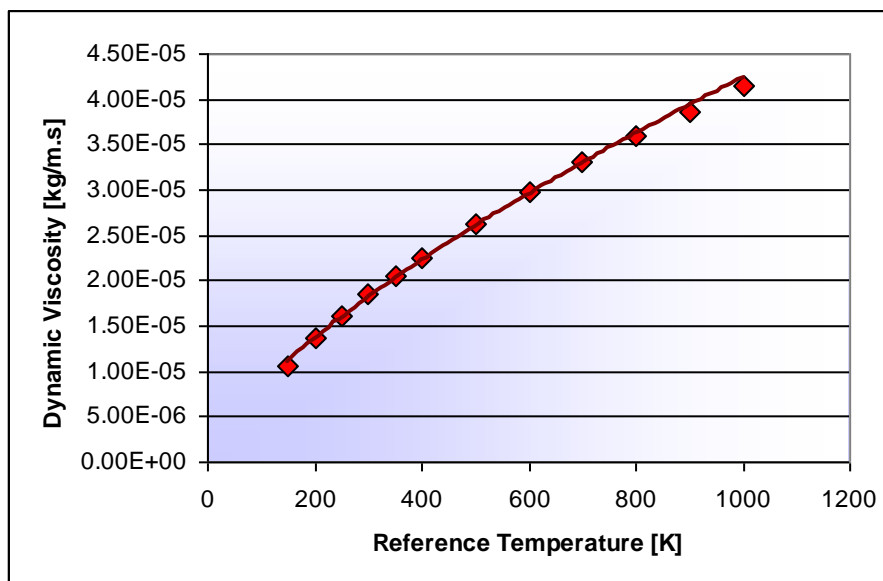
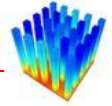


Figure 3-25: Dynamic viscosity of air (μ)

The air properties were calculated with linear interpolated temperatures between the inlet and outlet temperatures along the length of the heat sink. It was decided to use the gap width as the reference length on which to base the Reynolds and Nusselt numbers. Usually, the hydraulic diameter of the pins is used in most research, but for the cases in this study, the trends in the data are clearer when the gap width is used as the reference length. The Reynolds numbers for laminar flow are based on the fin



velocity, whereas the Reynolds numbers for turbulent flow are based on the approach velocity. Figure 3-26 below indicates the difference between the approach velocity and the fin velocity.

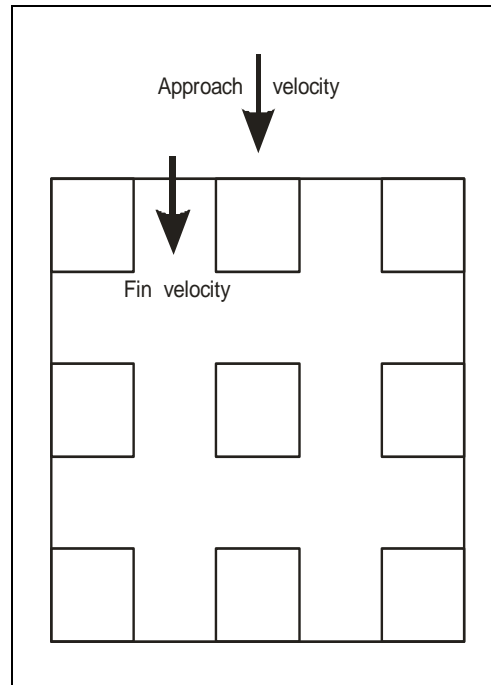


Figure 3-26: Difference between the approach and fin velocities

Another script was written, which used the data to create a more compact data set with one average Nusselt number for every heat sink solved, together with all the other non-dimensional parameters for the heat sink, representing the heat transfer on the edge of the leading face of every pin for every heat sink in the data set. This data set was then used to generate the equations for the heat transfer coefficients in laminar and turbulent flows.

The data set was divided into two, a laminar set and a turbulent set. Both sets were trimmed to contain only data for the relevant Reynolds number ranges. It was found that at very low Reynolds numbers, the heat transfer coefficients from the CFD solutions become doubtful. This is due to the flow starting to move into the natural convection region where the flow is buoyancy driven. Buoyancy was not taken into account in this CFD set-up. Table 3-3 shows the Reynolds number ranges for laminar and turbulent flows respectively.

**Table 3-3: Reynolds number ranges**

Flow region	Reynolds number range
Laminar flow	100 - 650
Turbulent flow	1 000 – 7 000

The heat transfer across the trailing faces of the heat sinks was divided into two parts. The first part was to determine the heat transfer coefficients on the edges of the trailing faces of the heat sinks. The second part was to create an equation that determines the heat transfer across the trailing face as a function of the edge heat transfer coefficient.

Similar to the Buckingham Pi theorem [47] for reducing the number of dimensional variables into smaller dimensionless groups, six non-dimensional geometric ratios, as well as six inverse ratios, can be defined with the four selected geometric parameters. But since all of them can be written as a combination of two other non-dimensional geometric parameters, it was decided to use only four of these parameters. The selected geometric parameters were:

- $\frac{W_{fin}}{W_{gap}}$
- $\frac{L_{fin}}{L_{gap}}$
- $\frac{L_{fin}}{W_{fin}}$
- $\frac{L_{gap}}{W_{gap}}$

The other two parameters can be calculated as follows:

- $\frac{W_{fin}}{L_{gap}} = \frac{W_{fin}}{W_{gap}} \cdot \frac{L_{gap}}{W_{gap}}$
- $\frac{W_{gap}}{L_{fin}} = \frac{1}{\frac{L_{gap}}{W_{gap}} \cdot \frac{L_{fin}}{L_{gap}}}$



Sub-sets of the two data sets mentioned were examined by setting two geometric parameters as constant and plotting graphs of Reynolds number against the edge Nusselt number for the remaining geometric parameter. From these graphs, the trends between the data could be analysed and determined. Regression lines were calculated to fit the graphs based on the selected geometric parameter. By varying another parameter and plotting the constants in the regression lines calculated for the first selected geometric parameter against the second geometric parameter, regression lines can be calculated for the constants in the first set of regression lines. This results in an equation for the Nusselt number based on the Reynolds number and two geometric parameters. One can then do this for all the combinations of the other geometric parameters and determine if it is possible to combine them into an equation that will fit all the data.

Another way of determining an equation that will fit the data is to select one parameter and calculate this parameter's regression line on the Nusselt number. Then keep the other parameters constant and divide the Nusselt number data of the entire set by the regression line of this selected parameter and plot these data points against the other parameters and search for trends in this way.

Detailed explanations for each of the laminar and turbulent flow equations follow in Sections 3.4 and 3.6 respectively.

After the equations for the heat transfer coefficients on the edges of the leading faces were determined, equations for the heat transfer coefficients along the leading faces could be determined.

A script was written, which created a Fluent journal file to extract data along the leading face of all the pins on all the heat sinks. Once again the average heat transfer coefficients were calculated from the third row up to the second last row of pins. The heat transfer coefficients along the faces were divided by the heat transfer coefficients on the edges of the faces. This resulted in a non-dimensional profile along the face ranging from zero to one. See Figure 3-27 for an example.

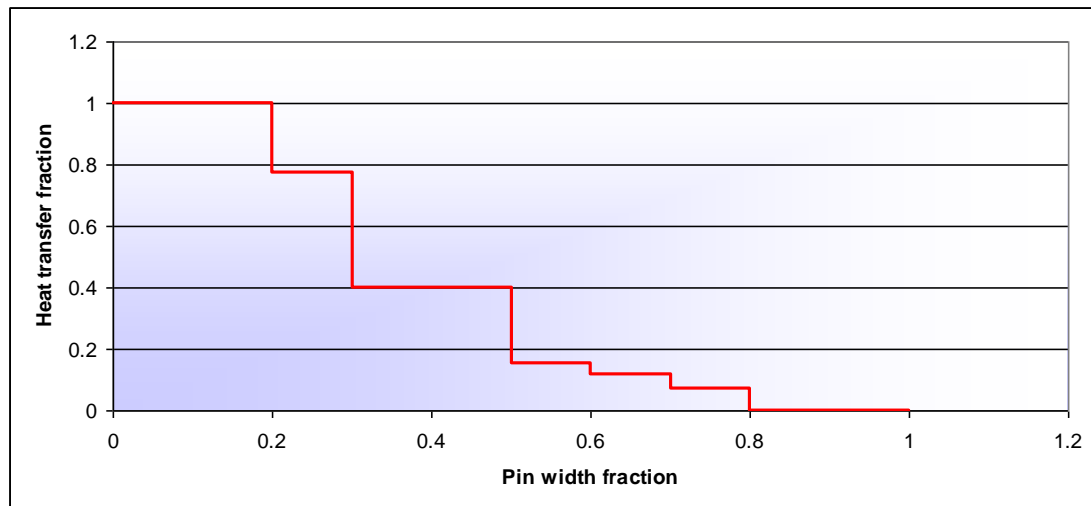


Figure 3-27: Non-dimensional heat transfer profile along the width of a pin

Simulating a function like this is rather complicated since it is neither a single value, nor a smooth function, but a list of discrete values. What makes it even more difficult is the coarse discretisation used.

The equation for the heat transfer distribution on the pin faces was created with the same methodology used in the creation of the edge coefficients. Detailed analyses for laminar and turbulent flows are described in Section 3.5 and Section 3.7 respectively.

Since the equations were created using constants calculated from regression line theory on local data points, the equations did not fit the entire data set very well. Rather than changing the constants manually to obtain improved heat transfer coefficient correlations, the optimisation theory was used to determine optimised coefficients for the equations on the data set. It was decided to mainly use the LFOPC optimisation procedure from Snyman [45] because of previous experience in this method. Three other optimisation procedures were also used. A very simple method was used to obtain a general location of the optimum range of parameters. Another one, named Dynamic-Q, which also uses the LFOPC algorithm, was applied to determine if the LFOPC optimum values were in the correct range. Finally, a non-linear optimisation algorithm from Matlab's Optimization Toolbox [58] was used to confirm the optimised coefficients from the LFOPC algorithm.



Several different objective functions are available to optimise the equations. The four main functions considered are:

- Minimising the maximum difference percentage in the data set;
- Minimising the average difference percentage in the data set;
- Minimising the maximum difference in the data set;
- Minimising the average difference in the data set.

The objective functions for minimising the maximum error percentage and the maximum difference are very simple. A mere search through the data set will give the value for the objective function. The two most widely used methods for calculating averages differences are the Root Mean Square (RMS) and Root Sum Square (RSS) values of the data set. These functions are a little more complicated to calculate than the maximum values.

The difference objective functions are calculated by subtracting the Nusselt numbers (from the equation to be optimised from the discrete values) from the CFD data set (Equation 42). The difference percentage objective functions are variations on the difference objective functions. The percentage differences are calculated by taking the differences between the CFD data set and the function to be optimised, and dividing it by the CFD data set values (Equation 43).

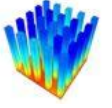
$$D_i = Nu_{CFD,i} - Nu_{eq}(\mathbf{x}, i) \quad (42)$$

$$E_i = \frac{Nu_{CFD,i} - Nu_{eq}(\mathbf{x}, i)}{Nu_{CFD,i}} \quad (43)$$

where

- $Nu_{CFD,i}$: Discrete Nusselt values in the data set
 $Nu_{eq}(\mathbf{x}, i)$: Calculated Nusselt value from the correlation
 i : Data point
 \mathbf{x} : Optimisation vector

After considering the possible objective functions, the root sum square of the difference percentages was selected as the most practical function to use in the



optimisation procedure. This will result in the minimisation of the average difference between the CFD values and the generated equations. The objective function is therefore defined as:

$$F(\mathbf{x}) = \sqrt{\sum_{i=1}^n \frac{(Nu_{CFD,i} - Nu_{eq}(\mathbf{x}, i))^2}{(Nu_{CFD,i})^2}} \quad (44)$$

where

- $Nu_{CFD,i}$: Discrete Nusselt values in the data set
- $Nu_{eq}(\mathbf{x}, i)$: Calculated Nusselt value from the correlation
- n : Number of series in the data set
- i : Series of parameters
- \mathbf{x} : Optimisation vector

This objective function produces somewhat complicated partial derivatives of each variable in the correlation. The partial derivatives look as follows:

$$\frac{\partial F}{\partial x_j} = \frac{1}{2} \left(\sum_{i=1}^n \frac{(Nu_{CFD,i} - Nu_{eq}(x_j, i))^2}{(Nu_{CFD,i})^2} \right)^{-\frac{1}{2}} \cdot \left(\sum_{i=1}^n \left(2 \frac{(Nu_{CFD,i} - Nu_{eq}(x_j, i))}{(Nu_{CFD,i})^2} \cdot \frac{\partial}{\partial x_j} (-Nu_{eq}(x_j, i)) \right) \right) \quad (45)$$

Because of the number of data points in the data set, the objective function and partial derivatives are calculated using a scripting language. Since the generated equation might be a complex function with even more complex partial derivatives, which can be computationally expensive to calculate, it was decided to simplify the derivatives by replacing them with first-order gradient functions.



The gradients will then look as follows:

$$\frac{\partial F}{\partial x_j} \approx \frac{\sqrt{\sum_{i=1}^n \frac{(Nu_{CFD,i} - Nu_{eq}(x_j + \Delta x_j, i))^2}{(Nu_{CFD,i})^2}}}{\Delta x_j} - \frac{\sqrt{\sum_{i=1}^n \frac{(Nu_{CFD,i} - Nu_{eq}(x_j, i))^2}{(Nu_{CFD,i})^2}}}{\Delta x_j} \quad (46)$$

The particular optimisation procedure for each equation is described in the sections below relevant to the specific equation.

3.4 LAMINAR FLOW

The temperatures and heat fluxes from the pins in the CFD models are extracted to calculate the heat transfer coefficients on each pin face. Ten narrow strips are used to retrieve the average heat transfer coefficient in the longitudinal direction as a function of the distance from the edge of the pins. This is done for all the pins on the heat sink. The heat transfer coefficients are non-dimensionalised with the thermal conduction coefficient and the hydraulic diameter between the pins to give the dimensionless Nusselt number. An average edge Nusselt number is calculated for each heat sink. This edge Nusselt number represents the first point on the heat transfer coefficient function across the pin faces. The actual function across the face will be discussed in Section 3.5. The yellow edges in Figure 3-28 represent the edges used for the calculation of the edge Nusselt number.

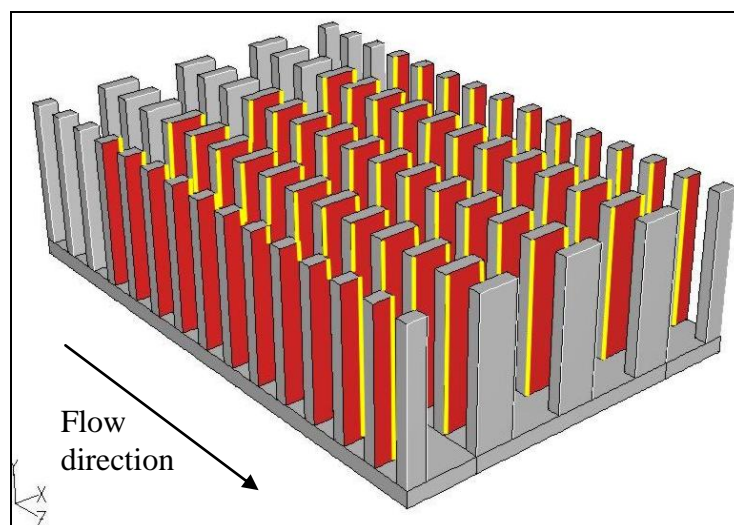


Figure 3-28: Edges on which the edge Nusselt number is calculated



Several graphs were drawn with the non-dimensional heat transfer coefficient (Nusselt number) compared with each non-dimensional geometric parameter to determine the effect each one has on the heat transfer coefficient.

Figure 3-29 to Figure 3-32 show the influences the different geometric parameters have on the Nusselt number. In these figures, two geometric parameters as well as the Reynolds number were kept constant while the variation of the selected parameter was plotted against the Nusselt number. The third geometric parameter varies proportionately to the selected parameter as a result of the selected non-dimensional parameters. Figure 3-33 shows the influence of the Reynolds number on the Nusselt number when all the geometric parameters are kept constant.

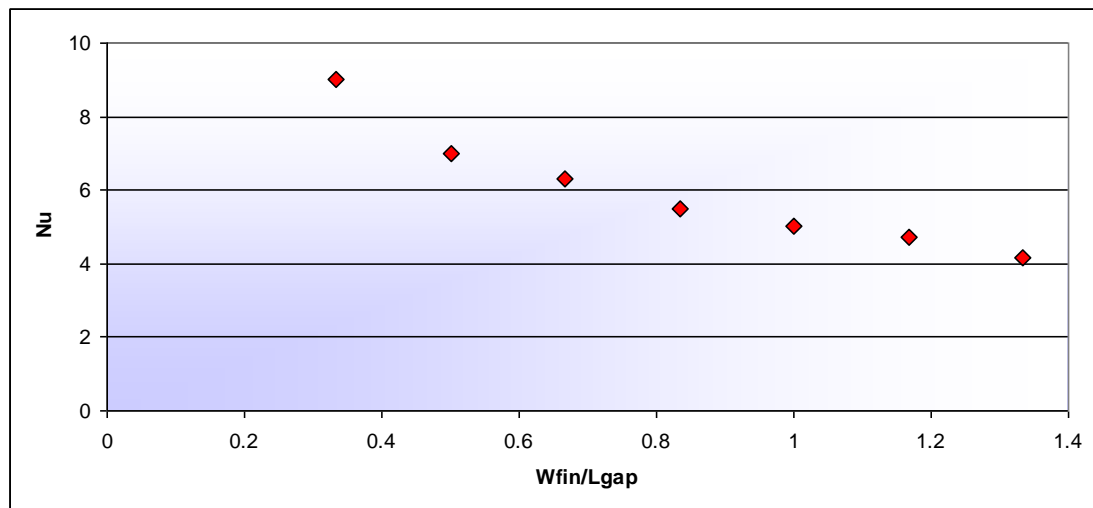


Figure 3-29: The influence of W_{fin}/L_{gap} on the Nusselt number

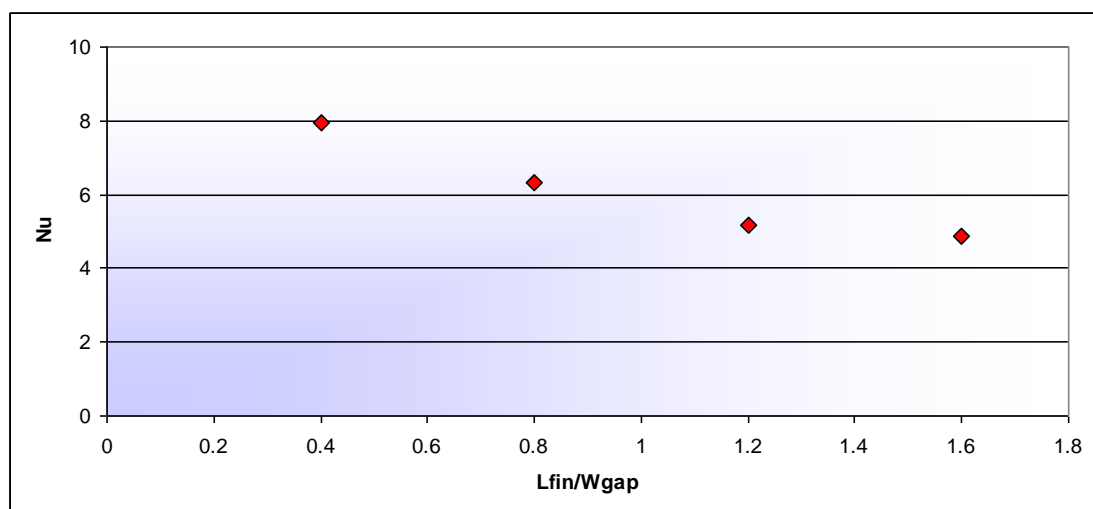


Figure 3-30: The influence of L_{fin}/W_{gap} on the Nusselt number

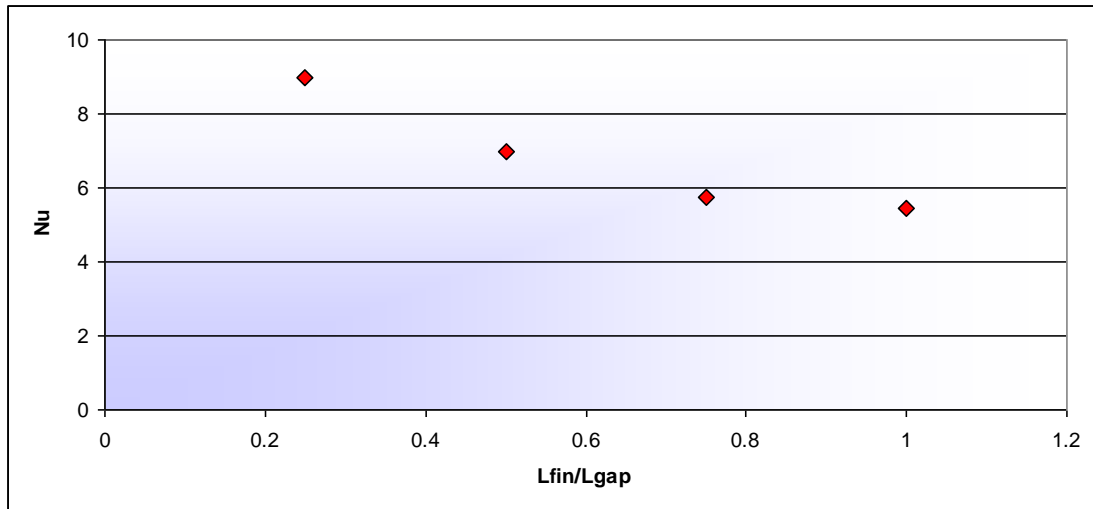


Figure 3-31: The influence of L_{fin}/L_{gap} on the Nusselt number

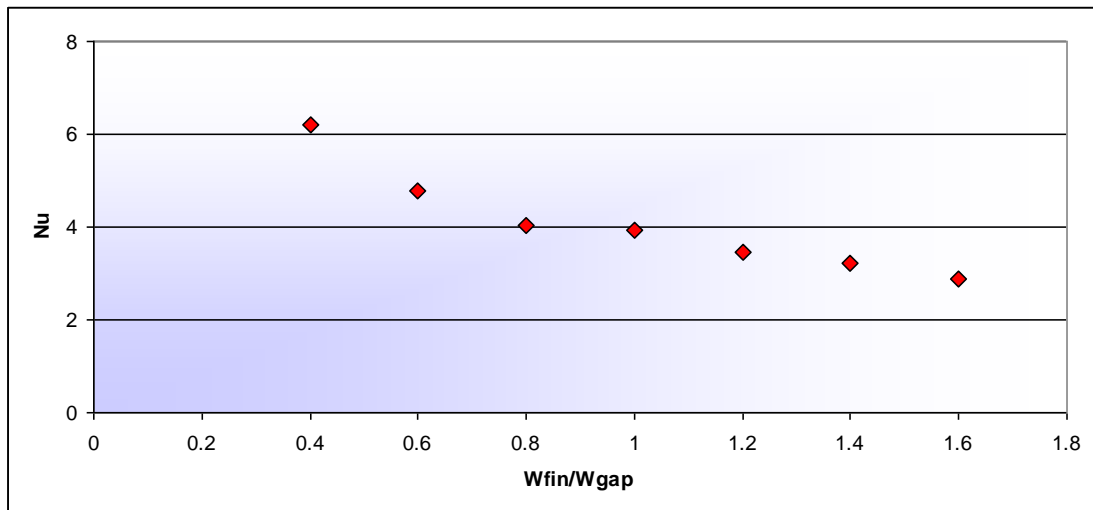


Figure 3-32: The influence of W_{fin}/W_{gap} on the Nusselt number

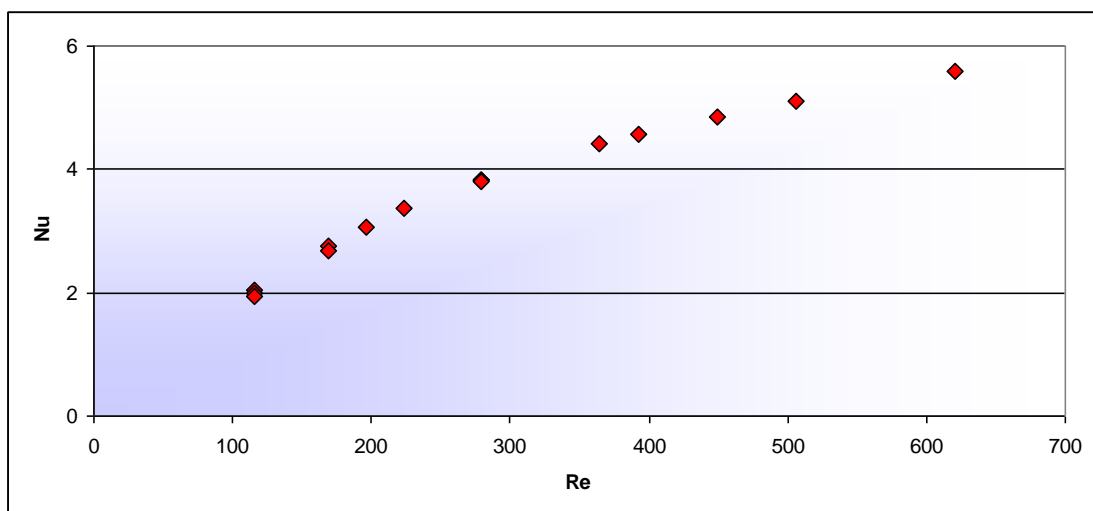


Figure 3-33: The influence of Reynolds number on the Nusselt number



Figure 3-34 to Figure 3-37 display the Nusselt number compared with the Reynolds number for the different values of the set of non-dimensional geometrical parameters.

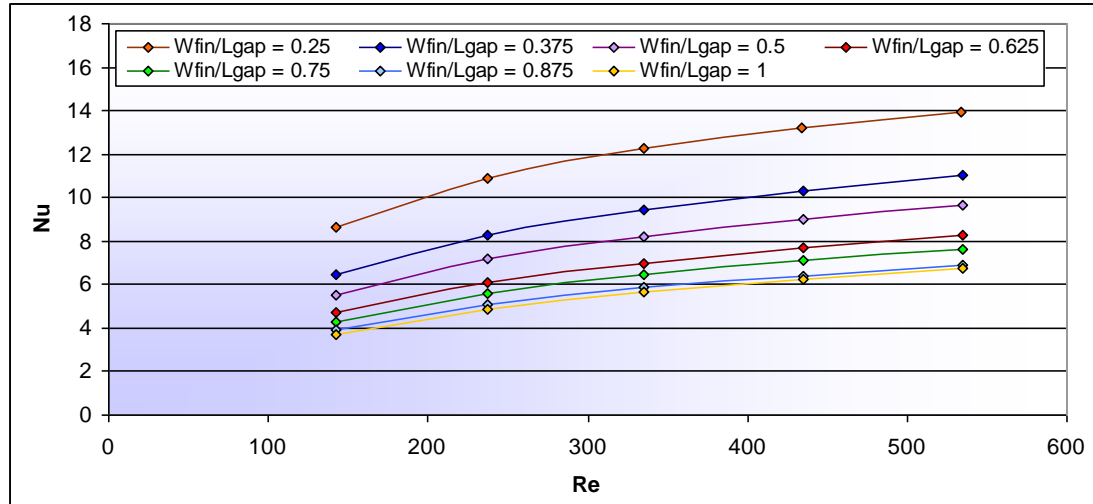


Figure 3-34: The effect of W_{fin}/L_{gap} on the Reynolds-Nusselt function

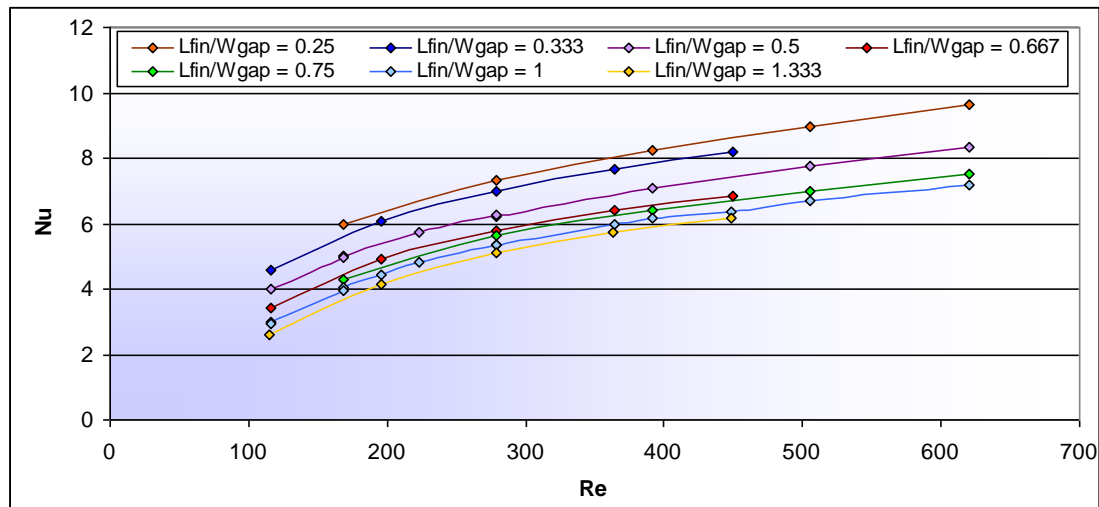


Figure 3-35: The effect of L_{fin}/W_{gap} on the Reynolds-Nusselt function

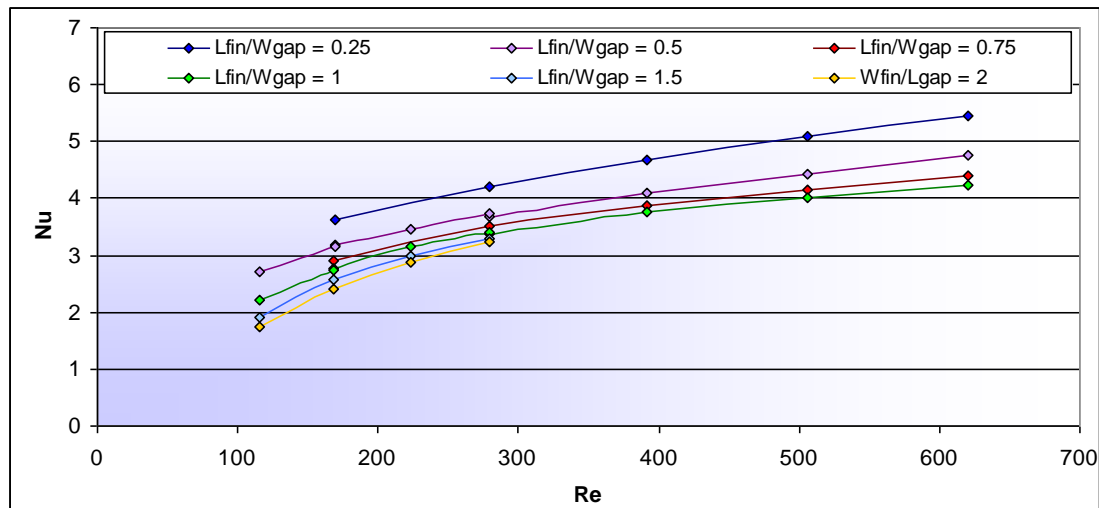


Figure 3-36: The effect of L_{fin}/L_{gap} on the Reynolds-Nusselt function

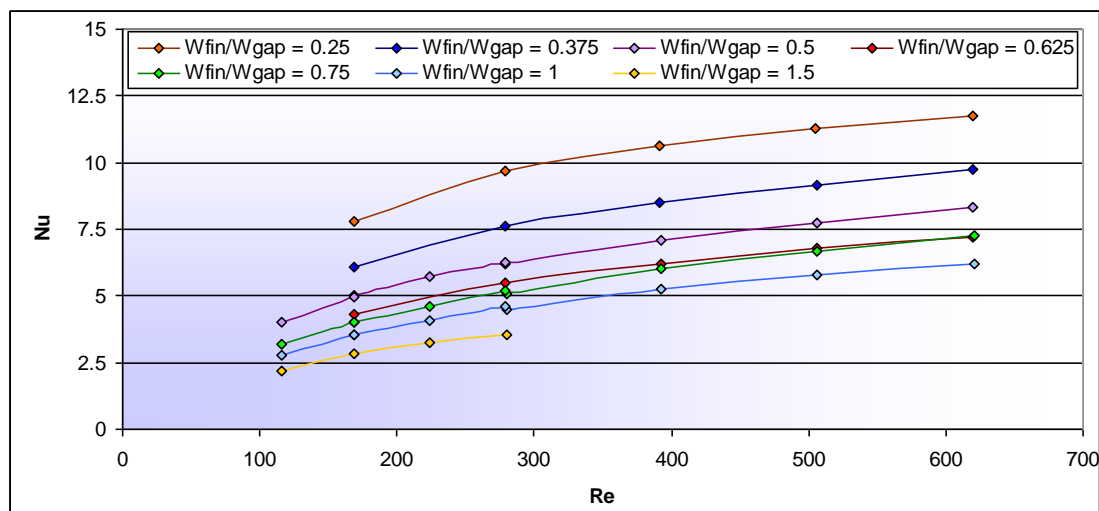


Figure 3-37: The effect of W_{fin}/W_{gap} on the Reynolds-Nusselt function

When plotting the Nusselt numbers against the Reynolds numbers, keeping the fin length, fin width and gap length constant, only varying the gap width, it is found that the values have only a small spread around a logarithmic curve. A representative graph is shown in Figure 3-38. This suggests that the gap width does not influence the Nusselt number significantly. Therefore, it was decided to try and combine the geometric parameters which do not contain the gap width, namely W_{fin}/L_{gap} and L_{fin}/L_{gap} , into a logarithmic function which fits the Nusselt numbers.

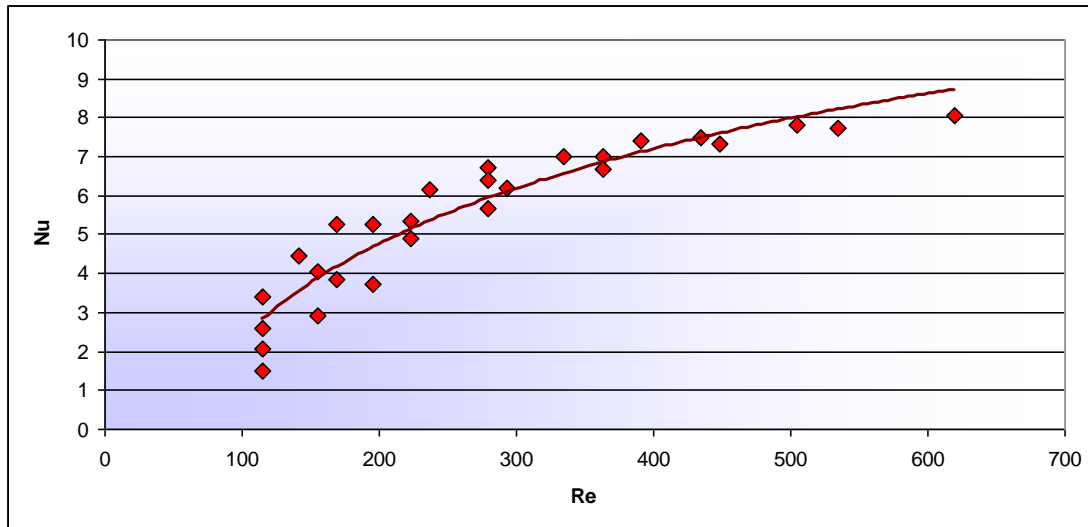


Figure 3-38: The Nusselt number as a function of Reynolds number with constants L_{fin} , L_{gap} and W_{fin} , but variable W_{gap}

Plotting Nusselt numbers against Reynolds numbers for different values of W_{fin}/L_{gap} , keeping L_{fin}/W_{gap} and L_{fin}/L_{gap} constant, results in graphs as shown in Figure 3-39. Logarithmic trend lines seem to fit the data the best. Trend lines between the Reynolds numbers and the Nusselt numbers are calculated by means of regression line theory.

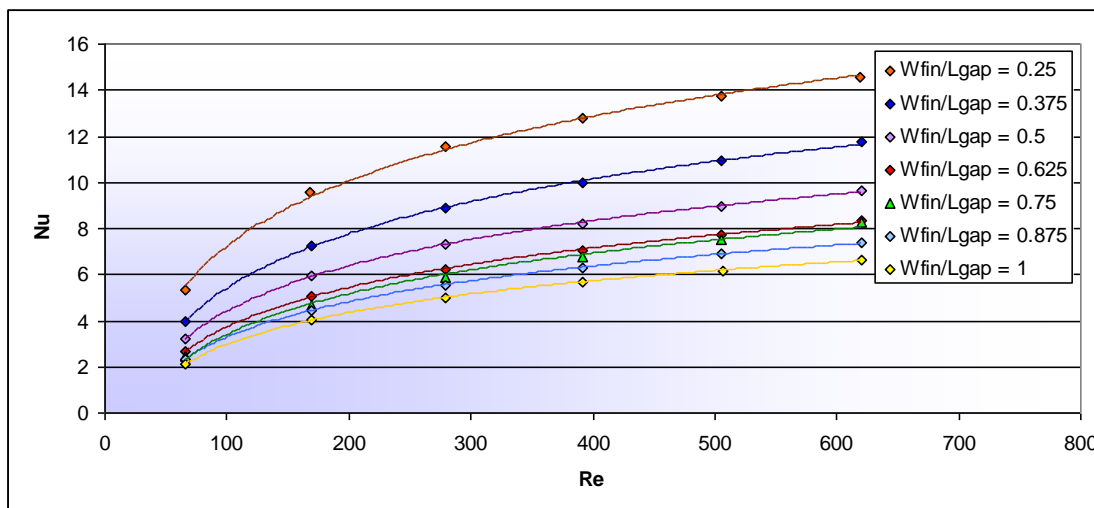


Figure 3-39: The effect of W_{fin}/L_{gap} on the Nusselt numbers

The trend lines in Figure 3-39 are in the following form:

$$Nu = a \ln(Re) - b \tag{47}$$



Plotting the two constants of each of the regression lines in Figure 3-39 above as a function of the W_{fin}/L_{gap} values, the result is two new functions as shown in Figure 3-40. For constant a as well as constant b , power law regression lines are calculated.

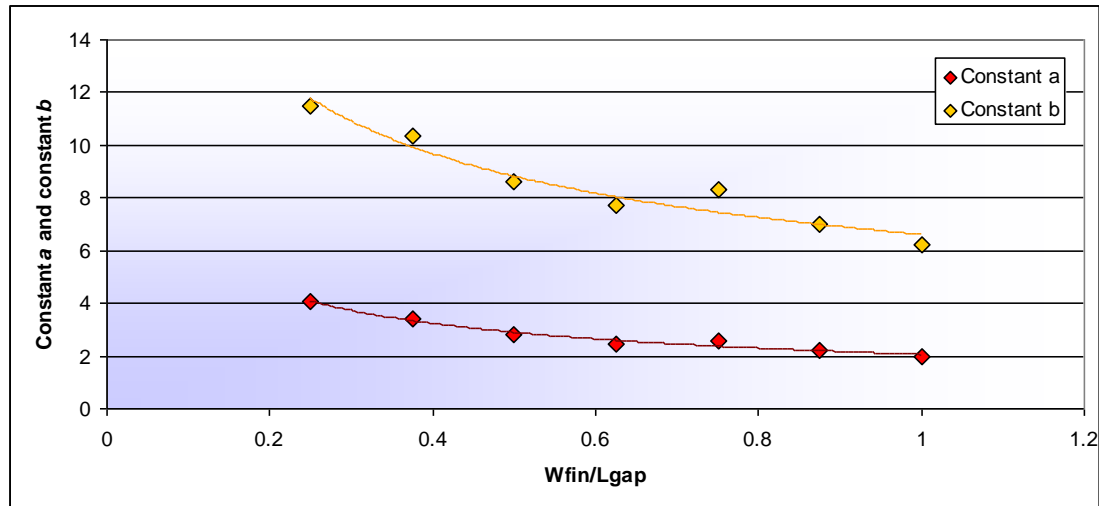


Figure 3-40: Constants a and b as a function of W_{fin}/L_{gap}

The two regression lines for constant a and constant b , together with the logarithmic regression line between the Reynolds numbers and the Nusselt numbers, can be combined to give a single equation for the non-dimensional heat transfer coefficient as a function of the Reynolds number and the W_{fin}/L_{gap} parameter for constant values of L_{fin}/W_{gap} and L_{fin}/L_{gap} .

$$Nu = \left[c_1 \left(\frac{W_{fin}}{L_{gap}} \right)^{c_2} \right] \ln(Re) - \left[c_3 \left(\frac{W_{fin}}{L_{gap}} \right)^{c_4} \right] \quad (48)$$

This procedure can be applied to all the values of L_{fin}/L_{gap} , keeping L_{fin}/W_{gap} constant. This results in a set of constants (c_1 to c_4) for each value of L_{fin}/L_{gap} . These values are plotted in Figure 3-41 and Figure 3-42. When plotting the data, the values of constants c_1 and c_3 represent power law functions. Constants c_2 and c_4 do not fit any simple function very well, so it was decided to fit a first-order equation (straight line) through the points. These four data points, derived from numerical simulations, are too few to be sure of the form the regression lines should take.

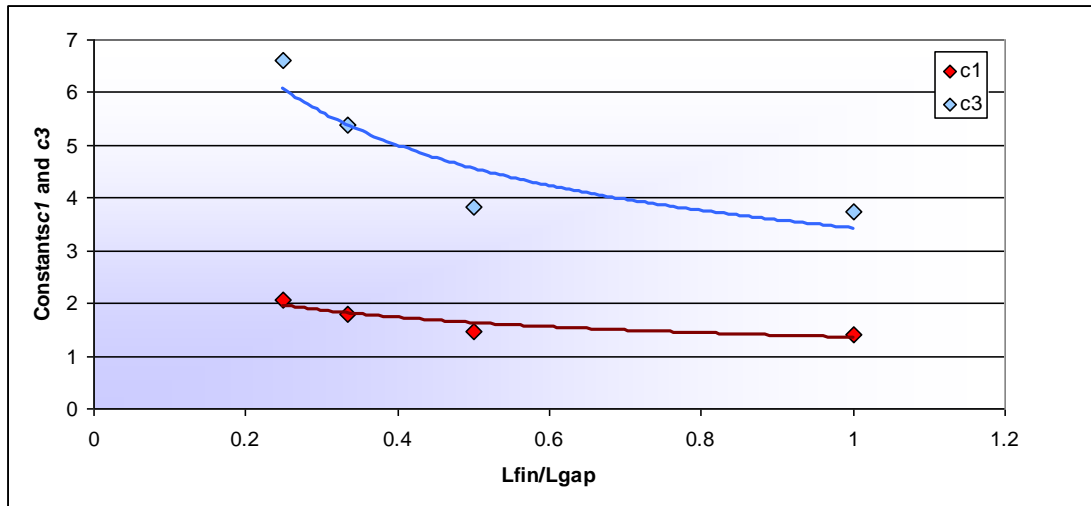


Figure 3-41: Constants c_1 and c_3 as a function of L_{fin}/L_{gap}

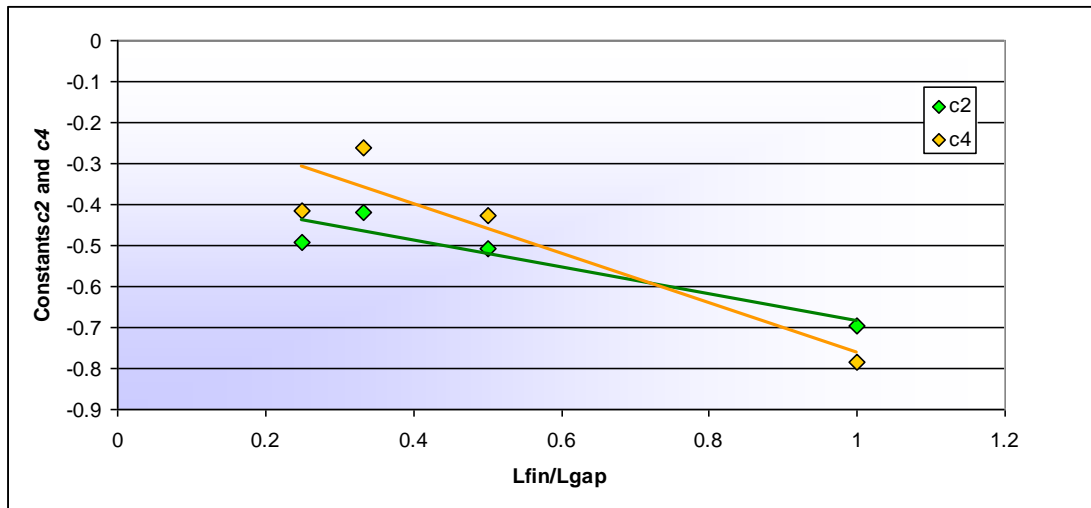


Figure 3-42: Constants c_2 and c_4 as a function of L_{fin}/L_{gap}

The regression lines for c_1 to c_4 are shown in Equation 49 below.

$$\begin{aligned}
 c_1 &= X_1 \left(\frac{L_{fin}}{L_{gap}} \right)^{X_2} \\
 c_2 &= X_3 \left(\frac{L_{fin}}{L_{gap}} \right) + X_4 \\
 c_3 &= X_5 \left(\frac{L_{fin}}{L_{gap}} \right)^{X_6} \\
 c_4 &= X_7 \left(\frac{L_{fin}}{L_{gap}} \right) + X_8
 \end{aligned} \tag{49}$$



Expanding Equation 48 for the Nusselt number with the regression lines for c_1 to c_4 , an equation for the Nusselt number as a function of L_{fin}/L_{gap} , W_{fin}/L_{gap} and Reynolds number can be written as shown below. The constants X_1 to X_8 are extracted from the regression lines shown in Figure 3-41 and Figure 3-42.

$$Nu_{pre} = \left(X_1 \left(\frac{L_{fin}}{L_{gap}} \right)^{X_2} \left(\frac{W_{fin}}{L_{gap}} \right)^{\left(X_3 \left(\frac{L_{fin}}{L_{gap}} \right) + X_4 \right)} \right) \ln(Re) - \left(X_5 \left(\frac{L_{fin}}{L_{gap}} \right)^{X_6} \left(\frac{W_{fin}}{L_{gap}} \right)^{\left(X_7 \left(\frac{L_{fin}}{L_{gap}} \right) + X_8 \right)} \right) \quad (50)$$

Figure 3-43 shows an example of the Nusselt numbers from the CFD compared with the Nusselt numbers calculated from the derived equation. This graph represents the data for constant L_{fin}/W_{gap} . A similar equation can be derived for each value of L_{fin}/W_{gap} solved, with the only difference being the values of constants X_1 to X_8 . Figure 3-44 shows the differences between the CFD and the calculated data. Figure 3-45 shows the Nusselt numbers from the preliminary equation as a function of the CFD Nusselt numbers. A perfect fit will fall on the black 45° line.

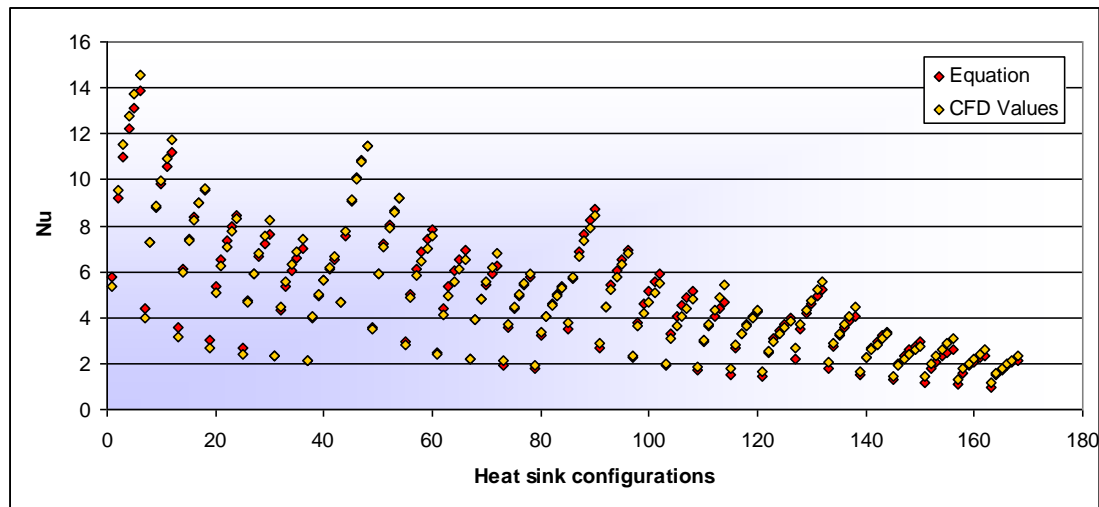


Figure 3-43: Comparison of the preliminary equation values with CFD values

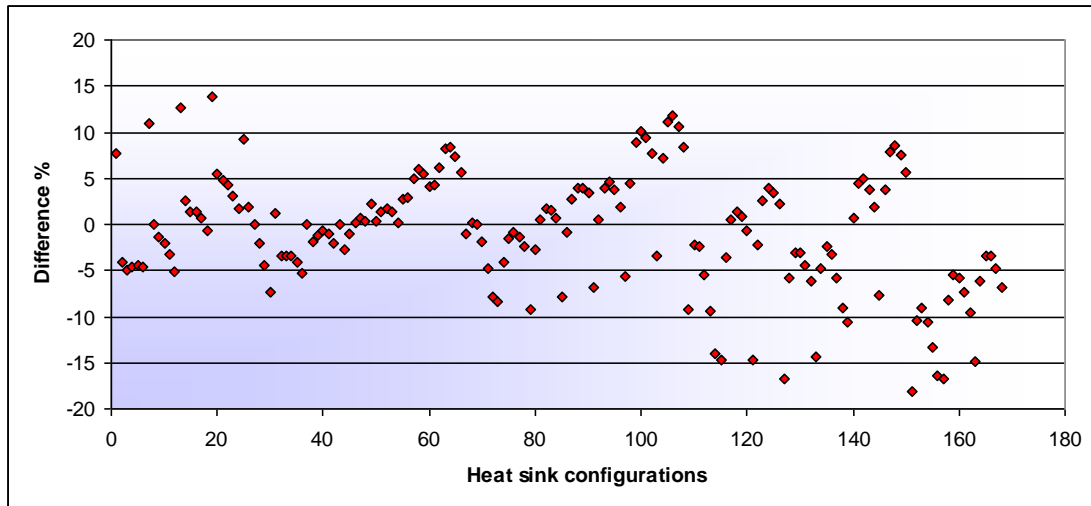


Figure 3-44: Differences between the preliminary equation and the CFD values in Figure 3-43

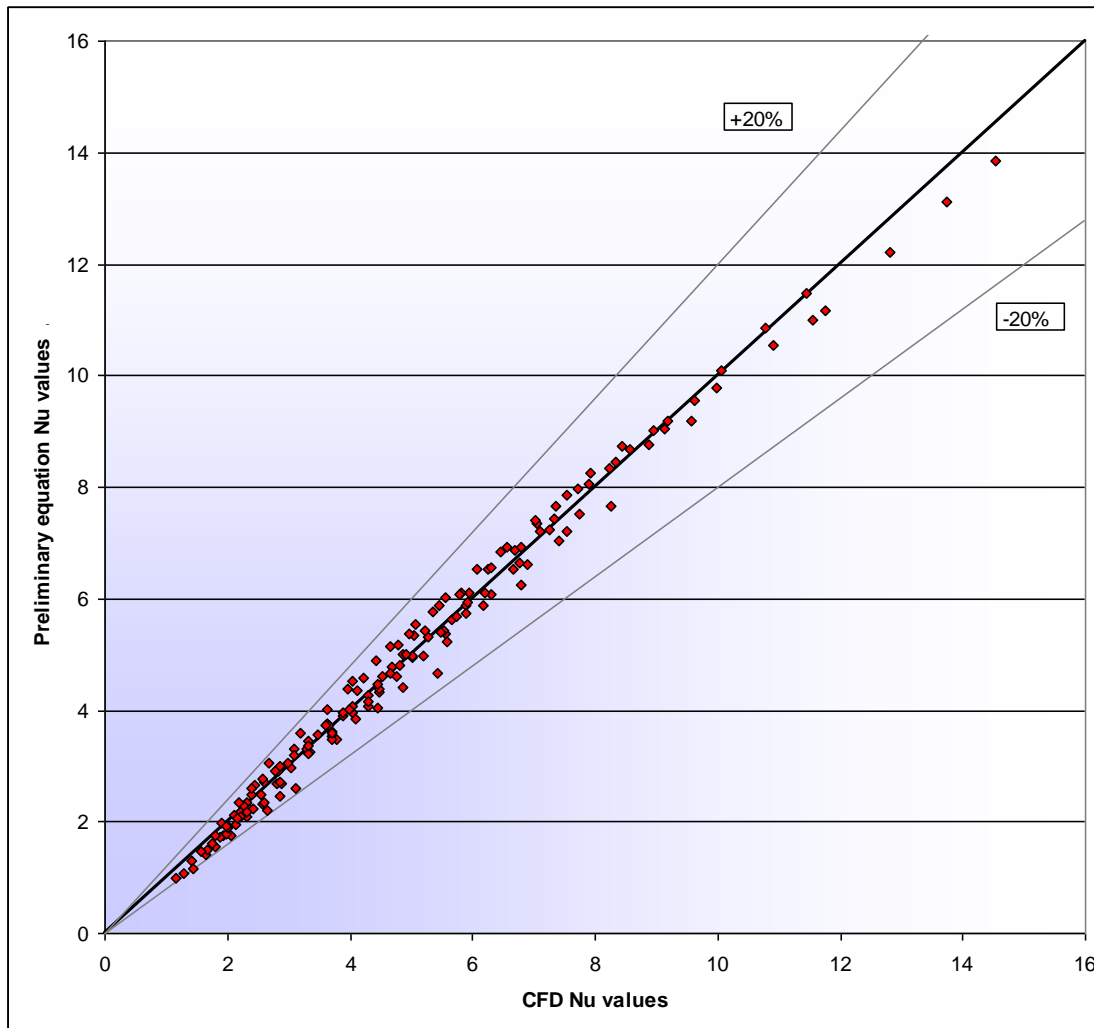


Figure 3-45: Preliminary equation Nusselt numbers as a function of CFD Nusselt numbers



From these two figures, one can see that the percentage differences on the lower Nusselt numbers are higher than those on the high Nusselt numbers. This is a result of the regression line calculation. Regression line theory does not take percentage or normalised differences into account, but the actual difference between the equation and the data to be fitted. A better fit can be generated by applying an optimisation scheme to the above equation, optimising the constants by using the percentage differences as the objective function.

Theoretically, these sets of constants could now be plotted for every $Lfin/Wgap$ value and new regression lines could be calculated for these constants. Then the newly created regression lines could be combined with the above equation to generate a single equation for the complete CFD data set. But in this case, the method resulted in data plots which did not fit any simple regression line very well, and the number of data points was too small to fit a higher-order regression line through the data with enough confidence. Therefore, another approach was needed.

It was decided to use the constant set for the $Lfin/Wgap=1$ series as the default, and then divide the other $Lfin/Wgap$ series with this series. This gives the differences between the $Lfin/Wgap=1$ series and the other series. Creating an equation that fits these differences, and multiplying it with the $Lfin/Wgap=1$ series, resulted in a fit for any $Lfin/Wgap$ series. The $Lfin/Wgap=1$ series was chosen because it is the series with the most data points.

Plotting different data points together with different combinations of the geometric parameters suggested a combination of a power law function on the Reynolds number with an exponential function on the $Lfin/Wgap$ parameter. A power law function for the $Wfin/Wgap$ parameter was also added. The complete difference equation is shown below.

$$Re \left(X_9 \left(\frac{Lfin}{Wgap} \right)^{X_{10} + X_{11}} \left(\frac{Lfin}{Lgap} \right)^{X_{12}} \left(\frac{Wfin}{Wgap} \right)^{-X_{13}} \left(\frac{Lfin}{Lgap} \right)^{X_{14}} \right) \left(\frac{Wfin}{Wgap} \right)^{X_{15}} \cdot \left(X_{16} \left(\frac{Lfin}{Lgap} \right)^{X_{17}} \left(\frac{Wfin}{Wgap} \right) + X_{18} \left(\frac{Lfin}{Lgap} \right)^{X_{19}} \right) \cdot e^{X_{20} \left(\frac{Lfin}{Wgap} \right)} \quad (51)$$



Combining this equation with the previous one for the $Lfin/Wgap$ series (Equation 50), gives the final form of the empirically determined Nusselt number (Equation 52). This equation approximates the Nusselt numbers calculated from the CFD values.

$$Nu_{eq} = X_1 \left(\left(\frac{Lfin}{Lgap} \right)^{X_2} \left(\frac{Wfin}{Lgap} \right)^{\left(X_3 \left(\frac{Lfin}{Lgap} \right)^{X_4} \right)} \right) \ln(Re) - \left(X_5 \left(\frac{Lfin}{Lgap} \right)^{X_6} \left(\frac{Wfin}{Lgap} \right)^{\left(X_7 \left(\frac{Lfin}{Lgap} \right)^{X_8} \right)} \right)$$

$$Re^{\left(X_9 \left(\frac{Lfin}{Wgap} \right)^{X_{10}} + X_{11} \left(\frac{Lfin}{Lgap} \right)^{X_{12}} \left(\frac{Wfin}{Wgap} \right)^{-X_{13}} \left(\frac{Lfin}{Lgap} \right)^{X_{14}} \right)} \left(\frac{Wfin}{Wgap} \right)^{X_{15}}$$

$$\left(X_{16} \left(\frac{Lfin}{Lgap} \right)^{X_{17}} \left(\frac{Wfin}{Wgap} \right) + X_{18} \left(\frac{Lfin}{Lgap} \right)^{X_{19}} \right) \cdot e^{-X_{20} \left(\frac{Lfin}{Wgap} \right)}$$
(52)

Figure 3-46 shows a comparison between the CFD data and the initial equation. The percentage differences between Reynolds numbers of 100 and 650 are shown in Figure 3-47. The percentage differences for very low Reynolds numbers are quite high due to the small Nusselt numbers. These small Nusselt numbers lean towards natural convection, which is not in the scope of this research. Figure 3-48 displays the equation values as a function of the CFD values. The straighter and thinner the line is, the better the equation represents the CFD data.

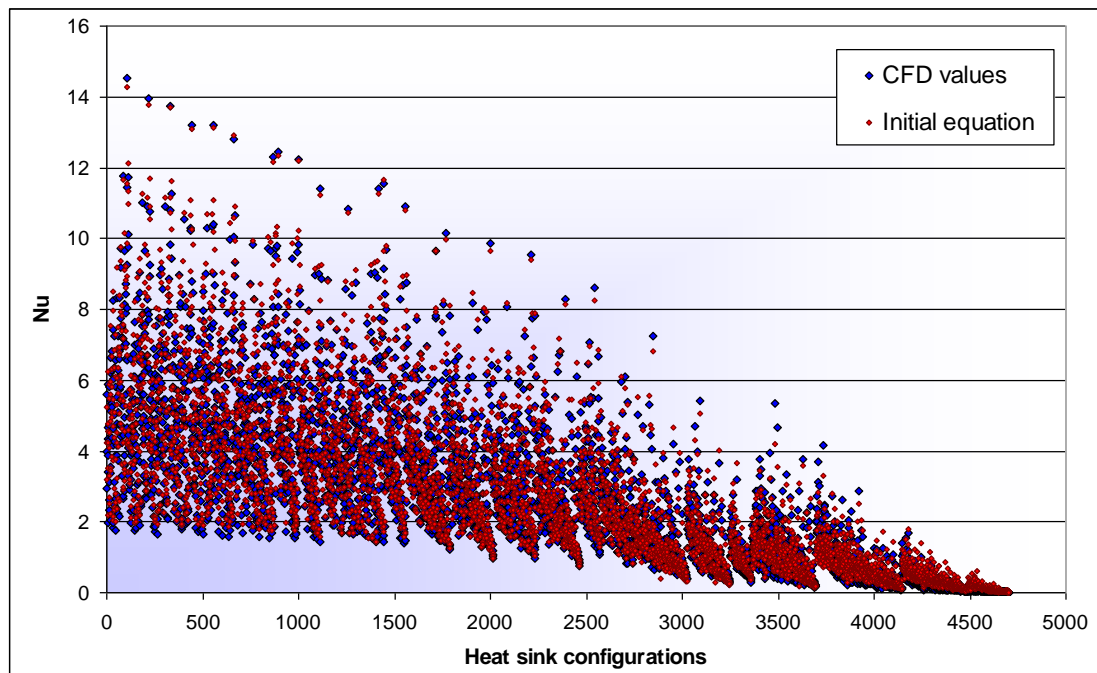


Figure 3-46: Comparison between CFD values and initial correlation

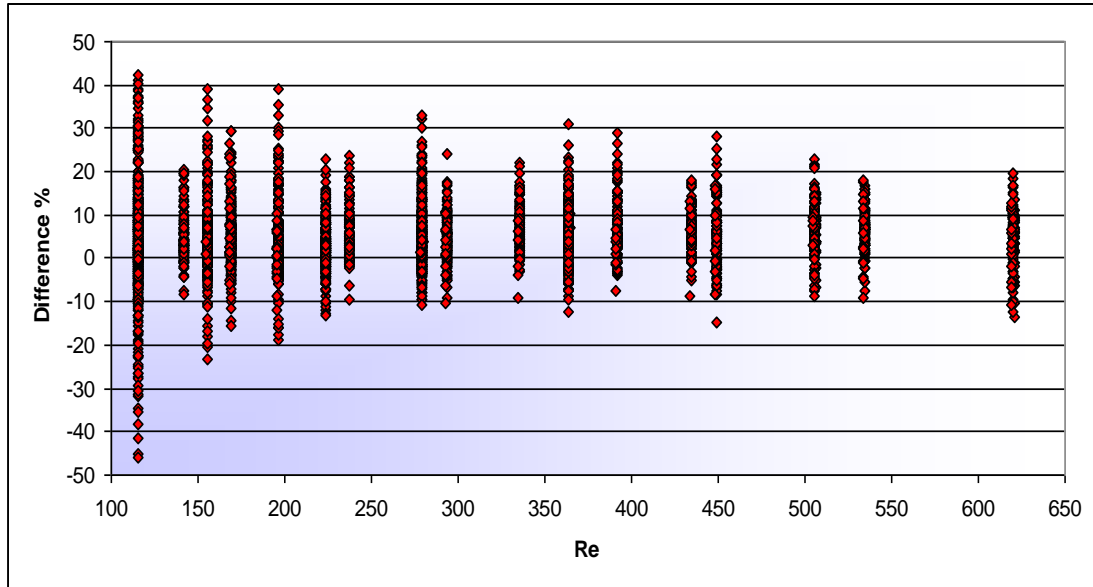


Figure 3-47: Percentage differences between CFD and initial correlation

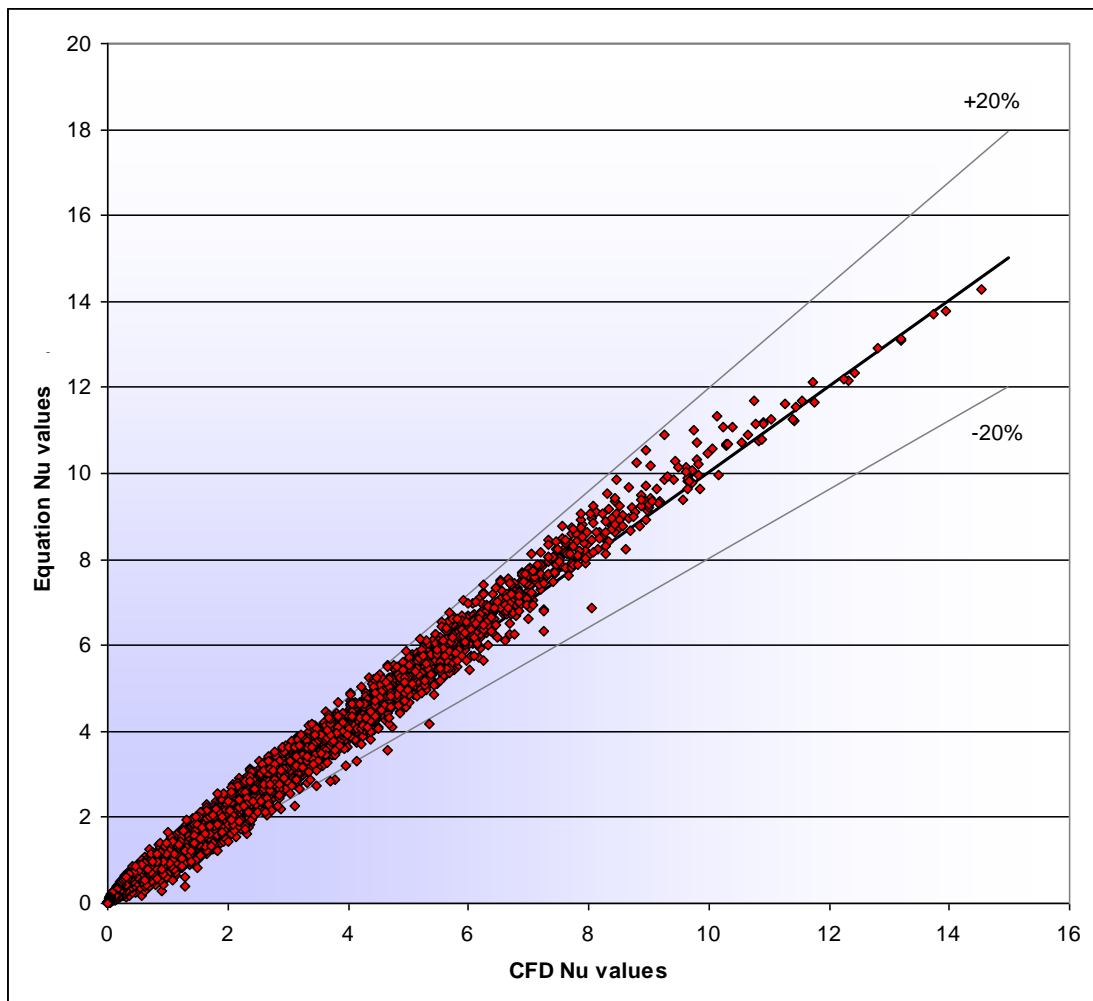


Figure 3-48: Equation Nusselt numbers as a function of CFD Nusselt numbers



The 20 equation constants are optimised with the LFOPC optimisation algorithm. First-order gradients are used instead of the real equation partial derivatives due to complexity of the equation. The optimisation algorithm is applied with different initial values to test the convergence. With some sets of starting values, the optimisation procedure does diverge. This can probably be prevented if side constraints are put on the coefficients being optimised, but since it is very difficult to determine appropriate side constraints none were imposed. It is believed that several local minima are clustered close together, which makes it difficult to determine the global minimum. The gradients are also small and quite similar over a large range of coefficient values. The objective function value also stays relatively constant although the values of the coefficients are still moving around. Only the data between Reynolds numbers 100 and 650 were used for the optimisation procedure.

The optimisation procedure is stopped after 30 000 iterations. The local minimum with the smallest objective function is selected as the optimum. Figure 3-49 shows the convergence history of the objective function.

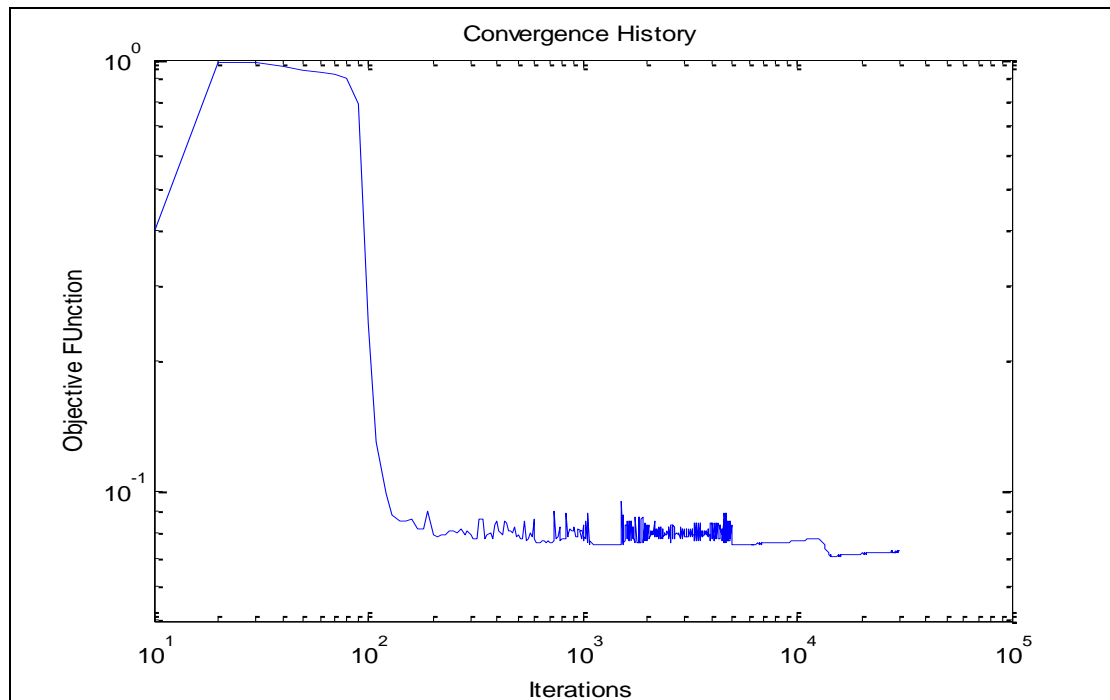


Figure 3-49: Convergence history of the objective function

After optimisation, it is found that data points with low Nusselt are too low. Therefore, an arctangent curve fit between the Nusselt numbers and the ratio between



the CFD values and the optimised equation is calculated to offset this inconsistency. The equation with the added curve fit is shown below. The constants of the final equation are displayed in Table 3-4.

$$Nu_{eq} = Nu_s (X_{21} - X_{22} \tan^{-1}(X_{23} Nu_s + X_{24}))$$

where

$$Nu_s = X_1 \left(\left(\frac{Lfin}{Lgap} \right)^{X_2} \left(\frac{Wfin}{Lgap} \right)^{X_3 \left(\frac{Lfin}{Lgap} \right) + X_4} \ln(Re) - \left(X_5 \left(\frac{Lfin}{Lgap} \right)^{X_6} \left(\frac{Wfin}{Lgap} \right)^{X_7 \left(\frac{Lfin}{Lgap} \right) + X_8} \right) \right) \quad (53)$$

$$Re \left(X_9 \left(\frac{Lfin}{Wgap} \right)^{X_{10} + X_{11}} \left(\frac{Lfin}{Lgap} \right)^{X_{12}} \left(\frac{Wfin}{Wgap} \right)^{X_{13}} \left(\frac{Lfin}{Lgap} \right)^{X_{14}} \right) \left(\frac{Wfin}{Wgap} \right)^{X_{15}}$$

$$\left(X_{16} \left(\frac{Lfin}{Lgap} \right)^{X_{17}} \left(\frac{Wfin}{Wgap} \right) + X_{18} \left(\frac{Lfin}{Lgap} \right)^{X_{19}} \right) \cdot e^{X_{20} \left(\frac{Lfin}{Wgap} \right)}$$

Table 3-4: Optimised constants for the final equation

Constant	Value	Constant	Value
X_1	14.4147	X_{13}	-0.7616
X_2	-0.0661	X_{14}	-0.2038
X_3	-0.1251	X_{15}	-0.0044
X_4	-0.4199	X_{16}	-0.4024
X_5	3.8455	X_{17}	0.8809
X_6	-0.0803	X_{18}	2.0115
X_7	-0.1196	X_{19}	0.7348
X_8	-0.4126	X_{20}	-2.5039
X_9	0.4123	X_{21}	24.6705
X_{10}	-1.2581	X_{22}	14.9042
X_{11}	0.0411	X_{23}	52.1538
X_{12}	0.7487	X_{24}	-0.8421

Figure 3-50 displays the percentage differences between the correlated equation and the CFD Nusselt numbers for all the heat sinks tested. The initial and the optimised



differences are shown. The majority, 99.4%, of the 3 024 configurations fall within a 20% error, and 90.7% fall within a 10% error. Figure 3-51 shows both the initial equation Nusselt numbers and the optimised equation Nusselt numbers as a function of the CFD Nusselt numbers. The optimised Nusselt numbers form a thinner line than that of the initial Nusselt numbers indicating a better fit. A comparison between the optimised equation and the CFD Nusselt numbers is shown in Figure 3-52. Configurations where the equation values are smaller than the CFD values are to the left, and configurations where the equation values are higher than the CFD values are to the right.

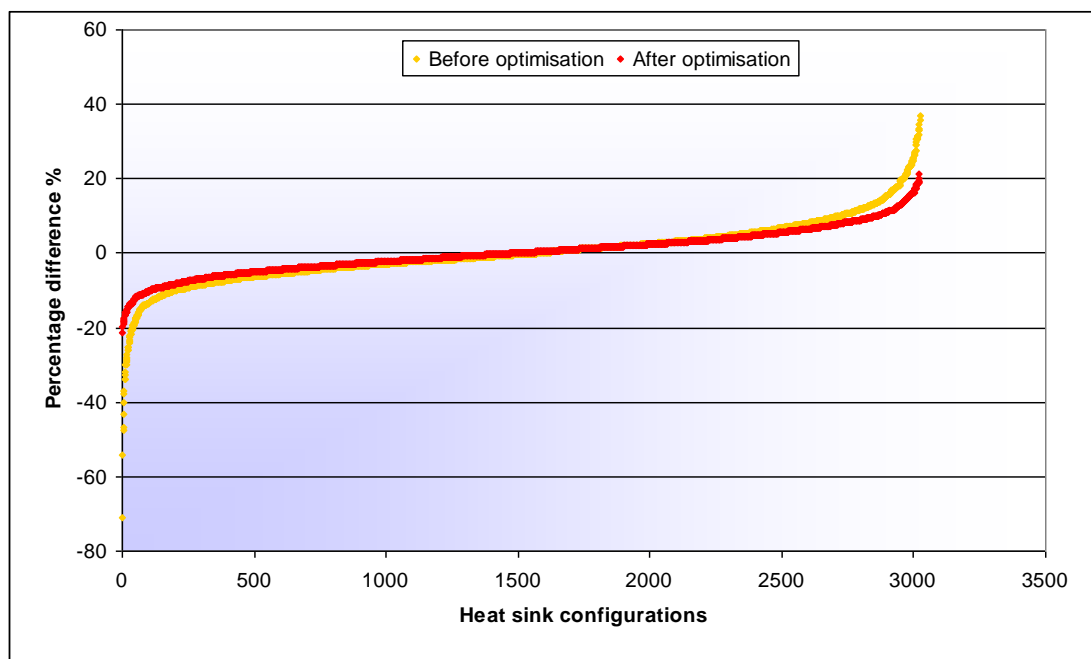


Figure 3-50: Percentage differences between CFD values and correlated equation before and after optimisation

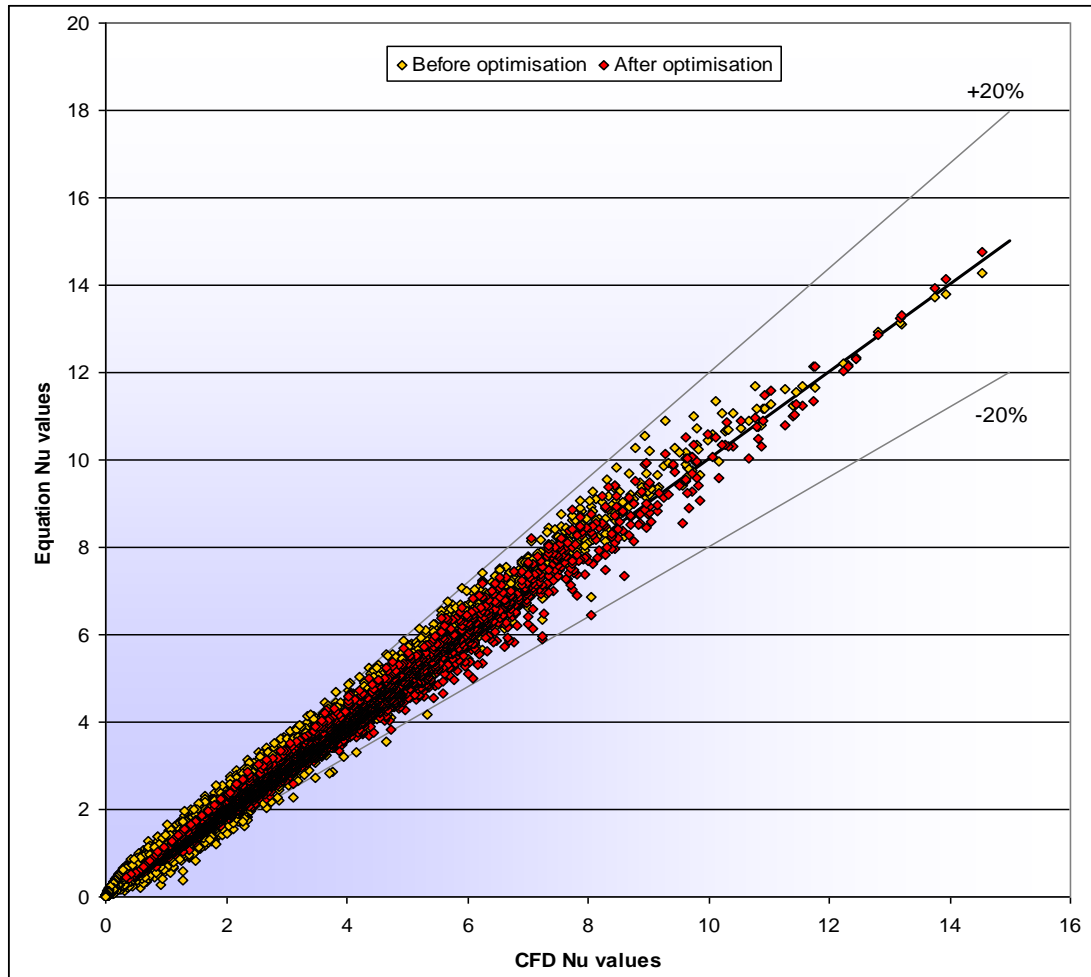
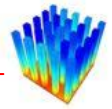


Figure 3-51: Equation Nusselt numbers as a function of CFD Nusselt number before and after optimisation

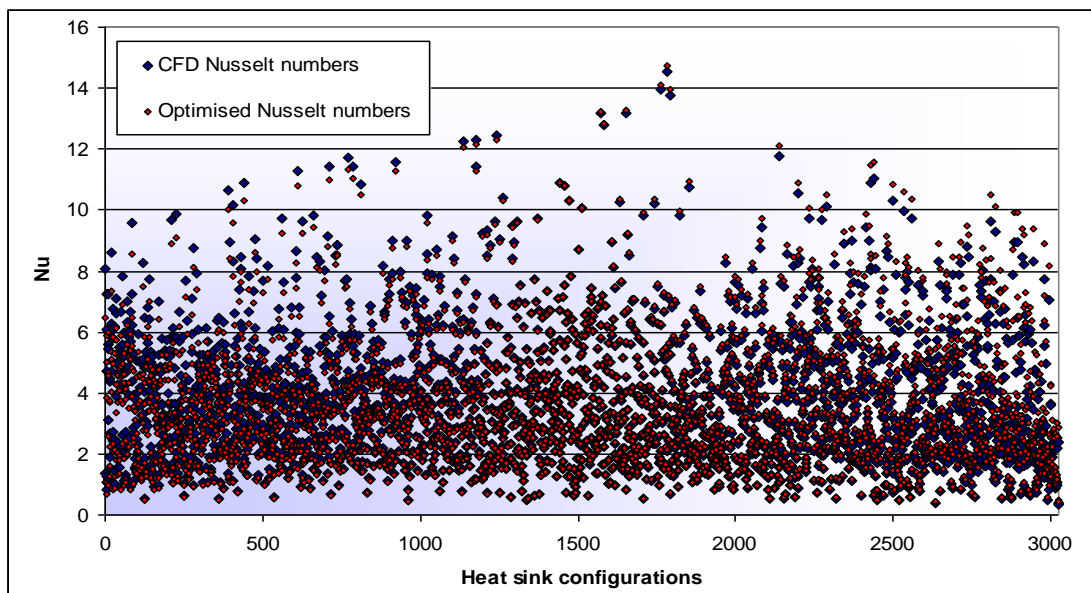


Figure 3-52: Comparison between CFD Nusselt numbers and the final laminar edge correlation



3.5 LAMINAR FACE EQUATION

The red faces in Figure 3-53 represent the faces on which the laminar face equation is calculated. Simulating the heat transfer coefficient across the faces of the pins is quite complicated since it is not a single value, but a whole range of values. The discretisation of the CFD model makes it even more difficult because it misrepresents the actual function on the face. An example of this function can be seen in Figure 3-54.

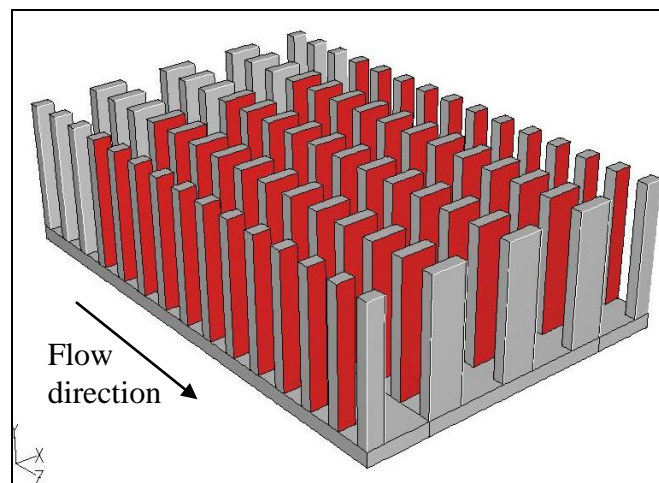


Figure 3-53: Contraction heat transfer coefficient faces

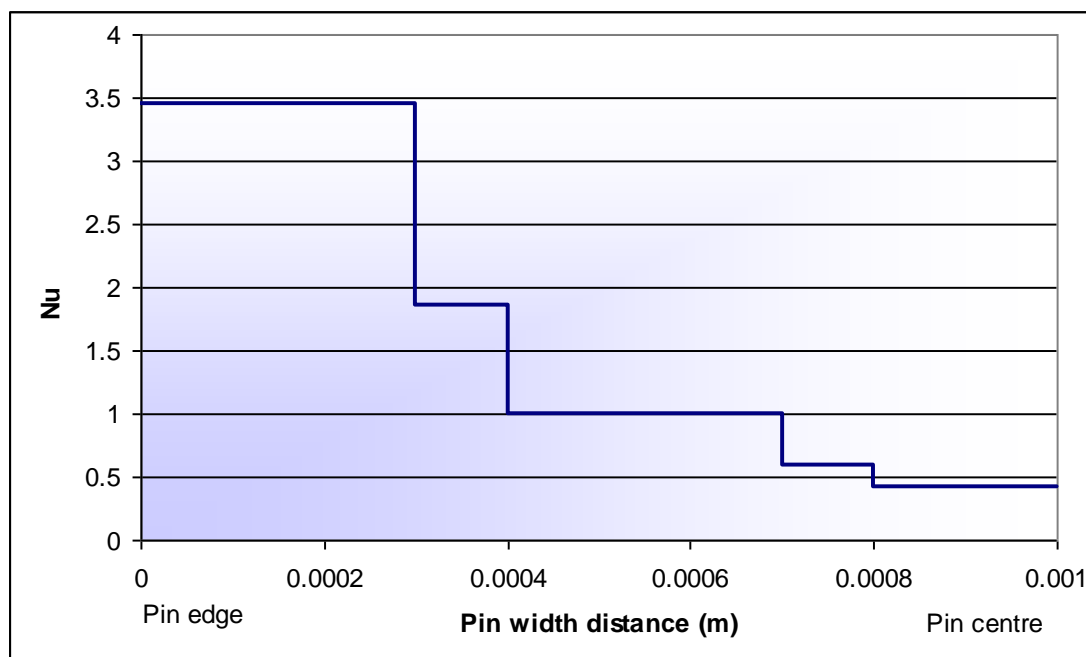


Figure 3-54: Nusselt number across the pin face



Initially, it was thought that an exponential curve will fit the rapidly declining Nusselt values along the width of the pins, but due to the coarse discretisation along the pin face the first section from the edge of the pin is horizontal, which cannot be represented with an exponential function. A hyperbolic tangent equation, shown in Figure 3-55, is therefore selected as the base function.

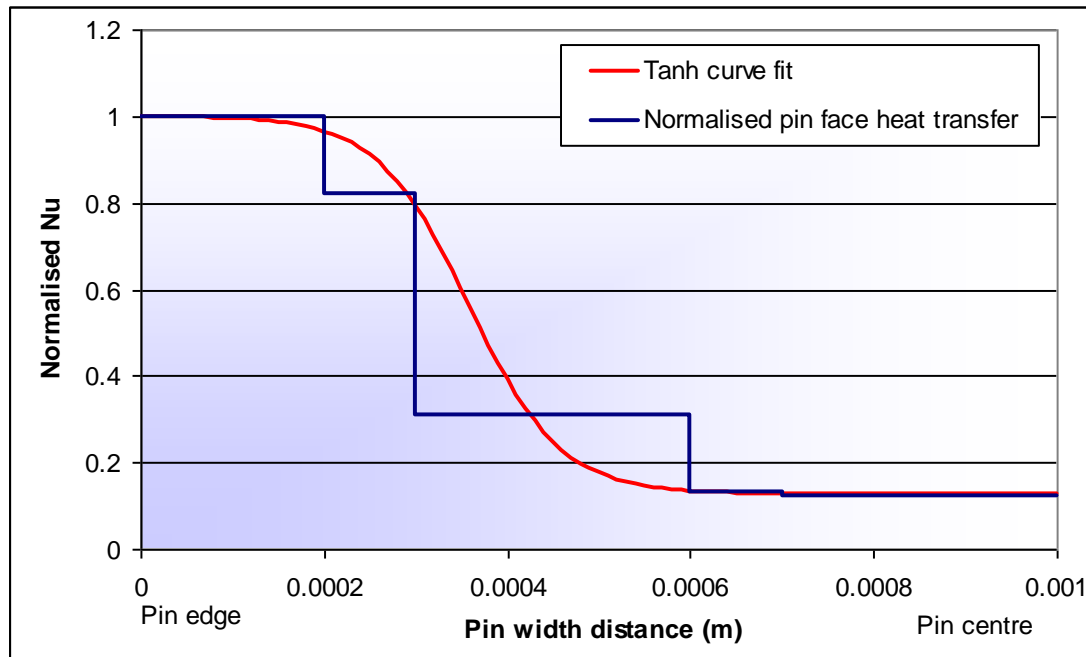


Figure 3-55: Hyperbolic tangent curve fit

Analysing the data in more detail, it can be seen that some heat sink configurations have a steady gradient at the centre of the pins, as shown in Figure 3-56. For these configurations, a hyperbolic tangent equation combined with a first-order equation will represent the CFD values better, but due to the coarse discretisation it was decided not to take this slope into account and only use a hyperbolic tangent function to characterise the heat transfer along the width of the pins.

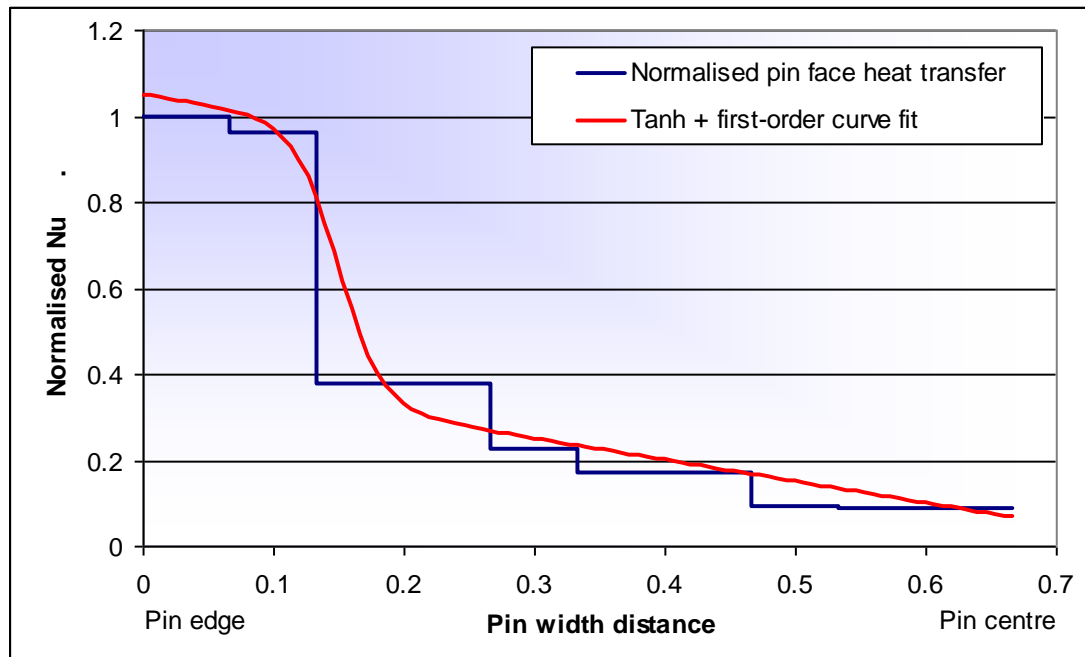


Figure 3-56: Combination of a hyperbolic tangent and first-order curve fit

The Nusselt numbers along the faces are non-dimensionalised by dividing them by the heat transfer values at the edges of the pins, which are in principle the average Nusselt numbers correlated in Section 3.4. The pin widths are also non-dimensionalised to be between zero and 10, where zero is the edges of the pins and 10 the centres of the pins. This was done because the heat transfer coefficients were extracted from 10 strips, and therefore it makes keeping track easier. This gives dimensionless functions between zero and 10 on the x -axis as well as between zero and one on the y -axis, which are called the heat transfer fraction equations (nNu , normalised Nusselt number).

By plotting the heat transfer fraction values with the same geometric parameters on top of each other (Figure 3-57), it is found that the Reynolds number does not affect these values significantly. The Reynolds number is already taken into account in the pin edge heat transfer equation created in Section 3.4.

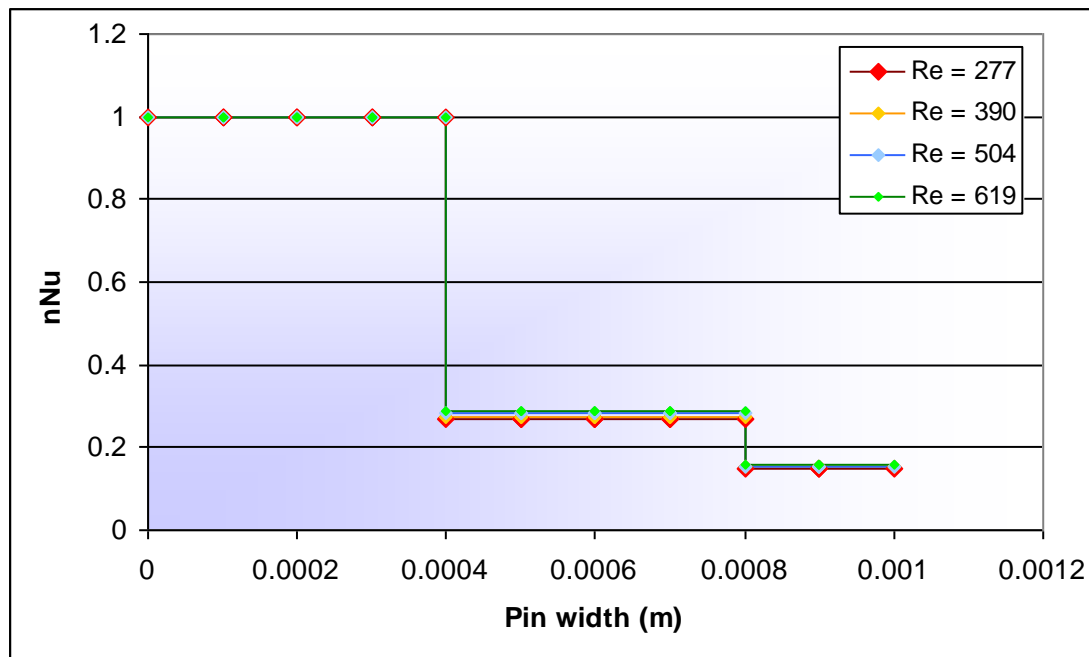


Figure 3-57: Normalised heat transfer on a single pin with different Reynolds numbers

To fit a hyperbolic tangent equation to these heat transfer fraction equations (nNu), it is written in the following form:

$$nNu_{eq} = \left(-\frac{1}{2}(1-a) \right) \tanh(b \cdot x + c) + \frac{1}{2}(1+a) \quad (54)$$

where

- a : The vertical offset on the right-hand side, representing the heat transfer at the centre of the pin
- b : The slope of the hyperbolic function
- c : The horizontal offset of the centre of the slope
- x : A distance along the pin width

The pin width is non-dimensionalised so that the edge is at zero and the centre of the pin is at 10. This is done by modifying the term in front of x in Equation 54.

$$nNu_{eq} = \left(-\frac{1}{2}(1-a) \right) \tanh \left(b \cdot \left(\frac{200}{W_{fin}} x \right) + c \right) + \frac{1}{2}(1+a) \quad (55)$$



The next step is to correlate a , b and c to the CFD data. Parameter a is correlated first, which fixes the boundaries of the correlation. After this has been completed, the gradient and offset can be determined.

After plotting several different geometric parameters against the pin centre normalised heat transfer coefficient, it was decided to create a correlation for all the $L_{fin}/L_{gap}=1$ configurations and then afterwards expand it to contain the entire data set. Disregarding the Reynolds numbers as discussed above, the data set is 168 configurations large.

The form of the correlation a and the coefficients are determined with the same method as discussed in the creation of the first correlation in Section 3.4. Keeping W_{fin}/W_{gap} constant and plotting the Nusselt numbers as a function of L_{gap}/W_{gap} result in graphs which can be fitted with power law regression lines. This is shown in Figure 3-58. The equation is shown below.

$$a = d_1 \left(\frac{L_{gap}}{W_{gap}} \right)^{d_2} \quad (56)$$

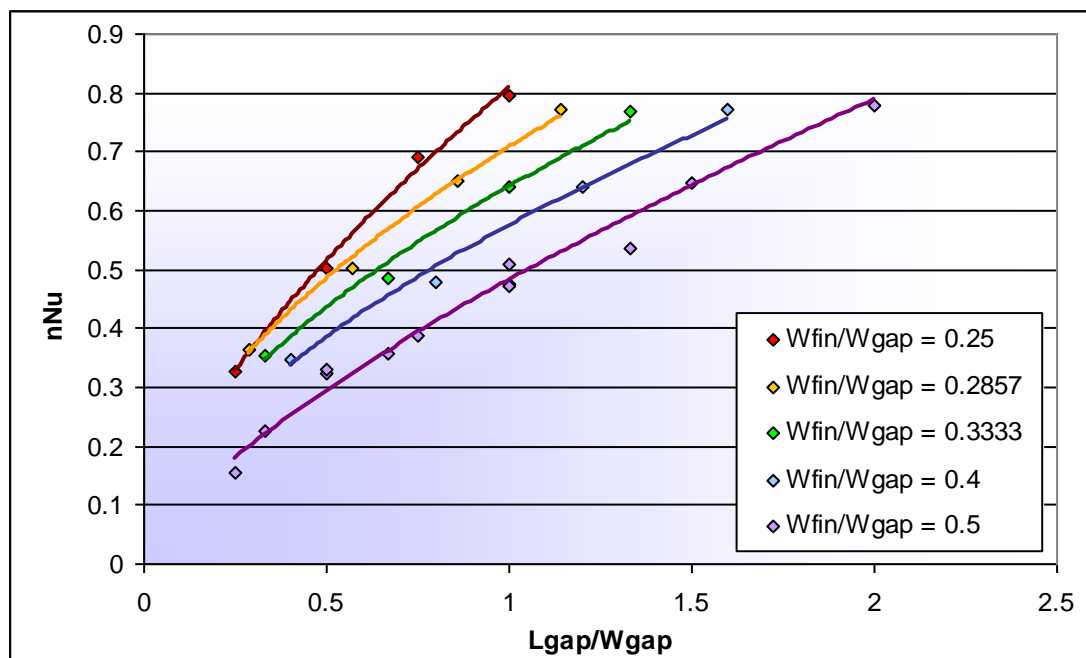


Figure 3-58: Pin centre Nusselt number as a function of L_{gap}/W_{gap}



A power law regression is then created for every value of L_{gap}/W_{gap} . This results in two sets of constants, which are then plotted against the W_{fin}/W_{gap} parameter, as shown in Figure 3-59.

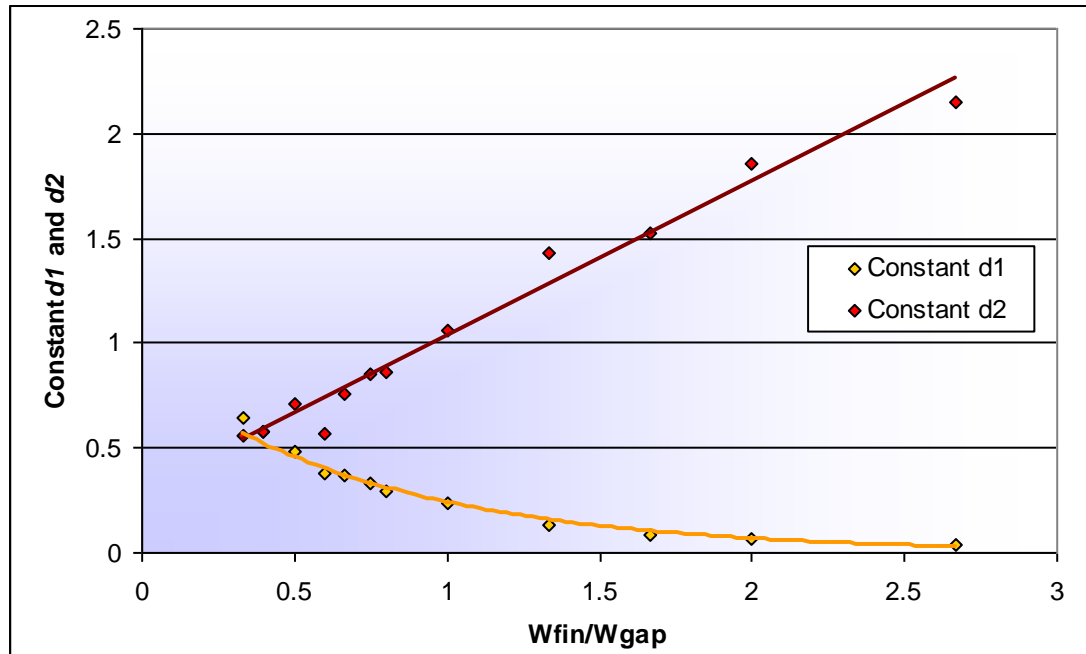


Figure 3-59: Constants d_1 and d_2 as functions of W_{fin}/W_{gap}

An exponential regression line is applied to constant d_1 and a first-order regression line is fitted to constant d_2 . Equation 57 shows the complete function for all the $L_{fin}/L_{gap}=1$ data points. Figure 3-60 displays the comparison between this equation and the CFD values.

$$a = \left(Z_1 \cdot e^{Z_2 \left(\frac{W_{fin}}{W_{gap}} \right)} \cdot \left(\frac{L_{gap}}{W_{gap}} \right)^{Z_3 \left(\frac{W_{fin}}{W_{gap}} \right) + Z_4} \right) \quad (57)$$

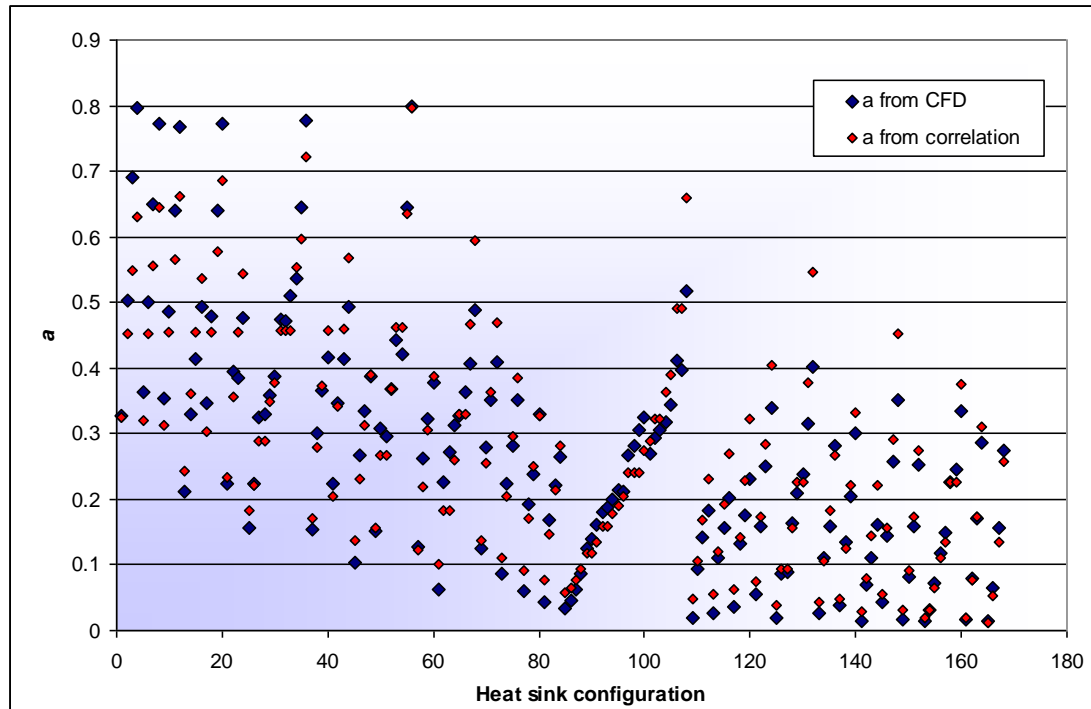


Figure 3-60: Parameter a for $L_{fin}/L_{gap}=1$

The non-dimensionalised centre pin heat transfer coefficients for all the heat sink configurations where L_{fin}/L_{gap} is not equal to one are divided by the calculated values from Equation 57 above. A correlation for these data points is created by inspecting the data and plotting the new data points against different parameters. The complete correlation for parameter a in Equation 54, taking all the data points into account, is displayed below. Figure 3-61 and Figure 3-62 display the CFD values compared with Equation 58.

$$a = \left(Z_1 \cdot e^{Z_2 \left(\frac{W_{fin}}{W_{gap}} \right)} \cdot \left(\frac{L_{gap}}{W_{gap}} \right)^{Z_3 \left(\frac{W_{fin}}{W_{gap}} \right) + Z_4} \right) \cdot e^{Z_5 \left(\frac{L_{fin}}{L_{gap}} \right)} \cdot \left(\frac{L_{gap}}{W_{gap}} \right)^{Z_6 \ln \left(\frac{L_{fin}}{L_{gap}} \right) - Z_7} \quad (58)$$

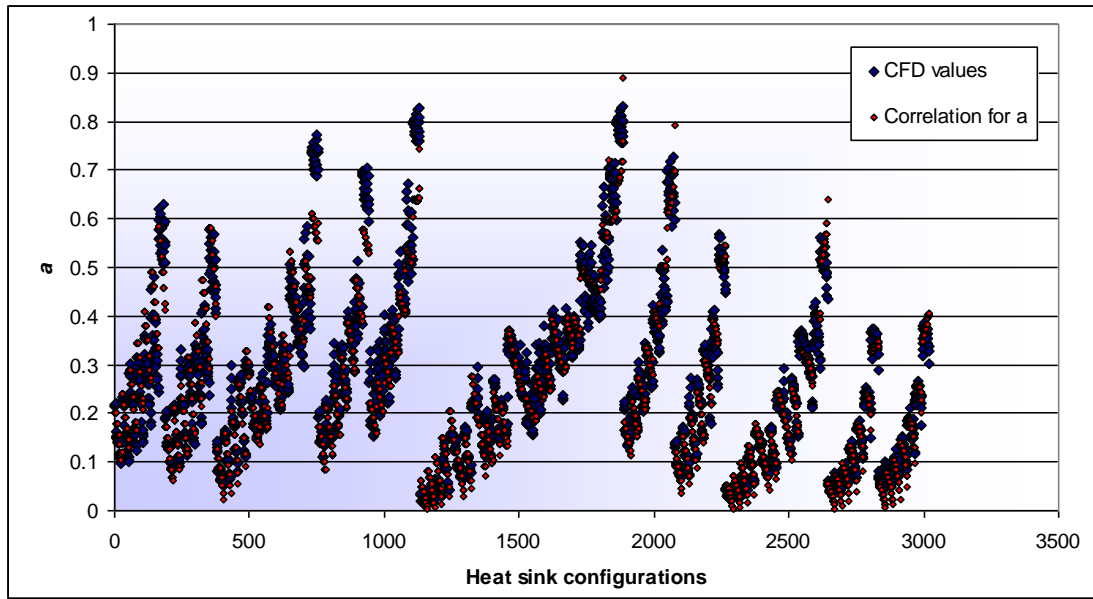


Figure 3-61: Comparison between CFD values and the correlation for a

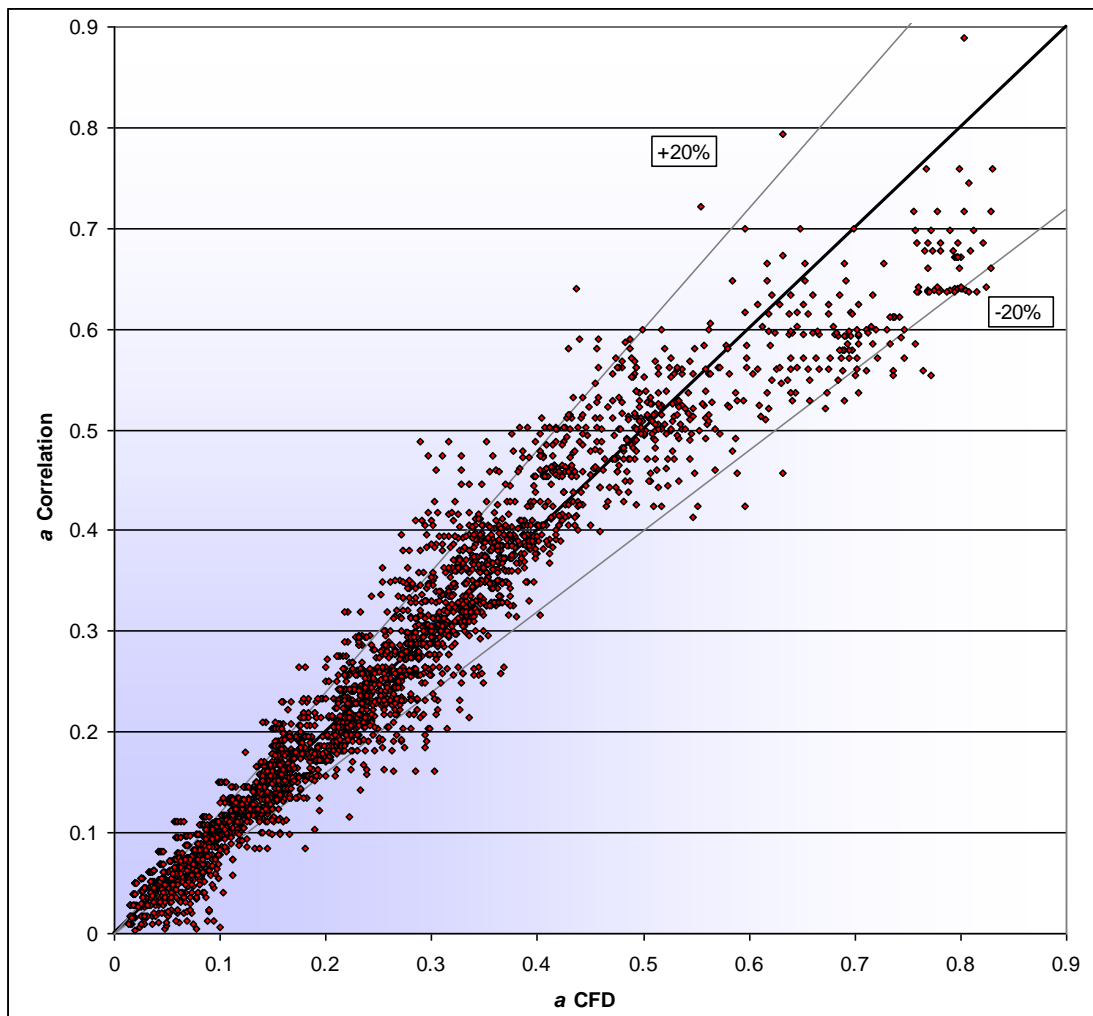


Figure 3-62: Correlation for a as a function of the CFD values for a



Following the correlation for parameter a , correlations for b and c in Equation 54 need to be set up. To examine the relationships between the geometric parameters and the gradient of the hyperbolic tangent equation, the data were transformed in such a way that the heat transfer values are located between zero and one. This is done with a simple first-order transformation. The heat transfer values along the width of the pins are then plotted for different values of each of the non-dimensional geometric parameters, keeping the other parameters constant. Figure 3-63, Figure 3-64 and Figure 3-65 display the transformed non-dimensional face heat transfer values as functions of L_{fin}/L_{gap} , L_{gap}/W_{gap} and W_{fin}/W_{gap} respectively.

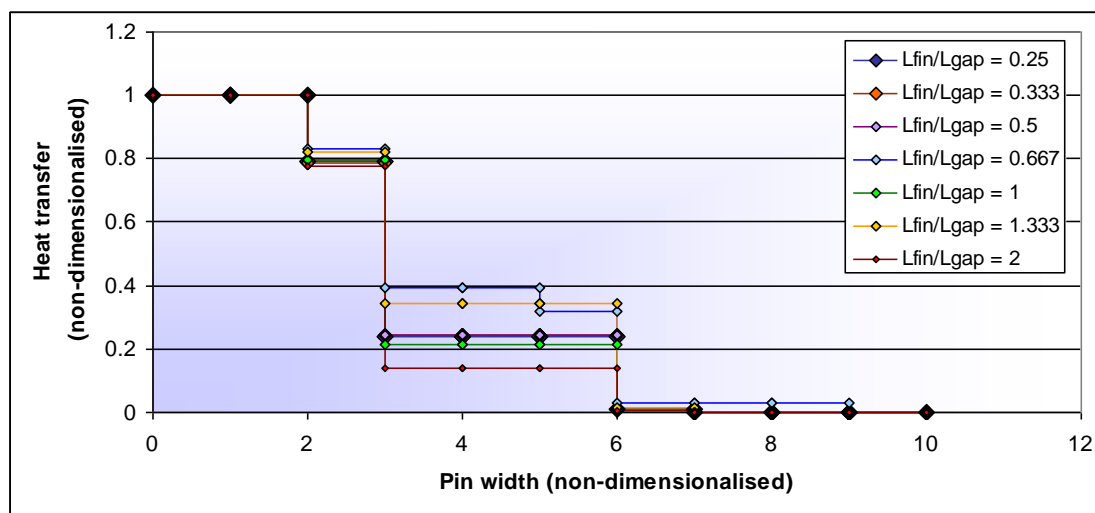


Figure 3-63: The effect of L_{fin}/L_{gap} on the pin heat transfer coefficient

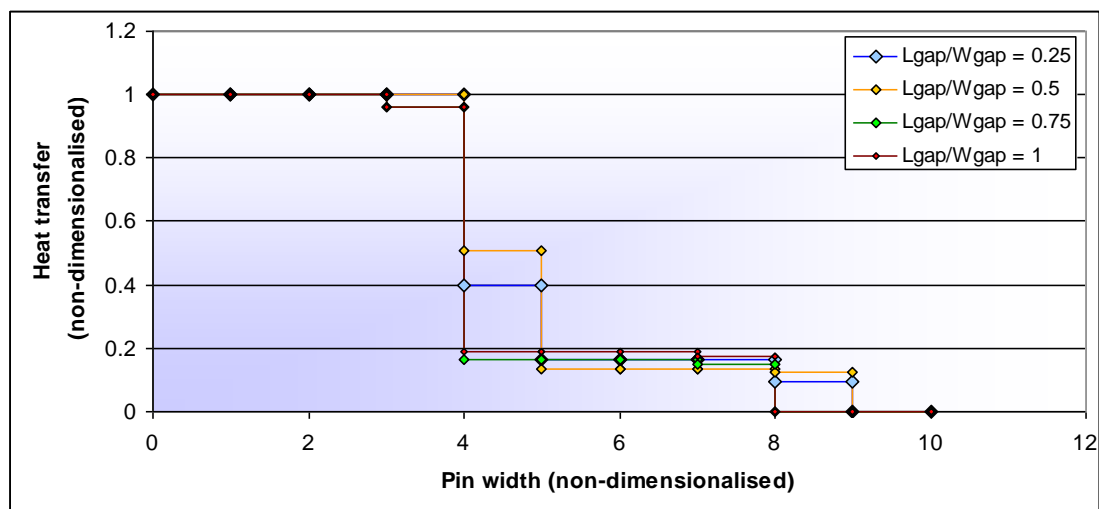


Figure 3-64: The effect of L_{gap}/W_{gap} on the pin heat transfer coefficient

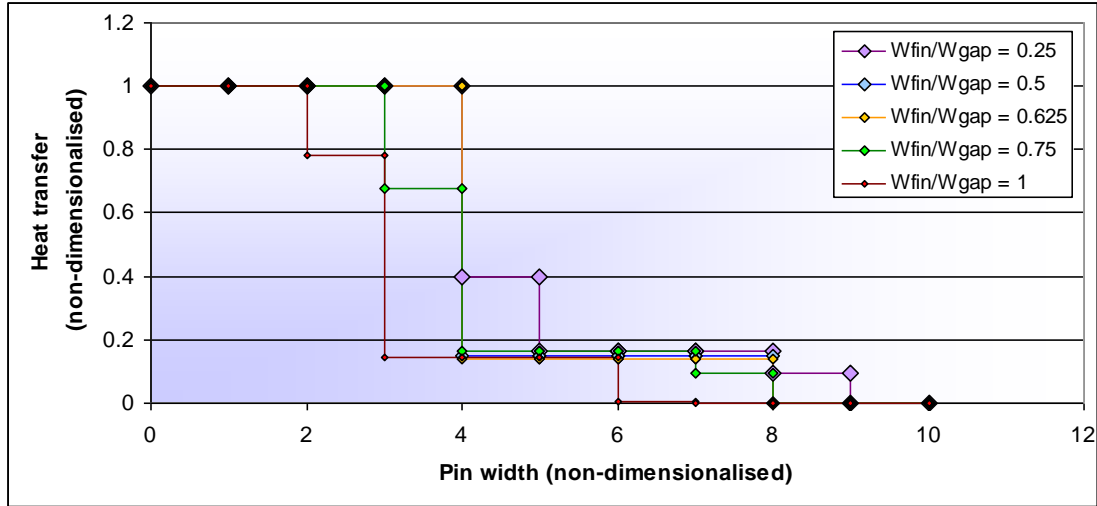
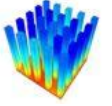


Figure 3-65: The effect of W_{fin}/W_{gap} on the pin heat transfer coefficient

The coarse discretisation makes it difficult to determine the influences of the different parameters. Figure 3-65 indicates that the W_{fin}/W_{gap} parameter influences the horizontal offset of the gradient. Other effects are not so clearly visible. After several attempts in applying functions to b and c , it was decided to use a combination of first-order and power law functions to represent the gradient movement. The following two equations are set up for b and c respectively.

$$b = \left(Z_8 \left(\frac{W_{fin}}{W_{gap}} \right)^{Z_9} + Z_{10} \right) \cdot \left(\frac{L_{gap}}{W_{gap}} \right)^{Z_{11}} + \left(Z_{12} \left(\frac{W_{fin}}{W_{gap}} \right)^{Z_{13}} + Z_{14} \right) \quad (59)$$

$$c = \left(Z_{15} \left(\frac{W_{fin}}{W_{gap}} \right)^{Z_{16}} + Z_{17} \right) \cdot \left(\frac{L_{gap}}{W_{gap}} \right)^{Z_{18}} + \left(Z_{19} \left(\frac{W_{fin}}{W_{gap}} \right)^{Z_{20}} + Z_{21} \right) \quad (60)$$



The final equation for the function across the pin width is shown as Equation 61.

$$\begin{aligned}
 nNu_{eq} &= \left(-\frac{1}{2}(1-a) \right) \tanh \left(b \cdot \left(\frac{200}{W_{fin}} x \right) + c \right) + \frac{1}{2}(1+a) \\
 a &= \left(Z_1 \cdot e^{Z_2 \left(\frac{W_{fin}}{W_{gap}} \right)} \cdot \left(\frac{L_{gap}}{W_{gap}} \right)^{Z_3 \left(\frac{W_{fin}}{W_{gap}} \right) + Z_4} \right) \cdot e^{Z_5 \left(\frac{L_{fin}}{L_{gap}} \right)} \cdot \left(\frac{L_{gap}}{W_{gap}} \right)^{Z_6 \ln \left(\frac{L_{fin}}{L_{gap}} \right) - Z_7} \\
 b &= \left(Z_8 \left(\frac{W_{fin}}{W_{gap}} \right)^{Z_9} + Z_{10} \right) \cdot \left(\frac{L_{gap}}{W_{gap}} \right)^{Z_{11}} + \left(Z_{12} \left(\frac{W_{fin}}{W_{gap}} \right)^{Z_{13}} + Z_{14} \right) \\
 c &= \left(Z_{15} \left(\frac{W_{fin}}{W_{gap}} \right)^{Z_{16}} + Z_{17} \right) \cdot \left(\frac{L_{gap}}{W_{gap}} \right)^{Z_{18}} + \left(Z_{19} \left(\frac{W_{fin}}{W_{gap}} \right)^{Z_{20}} + Z_{21} \right)
 \end{aligned} \tag{61}$$

The LFOPC optimisation procedure is also applied to this equation, but with a different objective function. In this case, the differences between the integrals of the equations and the CFD values are used. This results in a minimum error in the sum of the heat transfer coefficients across the faces. To simplify the process, the integrals were replaced by Riemann summations [61]. The objective function is shown in Equation 62.

$$F(Z_i) = \sum_j \left(nNu_{CFD,j} - \left(\int_j nNu_{eq} dx_j \right) \right)^2 \tag{62}$$

The derivatives of this function were once again approximated with first-order gradients. **Table 3-5** displays the constants of Equation 61 after optimisation of the coefficients.

**Table 3-5: Optimised constants for the laminar fraction equation**

Constant	Value	Constant	Value
Z_1	0.793791	Z_{12}	0.0864
Z_2	-1.4159	Z_{13}	-5.69E-04
Z_3	0.7224	Z_{14}	-0.0197
Z_4	-0.9266	Z_{15}	-0.2969
Z_5	0.1862	Z_{16}	1.7223
Z_6	0.3254	Z_{17}	0.7082
Z_7	-1.1724	Z_{18}	0.138
Z_8	-0.6893	Z_{19}	1.6921
Z_9	0.011	Z_{20}	0.8807
Z_{10}	0.673	Z_{21}	-3.9722
Z_{11}	0.2733		

Figure 3-66 displays the percentage differences between this equation and the original functions calculated from the CFD data. The percentage differences for the initial and the final constant values are shown. After optimisation, 98.7% of the configurations fall within a 20% error, and 85.9% fall within a 10% error. A comparison between the final integrals of the laminar pin width correlation and the CFD values is displayed in Figure 3-67. Figure 3-68 displays the equation Nusselt numbers as a function of the CFD Nusselt numbers.

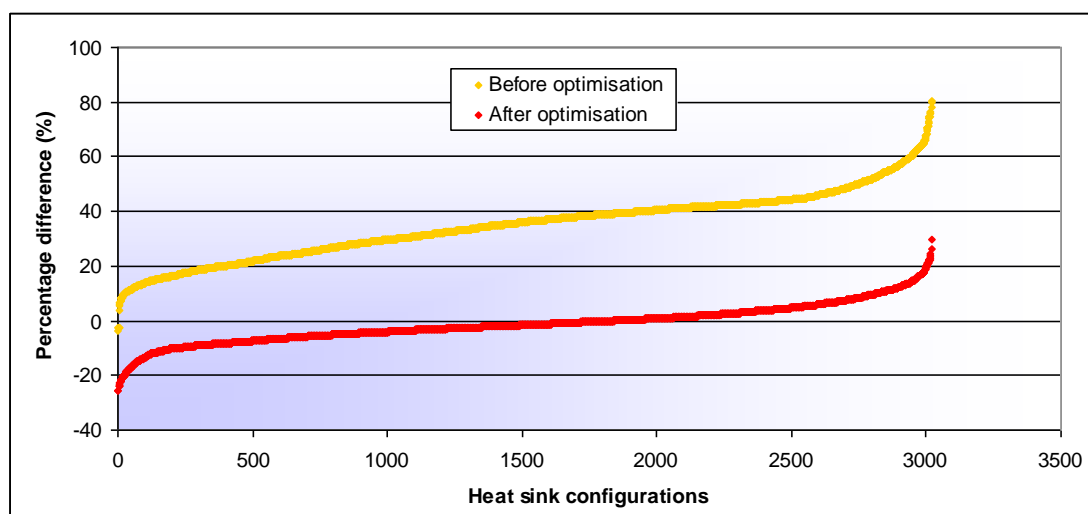


Figure 3-66: Percentage differences between CFD and integrated laminar pin width correlation Nusselt numbers

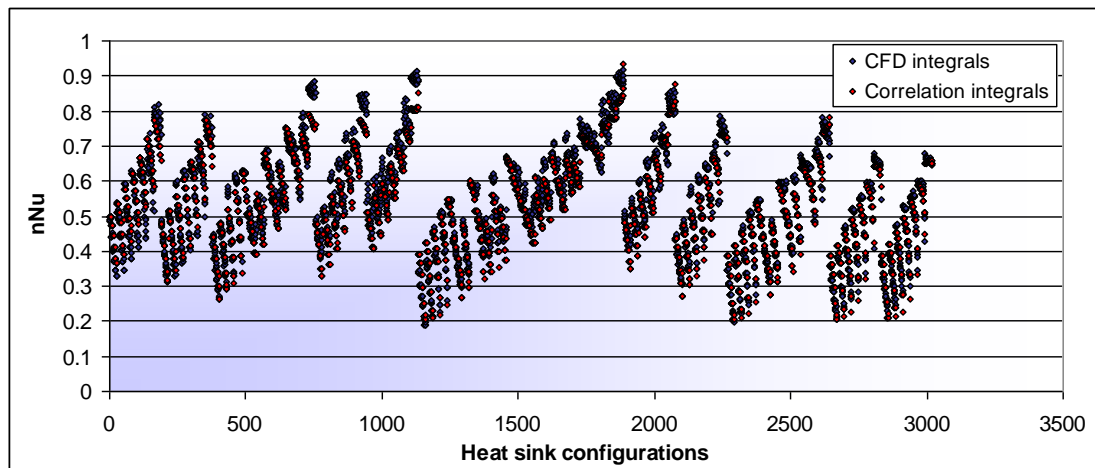


Figure 3-67: Comparison between integrated pin width correlation and the integrated CFD normalised Nusselt numbers

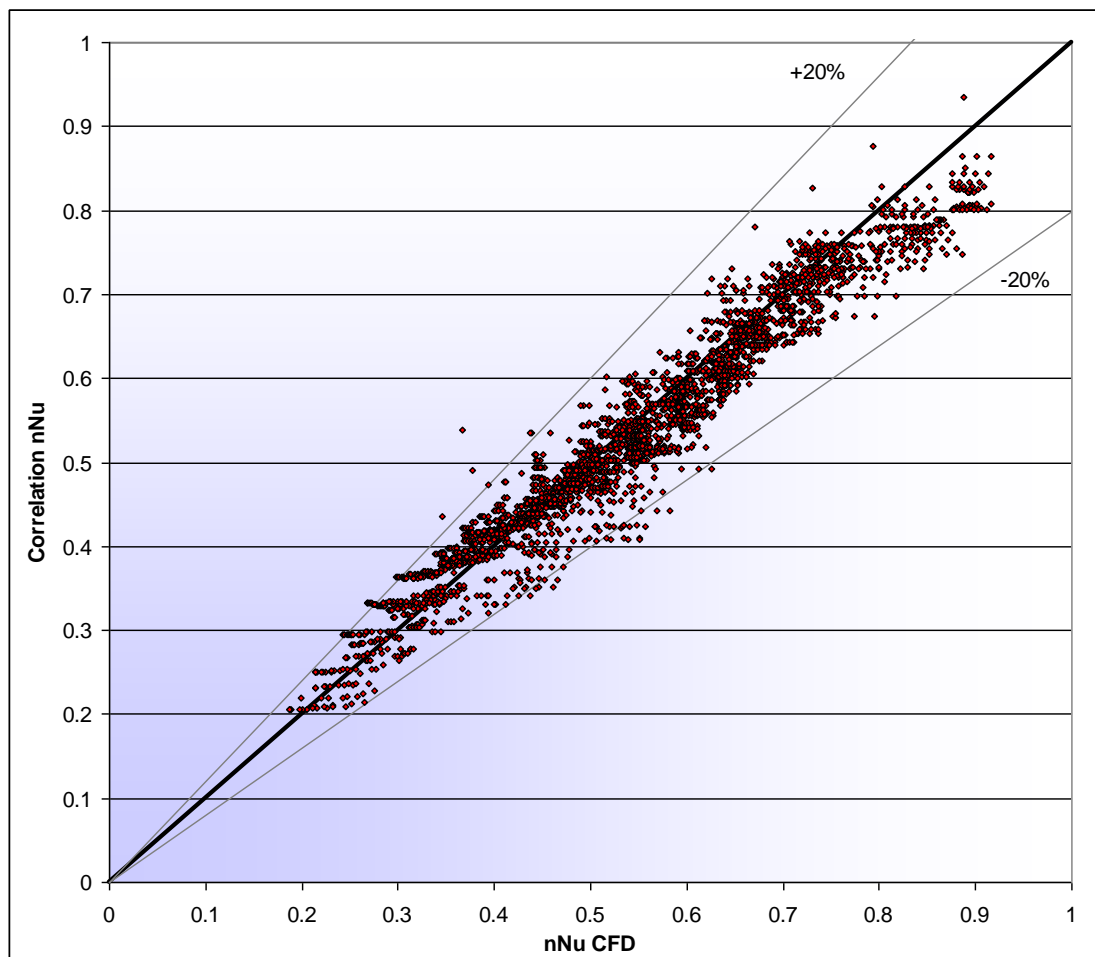
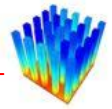


Figure 3-68: Correlation Nusselt numbers as a function of CFD Nusselt number



3.6 TURBULENT FLOW

The construction of the turbulent correlation follows the same method as the laminar correlation. The data used to correlate the turbulent equation range between Reynolds numbers of 1 500 and 7 000. The heat sink set for the turbulent data is somewhat smaller than the laminar heat sink set, as shown in Table 3-2 in Section 3.3. The heat transfer coefficients and the geometric parameters are non-dimensionalised in the same way as for the laminar equation.

Figure 3-69 to Figure 3-72 display the influence of the different non-dimensionalised geometric parameters on the pin edge Nusselt numbers. These figures are created by keeping the Reynolds number and two geometric parameters constant while the Nusselt number is plotted against the selected geometric parameter. Figure 3-73 shows the Nusselt number plotted against the Reynolds number for a constant set of geometric parameters. This figure indicates that the Nusselt number can be fitted to the Reynolds number via a logarithmic curve. The same characteristic is found in the laminar data.

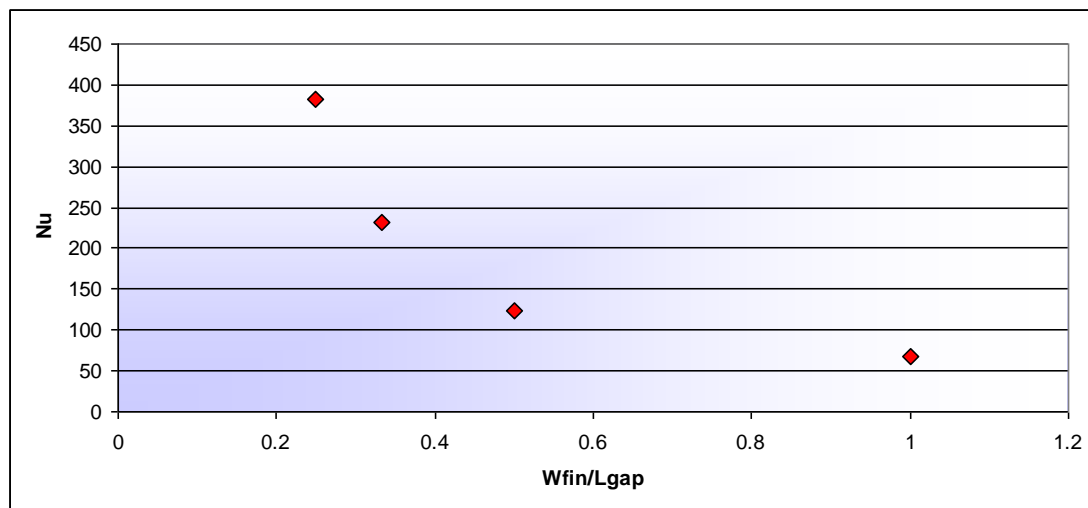


Figure 3-69: The influence of W_{fin}/L_{gap} on the Nusselt number

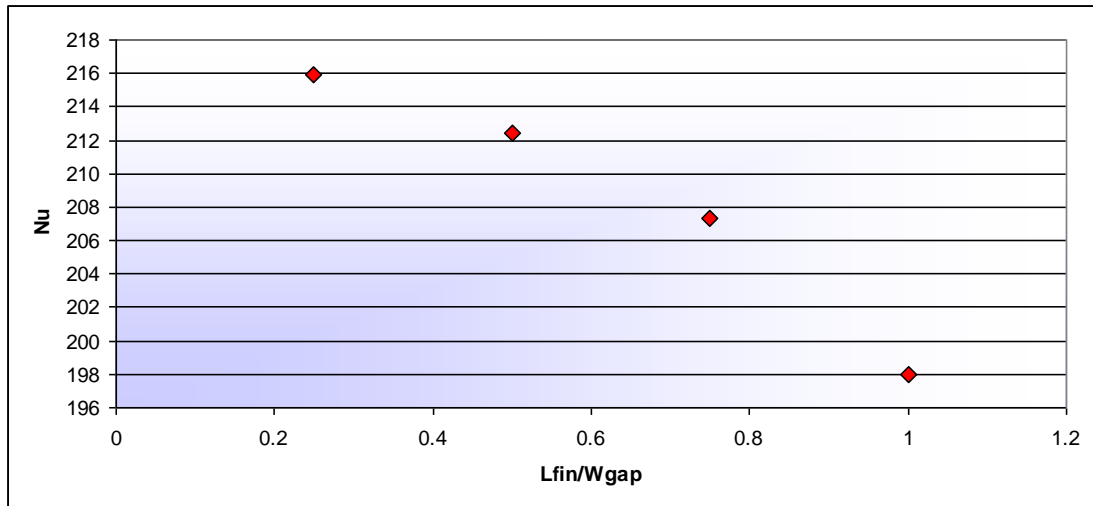


Figure 3-70: The influence of L_{fin}/W_{gap} on the Nusselt number

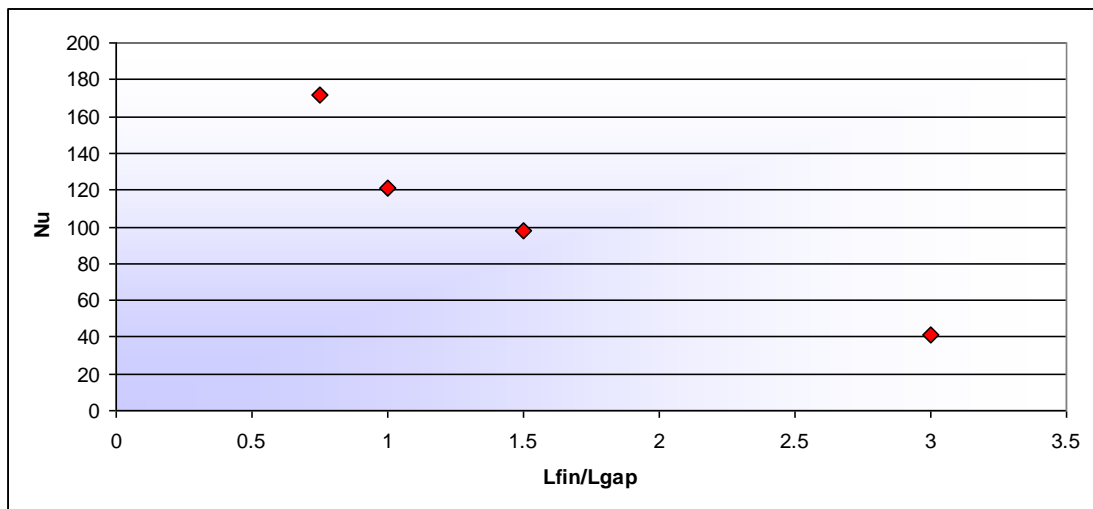


Figure 3-71: The influence of L_{fin}/L_{gap} on the Nusselt number

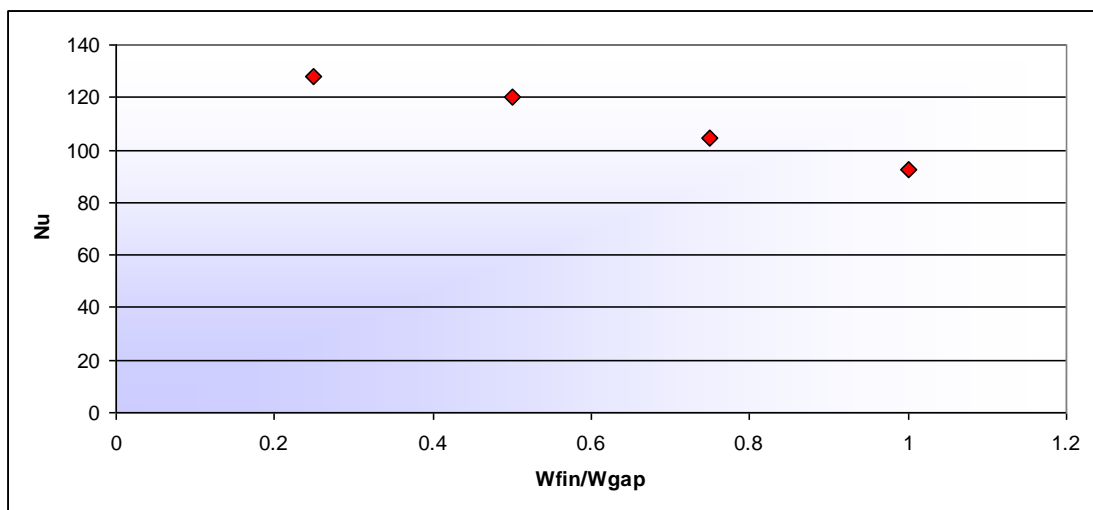


Figure 3-72: The influence of W_{fin}/W_{gap} on the Nusselt number

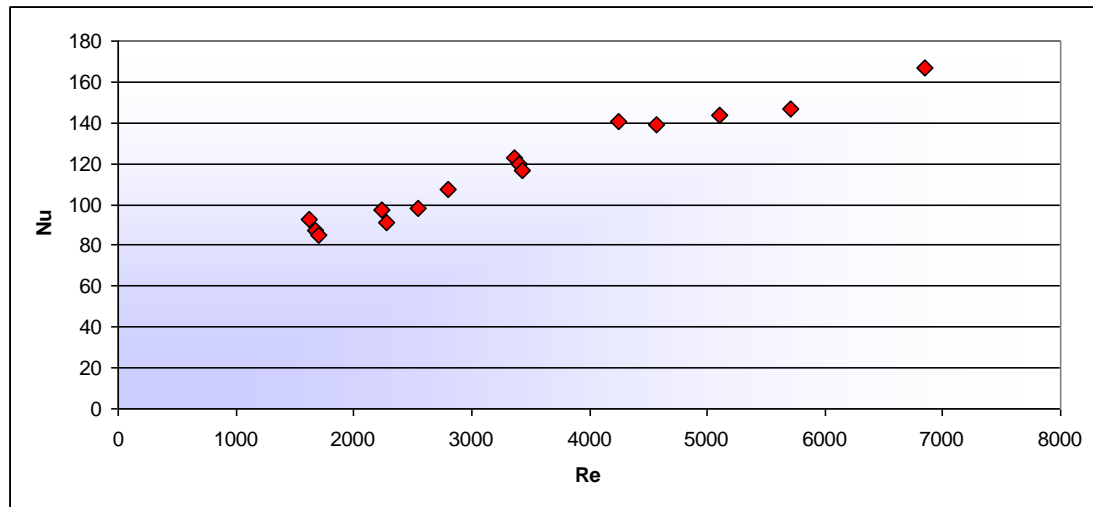


Figure 3-73: The influence of the Reynolds number on the Nusselt number

Figure 3-74 to Figure 3-77 display the Nusselt number as a function of the Reynolds number for different values of the geometric parameters. The functions shown in Figure 3-74 and Figure 3-75 overlap, which makes creating an equation difficult. Figure 3-76 and Figure 3-77 do not exhibit these overlaps; therefore it was decided to use these two parameters first.

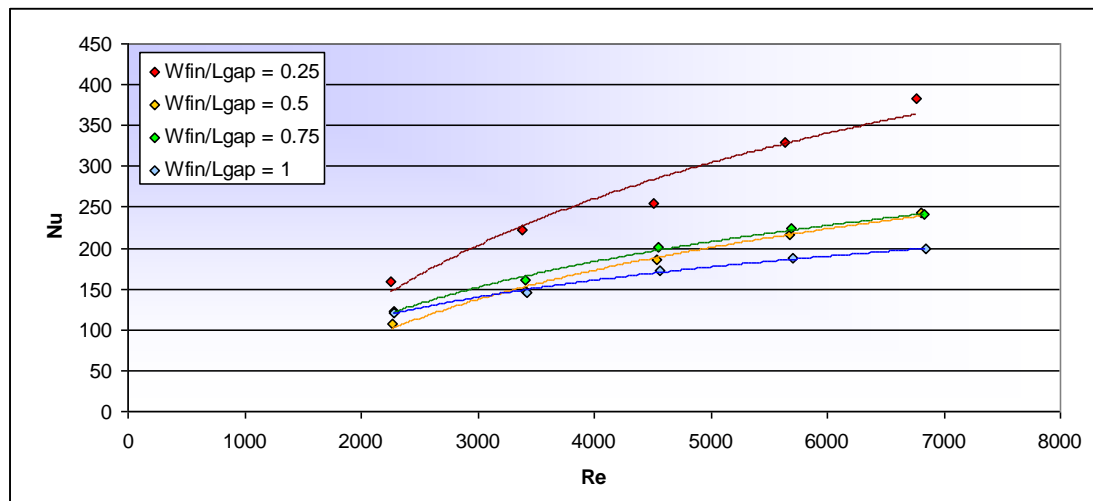


Figure 3-74: Nusselt as a function of Reynolds number for different values of W_{fin}/L_{gap}

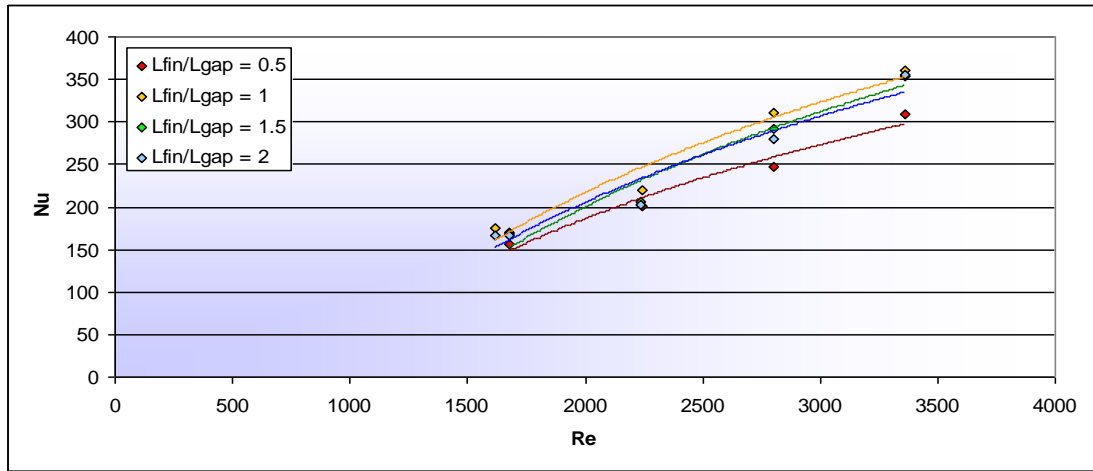


Figure 3-75: Nusselt as a function of Reynolds number for different values of L_{fin}/W_{gap}

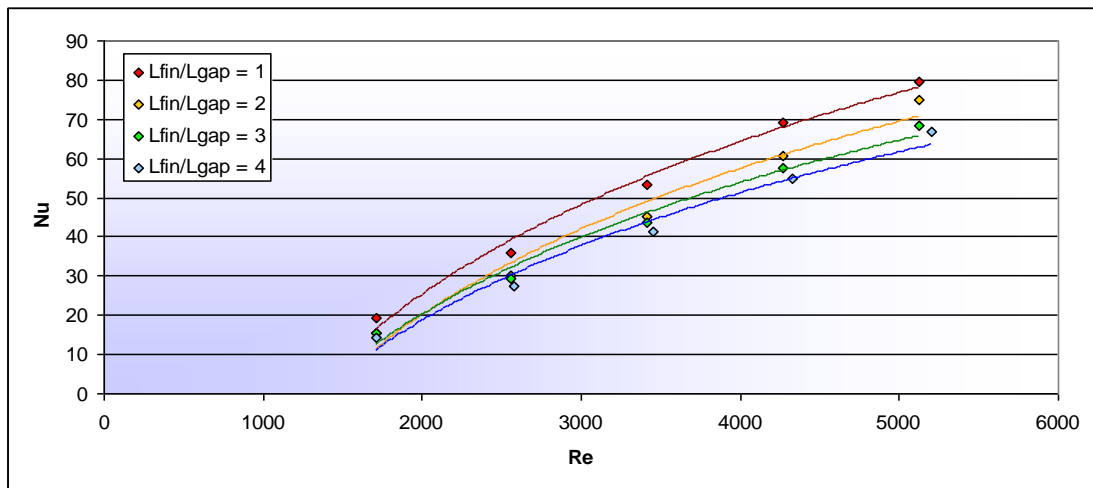


Figure 3-76: Nusselt as a function of Reynolds number for different values of L_{fin}/L_{gap}

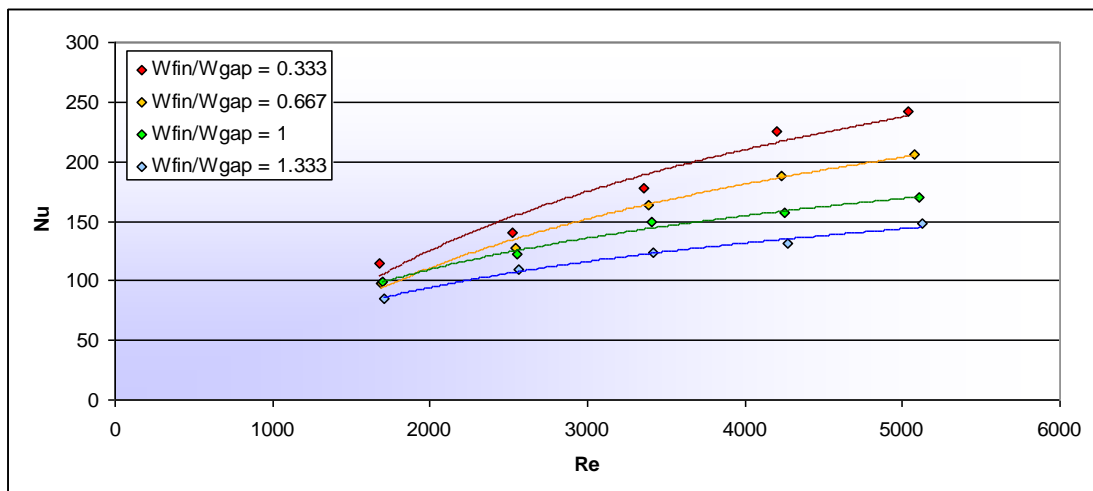


Figure 3-77: Nusselt as a function of Reynolds number for different values of W_{fin}/W_{gap}



Starting with the W_{fin}/W_{gap} parameter and the Reynolds number, a logarithmic equation is set up.

$$Nu = a \cdot \ln(Re) - b \quad (63)$$

Figure 3-78 shows functions of Nusselt number as a function of Reynolds number for different values of W_{fin}/W_{gap} . A large number of the data points do not lie on a smooth curve which fit the regression lines. This will cause large differences in the final equation. These differences may be attributed to several effects, such as changes in the flow characteristics at different Reynolds numbers, unconverged solutions, coarse meshes not capturing all the flow characteristics and numerical errors in the simulations.

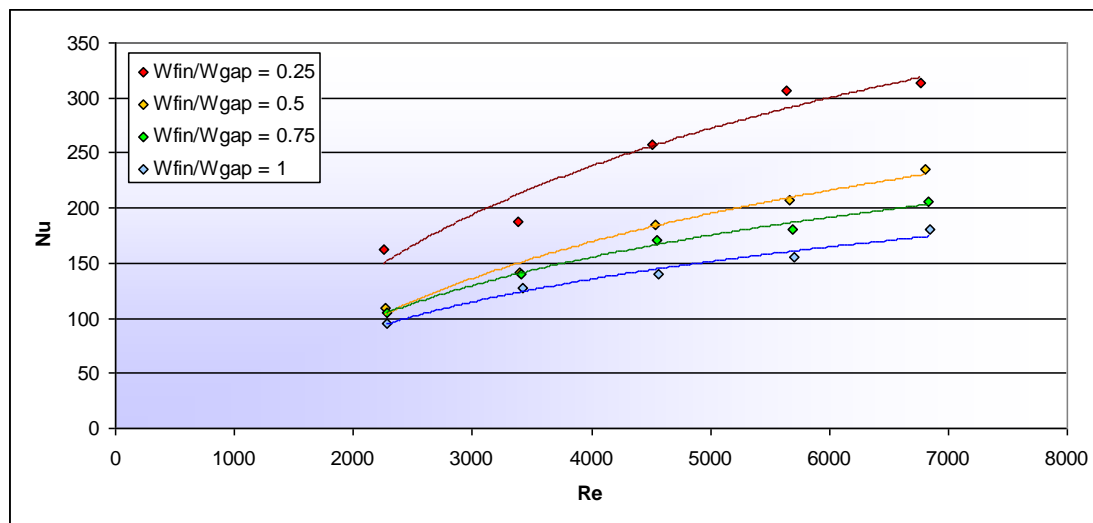


Figure 3-78: The effect of W_{fin}/W_{gap} and the Reynolds number on the Nusselt number

Plotting the coefficients of the regression lines from Figure 3-78 as functions of W_{fin}/W_{gap} , displayed in Figure 3-79, it is found that two new regression lines can be calculated. Coefficient a follows a power law curve and coefficient b follows a logarithmic curve.

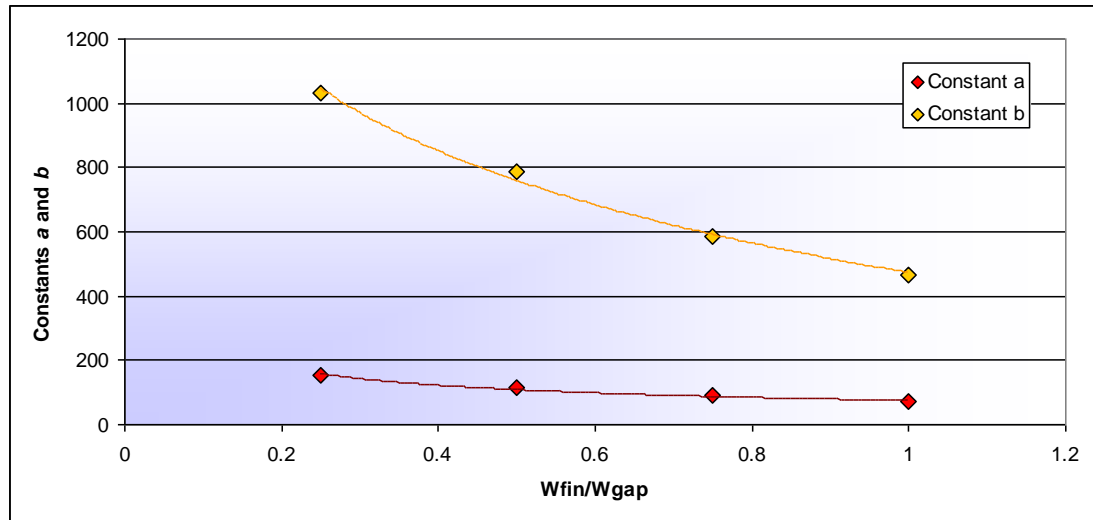


Figure 3-79: Constants a and b as functions of W_{fin}/W_{gap}

The two regression lines are shown below:

$$a = c_1 \left(\frac{W_{fin}}{W_{gap}} \right)^{-c_2} \quad (64)$$

$$b = -c_3 \ln \left(\frac{W_{fin}}{W_{gap}} \right) + c_4 \quad (65)$$

Equation 64 and Equation 65 can be combined with Equation 63 to form a correlation for the Nusselt number as a function of L_{fin}/W_{gap} and the Reynolds number with four constants.

$$Nu = \left[c_1 \left(\frac{W_{fin}}{W_{gap}} \right)^{-c_2} \right] \ln(Re) - \left[-c_3 \ln \left(\frac{W_{fin}}{W_{gap}} \right) + c_4 \right] \quad (66)$$

Now an additional parameter can be introduced. Following the same procedure for different values of L_{fin}/L_{gap} , a set of coefficients for Equation 66 is calculated for every value of L_{fin}/L_{gap} . These coefficients are plotted in Figure 3-80 to Figure 3-83. Coefficients c_1 and c_4 follow power law functions, while coefficient c_2 and c_3 follow logarithmic functions.

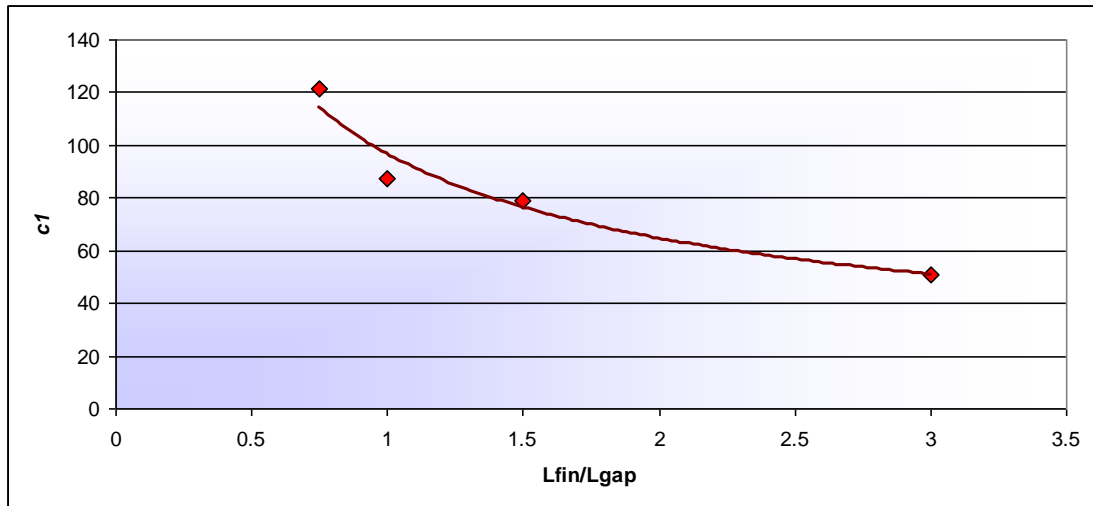


Figure 3-80: Constant c_1 as a function of L_{fin}/L_{gap}

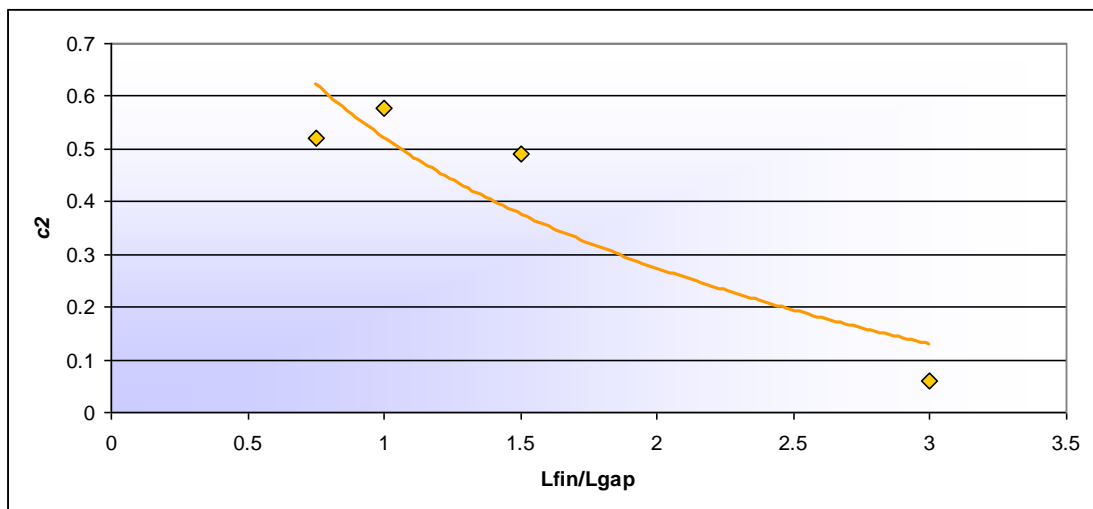


Figure 3-81: Constant c_2 as a function of L_{fin}/L_{gap}

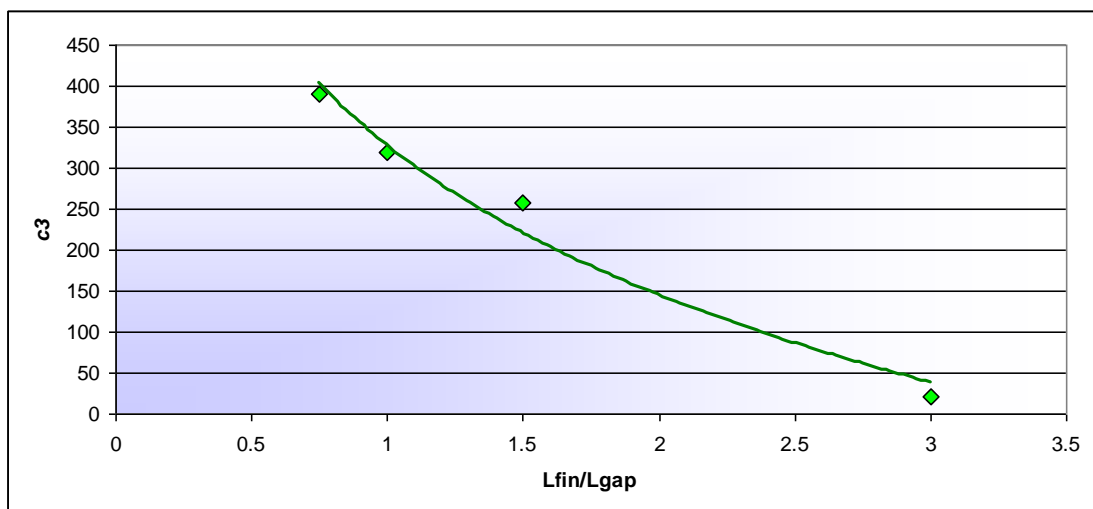


Figure 3-82: Constant c_3 as a function of L_{fin}/L_{gap}

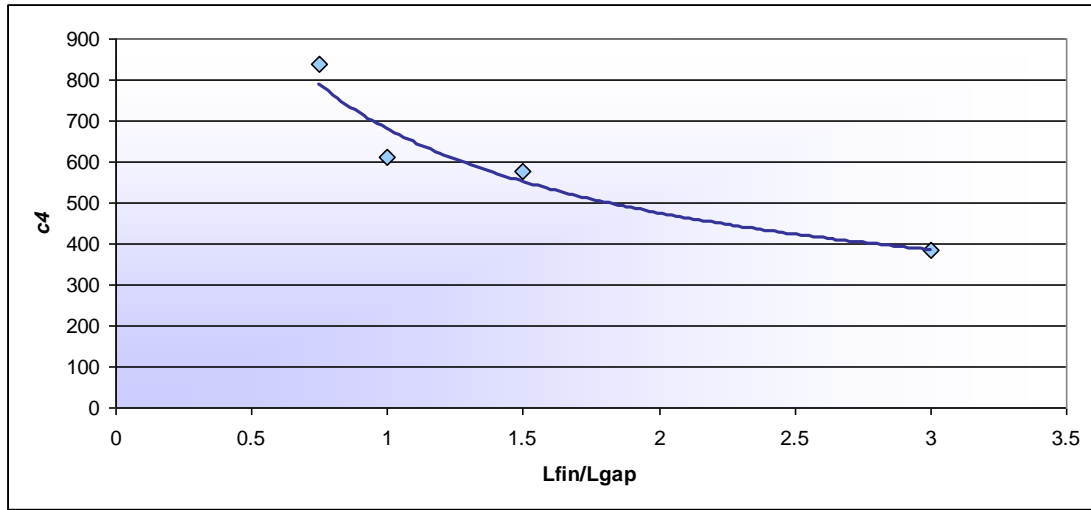


Figure 3-83: Constant c_4 as a function of L_{fin}/L_{gap}

Equation 67 to Equation 70 show the regression lines from the graphs above.

$$c_1 = d_1 \left(\frac{L_{fin}}{L_{gap}} \right)^{-d_2} \quad (67)$$

$$c_2 = -d_3 \ln \left(\frac{L_{fin}}{L_{gap}} \right) + d_4 \quad (68)$$

$$c_3 = -d_5 \ln \left(\frac{L_{fin}}{L_{gap}} \right) + d_6 \quad (69)$$

$$c_4 = d_7 \left(\frac{L_{fin}}{L_{gap}} \right)^{-d_8} \quad (70)$$

These four regression lines can be combined with Equation 66 to form the Nusselt number correlation as a function of Reynolds number, L_{fin}/L_{gap} and W_{fin}/W_{gap} .

$$Nu = \left[d_1 \left(\frac{L_{fin}}{L_{gap}} \right)^{-d_2} \left(\frac{W_{fin}}{W_{gap}} \right)^{-\left(-d_3 \ln \left(\frac{L_{fin}}{L_{gap}} \right) + d_4 \right)} \right] \ln(Re) - \left[-\left(-d_5 \ln \left(\frac{L_{fin}}{L_{gap}} \right) + d_6 \right) \ln \left(\frac{W_{fin}}{W_{gap}} \right) + d_7 \left(\frac{L_{fin}}{L_{gap}} \right)^{-d_8} \right] \quad (71)$$



Extending this methodology, one can generate regression lines for the eight coefficients in Equation 71 as functions of L_{fin}/W_{gap} , which will then include all the data points from the data set. When setting up the laminar correlation, applying this method a third time did not work very well, and a different path was followed. Creating these regression lines for the turbulent data, it is also apparent that the data do not fit the regression lines very well. Several other methods were tried to create an additional sub-equation, which will fit the data for other values of L_{fin}/L_{gap} onto the data where L_{fin}/L_{gap} is equal to one. Therefore, the methodology of subsequent regression lines on the coefficients was used. Regression lines are fitted to the eight coefficients in Equation 71, which give the following functions:

$$X_1 \left(\frac{L_{fin}}{W_{gap}} \right)^{X_2} \quad (72)$$

$$X_3 \left(\frac{L_{fin}}{W_{gap}} \right)^{X_4} \quad (73)$$

$$X_5 \left(\frac{L_{fin}}{W_{gap}} \right) + X_6 \quad (74)$$

$$X_7 \ln \left(\frac{L_{fin}}{W_{gap}} \right) + X_8 \quad (75)$$

$$X_9 \ln \left(\frac{L_{fin}}{W_{gap}} \right) + X_{10} \quad (76)$$

$$X_{11} \left(\frac{L_{fin}}{W_{gap}} \right) + X_{12} \quad (77)$$

$$X_{13} \left(\frac{L_{fin}}{W_{gap}} \right)^{X_{14}} \quad (78)$$

$$X_{15} \left(\frac{L_{fin}}{W_{gap}} \right)^{X_{16}} \quad (79)$$



When introducing the regressions above into Equation 71, the complete correlation for the Nusselt number is as follows:

$$Nu_{e,eq} = \left[\left(X_1 \left(\frac{Lfin}{Wgap} \right)^{X_2} \right) \left(\frac{Lfin}{Lgap} \right)^{-\left(X_3 \left(\frac{Lfin}{Wgap} \right)^{X_4} \right)} \right. \\ \left. \left(\frac{Wfin}{Wgap} \right)^{-\left(-\left(X_5 \left(\frac{Lfin}{Wgap} \right) + X_6 \right) \ln \left(\frac{Lfin}{Lgap} \right) + \left(X_7 \ln \left(\frac{Lfin}{Wgap} \right) + X_8 \right) \right)} \right] \ln(Re) - \\ \left[-\left(-\left(X_9 \ln \left(\frac{Lfin}{Wgap} \right) + X_{10} \right) \ln \left(\frac{Lfin}{Lgap} \right) + \left(X_{11} \left(\frac{Lfin}{Wgap} \right) + X_{12} \right) \right) \ln \left(\frac{Wfin}{Wgap} \right) + \right. \\ \left. \left(X_{13} \left(\frac{Lfin}{Wgap} \right)^{X_{14}} \right) \left(\frac{Lfin}{Lgap} \right)^{-\left(X_{15} \ln \left(\frac{Lfin}{Wgap} \right) + X_{16} \right)} \right] \quad (80)$$

Table 3-6 shows the values for the constants X_1 to X_{16} in Equation 80.

Table 3-6: Constants X_1 to X_{16} for the turbulent edge Nusselt number equation

Constant	Value	Constant	Value
X_1	86.1968	X_9	-9.1688
X_2	0.598	X_{10}	7.8171
X_3	0.7671	X_{11}	-9.5115
X_4	0.043	X_{12}	38.422
X_5	0.00329	X_{13}	564.6
X_6	0.0007392	X_{14}	0.5226
X_7	-0.0235	X_{15}	0.0322
X_8	0.0767	X_{16}	0.6977

The percentage differences between the CFD pin edge Nusselt numbers and the correlated equation with the initial coefficients are very high. This is probably because of the three iterations of regression lines calculations. The percentage difference to the power of four is used as the objective function for the optimisation



procedure. The fourth power is chosen to award a higher weight to data points with larger differences.

After optimisation, the correlation differences improved significantly, with 84.6% of the data lying within a difference of 20%, and 49.2% of the data within a difference of 10%. All the data points lie within a 40% margin. The initial and final differences after optimisation for the complete data set are shown in Figure 3-84. Figure 3-85 displays the initial and optimised edge Nusselt numbers as a function of the CFD edge Nusselt numbers. The optimised values cluster around the optimal line while a lot of the initial points lie far away. Figure 3-86 displays the calculated Nusselt numbers from the correlation on top of the CFD values for the entire data set. These figures suggest that the correlation does not capture the higher Nusselt numbers accurately. This is because there are very few large Nusselt numbers in the data set and therefore the higher Nusselt number range does not feature prominently in the optimisation algorithm.

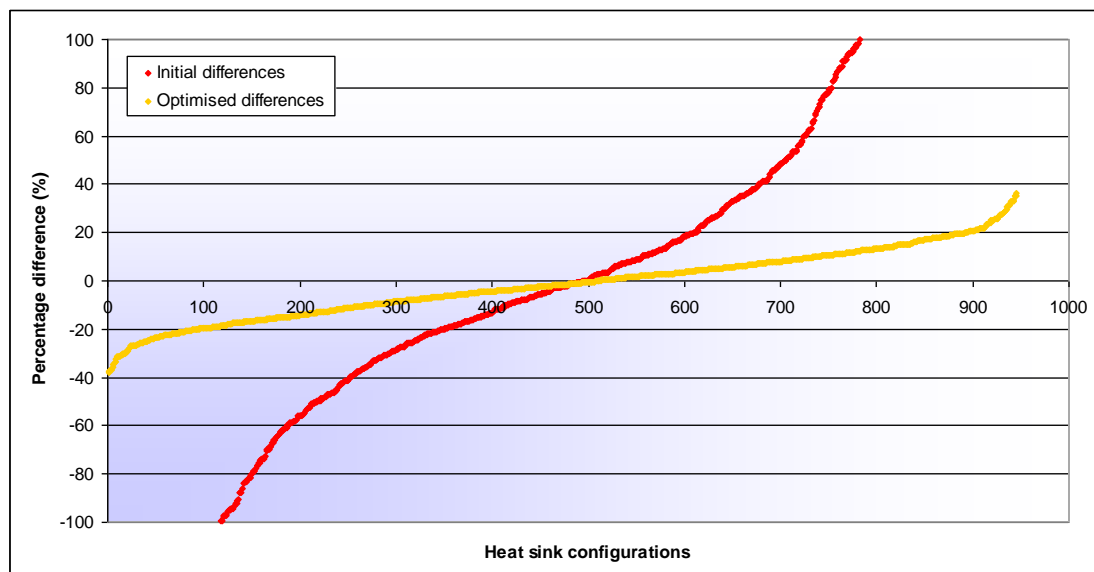


Figure 3-84: Percentage difference before and after optimisation

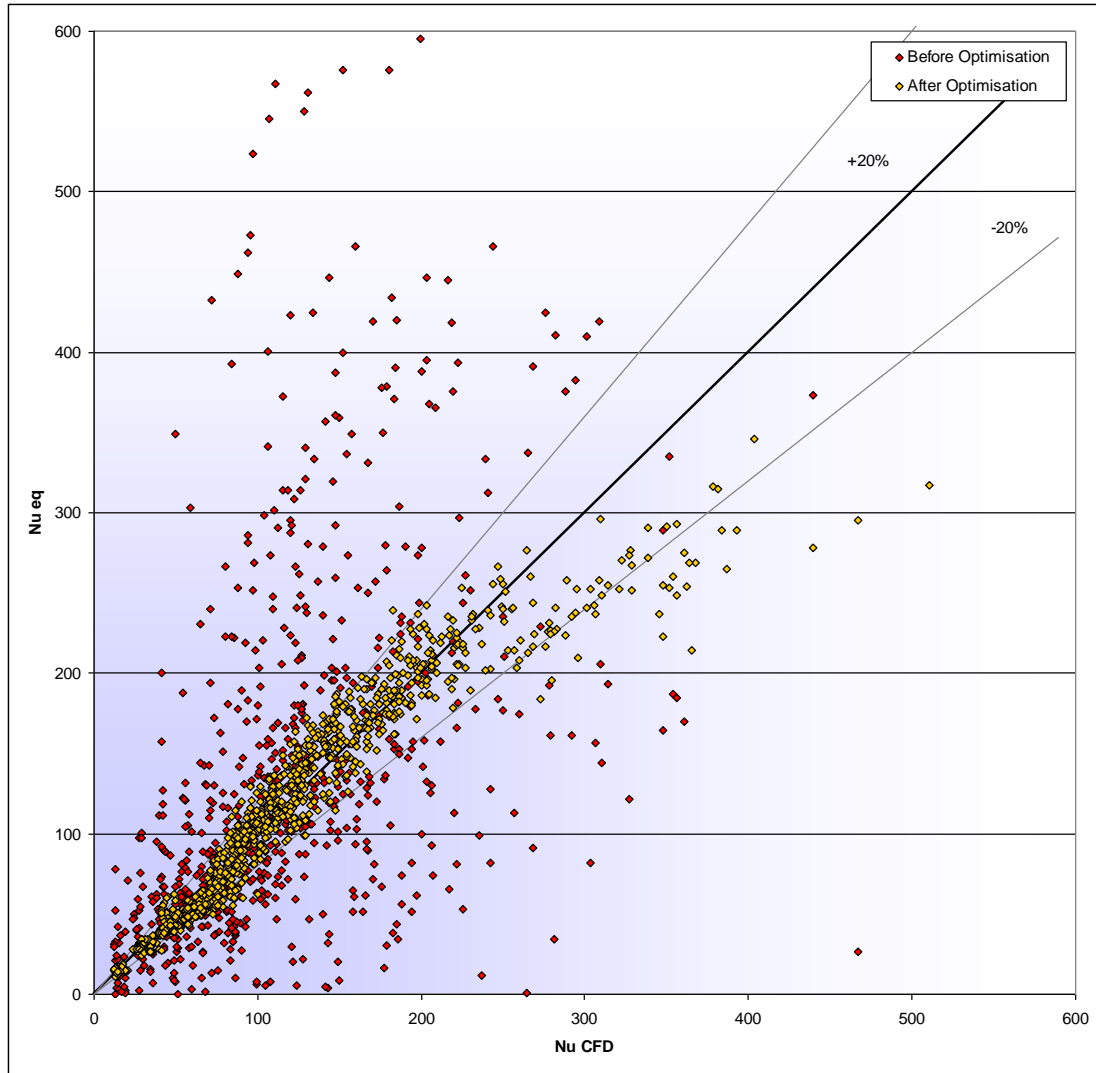
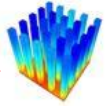


Figure 3-85: Equation Nusselt numbers relative to CFD Nusselt numbers

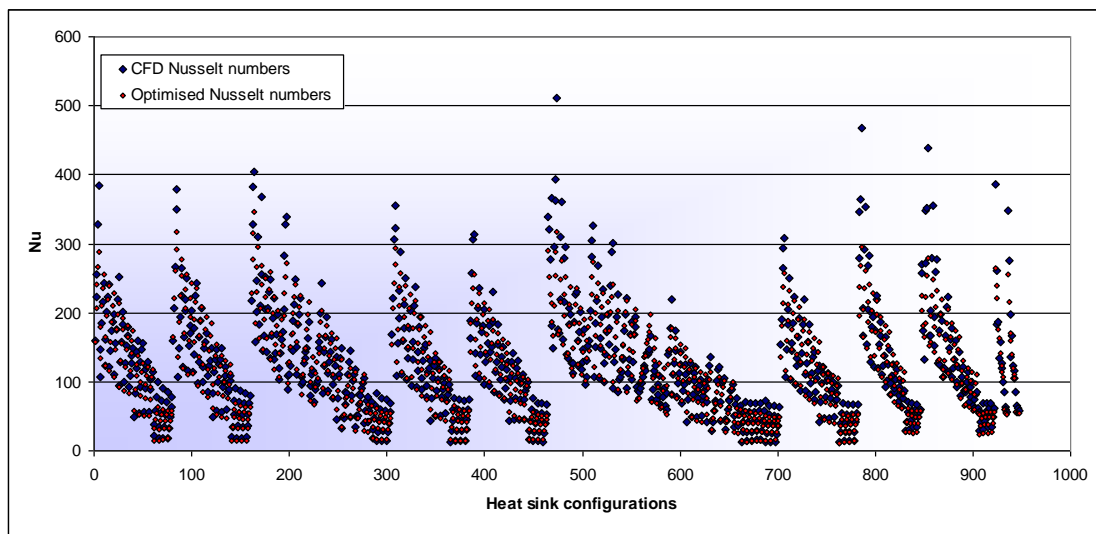
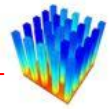


Figure 3-86: Comparison between CFD Nusselt numbers and the optimised equation



3.7 TURBULENT FACE EQUATION

Once again a hyperbolic tangent equation is fitted to the turbulent face data. The pin heat transfer data looks similar to those shown in the laminar face section. The data are normalised by the pin edge Nusselt number, which is correlated in Section 3.6. The pin widths are also non-dimensionalised to values between zero and 10, where zero is the edge of a pin and 10 the centre of a pin. This gives dimensionless functions between zero and ten on the x -axis as well as between zero and one on the y -axis, which is called the turbulent heat transfer fraction equations or normalised Nusselt number (nNu).

The normalised turbulent hyperbolic tangent Nusselt number equation is chosen to be the same as for the laminar case, but the sub-correlation for the coefficients will differ. The correlation is

$$nNu_{eq} = \left(-\frac{1}{2}(1-a) \right) \tanh(b \cdot x + c) + \frac{1}{2}(1+a) \quad (81)$$

where

- a : The vertical offset on the right-hand side, representing the heat transfer at the centre of the pin
- b : The slope of the hyperbolic function
- c : The horizontal offset of the centre of the slope
- x : A distance along the pin width

The first step is to correlate the normalised Nusselt values for the pin centres (a). Once again it is found that the Reynolds number does not influence the normalised Nusselt numbers significantly. It is also found that the L_{fin}/L_{gap} parameter does not influence the data too much, as shown in Figure 3-87. Therefore, it was decided to average the data sets of constant L_{gap}/W_{gap} and constant W_{fin}/W_{gap} .

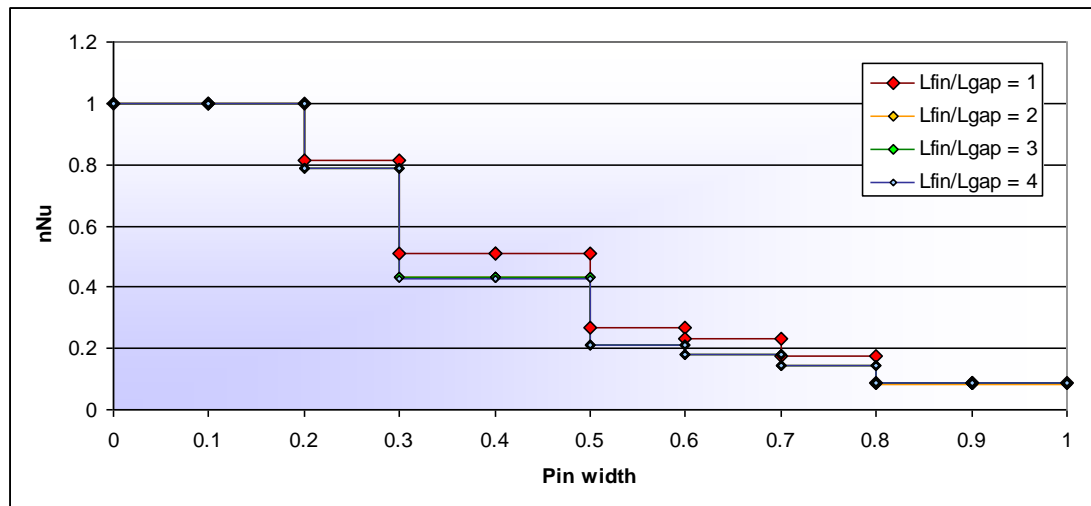
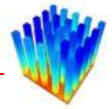


Figure 3-87: Normalised Nusselt numbers as a function of L_{fin}/L_{gap}

Figure 3-88 displays the normalised Nusselt numbers along the pin width for different values of L_{gap}/W_{gap} with a constant W_{fin}/W_{gap} value and averaged L_{fin}/L_{gap} values. This figure shows that the curves do not get progressively larger or smaller with an increase of L_{gap}/W_{gap} and overlap in certain instances. This causes trouble when trying to generate a correlation for the data.

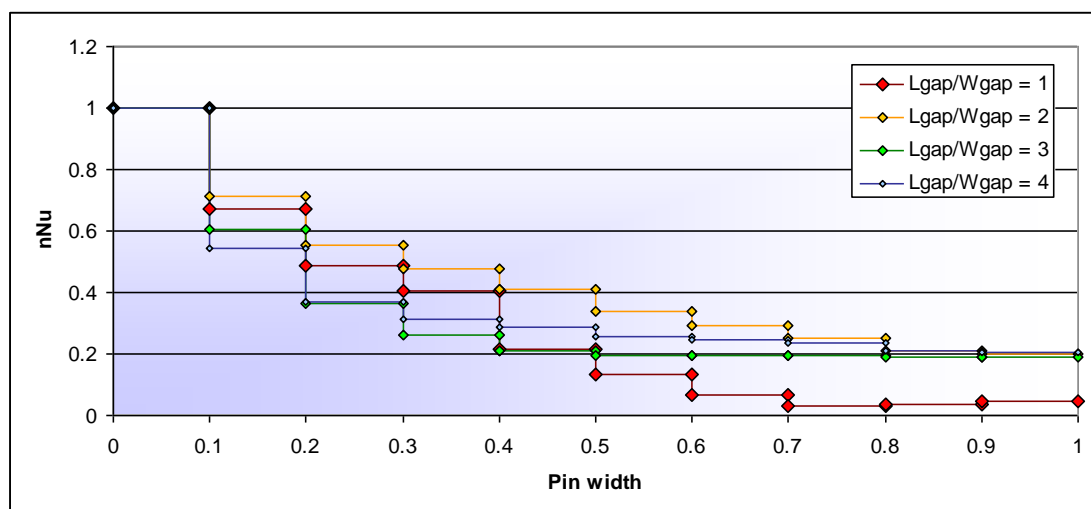


Figure 3-88: Normalised Nusselt numbers as a function of L_{gap}/W_{gap}

Figure 3-89 displays the normalised pin centre Nusselt numbers for a constant value of W_{fin}/W_{gap} . The data do not follow a simple trend line. When comparing all the graphs for the different constant values of W_{fin}/W_{gap} , it was decided to start off with a linear regression and see how this fits the complete data set.

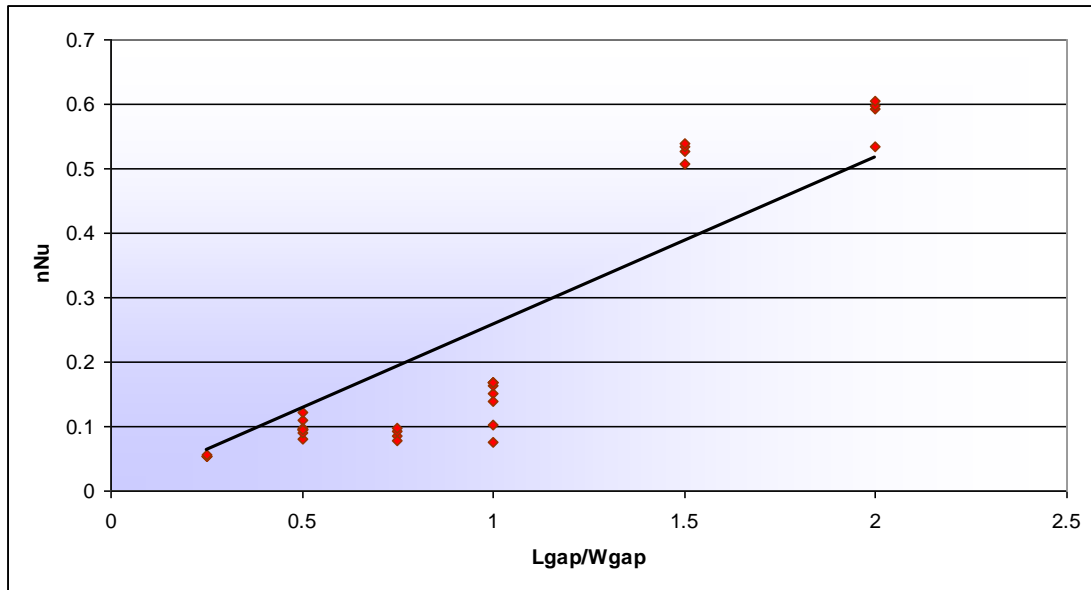


Figure 3-89: Pin centre normalised Nusselt numbers as a function of L_{gap}/W_{gap}

The correlation in Figure 3-89 above is of the form:

$$a = m \left(\frac{L_{gap}}{W_{gap}} \right) \quad (82)$$

The gradients m can be plotted as a function of constant values of W_{fin}/W_{gap} , as shown in Figure 3-90. Initially, it was thought that a power law or exponential curve will fit the data, but neither fitted the data well. Therefore, an arctangent curve is fitted to the data.

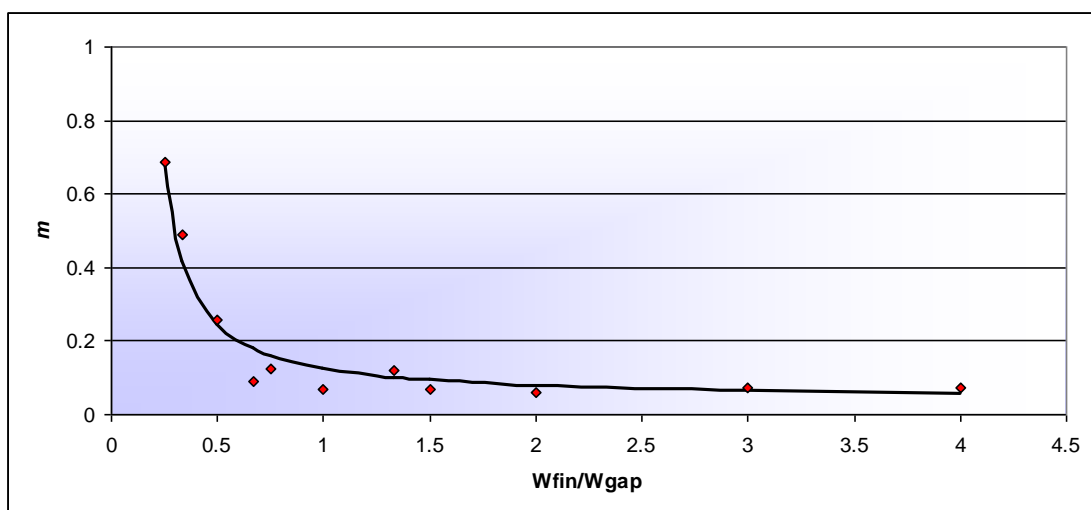


Figure 3-90: Coefficient m as a function of W_{fin}/W_{gap}



The equation for the correlation is shown below (Equation 83). Since this function could not be fitted with standard regression line theory, the zero-order optimisation algorithm, discussed in Section 2.6.4, is applied together with visual inspection to calculate the coefficients. The simple algorithm was used since it is quick to set up and high accuracy is not needed. The complete equation for the centre normalised Nusselt numbers is shown in Equation 84. A comparison between the CFD pin centre normalised Nusselt numbers and the correlation is shown in Figure 3-91.

$$m = 23.6 - 15 \tan^{-1} \left(200 \left(\frac{W_{fin}}{W_{gap}} \right) - 27 \right) \quad (83)$$

$$a = \left(23.6 - 15 \tan^{-1} \left(200 \left(\frac{W_{fin}}{W_{gap}} \right) - 27 \right) \right) \left(\frac{L_{gap}}{W_{gap}} \right) \quad (84)$$

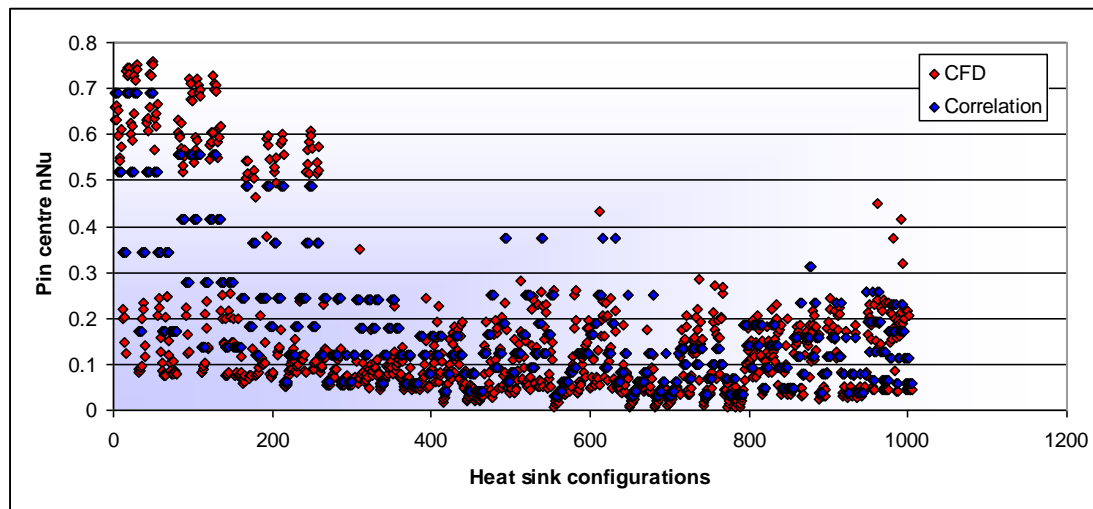
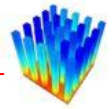


Figure 3-91: Pin centre normalised Nusselt numbers

The next step is to correlate functions for b and c in Equation 81. Since a is already correlated, the part that is left simplifies to

$$nNu_p = -0.5 \tanh(b \cdot x + c) + 0.5 \quad (85)$$



Keeping W_{fin}/W_{gap} constant and using the averaged L_{fin}/L_{gap} data, the pin data can be plotted for different values of L_{gap}/W_{gap} , as shown in Figure 3-92.

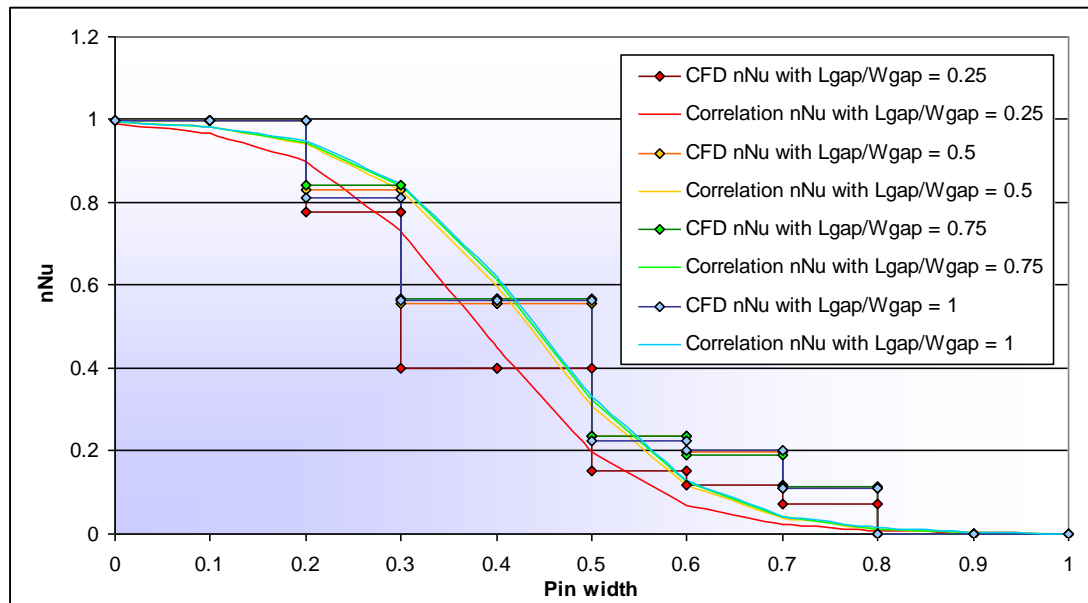


Figure 3-92: Pin width normalised Nusselt numbers as a function of L_{gap}/W_{gap}

By manually editing the coefficients in Equation 85 above, it is found that acceptable correlations can be found by keeping coefficient b (the hyperbolic tangent gradient) constant varying coefficient c as a function of L_{gap}/W_{gap} . These correlations are also shown in Figure 3-92.

The guessed coefficients plotted against L_{gap}/W_{gap} are displayed in Figure 3-93. This can be done for all values of W_{fin}/W_{gap} . Examining the coefficients, it is found that the maximum is always at an L_{gap}/W_{gap} value of one for each value of W_{fin}/W_{gap} . With this fact in mind, it was decided to take the logarithm of L_{gap}/W_{gap} so that the maximum will always lie at $x = 0$. This new graph is shown in Figure 3-94.

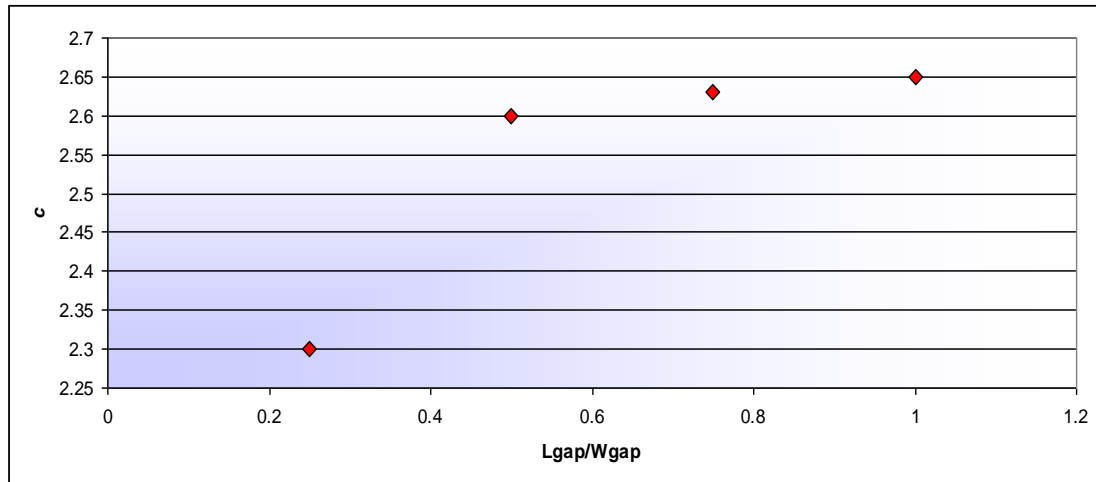


Figure 3-93: Hyperbolic tangent gradient offset as a function of $Lgap/Wgap$

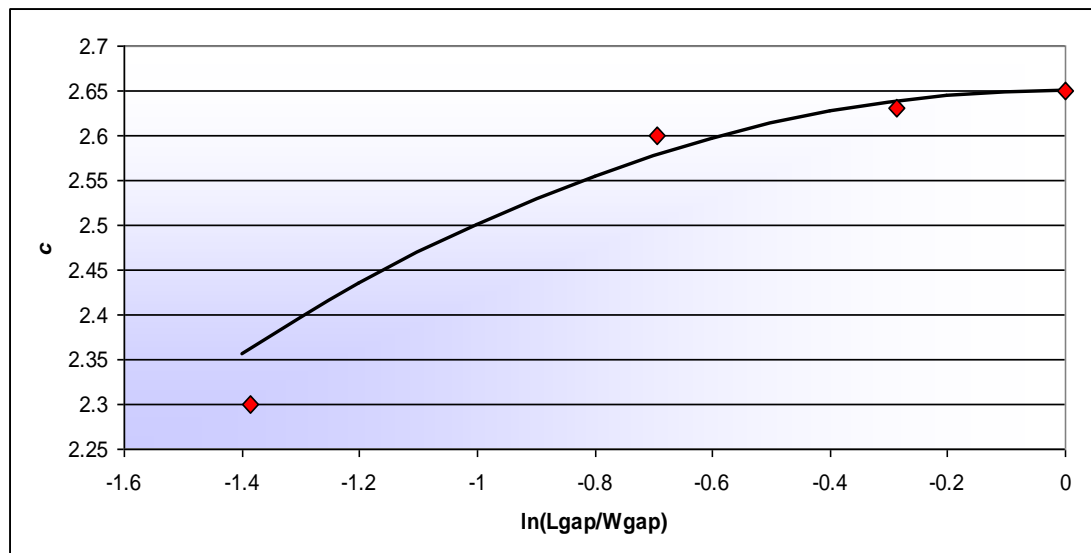


Figure 3-94: Hyperbolic tangent gradient offset (c) as a function of $\ln(Lgap/Wgap)$

It is found that a second-order regression line can be calculated for this data.

$$c = d_1 \left(\ln \left(\frac{Lgap}{Wgap} \right) \right)^2 + d_2 \left(\ln \left(\frac{Lgap}{Wgap} \right) \right) + d_3 \quad (86)$$

Since the maximum is at $\ln \left(\frac{Lgap}{Wgap} \right) = 0$, d_2 is equal to zero. Therefore, the correlation

simplifies to

$$c = d_1 \left(\ln \left(\frac{Lgap}{Wgap} \right) \right)^2 + d_3 \quad (87)$$



Figure 3-95 displays the coefficient d_1 for different values of W_{fin}/W_{gap} together with a third order polynomial regression line. Coefficient d_3 is shown in Figure 3-96. The maximum value of d_3 is also where W_{fin}/W_{gap} is equal to one, and therefore logarithm of W_{fin}/W_{gap} will be used for the correlation. d_3 as a function of the logarithm of W_{fin}/W_{gap} and a second-order regression line is displayed in Figure 3-97.

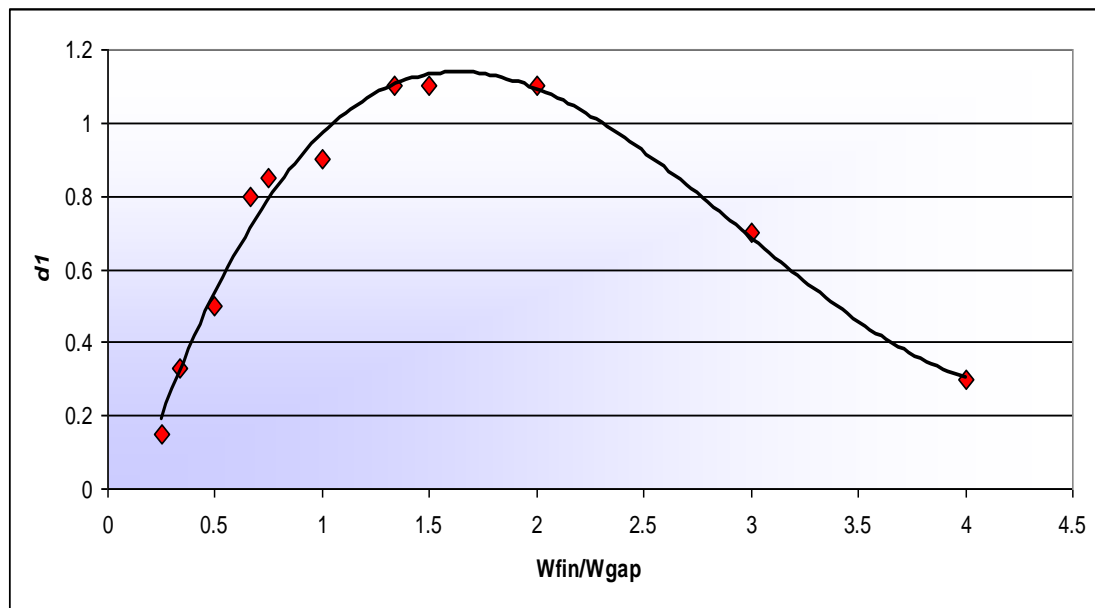


Figure 3-95: Coefficient d_1 as a function of W_{fin}/W_{gap}

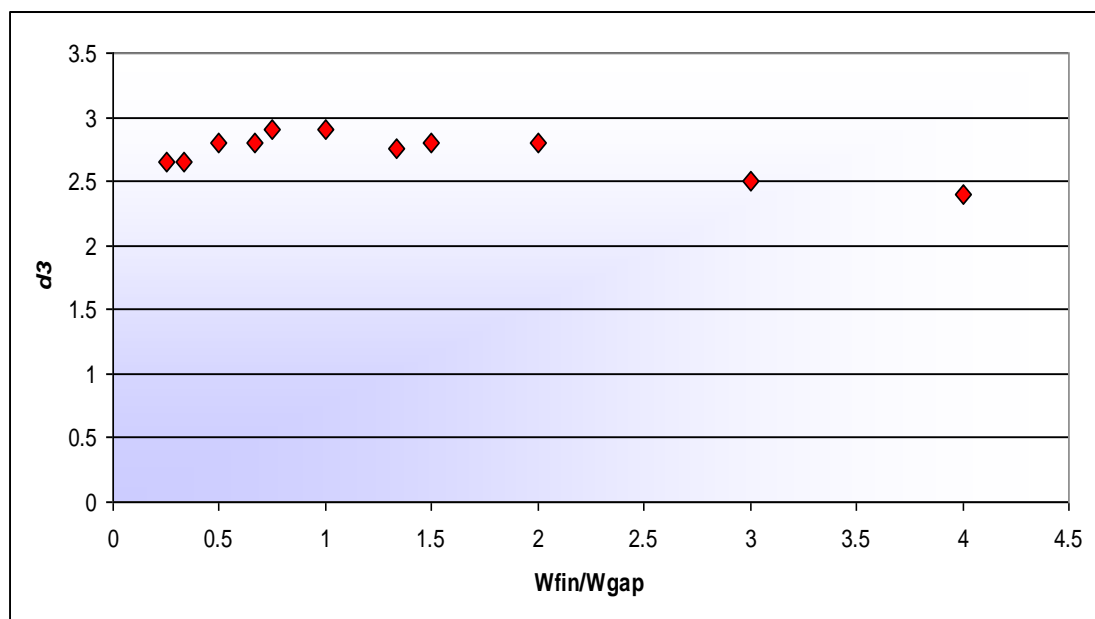


Figure 3-96: Coefficient d_3 as a function of W_{fin}/W_{gap}

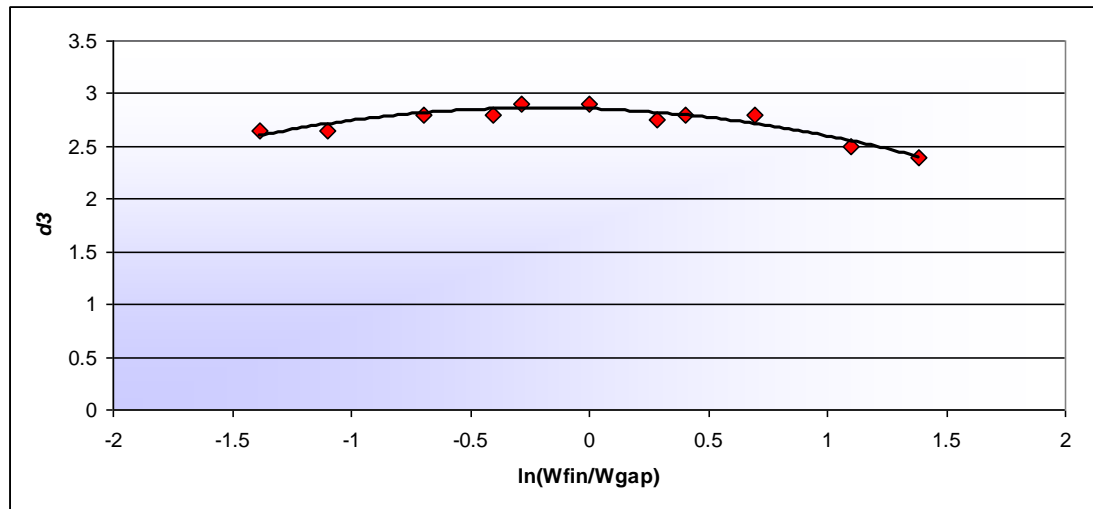


Figure 3-97: Coefficient d_3 as a function of $\ln(W_{fin}/W_{gap})$

The regressions for d_1 and d_3 are displayed below. Combining these two regression lines with Equation 87 results in the complete equation for constant c .

$$d_1 = g_1 \left(\frac{W_{fin}}{W_{gap}} \right)^3 + g_2 \left(\frac{W_{fin}}{W_{gap}} \right)^2 + g_3 \left(\frac{W_{fin}}{W_{gap}} \right) + g_4 \quad (88)$$

$$d_3 = h_1 \left(\ln \left(\frac{W_{fin}}{W_{gap}} \right) \right)^2 + h_2 \left(\ln \left(\frac{W_{fin}}{W_{gap}} \right) \right) + h_3 \quad (89)$$

$$c = \left(g_1 \left(\frac{W_{fin}}{W_{gap}} \right)^3 + g_2 \left(\frac{W_{fin}}{W_{gap}} \right)^2 + g_3 \left(\frac{W_{fin}}{W_{gap}} \right) + g_4 \right) \left(\ln \left(\frac{L_{gap}}{W_{gap}} \right) \right)^2 + \left(h_1 \left(\ln \left(\frac{W_{fin}}{W_{gap}} \right) \right)^2 + h_2 \left(\ln \left(\frac{W_{fin}}{W_{gap}} \right) \right) + h_3 \right) \quad (90)$$

The only coefficient left to correlate in Equation 85 is b . Figure 3-98 displays guessed values of coefficient b as a function of W_{fin}/W_{gap} . The stair-stepping effect visible in Figure 3-98 formed the idea for using a hyperbolic tangent correlation for this coefficient. The logarithm of W_{fin}/W_{gap} is used to centre the data around the y-axis. The modified graph is shown in Figure 3-99 together with the hyperbolic tangent correlation.

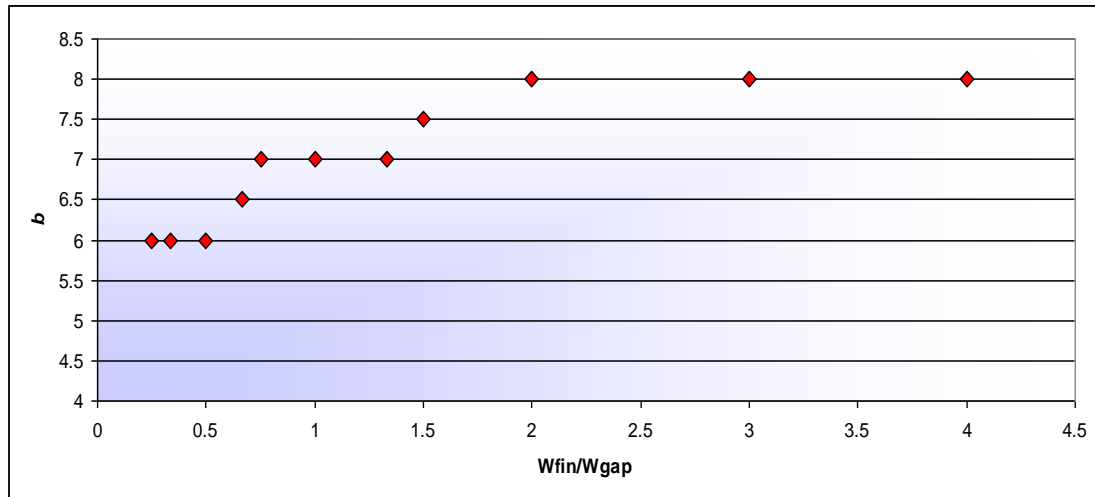


Figure 3-98: Coefficient b as a function of W_{fin}/W_{gap}

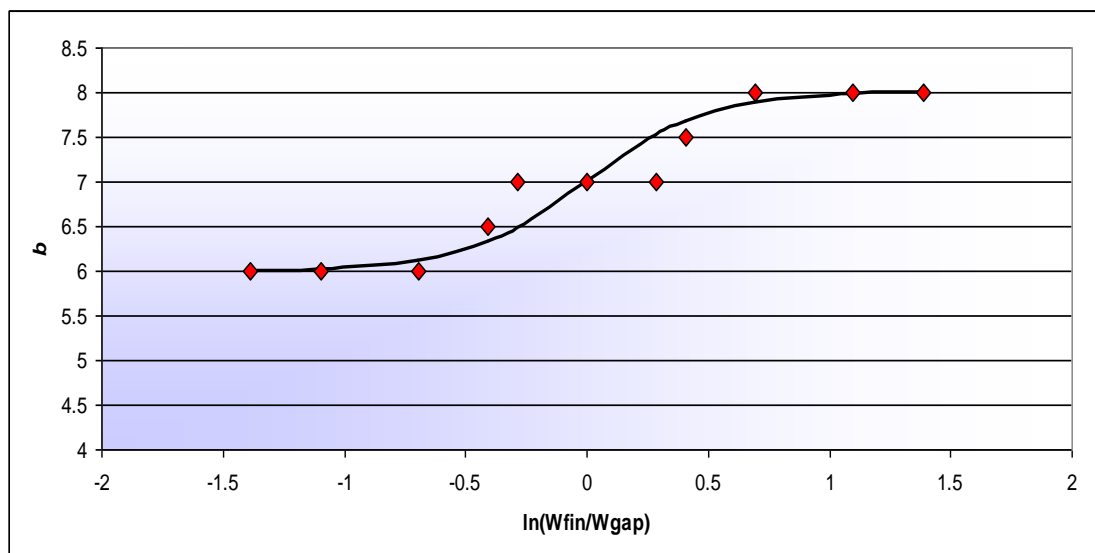


Figure 3-99: Coefficient b as a function of $\ln(W_{fin}/W_{gap})$

The equation for the correlation for the regression line is

$$b = \tanh\left(2 \ln\left(\frac{W_{fin}}{W_{gap}}\right) + 7\right) \quad (91)$$

The complete correlation for the turbulent normalised Nusselt number along the pin width is shown below:

$$nNu_{eq} = \left(-\frac{1}{2}(1-a)\right) \tanh\left(b \cdot \frac{2}{W_{fin}} x + c\right) + \frac{1}{2}(1+a) \quad (92)$$



where

$$a = \left(Z_1 - Z_2 \tan^{-1} \left(Z_3 \left(\frac{W_{fin}}{W_{gap}} \right) - Z_4 \right) \right) \left(\frac{L_{gap}}{W_{gap}} \right)$$

$$b = \tanh \left(Z_{12} \ln \left(\frac{W_{fin}}{W_{gap}} \right) + Z_{13} \right)$$

$$c = \left(Z_5 \left(\frac{W_{fin}}{W_{gap}} \right)^3 + Z_6 \left(\frac{W_{fin}}{W_{gap}} \right)^2 + Z_7 \left(\frac{W_{fin}}{W_{gap}} \right) + Z_8 \right) \left(\ln \left(\frac{L_{gap}}{W_{gap}} \right) \right)^2$$

$$+ \left(Z_9 \left(\ln \left(\frac{W_{fin}}{W_{gap}} \right) \right)^2 + Z_{10} \left(\ln \left(\frac{W_{fin}}{W_{gap}} \right) \right) + Z_{11} \right)$$

Table 3-7 shows the values for coefficients Z_1 to Z_{13} in Equation 92.

Table 3-7: Constants for the turbulent face equation

Constant	Value	Constant	Value
Z_1	23.5195	Z_9	0.0743
Z_2	14.9475	Z_{10}	-0.1558
Z_3	239.1126	Z_{11}	2.567
Z_4	-38.8957	Z_{12}	1.6655
Z_5	-0.0211	Z_{13}	6.8811
Z_6	0.1987		
Z_7	1.3612		
Z_8	0.2899		

The objective function used for the optimisation of the normalised pin face Nusselt number correlation is the root sum square of the percentage difference between the CFD values and the equation to the power of four. The differences between the CFD values and the correlation before and after optimisation are shown in Figure 3-100. After optimisation, 99.4% of the values lie within a 30% margin, with 89.3% within 20% and 52.8% within 10%. The equation values are plotted against the CFD values in Figure 3-101. The figure indicates that heat sink configurations with high integrated normalised Nusselt numbers are worse off after optimisation, but overall the correlations fit the data set better. Figure 3-102 displays the final correlated values compared with the CFD values for the entire turbulent data set.

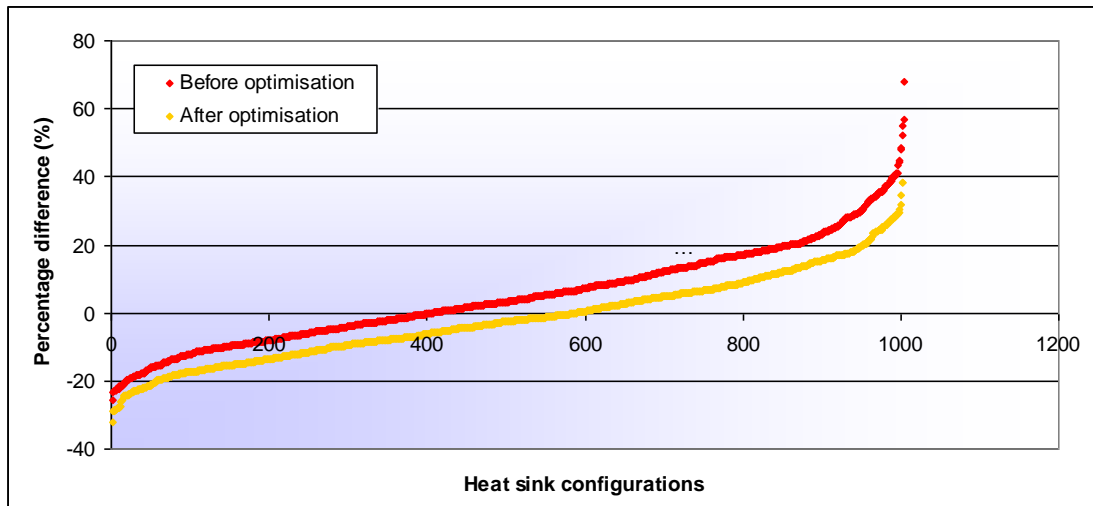


Figure 3-100: Percentage difference between the Nusselt number face correlation and the CFD values

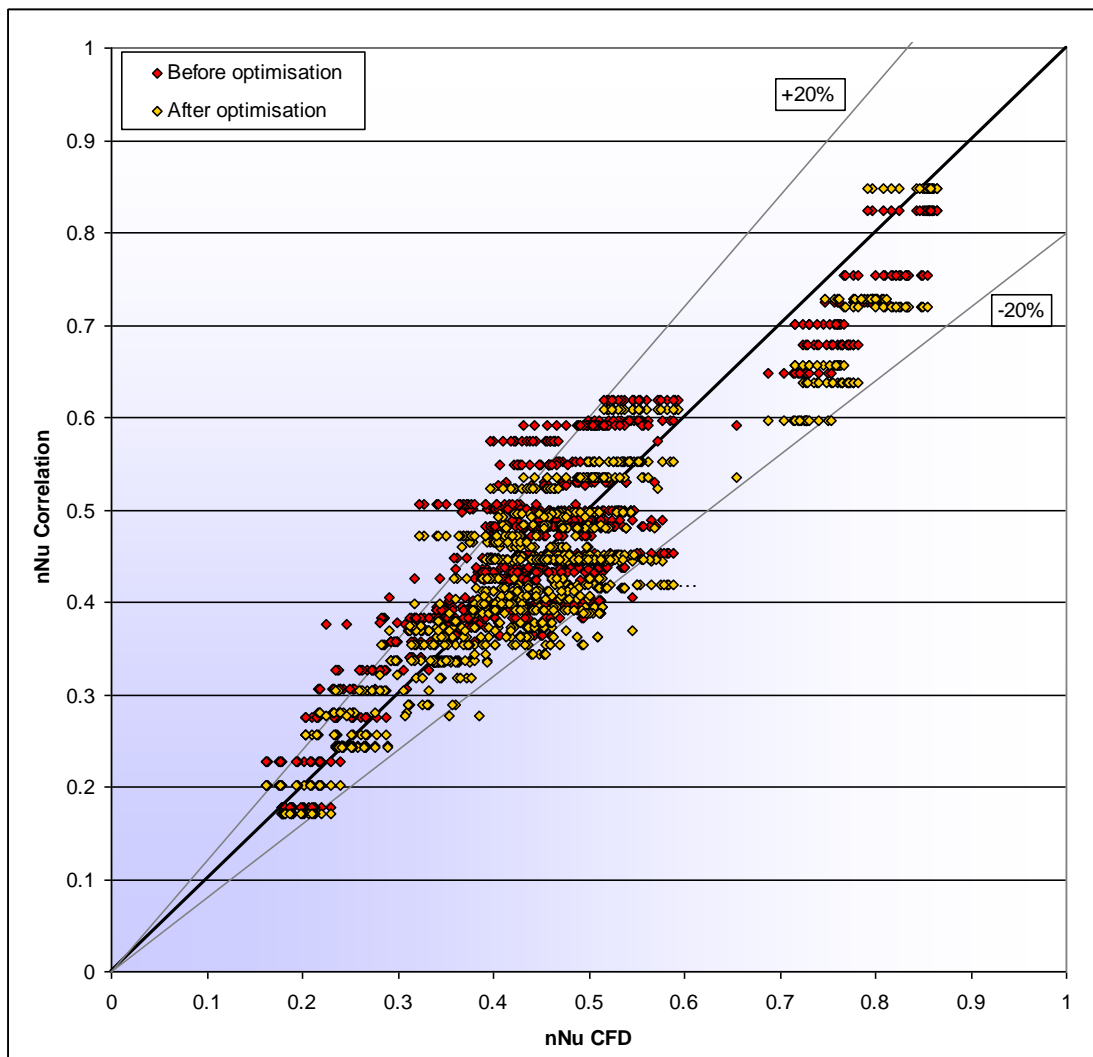


Figure 3-101: Equation Nusselt numbers compared with CFD Nusselt numbers

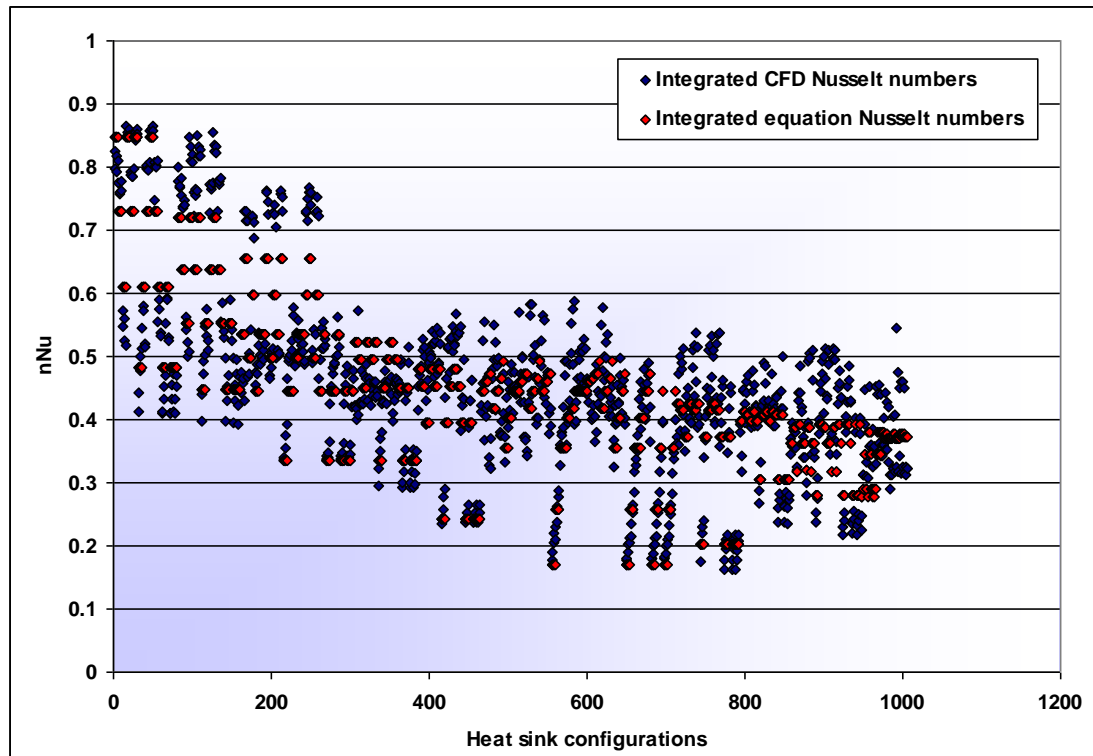


Figure 3-102: Comparison between the integrated CFD pin Nusselt numbers and the integrated optimised pin equation Nusselt numbers



3.8 COMBINATION OF EQUATIONS

The four correlations created in the previous sections can now be used to calculate the Nusselt number anywhere on the contraction-side of the heat sink range used to create the correlation.

Combining Equation 53 and Equation 61, the complete correlation for the contraction heat transfer coefficient for laminar flow is as follows:

$$h_c = \frac{Nu_{eq} k}{Wfin} \quad (93)$$

$$Nu_{eq} = Nu_{e,eq} \cdot nNu_{eq}$$

where

$$Nu_{e,eq} = Nu_s \left(X_{21} - X_{22} \tan^{-1} (X_{23} Nu_s + X_{24}) \right)$$

$$Nu_s = X_1 \left(\left(\frac{Lfin}{Lgap} \right)^{X_2} \left(\frac{Wfin}{Lgap} \right)^{\left(X_3 \left(\frac{Lfin}{Lgap} \right) + X_4 \right)} \ln(Re) - \left(X_5 \left(\frac{Lfin}{Lgap} \right)^{X_6} \left(\frac{Wfin}{Lgap} \right)^{\left(X_7 \left(\frac{Lfin}{Lgap} \right) + X_8 \right)} \right) \right)$$

$$Re = \left(X_9 \left(\frac{Lfin}{Wgap} \right) + X_{10} + X_{11} \left(\frac{Lfin}{Lgap} \right)^{X_{12}} \left(\frac{Wfin}{Wgap} \right)^{-X_{13}} \left(\frac{Lfin}{Lgap} \right)^{X_{14}} \right) \left(\frac{Wfin}{Wgap} \right)^{X_{15}}$$

$$\left(X_{16} \left(\frac{Lfin}{Lgap} \right)^{X_{17}} \left(\frac{Wfin}{Wgap} \right) + X_{18} \left(\frac{Lfin}{Lgap} \right)^{X_{19}} \right) \cdot e^{-X_{20} \left(\frac{Lfin}{Wgap} \right)}$$

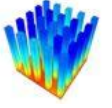
$$nNu_{eq} = \left(-\frac{1}{2} (1-a) \right) \tanh \left(b \cdot \left(\frac{200}{Wfin} x \right) + c \right) + \frac{1}{2} (1+a)$$

$$a = \left(Z_1 \cdot e^{Z_2 \left(\frac{Wfin}{Wgap} \right)} \cdot \left(\frac{Lgap}{Wgap} \right)^{Z_3 \left(\frac{Wfin}{Wgap} \right) + Z_4} \right) \cdot e^{Z_5 \left(\frac{Lfin}{Lgap} \right)} \cdot \left(\frac{Lgap}{Wgap} \right)^{Z_6 \ln \left(\frac{Lfin}{Lgap} \right) - Z_7}$$

$$b = \left(Z_8 \left(\frac{Wfin}{Wgap} \right)^{Z_9} + Z_{10} \right) \cdot \left(\frac{Lgap}{Wgap} \right)^{Z_{11}} + \left(Z_{12} \left(\frac{Wfin}{Wgap} \right)^{Z_{13}} + Z_{14} \right)$$

$$c = \left(Z_{15} \left(\frac{Wfin}{Wgap} \right)^{Z_{16}} + Z_{17} \right) \cdot \left(\frac{Lgap}{Wgap} \right)^{Z_{18}} + \left(Z_{19} \left(\frac{Wfin}{Wgap} \right)^{Z_{20}} + Z_{21} \right)$$

$$Re = \frac{\rho V_{pins} 2Wfin}{\mu} \quad 100 \leq Re \leq 600$$



The same can be done for the turbulent regime by combining Equation 80 and Equation 92. The complete correlation for the contraction heat transfer coefficient for turbulent flow is as follows:

$$h_c = \frac{Nu_{eq} k}{2Wfin} \quad (94)$$

$$Nu_{eq} = Nu_{e,eq} \cdot nNu_{eq}$$

where

$$Nu_{e,eq} = \left[\left(X_1 \left(\frac{Lfin}{Wgap} \right)^{X_2} \right) \left(\frac{Lfin}{Lgap} \right)^{-\left(X_3 \left(\frac{Lfin}{Wgap} \right)^{X_4} \right)} \right. \\ \left. \left(\frac{Wfin}{Wgap} \right)^{-\left(-\left(X_5 \left(\frac{Lfin}{Wgap} \right)^{X_6} \right) \ln \left(\frac{Lfin}{Lgap} \right) + \left(X_7 \ln \left(\frac{Lfin}{Wgap} \right) + X_8 \right) \right)} \right] \ln(Re) - \\ \left[-\left(-\left(X_9 \ln \left(\frac{Lfin}{Wgap} \right) + X_{10} \right) \ln \left(\frac{Lfin}{Lgap} \right) + \left(X_{11} \left(\frac{Lfin}{Wgap} \right) + X_{12} \right) \right) \ln \left(\frac{Wfin}{Wgap} \right) + \right. \\ \left. \left(X_{13} \left(\frac{Lfin}{Wgap} \right)^{X_{14}} \right) \left(\frac{Lfin}{Lgap} \right)^{-\left(X_{15} \ln \left(\frac{Lfin}{Wgap} \right) + X_{16} \right)} \right]$$

$$nNu_{eq} = \left(-\frac{1}{2}(1-a) \right) \tanh \left(b \cdot \frac{2}{Wfin} x + c \right) + \frac{1}{2}(1+a)$$

$$a = \left(Z_1 - Z_2 \tan^{-1} \left(Z_3 \left(\frac{Wfin}{Wgap} \right) + Z_4 \right) \right) \left(\frac{Lgap}{Wgap} \right)$$

$$b = -\left(\tanh \left(Z_{12} \ln \left(\frac{Wfin}{Wgap} \right) \right) + Z_{13} \right)$$

$$c = \left(Z_5 \left(\frac{Wfin}{Wgap} \right)^3 + Z_6 \left(\frac{Wfin}{Wgap} \right)^2 + Z_7 \left(\frac{Wfin}{Wgap} \right) + Z_8 \right) \left(\ln \left(\frac{Lgap}{Wgap} \right) \right)^2$$

$$+ \left(Z_9 \left(\ln \left(\frac{Wfin}{Wgap} \right) \right) \right)^2 + Z_{10} \left(\ln \left(\frac{Wfin}{Wgap} \right) \right) + Z_{11}$$

$$Re = \frac{\rho V_{approach} 2Wfin}{\mu} \quad 1000 \leq Re \leq 6000$$



For the transitional flow domain ($600 \leq Re \leq 1000$), it is suggested to use a first-order interpolation between the laminar heat transfer coefficient at a Reynolds number of 600 and the turbulent heat transfer coefficient at a Reynolds number of 1 000. There seems to be a linear trend in the transitional flow region when looking at published literature data [62] [63] [64]. This suggestion can be examined in future research.

Figure 3-103 and Figure 3-104 display comparisons between the correlations for the laminar and turbulent regions, and the original CFD values respectively.

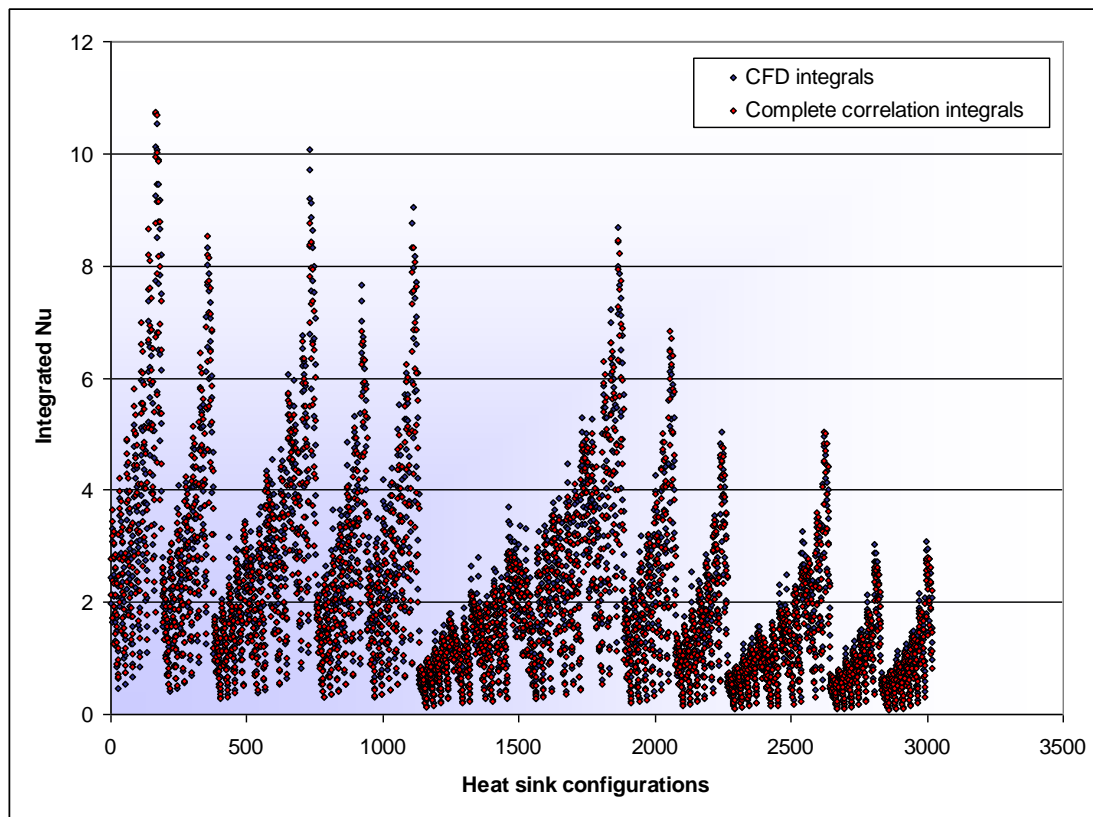


Figure 3-103: Comparison between the integrated complete laminar correlation values and the integrated CFD Nusselt numbers

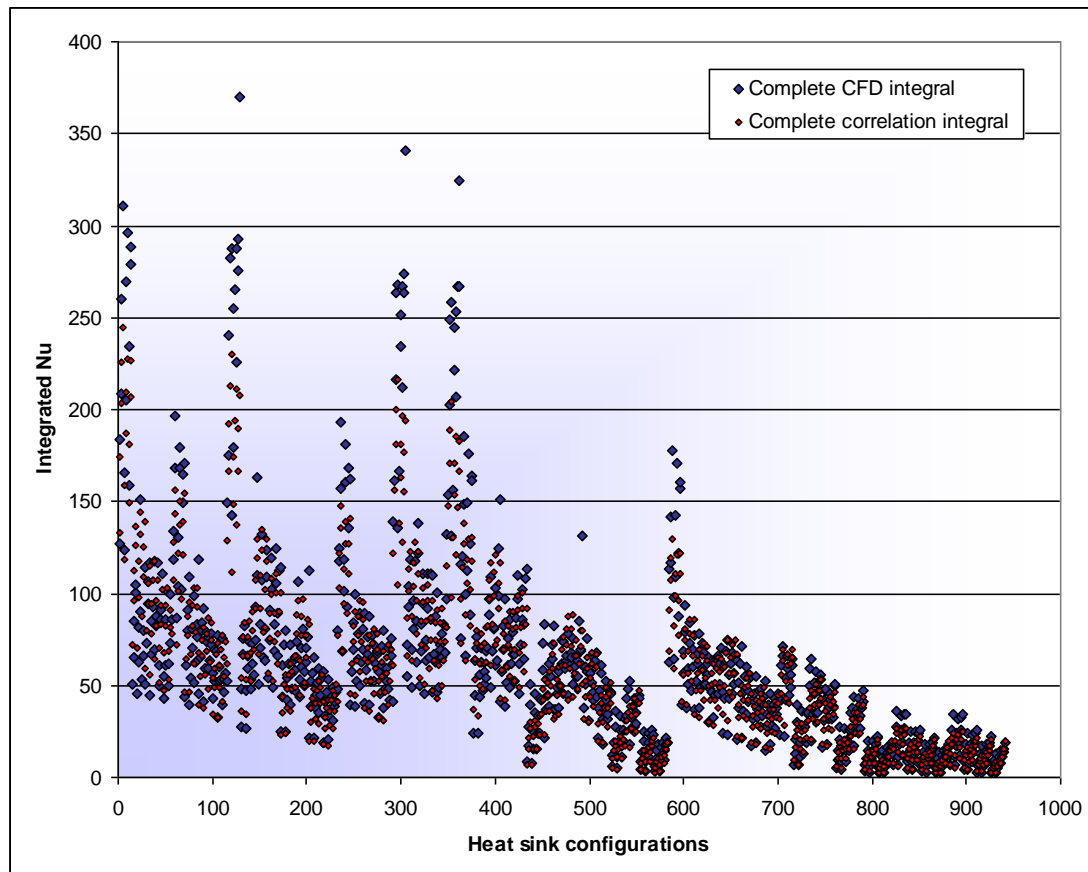


Figure 3-104: Comparison between the integrated complete turbulent correlation values and the integrated CFD Nusselt numbers

Figure 3-105 and Figure 3-106 show examples of the laminar and turbulent correlations together with the respective CFD data. Each of these two figures is based on a different heat sink configuration. Figure 3-107 shows the percentage differences between the combined laminar correlation and the CFD data. When comparing the data points, 99.7% lie within a difference of 30%, 97.0% within 20% and 77.6% within 10%. Figure 3-108 shows the percentage differences for the turbulent correlation. When comparing the complete turbulent correlation with the CFD data, 95.1% of the points lie within 30%, 82.1% fall within 20% and 49.4% fall within 10%. The coefficients for the two complete equations are summarised in Table 3-8 and Table 3-9 respectively.

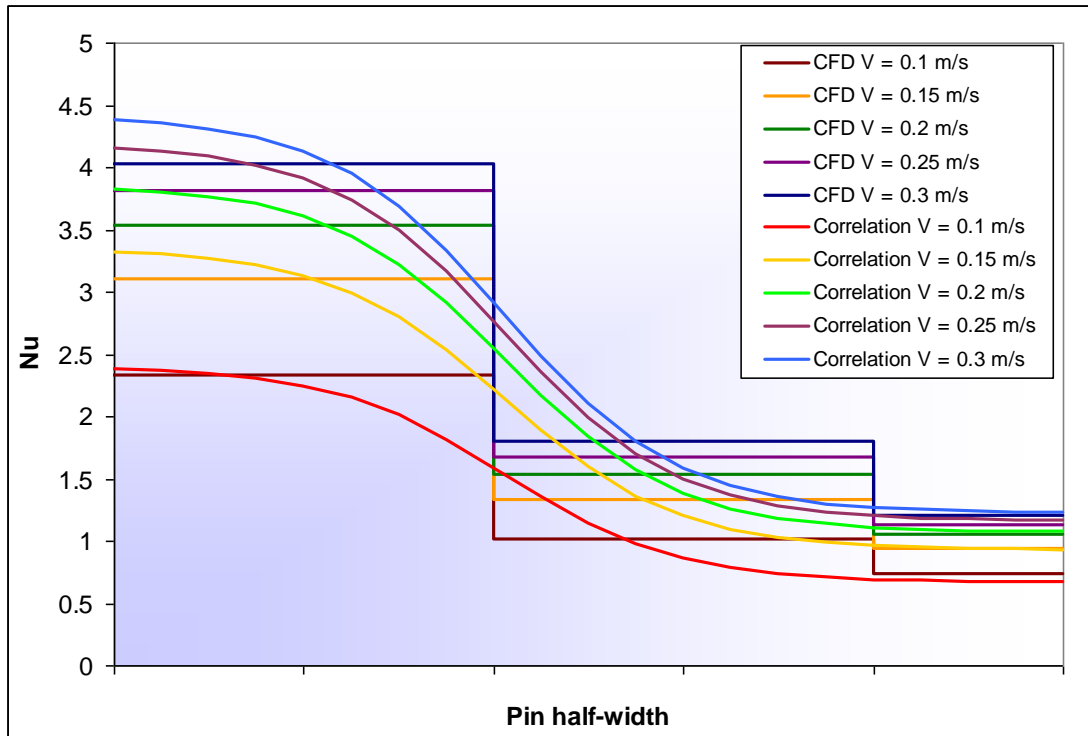


Figure 3-105: Example of the laminar correlation together with the relevant CFD data, on a single heat sink configuration

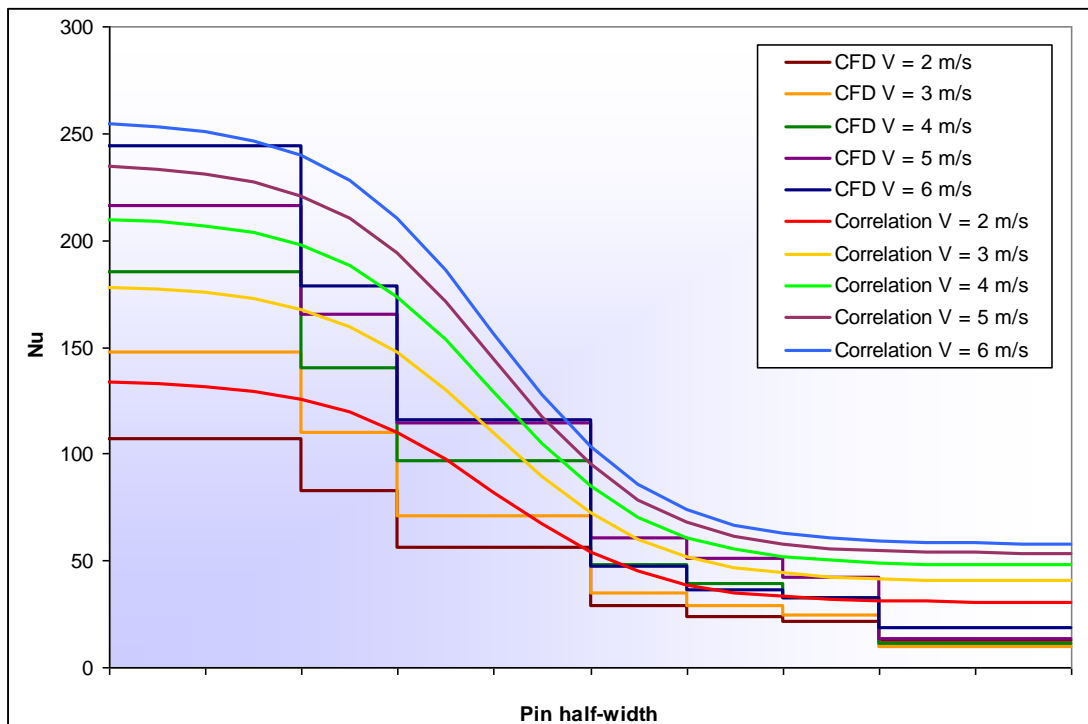


Figure 3-106: Example of the turbulent correlation together with the relevant CFD data, on a single heat sink configuration

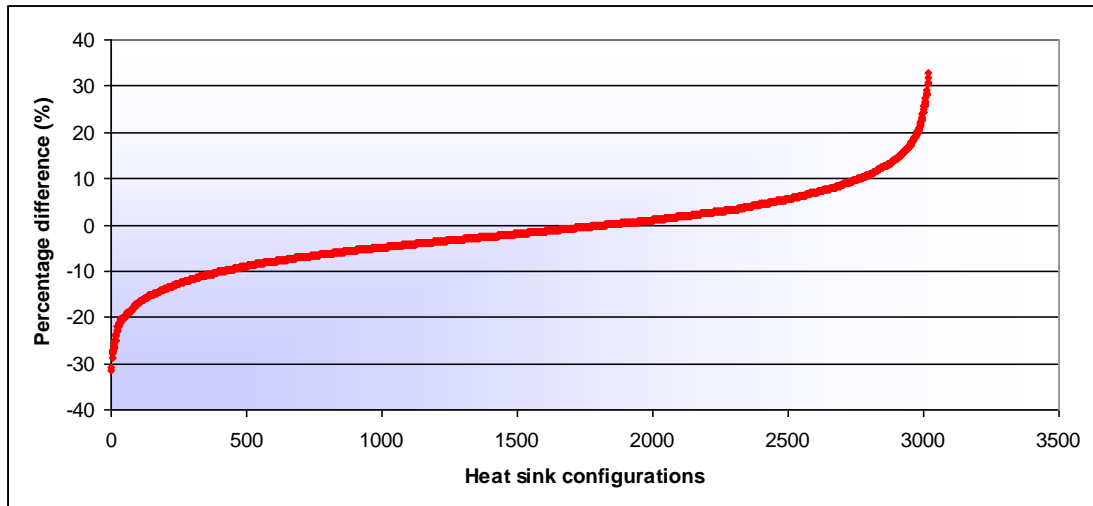


Figure 3-107: Percentage difference between CFD and complete laminar correlation Nusselt numbers

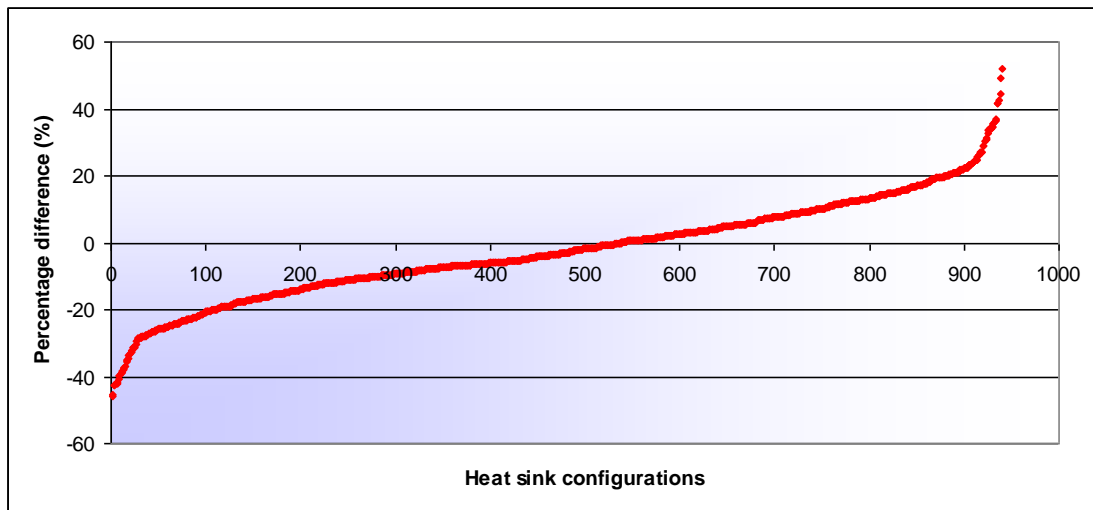


Figure 3-108: Percentage difference between CFD and complete turbulent correlation Nusselt numbers

**Table 3-8: Coefficients for the complete laminar correlation**

Constant	Value	Constant	Value
X_1	14.4147	Z_1	0.793791
X_2	-0.0661	Z_2	-1.4159
X_3	-0.1251	Z_3	0.7224
X_4	-0.4199	Z_4	-0.9266
X_5	3.8455	Z_5	0.1862
X_6	-0.0803	Z_6	0.3254
X_7	-0.1196	Z_7	-1.1724
X_8	-0.4126	Z_8	-0.6893
X_9	0.4123	Z_9	0.011
X_{10}	-1.2581	Z_{10}	0.673
X_{11}	0.0411	Z_{11}	0.2733
X_{12}	0.7487	Z_{12}	0.0864
X_{13}	-0.7616	Z_{13}	-5.69E-04
X_{14}	-0.2038	Z_{14}	-0.0197
X_{15}	-0.0044	Z_{15}	-0.2969
X_{16}	-0.4024	Z_{16}	1.7223
X_{17}	0.8809	Z_{17}	0.7082
X_{18}	2.0115	Z_{18}	0.138
X_{19}	0.7348	Z_{19}	1.6921
X_{20}	-2.5039	Z_{20}	0.8807
X_{21}	24.6705	Z_{21}	-3.9722
X_{22}	14.9042		
X_{23}	52.1538		
X_{24}	-0.8421		

**Table 3-9: Coefficients for the complete turbulent correlation**

Constant	Value	Constant	Value
X_1	86.1968	Z_1	23.5195
X_2	0.598	Z_2	14.9475
X_3	0.7671	Z_3	239.1126
X_4	0.043	Z_4	-38.8957
X_5	0.00329	Z_5	-0.0211
X_6	0.0007392	Z_6	0.1987
X_7	-0.0235	Z_7	1.3612
X_8	0.0767	Z_8	0.2899
X_9	-9.1688	Z_9	0.0743
X_{10}	7.8171	Z_{10}	-0.1558
X_{11}	-9.5115	Z_{11}	2.567
X_{12}	38.422	Z_{12}	1.6655
X_{13}	564.6	Z_{13}	6.8811
X_{14}	0.5226		
X_{15}	0.0322		
X_{16}	0.6977		

3.9 CONCLUSION

This chapter described the methodology developed for generating heat transfer correlations, as well as correlations created with this methodology. The first part was to validate the Computational Fluid Dynamics models that were used in the study to generate the necessary data. The models were validated against an existing heat sink set, which is frequently seen in literature. Secondly, the methodology was created. This involved determining the parameters for the correlation, creating a method for generating and extracting data, determining a method for correlating the data, and setting up an optimisation strategy to increase the accuracy of the correlations. The following chapter will discuss the application of these correlations to several case studies.



CHAPTER 4: APPLICATION OF THE EQUATIONS IN CASE STUDIES

4.1 INTRODUCTION

The laminar and turbulent correlations, derived in Chapter 4, were compared with the CFD simulations used in creating the data for this research project, as well as with data retrieved from existing literature on experimental measurements on heat sinks. The thermal resistance was used to compare the correlations with the CFD and literature data. The first section examines the differences in applying the correlated equations to different regions of the heat sinks. The second section compares the differences between the correlations and the CFD data for several heat sink configurations. The last section compares the correlations with literature data.

The thermal resistance, measured in Kelvin per Watt, is defined as the temperature increase from the base of the heat sink to the ambient temperature relative to the power applied to the heat sink base.

$$R_{th} = \frac{T_B - T_e}{Q} \quad [\text{K/W}] \quad (95)$$

where

T_B : Average base temperature [K]

T_e : Ambient temperature at inlet [K]

Q : Heat input [W]

4.2 CORRELATION APPLIED TO DIFFERENT REGIONS

Since the correlations are created by only using data from the fourth row to the second last row of pins on 15-row pin fin heat sinks, applying the correlation to all the rows might result in high errors on the heat transfer.



The first comparison is created by applying the correlation only to the faces used to extract the data for creating the correlations. For the second comparison, the correlation is applied to all the contraction faces. In the third case, the correlation is applied to the contraction (rear) and expansion (front) faces. When examining the heat transfer, it was seen that the profiles on the expansion-side looked very similar to those on the contraction-side. The idea emerged that it might be possible to use the contraction correlation also on the expansion-side. Figure 4-1 indicates the faces to which the correlations are applied. For the rest of the heat sink faces in all the comparisons, the heat transfer coefficients were extracted from the original CFD simulations.

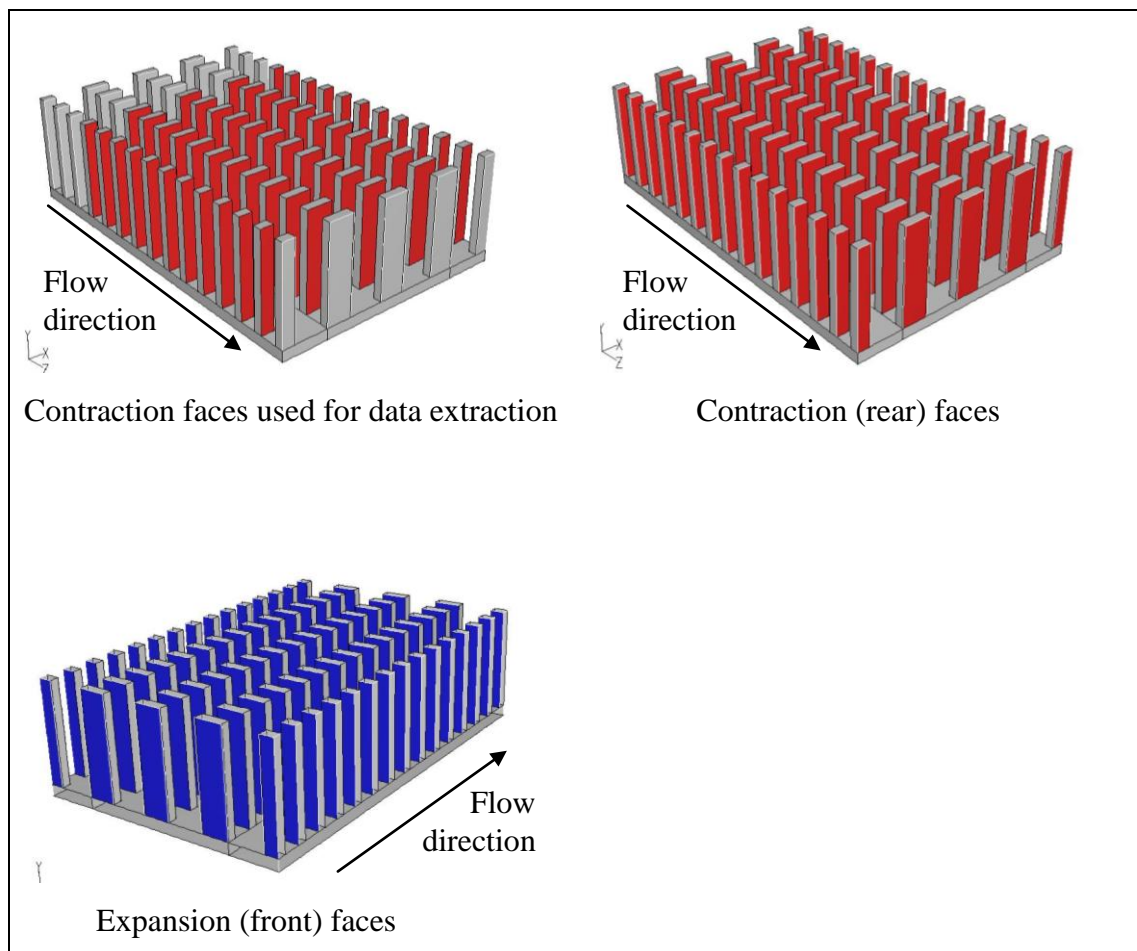


Figure 4-1: Faces to which the correlation has been applied

Table 4-1 summarises the thermal resistance (R_{th}) for the comparisons shown above. Thermal resistances were calculated for five turbulent Reynolds numbers.



Table 4-1: Thermal resistance comparisons for different combinations of faces with correlations applied to them

Velocity [m/s]	R_{th} CFD [K/W]	R_{th} Used contraction faces [K/W]	R_{th} All contraction faces [K/W]	R_{th} Front and rear faces [K/W]
1.99	1.061	1.049	1.044	1.164
2.98	0.781	0.767	0.804	0.829
3.97	0.648	0.645	0.677	0.698
4.95	0.587	0.578	0.605	0.611
5.94	0.534	0.525	0.554	0.557

Figure 4-2 below displays the thermal resistances for the original CFD simulations, the simulations where the correlation is applied to all the contraction faces, and the simulations where the correlation is applied only to the faces used for data extraction. This figure shows that applying the correlation to all 15 rows of pins results in small errors between the original CFD simulations and the correlated simulations.

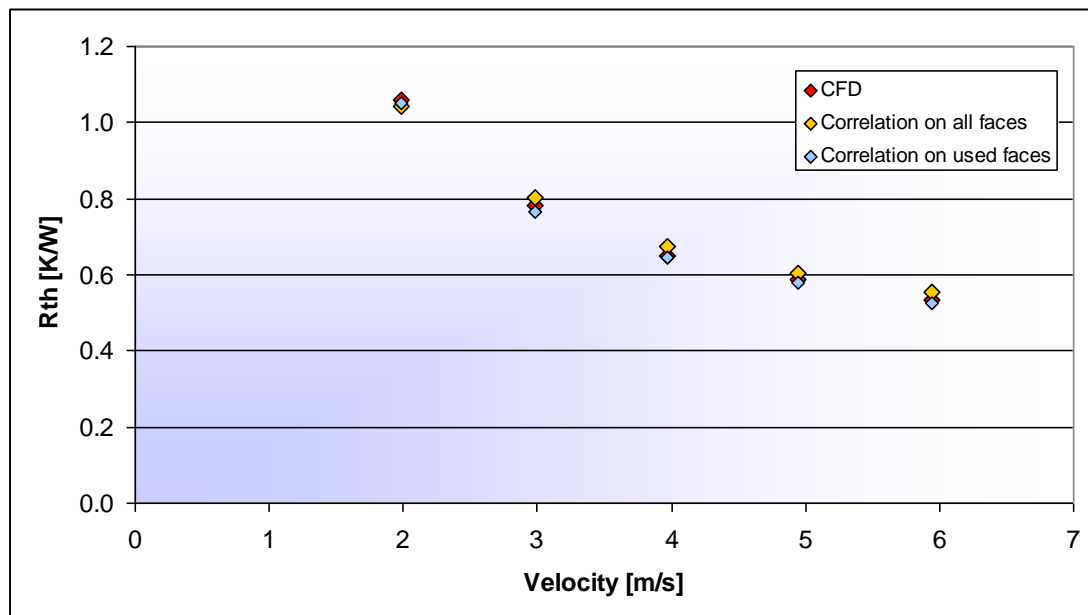
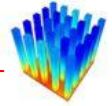


Figure 4-2: Thermal resistance for different cases of contraction faces used
[K/W]

Figure 4-3 shows the thermal resistance of the original CFD simulations, simulations with the correlation applied to all contraction faces and simulations with the correlation applied to the contraction and expansion faces. This figure indicates that



using the contraction coefficient correlation on the expansion-side does not result in very large errors. This can be examined in further research.

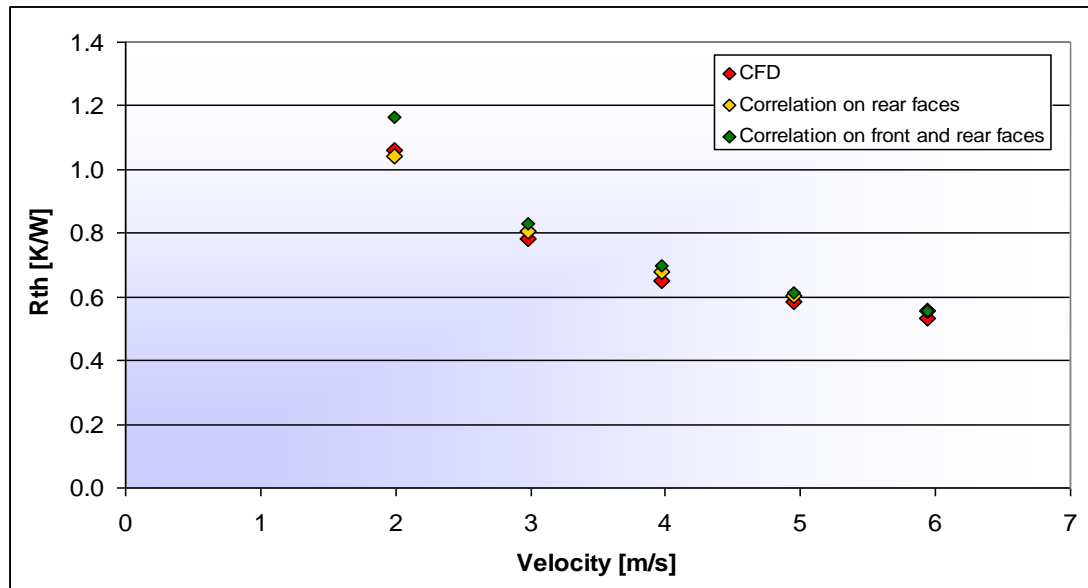


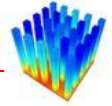
Figure 4-3: Thermal resistance where the correlation has been applied to front and rear of pins [K/W]

The temperature distributions on the heat sinks for the cases with a velocity of 3 m/s with the four different boundary condition sets are shown in Figure 4-4 to Figure 4-7.

The temperature distributions of the two simulations where the correlation has been applied only to the faces used for extracting the data and where the correlation has been applied to all the contraction faces are very similar. The heat sink where the correlation has been applied to all the contraction faces has slightly higher temperatures. This is because there is actually a spike in the real heat transfer coefficient in the first row of cells, which is not taken into account in this case.

For the case where the correlation has been applied to the rear and front faces, the temperatures are higher than in the previous two cases. The temperature profiles in all three cases differ by less than one percent from each other.

For this specific heat sink configuration, all three cases where the correlation has been used have higher temperatures than the full CFD simulation. The largest difference between the full CFD simulation and the cases where the correlation has been used is



on the last row of pins. On the full CFD simulation, the temperatures at the top of the pins drop in temperature more than in the correlated simulations. This can be attributed to changes in flow characteristics in the wake of the full CFD heat sink, which are not accounted for in the correlated cases.

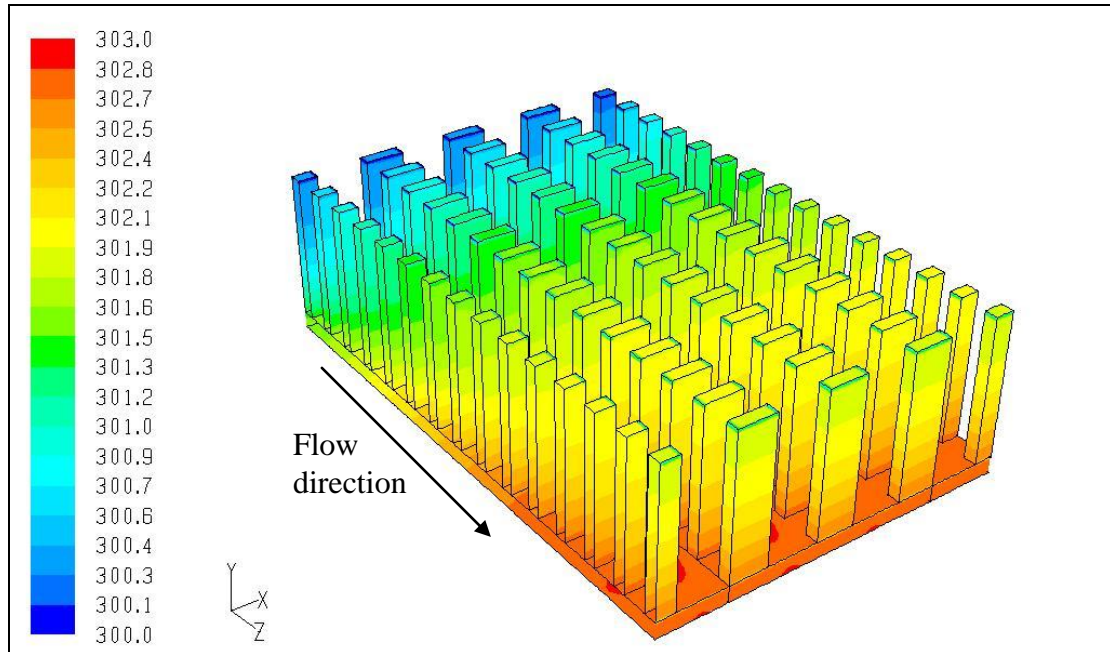


Figure 4-4: Temperature distribution for an original CFD simulation (3 m/s) [K]

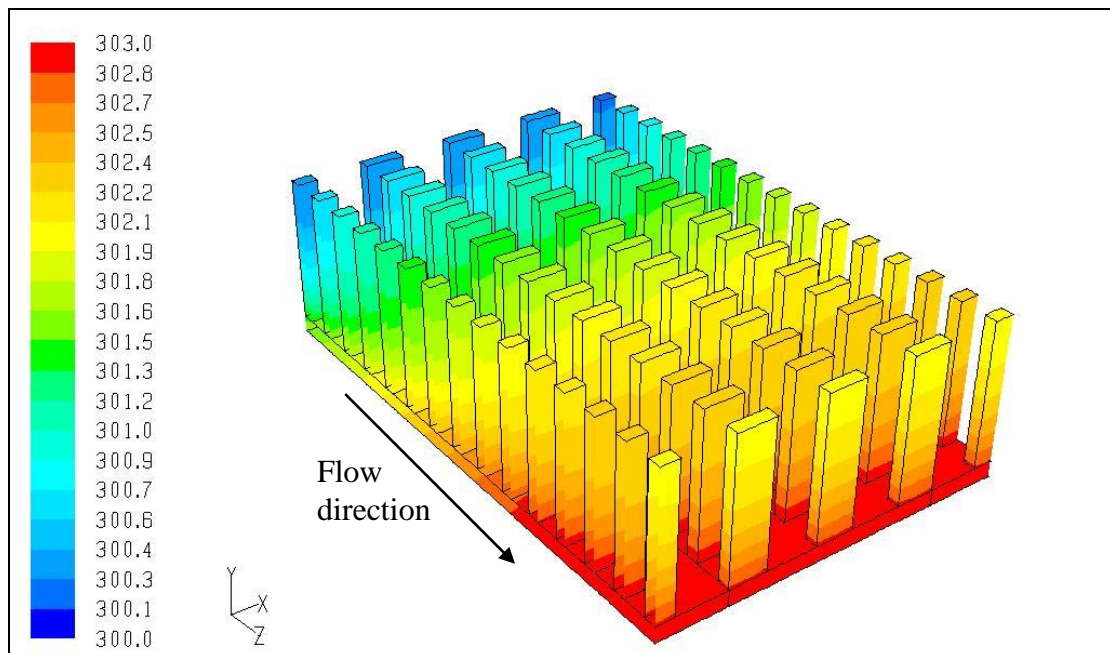


Figure 4-5: Temperature distribution for a case where the correlation has been applied to the faces used for data extraction (3 m/s) [K]

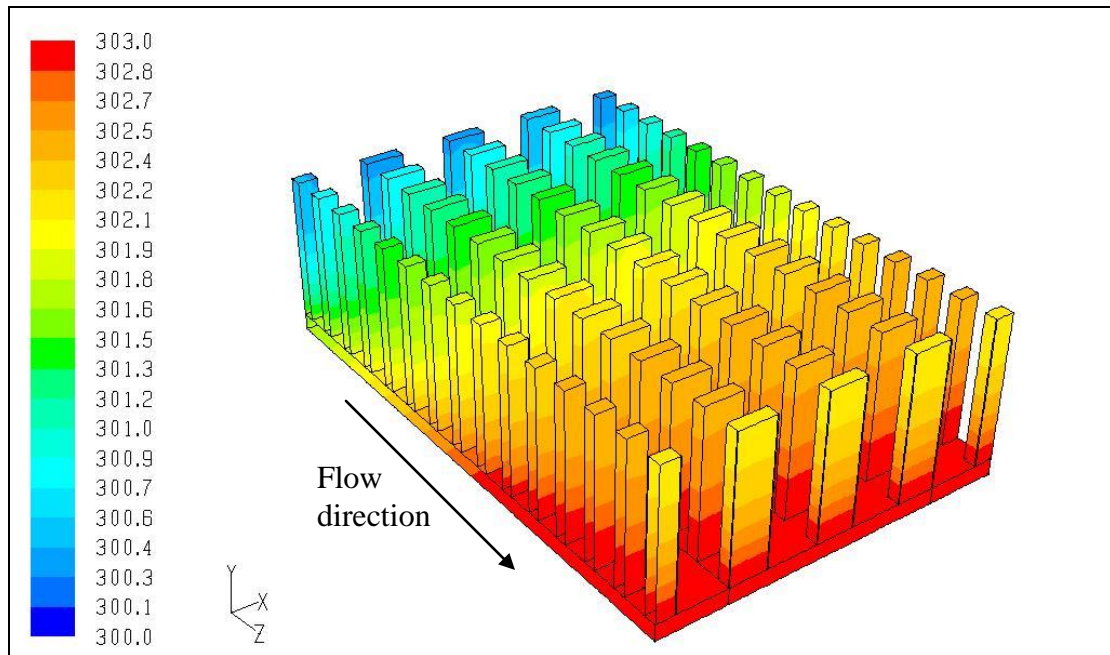
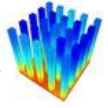


Figure 4-6: Temperature distribution for a case where the correlation has been applied to all the contraction faces (3 m/s) [K]

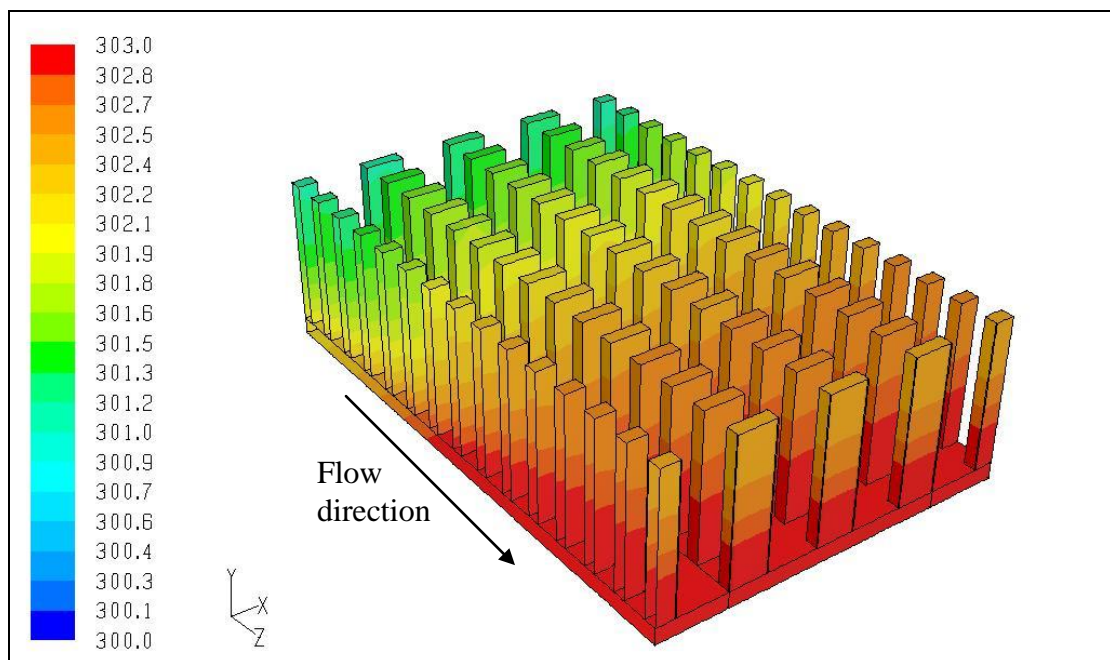


Figure 4-7: Temperature distribution for a case where the correlation has been applied to the contraction and expansion faces (3 m/s) [K]



4.3 CORRELATION COMPARED WITH CFD DATA

Thermal resistances were calculated for three heat sink configurations with five laminar Reynolds numbers and five turbulent Reynolds numbers. The three heat sink configurations are shown in Figure 4-8 below. The heat sinks chosen represent various differences between the extracted CFD data and the correlation. For the first heat sink chosen, the correlated heat transfer is on average 20% less. The second heat sink results in correlated heat transfer coefficients close to the CFD values. For the third heat sink, the heat transfer coefficients from the correlation are on average 25% higher than the CFD values. The correlation is applied to all the contraction faces.

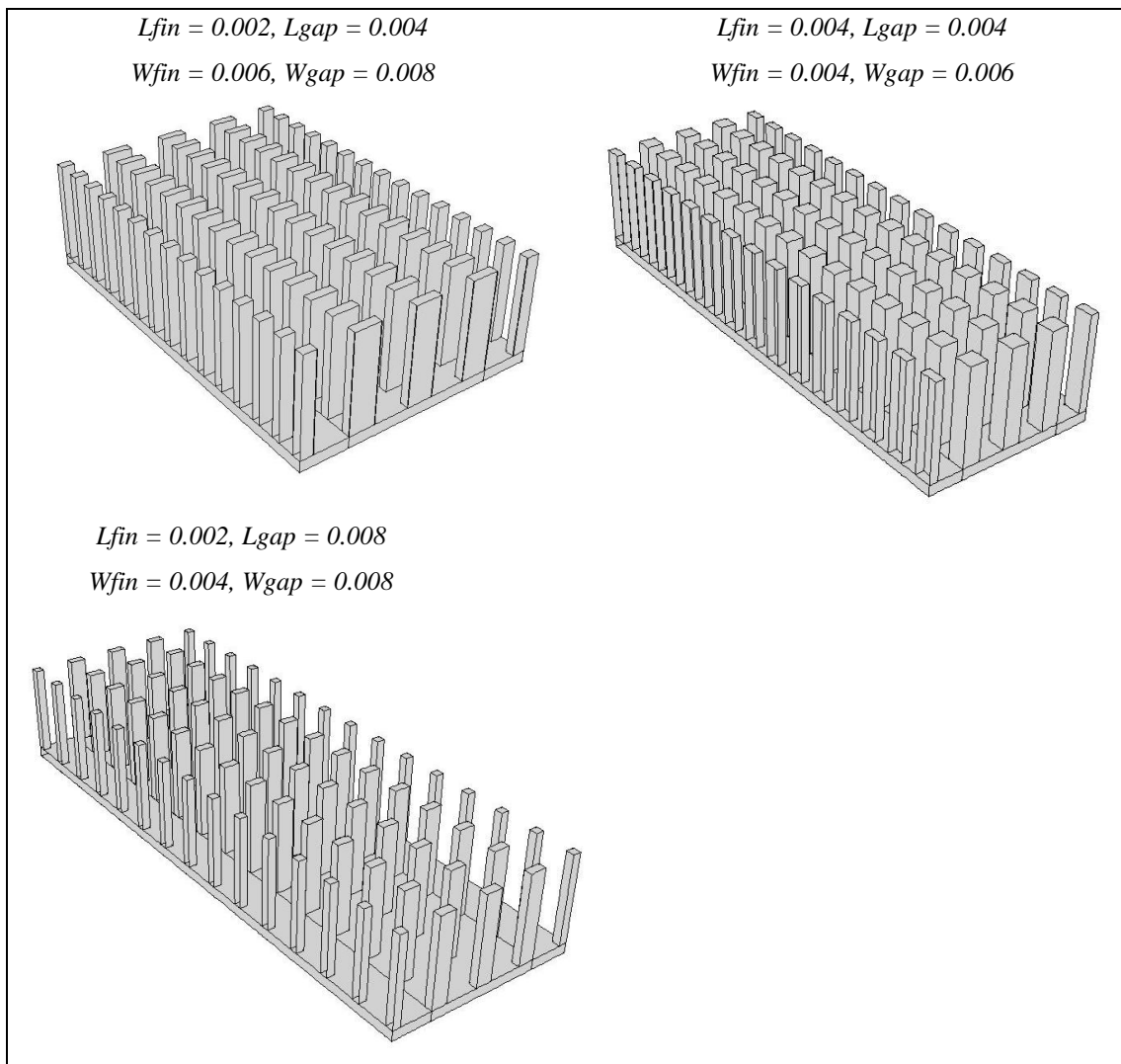


Figure 4-8: Heat sink configurations



4.3.1 Heat sink configuration: $L_{fin}= 0.002$, $L_{gap}= 0.004$, $W_{fin}= 0.006$, $W_{gap}= 0.008$

Table 4-2 summarises the thermal resistances for this heat sink. When the correlation heat transfer coefficients are lower than the extracted CFD values (the differences are negative), the total heat transfer is less, and therefore the average heat sink base temperature will be higher than the CFD data. This results in a larger thermal resistance for the correlation than for the CFD simulation, which means the thermal resistance difference will be positive.

Table 4-2: Thermal resistance comparisons for heat sink, Configuration 1

Velocity [m/s]	R_{th} CFD [K/W]	R_{th} Correlation [K/W]	Difference between CFD and correlated thermal resistance [%]	Difference between extracted data and correlation [%]
0.10	7.86	7.50	-4.66	-3.87
0.15	6.23	5.93	-4.89	-5.38
0.20	5.33	5.11	-4.17	-12.24
0.25	4.73	4.55	-3.89	-19.75
0.30	4.29	4.20	-2.23	-26.87
1.99	1.06	1.04	-1.59	-7.77
2.98	0.78	0.80	2.92	-22.17
3.97	0.65	0.68	4.38	-28.47
4.95	0.59	0.61	3.19	-23.70
5.94	0.53	0.55	3.78	-26.73

Figure 4-9 shows the thermal resistances summarised in Table 4-2. The differences are shown in Figure 4-10. The temperature distributions on the CFD simulation and the correlated simulation for a velocity of 4 m/s are displayed in Figure 4-11 and Figure 4-12 respectively.

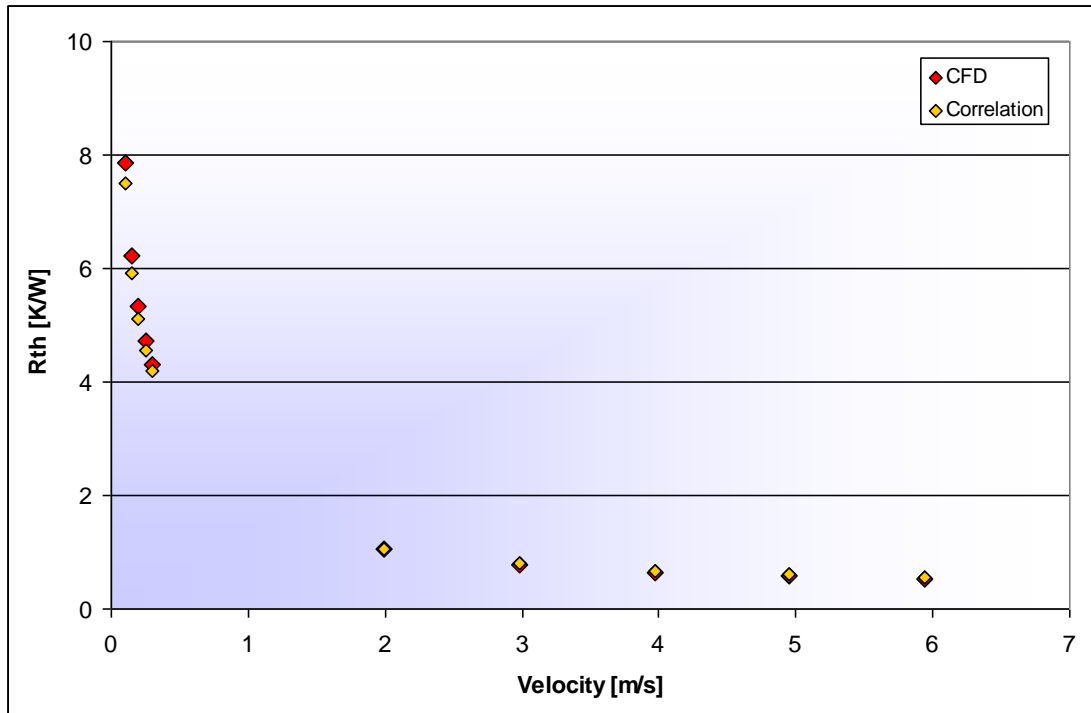


Figure 4-9: Thermal resistance as a function of velocity, Configuration 1 [K/W]

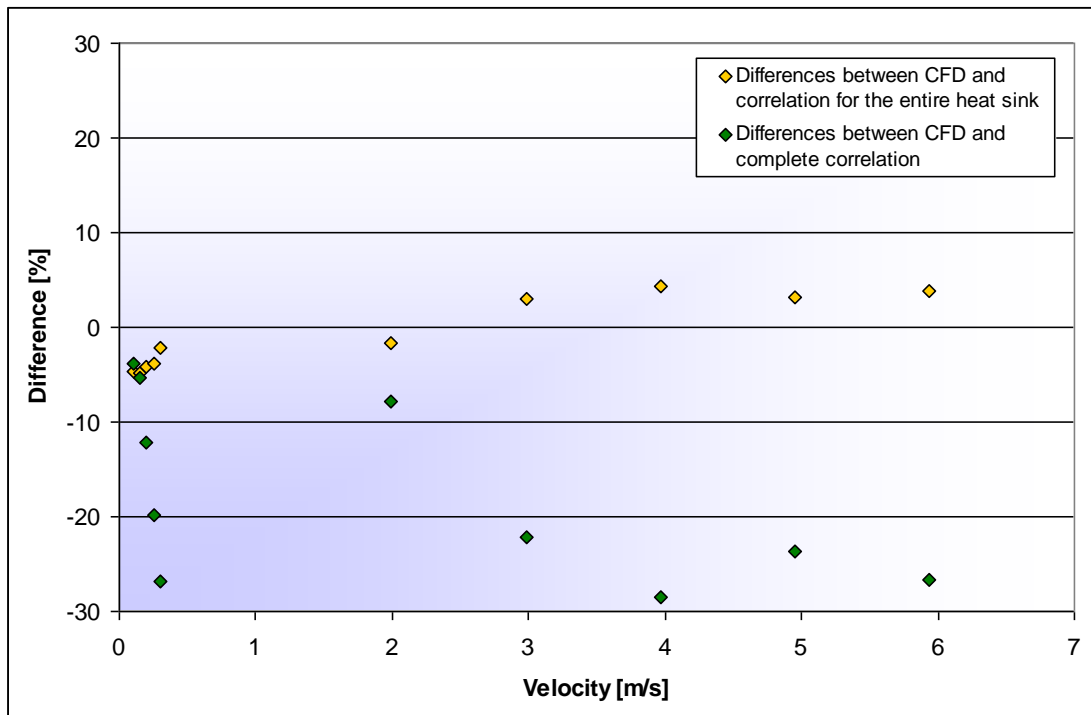


Figure 4-10: Differences in thermal resistance as a function of velocity, Configuration 1 [%]

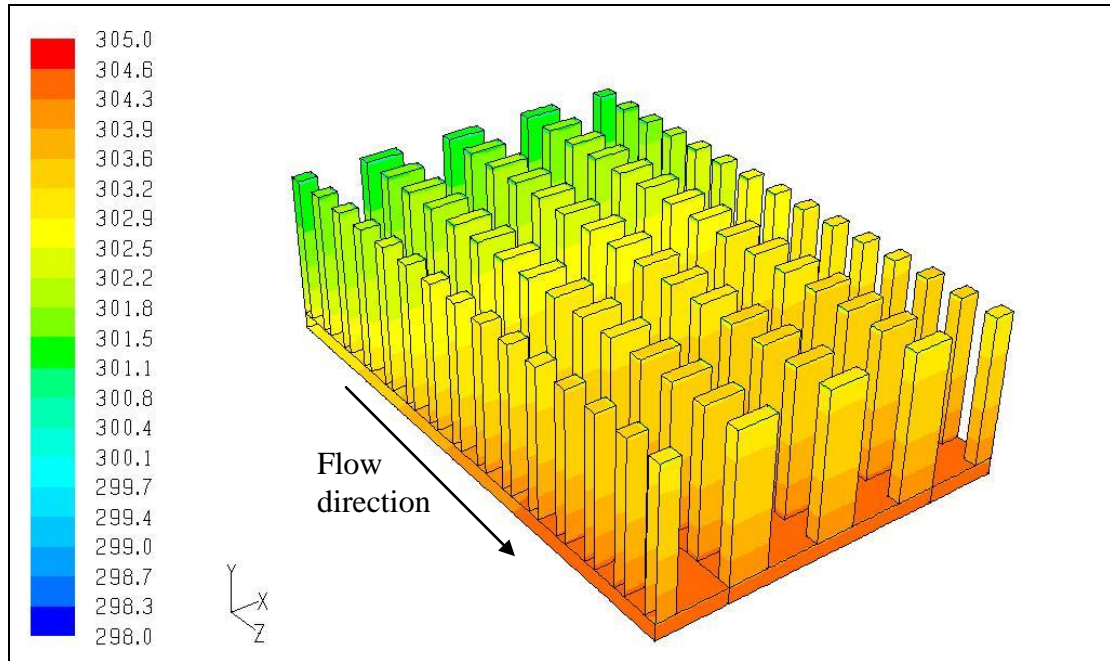


Figure 4-11: Temperature distribution for the CFD simulation (4 m/s), Configuration 1 [K]

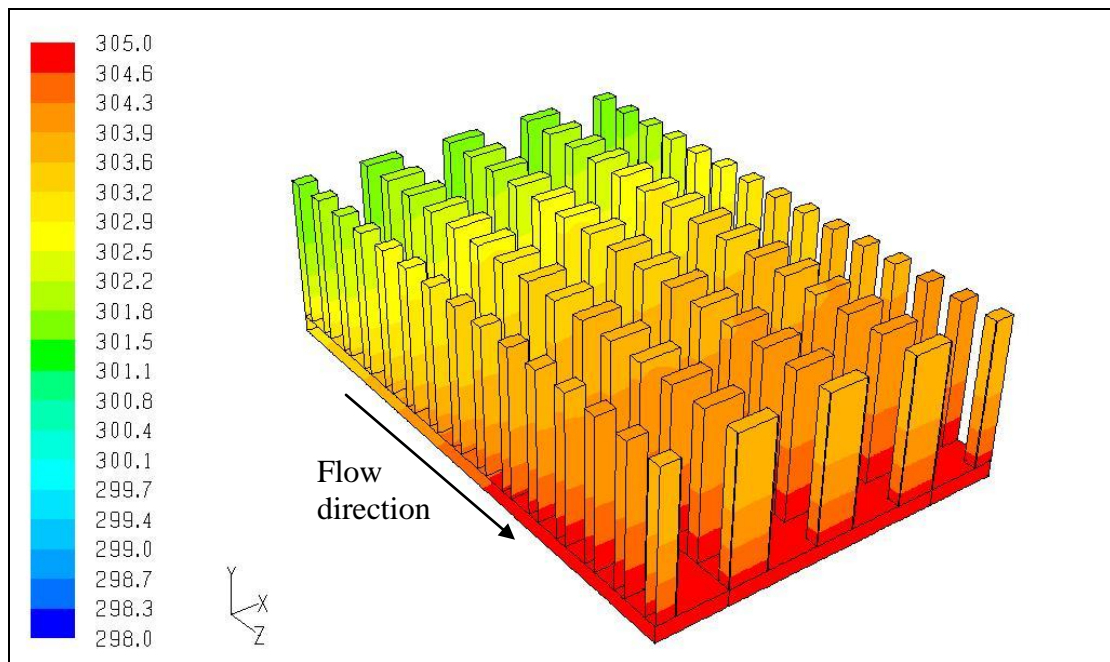


Figure 4-12: Temperature distribution for the correlated simulation (4 m/s), Configuration 1 [K]



4.3.2 Heat sink configuration: $L_{fin}= 0.004$, $L_{gap}= 0.004$, $W_{fin}= 0.004$, $W_{gap}= 0.006$

The calculated thermal resistances are shown in Table 4-3. The fact that the contraction-side of the heat sink contributes only a fraction of the total heat transfer from the heat sink to the air should result in overall differences lower than the correlation differences. From this table, it is apparent that this is not the case. One factor influencing this is the averaging used in the calculation of the correlation. A second factor is that the correlation is applied to all the contraction faces and not only to the ones used to extract data from for the creation of the correlation.

Table 4-3: Thermal resistance comparisons for heat sink, Configuration 2

Velocity [m/s]	R_{th} CFD [K/W]	R_{th} Correlation [K/W]	Difference between CFD and correlated thermal resistance [%]	Difference between extracted data and correlation [%]
0.09	7.61	7.44	-2.22	-6.71
0.13	5.79	5.59	-3.50	-1.91
0.18	4.88	4.69	-3.75	-0.72
0.21	4.31	4.18	-2.98	-0.66
0.32	4.23	4.06	-3.94	-1.40
1.99	0.96	0.86	-9.98	5.26
2.98	0.71	0.70	-1.60	-3.88
3.97	0.61	0.59	-2.37	1.03
4.95	0.53	0.52	-2.57	-3.77
5.94	0.48	0.47	-2.33	-6.40

Figure 4-13 displays the thermal resistances summarised in Table 4-3. The CFD and correlation data lie very close to each other for all the Reynolds numbers. The percentage differences are displayed in Figure 4-14. Figure 4-15 and Figure 4-16 show the temperature distribution of the CFD simulation and the correlation respectively for a velocity of 4 m/s.

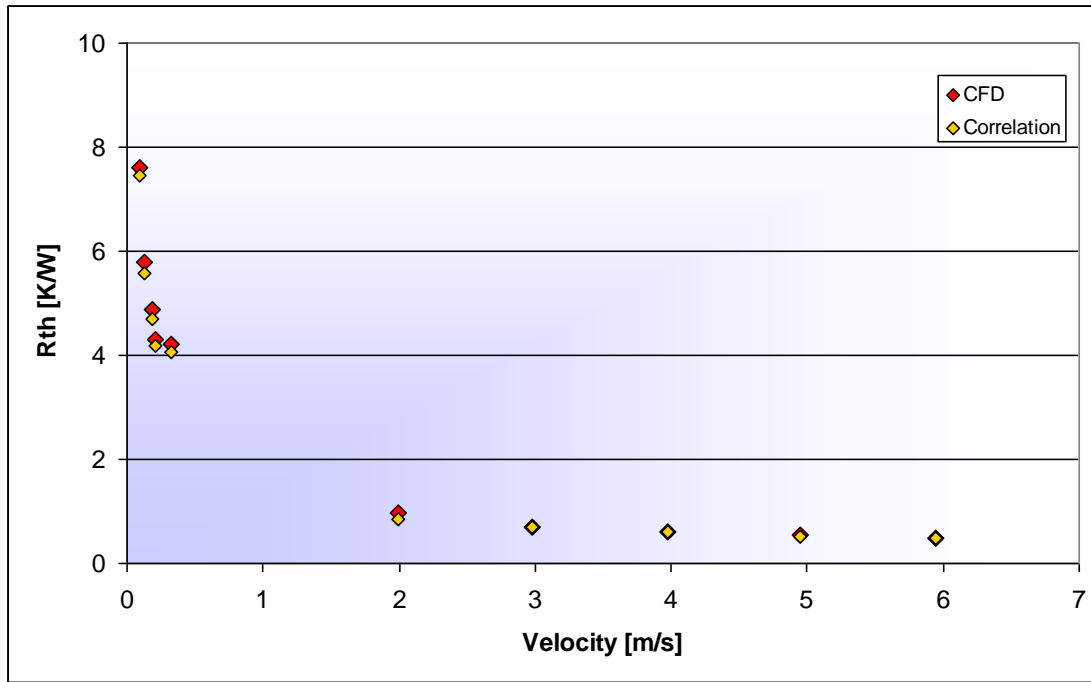


Figure 4-13: Thermal resistance as a function of velocity, Configuration 2 [K/W]

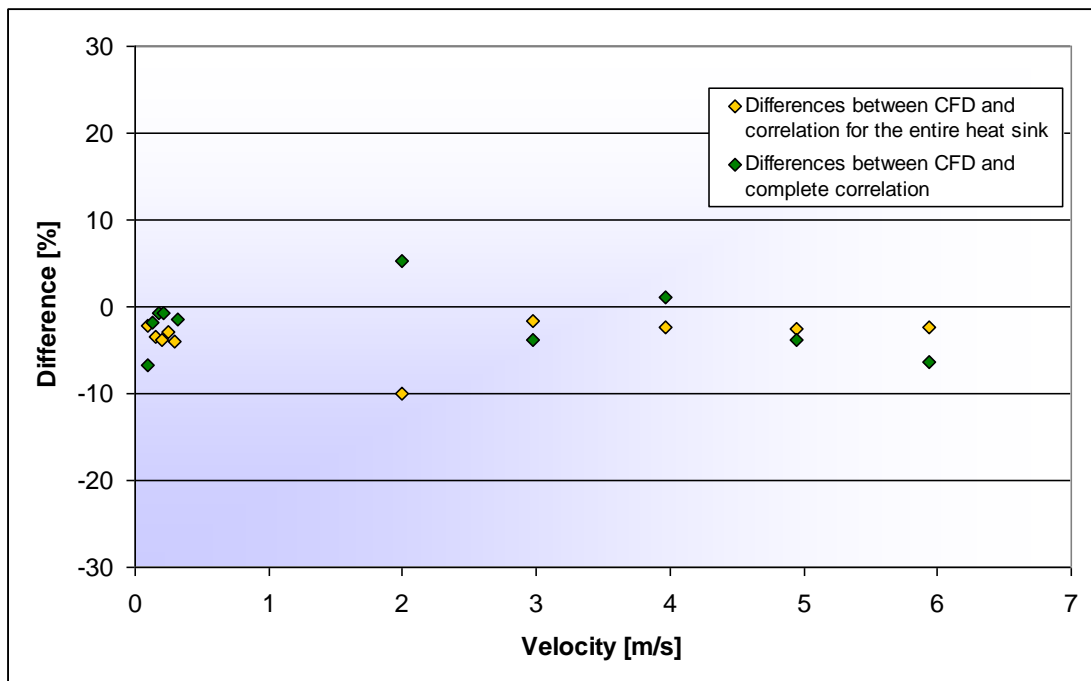


Figure 4-14: Differences in thermal resistance as a function of velocity, Configuration 2 [%]

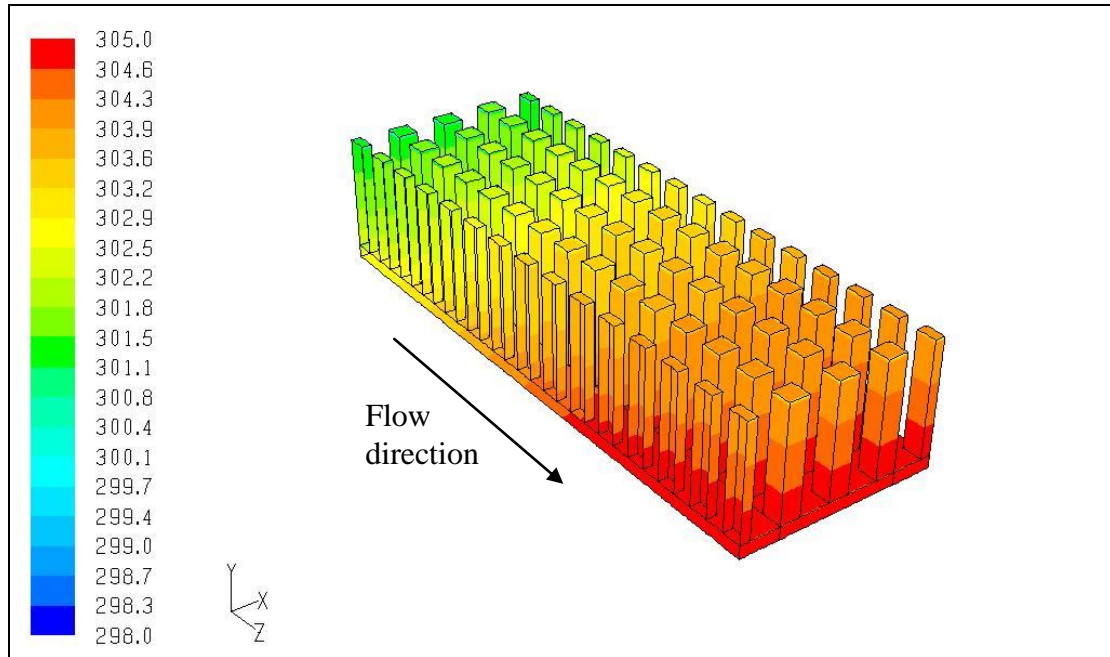
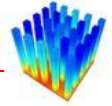


Figure 4-15: Temperature distribution for the CFD simulation (4 m/s), Configuration 2 [K]

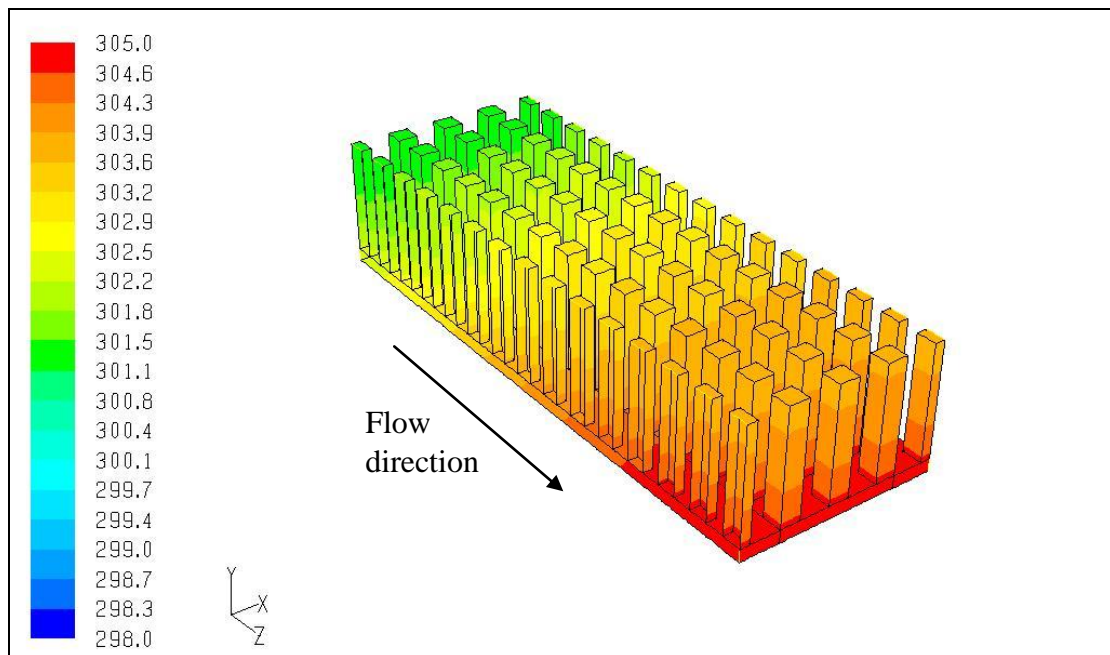


Figure 4-16: Temperature distribution for the correlated simulation (4 m/s), Configuration 2 [K]



4.3.3 Heat sink configuration: $L_{fin}= 0.002$, $L_{gap}= 0.008$, $W_{fin}= 0.004$, $W_{gap}= 0.008$

Table 4-4 shows the thermal resistances for this heat sink at the simulated Reynolds numbers. The correlation differences are positive high relative to the complete set. This results in negative differences between the correlated simulation and the CFD simulation thermal resistances. When looking at the absolute difference between the equations and the simulations, the differences for the complete heat sink are on average less than half of the original correlation.

Table 4-4: Thermal resistance comparisons for heat sink, Configuration 3

Velocity [m/s]	R_{th} CFD [K/W]	R_{th} Correlation [K/W]	Difference between CFD and correlated thermal resistance [%]	Difference between extracted data and correlation [%]
0.10	6.93	6.43	-7.24	5.36
0.15	5.44	4.81	-11.72	16.02
0.20	4.68	4.11	-12.13	19.40
0.25	4.20	3.69	-12.18	19.24
0.30	3.85	3.39	-11.99	17.20
1.99	0.96	0.74	-22.72	41.61
2.98	0.79	0.65	-17.08	46.73
3.97	0.68	0.61	-10.39	33.46
4.95	0.60	0.54	-10.23	25.39
5.94	0.56	0.50	-10.21	30.42

The thermal resistances from Table 4-4 are shown in Figure 4-17. The percentage differences are shown in Figure 4-18. The temperature distribution of the CFD simulation and the correlation for a velocity of 4 m/s are shown in Figure 4-19 and Figure 4-20 respectively.

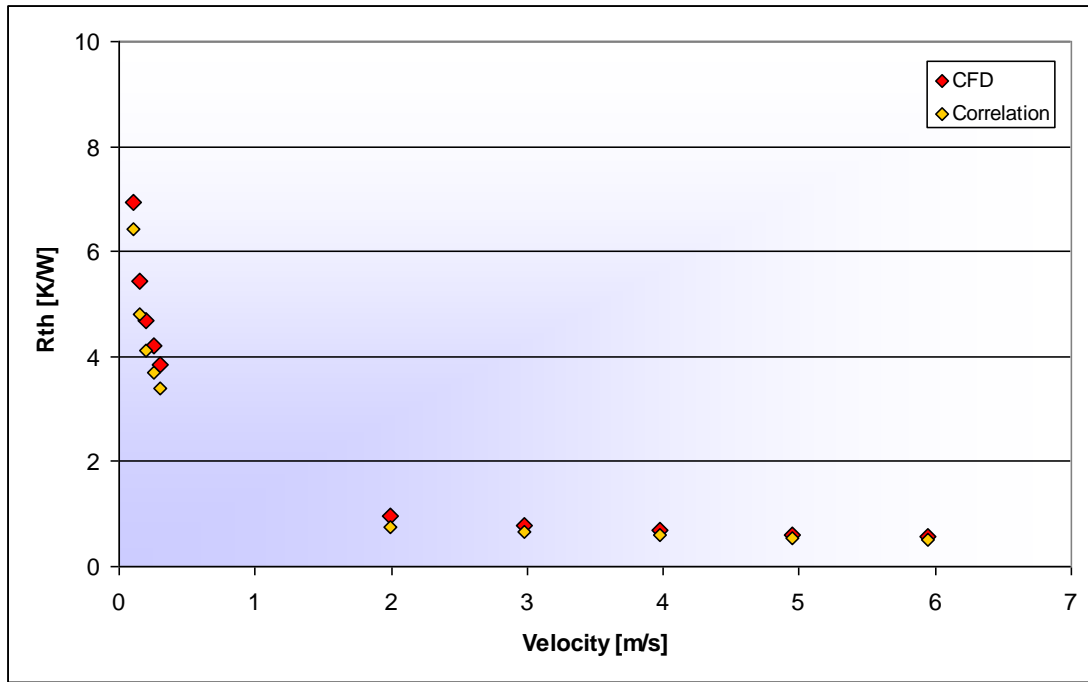


Figure 4-17: Thermal resistance as a function of velocity, Configuration 3 [K/W]

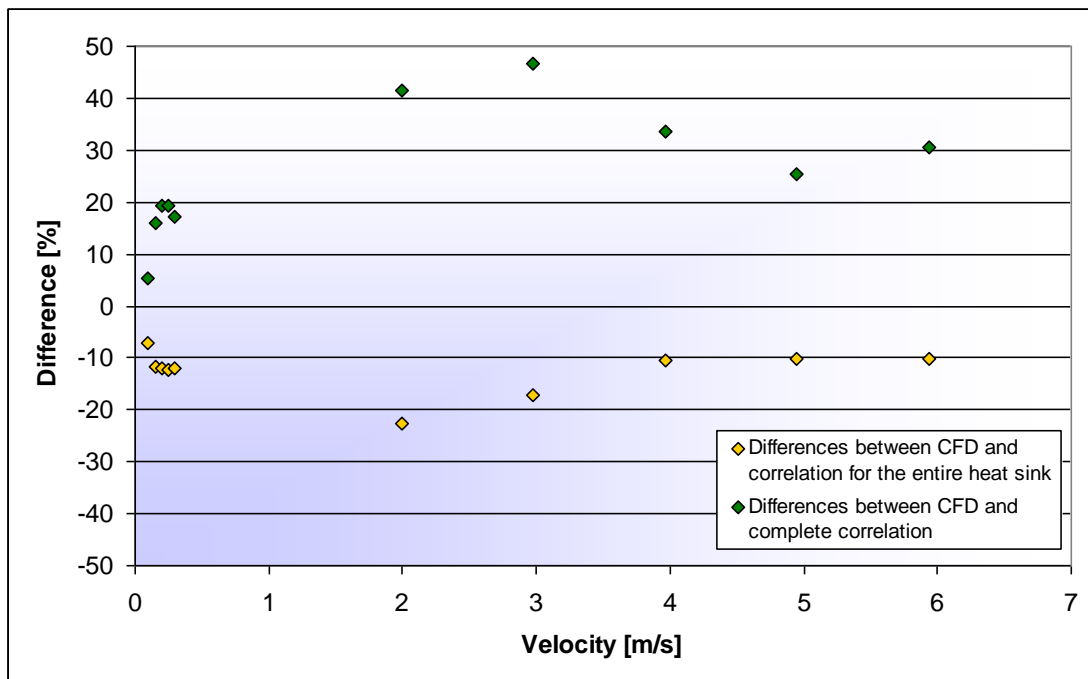


Figure 4-18: Differences in thermal resistance as a function of velocity, Configuration 3 [%]

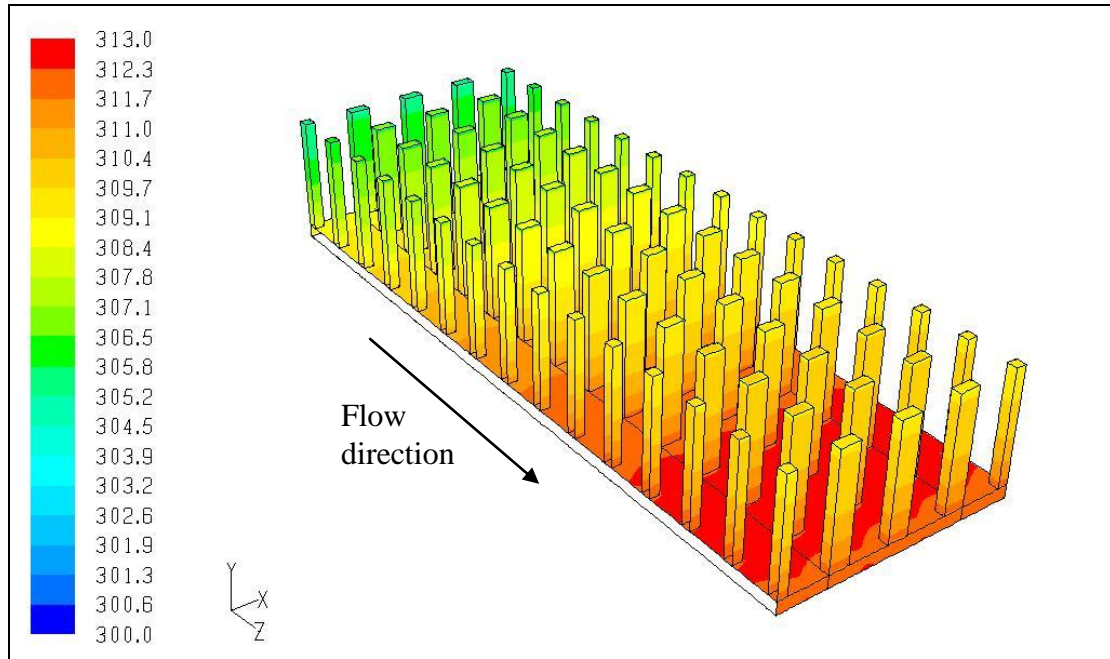


Figure 4-19: Temperature distribution for the CFD simulation (4 m/s), Configuration 3 [K]

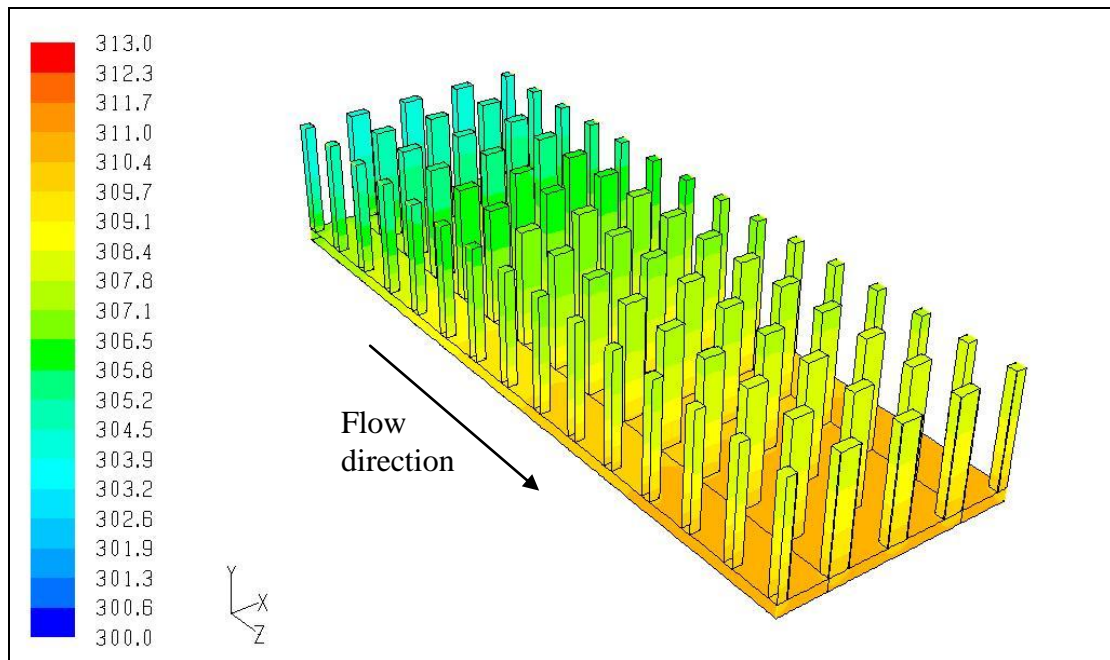


Figure 4-20: Temperature distribution for the correlated simulation (4 m/s), Configuration 3 [K]



4.4 CORRELATION COMPARED WITH LITERATURE DATA

A heat sink which is regularly used in literature [27] was chosen to compare the correlation with. Figure 4-21 displays the geometry of this heat sink. The pins on this heat sink are square and the distance between the pins is a little more than twice the pin width. This heat sink is not part of the heat sink set used to extract data from for the correlation creation. Figure 4-22 displays the thermal resistances for several Reynolds numbers for CFD simulations of the selected heat sink as well as for simulation using the correlation.

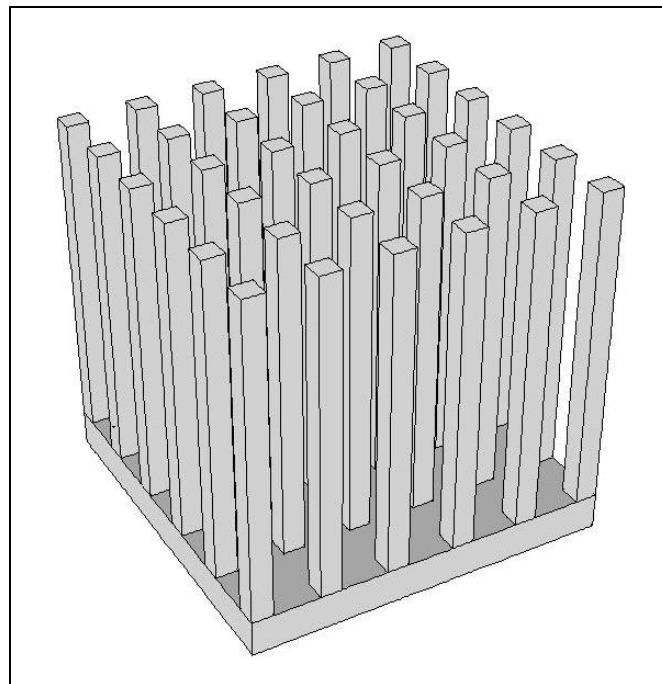


Figure 4-21: Heat sink geometry from literature [27]

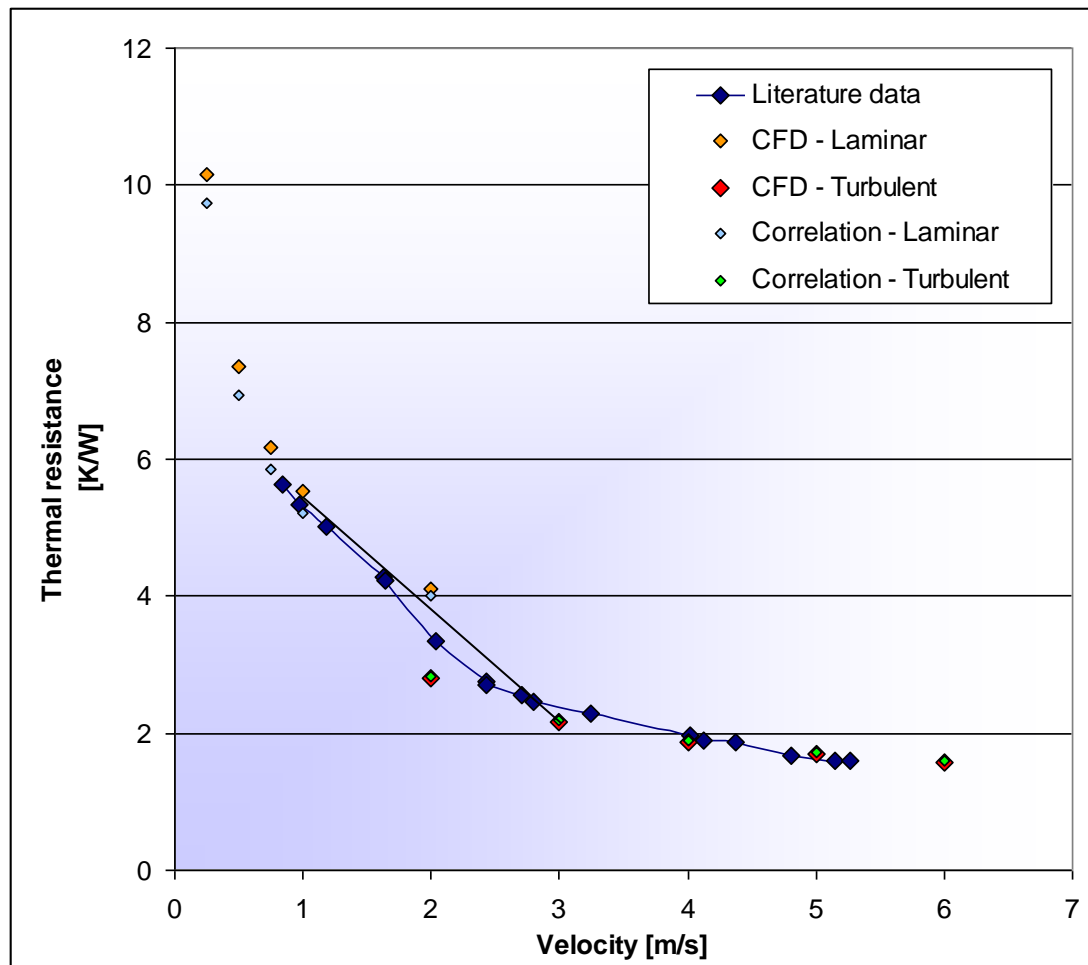
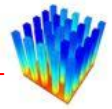


Figure 4-22: Correlation comparison with literature data

The maximum visible error of 16% is at a velocity of 2 m/s where the laminar and turbulent data meet, but the correlations are not valid in this region because these velocities fall within the transitional flow domain. The rest of the simulated thermal resistances are very close to the data from the literature graph. One can also see that when connecting the data points at 1 m/s and 3 m/s with a straight line, the correlated data are still in an acceptable error range from the literature data. This indicates that the data for the transitional flow domain can be interpolated from the laminar and turbulent equations.

This comparison shows that the equation with correlated coefficients is acceptable as a thermal analysis tool to replace complete CFD simulations.



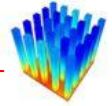
4.5 CONCLUSION

This chapter applied the correlations developed in Chapter 3 to several different test cases. Firstly, three cases were examined where the faces on which the correlation has been applied were varied. Initially, the correlation was only applied to the contraction faces used for data extraction, and secondly, the correlation was applied to all the contraction faces. In the third case, the correlation for the contraction coefficients was applied to the contraction- and expansion-sides of the heat sink. It was found that all three cases resulted in thermal resistances very close to the original CFD simulation.

Secondly, the correlation was applied to three different heat sink configurations, one representing the cases where the correlation resulted in lower heat transfer coefficients than those from the CFD data, one case very close to those from the CFD data, and the third configuration representing cases where the correlation resulted in higher heat transfer coefficients than those from the CFD simulations. In the two cases where the correlation resulted in heat transfer coefficients very different from those from the CFD, the heat sink thermal resistance differences were about half the size of the correlation differences. In the case where the correlation was close to the extracted CFD data, the thermal resistances of the correlated simulations were similar to those from the CFD simulations.

Lastly, CFD simulations making use of the correlation were compared with measured thermal resistances from heat sink configurations from literature. The simulations with the correlation compared very well with the data from literature with the exception of the transitional region where the correlation is not valid.

Overall, the cases making use of the correlation compared well with the CFD simulations and the data from literature. This indicates that the correlation can be used in heat transfer problems as a replacement for a full CFD simulation where flow around the heat sinks is solved together with the energy equation.



CHAPTER 5: CONCLUSION AND RECOMMENDATIONS

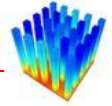
5.1 CONCLUSION

The packaging industry is continually shrinking electronic package sizes. This results in ever-growing power densities in electronic components, which need to be dissipated. The most common method for cooling the electronic components is to add a heat sink to it. This increases the surface area available for heat transfer to a cooling fluid resulting in a lower thermal resistance. These heat sinks take up space in the electronic products, which is effectively wasted when looking at the power densities. Therefore, engineers need to design the most effective, or optimised heat sink for every application.

One method for optimising these heat sink designs is to use CFD (Computational Fluid Dynamics) to simulate different cooling designs, but this is computationally very expensive. For the majority of problems, the designer solves a few heat sinks with selected properties and geometry, and picks the one with the lowest thermal resistance as the final design. The performance of the design is therefore entirely a function of the knowledge and expertise of the designer and might not even be close to the optimum design.

If the flow solver component of the CFD simulation is replaced by a flow network solver, only the temperature distribution in the heat sink design needs to be solved with a curvilinear form of the discretised diffusion equation. Heat transfer coefficients, calculated from the flow network data, are then used as boundary conditions on the heat sink surfaces.

The objective of this study was to create a correlation for the convection heat transfer coefficients for rectangular pin fin heat sinks used as a boundary condition on the heat



sink surfaces. This dissertation discussed the methodology formed for creating this correlation, summarised the correlation, and evaluated the usability of the correlation.

The methodology applied in this study, as well as all steps in creating the correlation, was discussed in Chapter 3. The methodology consisted of several steps ranging from data generation to data fitting and optimisation.

The first step was to create a parametric CFD model, which was used for data generation. This was done in Icepak, which has a built-in function to manage parameters. The CFD model was validated against a selected heat sink set. This heat sink set is seen frequently in the literature and therefore numerous experimental measurements were available. This eliminated the need for an experimental test rig. After validating the model, the parameters on which the correlation would be based had to be determined. The next step was to develop a method for automatically solving the CFD simulation for obtaining the needed data, as well extracting the relevant data from the simulations. The extracted data had to be in some form which could be easily manipulated and simple enough to obtain characteristics from. Several scripts were written to save the extracted data into delimited data sets. Each line in the data sets represented a particular heat sink configuration with all its input variables and extracted data necessary for creating the correlations.

The data were broken into four sections, first into laminar and turbulent sections, and then also into edge heat transfer coefficients and face heat transfer coefficients. A correlation was created for each of the four sections. The edge and face heat transfer coefficient correlations were then combined into a correlation for laminar and a correlation for turbulent flow respectively. This was done by evaluating combinations of regression lines while searching for trends in the data sets. After the correlations had been developed, mathematical optimisation procedures were applied to the correlations to obtain the optimum coefficients for the correlations. After optimisation, 98.6% of the 4 000 correlated heat sink configurations had a difference of less than 30% between the correlation and the CFD simulation, 93.4% had a difference of less than 20%, and 70.8% had a difference of less than 10%.



After optimising the correlations on the data set, they had to be tested in practical applications. Firstly, the thermal resistances of full CFD simulations with flow were compared with those of heat sinks where the correlations were applied to several different sets of surfaces. All three surface sets compared very well with the CFD simulation. Secondly the correlations were tested on three different heat sink configurations which represented different error categories of the correlation. One heat sink represented cases where the correlation heat transfer coefficients were lower than those from the CFD data, another heat sink represented cases where the correlated heat transfer coefficients resulted in higher values than those from the CFD data, and one heat sink where the correlation resulted in coefficients close to those from the CFD data. For all three cases, the correlation performed as expected, resulting in smaller differences in the thermal resistances than the differences between the CFD data and the correlations for all the cases where the differences between the correlation and the CFD data were in the order of 15% or more. For the cases where the correlation resulted in coefficients closer to those from the CFD data, the percentage differences between the correlated thermal resistances and the CFD thermal resistances stayed in the same order.

Finally, the correlations were tested on a heat sink from literature, which was not part of the original set used for data extraction. The simulations with the correlation compared very well with the measured data from the literature. Even in the transitional flow region, which did not form part of this study, both correlations resulted in thermal resistances that might be acceptable for rough design studies. The simulations making use of the correlations compared well with the testing heat sinks in all the assessments. This indicates that both correlations can be used with confidence in design problems as a replacement for complete CFD simulations with flow.



5.2 RECOMMENDATIONS AND FUTURE WORK

A few areas for future work, which can follow from this study, have been identified. These areas are discussed below.

5.2.1 Refining the mesh

The coarseness of the mesh on the CFD simulations used for data extraction did influence the accuracy of the correlation. It also made searching for an applicable pin width formulation extremely difficult because of the large discontinuities between consecutive bands on the pin width. With a finer mesh, the bands along the length will be thinner and the discontinuities will not have such a pertinent effect on the shape of the profile along the width of the pin. A finer mesh will also result in more accurate values for the heat transfer coefficients at the pin edges.

5.2.2 Extending the correlation to the transitional flow region

Correlations for the laminar flow region and the turbulent flow region have been developed, but there is still a gap in the transitional flow region. Electronics cooling applications do sometimes run in the transitional area, which means the gap needs to be filled. From this study, it is suggested to linearly interpolate on the Reynolds numbers between the highest laminar flow heat transfer coefficient and the lowest turbulent flow heat transfer coefficient.

Since current turbulence models have been enhanced and new transitional flow turbulence models have been developed in the past few years, a study could be conducted where a correlation is developed for the transitional flow region.

5.2.3 Including additional terms for fluids other than air

The current correlations are based on air as the cooling fluid, which might not always be the case. Although most current electronic water-cooling systems do not use pin fin heat sinks, this might change in the future. It is recommended that the effect of



cooling fluid properties on the heat transfer coefficients should be examined. Non-dimensional parameters like the Prandtl number, approximating the ratio between momentum diffusivity and thermal diffusivity, can be incorporated into the correlations.

5.2.4 Applying the correlation generation methodology to other areas

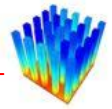
The methodology for generating the correlations worked quite well. The method of incremental regression line calculations, where the coefficient of the current regression line calculated from a specific variable is used in the next regression line calculation with another variable, worked extremely well up to three variables. This suggests that the methodology has the potential to be easily applied to numerous problems with three variables or less.

It has been shown in the study that the contraction correlations could be used on the expansion faces as well, but with a slight increase in error. A study could be done to develop a correlation for the expansion faces based on the current study.

This study limited the ratios between the different geometric parameters to values between 0.25 and four. A study could be conducted where larger ratios are evaluated, effectively bridging the gap between pin fins and extruded fin heat sinks.

Studies on different fin geometries, for example, round pins, could be performed. Round pins, for example, will only have two non-dimensional geometric parameters and the Reynolds number to account for. This means the total number of parameters is three. As previously mentioned, this should work quite well with the developed methodology. Some research can also be done on staggered pins instead of in-line pins as examined in this study.

Another option is to look at heat sinks which are not shrouded. The effects of space around the heat sinks can be included in the correlation. Also, the effect of the heat sink base on the heat transfer coefficient profile close to the base can be examined.



REFERENCES

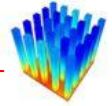
- [1] Khan WA, Culham JR, Yovanovich MM, *Performance of Shrouded Pin-Fin Heat Sinks for Electronic Cooling*, Journal of Thermophysics and Heat Transfer, Vol 20, No 3, pp. 408-414, 2006
- [2] Brucker KA, Majdalani J, 'Equivalent Thermal Conductivity for Compact Heat Sink Models Based on the Churchill and Chu Correlation', *IEEE Transactions on Components and Packaging Technologies*, Vol. 26, pp. 158-164, 2003
- [3] Shi ZF, Lu ACW, Tan YM, And KH, Tan R, Tan E, 'Heat sink design optimization for optical transponders', *International Symposium on Microelectronics*, Vol. 4931, pp. 330-335, 2002
- [4] Lee S, *How to Select a Heat Sink*, Advanced Thermal Engineering Aavid Thermal Thechnologies Inc.
- [5] Radmehr A, Kellar KM, Kelly P, Patankar SV, Kang SS, *Analysis of the Effect of Bypass on the Performance of Heat Sinks Using Flow Network Modeling (FNM)*, Fifteenth Annual IEEE Semiconductor Thermal Measurement and Management Symposium, pp. 42-47, 1999
- [6] Qfinsoft Technologies, 'Qfin 4 Basic', 2006
- [7] Kang S, Holahan M, 'The Thermal Resistance of Pin Fin Heat Sinks in Transverse Flow', *Proceedings of IPACK03*, pp. 237-244, 2003
- [8] Wirtz RA, Mathur A, 'Convective Heat Transfer Distribution on the Surface of an Electronic Package', *Journal of Electronic Packaging*, Vol. 116, pp. 49-54, 1994
- [9] Barrett AV, Obinelo IF, 'Characterization of Longitudinal Fin Heat Sink Thermal Performance and Flow Bypass Effects through CFD Methods', *Thirteenth Annual Semiconductors Thermal Measurement and Management Symposium (SEMI-THERM XIII)*, pp. 158-164, 1997
- [10] White FM, *Viscous Fluid Flow*, 2nd Edition, New York, McGraw-Hill Inc., 1991



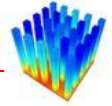
- [11] Mills AF, *Basic Heat and Mass Transfer*, 2nd Edition, New Jersey, Prentice-Hall Inc., 1999
- [12] Narasimhan S, Majdalani J, 'Characterization of Compact Heat Sink Models in Natural Convection', *IEEE Transactions on Components and Packaging Technologies*, Vol. 25, pp. 78-86, 2002
- [13] Krishnan S, 'Compact Models for Parallel Plate and Pin-Fin Heat Sinks', 2002
- [14] Kim D, Kim SJ, Ortega A, 'Compact Modeling of Fluid Flow and Heat Transfer in Pin Fin Heat Sinks', *Journal of Electronic Packaging*, Vol. 126, pp. 342-350, 2004
- [15] Department of Computing and Electronic Technology, 'The DELPHI Method',
http://www.ami.ac.uk/courses/ami4817_dti/restricted/u07/supplementary/sup_02.html, University of Bolton, 2007
- [16] Shidore S, Sahrapour A, 'DELPHI Compact Models Revolutionize Thermal Design', Flowmerics Inc., 2005
- [17] Malhammar A, 'Thermal Component Models', Part 1 to Part 4, Articles from Coolingzone online magazine, www.coolingzone.com, 2002-2003
- [18] Culham JR, Yovanovich MM, Lee S, 'Thermal Modeling of Isothermal Cuboids and Rectangular Heat Sinks Cooled by Natural Convection', *IEEE Transactions on Components, Packaging, and Manufacturing Technology*, Vol. 18, pp. 559-566, 1995
- [19] Agonafer D, Free A, 'Conjugate Model of a Pin Fin Heat Sink Using a Hybrid Conductance and CFD Model within an Integrated MCAE Tool', *Eurotherm Seminar No. 45*, 1995
- [20] Ahmed GR, Yovanovich MM, 'Analytical Method for Forced Convection from Flat Plates, Circular Cylinders and Spheres', *Journal of Thermophysics and Heat Transfer*, Vol. 9, pp. 516-523, 1995
- [21] Kahn WA, Culham JR, Yovanovich MM, 'Modeling of Cylindrical Pin-Fin Heat Sinks for Electronic Packaging', *21st IEEE Semi-therm Symposium*, 2005
- [22] Kang S, Holahan M, 'The Thermal Resistance of Pin Fin Heat Sinks in Transverse Flow', *Advances in Electronic Packaging*, Vol. 2, pp. 237-244, 2003



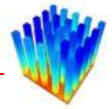
- [23] Kobus CJ, Oshio T, 'Predicting the thermal performance characteristics of staggered vertical pin fin array heat sinks under combined mode radiation and mixed convection with impingement flow', *International Journal of Heat and Mass Transfer*, Vol. 48, pp. 2684-2696, 2005
- [24] Figliola RS, Thomas PG, 'An Approximate Method for Predicting Laminar Heat Transfer Between Parallel Plates Having Embedded Heat Sources', *Journal of Electronic Packaging*, Vol. 117, pp. 63-68, 1995
- [25] Najafi M, Scott RR, 'Average Heat Transfer Coefficients for Laminar and Turbulent Flow over Partially Heated Flat Plates', *Proceedings of the 31st Intersociety Energy Conversion Engineering Conference (IECEC)*, Vol. 3, 1996
- [26] Yeh JJ, Chyu MK, 'Heat Transfer of Staggered Pin Fin Arrays', Graduate Student Conference, Carnegie Mellon University, Pittsburgh, PA., 1998
- [27] Dogruoz MB, Urdaneta M, Ortega A, 'Experiments and Modelling of the Heat Transfer of In-line Square Pin Fin Heat Sinks with Top Bypass Flow', *ASME International Mechanical Engineering Congress & Exposition (IMECE)*, 2002
- [28] Zapach T, Newhouse T, Taylor J, Thomasing P, 'Experimental Verification of a Model for the Optimization of Pin Fin Heatsinks', *Intersociety Conference on Thermal Phenomena*, pp. 63-69, 2000
- [29] Ahmed GR, Yovanovich MM, 'Experimental Study of Forced Convection from Isothermal Circular and Square Cylinders and Toroids', *Journal of Heat Transfer*, Vol. 119, pp. 70-79, 1997
- [30] Chapman CL, Lee, S, Schmidt BL, 'Thermal Performance of an Elliptical Pin Fin Heat Sink', *Tenth IEEE Semi-Therm Symposium*, 1994
- [31] Maudgal VK, Sunderland JE, 'An Experimental Study of Forced Convection Heat Transfer from In-line Pin Fin Arrays', *Thirteenth IEEE Semi-Therm Symposium*, pp. 149-157, 1997
- [32] Ryu HC, Kim D, Kim SJ, 'Experimental Analysis of Shrouded Pin Fin Heat Sinks for Electronic Equipment Cooling', *Inter Society Conference on Thermal Phenomena*, pp. 261-266, 2002
- [33] Shaukatullah H, Storr WR, Hansen BJ, Gaynes MA, 'Design and Optimization of Pin Fin Heat Sinks for Low Velocity Applications', *IEEE*



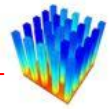
- Transactions on Components, Packaging, and Manufacturing Technology*, Vol. 19, pp. 486-494, 1996
- [34] Rizzi M, Catton I, ‘An Experimental Study of Pin Fin Heat Sinks and Determination of End Wall Heat Transfer’, *Proceedings of the ASME Summer Heat Transfer Conference*, pp. 445-452, 2003
- [35] Reddy AV, Hammoud JY, ‘Experimental and Numerical Simulation Study of Heat Sinks with Impingement Flow at High Reynolds Numbers’, *Nineteenth Annual IEEE Semiconductor Thermal Measurement and Management Symposium*, pp. 176- 178, 2003
- [36] Zheng N, Wirtz RA, ‘Cylindrical Pin-Fin Fan-Sink Heat Transfer and Pressure Drop Correlations’, *IEEE Transactions on Components and Packaging Technologies*, Vol. 25, pp. 15-22, 2002
- [37] Jung HH, Maveety JG, ‘Pin-Fin Heat Sink Modeling and Characterization’, *Sixteenth IEEE Semi-Therm Symposium*, pp. 260-265, 2000
- [38] Kobus CJ, Oshio T, ‘Development of a Theoretical model for Predicting the Thermal Performance Characteristics of a Vertical Pin-Fin Array Heat Sink under Combined Forced and Natural Convection with Impinging Flow’, *International Journal of Heat and Mass Transfer*, Vol. 48, pp. 1053-1063, 2005
- [39] Shah A, Sammakia B, Srihari H, Ramakrishna K, ‘A Numerical study of the thermal performance of an impingement heat sink – fin shape optimization’, *IEEE Transactions on Components and Packaging Technologies*, Vol. 27, pp. 710-717, 2004
- [40] Loh CK, Nelson D, Chou, DJ, ‘Optimization of Heat Sink Design and Fan Selection in Portable Electronics Environment’, Technical Report, Enertron Inc., 2004
- [41] Arik M, Nagulapally M, Brzozowski S, Glaser J, ‘Thermal design and optimization of harsh environment power electronics in natural convection heat transfer’, *Proceedings of ASME Summer Heat Transfer Conference*, 2003
- [42] Lee S, ‘Optimum design and selection of heat sinks’, *IEEE Transactions on Components, Packaging, and Manufacturing Technology*, Vol. 18, pp. 812-817, 1995



- [43] Biber CR, Fijol S, ‘Fan-Plus-Heatsink “Optimization” – Mechanical and Thermal Design with Reality’, *Proceedings of the International Systems Packaging Symposium*, pp. 285-289, 1999
- [44] Qfinsoft Technologies, ‘Qfin 4 : Training notes’, 2007
- [45] Snyman JA, *Practical Mathematical Optimization: An Introduction to Basic Optimization Theory and Classic and New Gradient-based Algorithms*, Springer, 2005
- [46] Fluent Inc., *Icepak*, Version 3.1, Centerra Resource Park, 10 Cavendish Court, Lebanon, New Hampshire, USA, 2001 (www.icepak.com)
- [47] White FM, *Fluid Mechanics*, 4th Edition, McGraw-Hill International Editions, New York, 1999
- [48] Spalart P, Allmaras S, *A One-Equation Turbulence Model for Aerodynamic Flows*, Technical Report AIAA, Vol. 92, 1992
- [49] Launder BE, Spalding DB, *Lectures in Mathematical Models of Turbulence*, Academic Press, 1972
- [50] Orszag SA, Yakhot V, Flannery WS, Boysan F, Choudhury D, Maruzewski J, Patel B, *Renormalization Group Modeling and Turbulence Simulations*, International Conference on Near-Wall Turbulent Flows, 1993
- [51] Shih TH, Liou WW, Yang Z, Zhu J, *A New $k-\epsilon$ Eddy-Viscosity Model for High Reynolds Number Turbulent Flows – Model Development and Validation*, *Computer Fluids*, Vol. 24, pp. 227-238, 1995
- [52] Wilcox DC, *Turbulence Modeling for CFD*, DCW Industries Inc., 1998
- [53] Menter FR, *Two-Equation Eddy-Viscosity Turbulence Models for Engineering Applications*, *AIAA Journal*, Vol. 32, pp. 1598-1605, 1994
- [54] Launder BE, Reece GJ, Rodi W, *Progress in the Development of a Reynolds-Stress Turbulence Closure*, *Journal of Fluid Mechanics*, Vol. 68, pp. 537-566, 1975
- [55] Fluent Inc., *Fluent Version 6 Manuals*, Centerra Resource Park, 10 Cavendish Court, Lebanon, New Hampshire, USA, 2001 (www.fluent.com)
- [56] The Mathworks Inc., *Matlab Help Files*, Version 7, 2004 (www.mathworks.com)
- [57] MDOG, *Toolkit for Design Optimisation*, Version 1.2d, 2002
- [58] The Mathworks Inc., *The Optimization Toolbox 2.0 for use with Matlab*, 24 Prime Park Way, Natick, Massachusetts, 1999 (www.mathworks.com)



- [59] Lei N, Ortega A, 'Experimental Thermal Characterization of Pin Fin Heat Sinks with Top and Side Bypass', *Proceedings of IPACK2005*, 2005
- [60] The Scilab Consortium, Scilab, Version 3.1.1, 2005
- [61] Stewart J, *Calculus: Early Transcendentals*, 4th Edition, Brooks/Cole Publishing Company, California 1999
- [62] Olivier JA, Meyer JP, Liebenberg L, 'Single-phase heat transfer and pressure drop of the cooling water inside smooth tubes for transitional flow with different inlet geometries' *HVAC&R Research*, Vol. 16, No. 4, Accepted for publication, 2010
- [63] Meyer JP, Liebenberg L, Olivier JA, 'Transitional adiabatic pressure drop inside enhanced tubes for fully developed and developing flow with different types of inlet disturbances', *International Journal of Heat and Mass Transfer*, Submitted for review in 2010
- [64] Meyer JP, Liebenberg L, Olivier JA, 'Transitional heat transfer and pressure drop inside enhanced tubes with the cooling of water for various inlet disturbances', *International Journal of Heat and Mass Transfer*, Submitted for review in 2010



APPENDIX A

Script file to create a journal file to solve the case files in the current directory

```
// Create Journal to solve and output data for existing pin fin case files in current
// directory based on selected parameters
// Stephan Schmitt
// 11/07/2005

filelist = dir('*.dat.gz');
filelist = filelist(2);

By = 0.0025;
Fy = 0.025;
Cz = 0.4;
Nz = 15;
Nx = 5;
//Vz = [2 3 4 5 6];

[fid,err] = mopen('total_journal.jou','w');

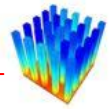
for k = 1 : size(filelist,1),
    k
    filelist2 = ls(strsubst(filelist(k),'.dat.gz','.tra'));
    if filelist2 == [],
        filelist2 = filelist2(2);

        Lfin_index = strindex(filelist(k),'Lfin_');
        Lgap_index = strindex(filelist(k),'Lgap_');
        // Cz_index = strindex(filelist(k),'Cz_');
        Wfin_index = strindex(filelist(k),'Wfin_');
        Wgap_index = strindex(filelist(k),'Wgap_');
        // Nx_index = strindex(filelist(k),'Nx_');
        Vz_index = strindex(filelist(k),'Vz_');
        // Fy_index = strindex(filelist(k),'Fy_');
        // By_index = strindex(filelist(k),'By_');
        dot_index = strindex(filelist(k),'.');
        rke_index = strindex(filelist(k),'rke');
        Wfin = evstr(strsubst(part(filelist(k),(Wfin_index+5):(Wgap_index-2)),'_','.'));
        // Nx = evstr(strsubst(part(filelist(k),(Nx_index+3):(Wgap_index-2)),'_','.'));
        // Fy = evstr(strsubst(part(filelist(k),(Fy_index+3):(By_index-2)),'_','.'));
        Wgap = evstr(strsubst(part(filelist(k),(Wgap_index+5):(Vz_index-2)),'_','.'));
        Lfin = evstr(strsubst(part(filelist(k),(Lfin_index+5):(Lgap_index-2)),'_','.'));
        Lgap = evstr(strsubst(part(filelist(k),(Lgap_index+5):(Wfin_index-2)),'_','.'));
        Vz = evstr(strsubst(part(filelist(k),(Vz_index+3):(rke_index-1)),'_','.'));
        // Nz = Nx

        Bz = (Nz-1)*Lgap+Nz*Lfin;
        Bx = (Nx-1)*Wgap+(Nx-1)*Wfin;
        // 5/Bx/Bz
        casname = part(filelist(k),1:(Vz_index-2))+'.cas.gz'
//start journal creation

    fprintf(fid,'/file/read-case\n');
    fprintf(fid,casname+'\n');
    fprintf(fid,'yes\n');

    // create faces
    // y-clip
    fprintf(fid,'/surface/isoclip\n');
    fprintf(fid,'y-coordinate\n');
    fprintf(fid,'hs_yclip\n');
    fprintf(fid,'heatsink_1-side1-1\n'); //heatsink_1-side2-1
    fprintf(fid,string(By+0.002)+'\n');
    fprintf(fid,string(By+Fy-0.002)+'\n');
    // z-clips
    for i = 1 : Nz,
        fprintf(fid,'/surface/isoclip\n');
```



```

fprintf(fid,'z-coordinate\n');
fprintf(fid,'hs_zclip_'+string(i)+'\n');
fprintf(fid,'hs_yclip\n');
fprintf(fid,string(-Bz/2-0.0001+(i-1)*(Lfin+Lgap))+'\n');
fprintf(fid,string(-Bz/2+0.0001+(i-1)*(Lfin+Lgap))+'\n');
// x-clips

fprintf(fid,'/surface/isoclip\n');
fprintf(fid,'x-coordinate\n');
fprintf(fid,'hs_xclip_'+string(i)+'_l1\n');
fprintf(fid,'hs_zclip_'+string(i)+'\n');
fprintf(fid,string(-Bx/2-0.000001+Wfin/2))+'\n');
fprintf(fid,string(-Bx/2-Wfin/10+Wfin/2))+'\n');

for j = 2 : Nx-1,
fprintf(fid,'/surface/isoclip\n');
fprintf(fid,'x-coordinate\n');
fprintf(fid,'hs_xclip_'+string(i)+'_'+string(j)+'r\n');
fprintf(fid,'hs_zclip_'+string(i)+'\n');
fprintf(fid,string(-Bx/2+0.000001+(j-1)*(Wgap)+(j-1.5)*(Wfin))+'\n');
fprintf(fid,string(-Bx/2+Wfin/10+(j-1)*(Wgap)+(j-1.5)*(Wfin))+'\n');
fprintf(fid,'/surface/isoclip\n');
fprintf(fid,'x-coordinate\n');
fprintf(fid,'hs_xclip_'+string(i)+'_'+string(j)+'l1\n');
fprintf(fid,'hs_zclip_'+string(i)+'\n');
fprintf(fid,string(-Bx/2-0.000001+(j-1)*(Wgap)+(j-0.5)*(Wfin))+'\n');
fprintf(fid,string(-Bx/2-Wfin/10+(j-1)*(Wgap)+(j-0.5)*(Wfin))+'\n');
end

fprintf(fid,'/surface/isoclip\n');
fprintf(fid,'x-coordinate\n');
fprintf(fid,'hs_xclip_'+string(i)+'_'+string(Nx)+'r\n');
fprintf(fid,'hs_zclip_'+string(i)+'\n');
fprintf(fid,string(Bx/2+0.000001-Wfin/2))+'\n');
fprintf(fid,string(Bx/2+Wfin/10-Wfin/2))+'\n');

end
//

//residuals edit

fprintf(fid,'/solve/monitors/residual/convergence-criteria\n');
fprintf(fid,'0.001\n');
fprintf(fid,'0.001\n');
fprintf(fid,'0.001\n');
fprintf(fid,'0.001\n');
fprintf(fid,'3e-8\n');

//turbulence model

fprintf(fid,'/define/models/viscous/ke-realizable\n');
fprintf(fid,'yes\n');
fprintf(fid,'/define/models/viscous/near-wall-treatment/enhanced-wall-
treatment\n');
fprintf(fid,'yes\n');

//2nd order

fprintf(fid,'/solve/set/discretization-scheme/epsilon\n');
fprintf(fid,'1\n');
fprintf(fid,'/solve/set/discretization-scheme/k\n');
fprintf(fid,'1\n');
fprintf(fid,'/solve/set/discretization-scheme/mom\n');
fprintf(fid,'1\n');
fprintf(fid,'/solve/set/discretization-scheme/temperature\n');
fprintf(fid,'1\n');
fprintf(fid,'/solve/set/discretization-scheme/pressure\n');
fprintf(fid,'10\n');

// velocity loop
for cnt = 1 : length(Vz),

fprintf(fid,'/define/boundary-conditions/velocity-inlet\n');
fprintf(fid,'fan_1-side1\n');
fprintf(fid,'yes\n');//magnitude direction

```



```

fprintf(fid,'yes\n');//absolute
fprintf(fid,'no\n');//profile
fprintf(fid,string(Vz(cnt))+'\n');//velocity magnitude
fprintf(fid,'yes\n');//cartesian coordinate system
fprintf(fid,'no\n');//use profile x
fprintf(fid,'0\n');//component x
fprintf(fid,'no\n');//use profile y
fprintf(fid,'0\n');//component y
fprintf(fid,'no\n');//use profile z
fprintf(fid,'1\n');//component z
fprintf(fid,'no\n');//use profile temperature
fprintf(fid,'293.15\n');//temperature
fprintf(fid,'no\n');//turbulence method: k+e
fprintf(fid,'no\n');//turbulence method: int+length
fprintf(fid,'no\n');//turbulence method: int+visc
fprintf(fid,'yes\n');//turbulence method: int+diam
fprintf(fid,'5\n');//intensity

fprintf(fid,string(8*(Wfin+Wgap)*(Fy+By)/(Fy+By+4*Wfin+4*Wgap))+'\n');//intensity

fprintf(fid,'/define/boundary-conditions/wall\n');
fprintf(fid,'source_1-side1\n');//name
fprintf(fid,'\n');//wall thickness
fprintf(fid,'\n');//use profile heat generation rate
fprintf(fid,'\n');//heat generation rate
fprintf(fid,'\n');//material
fprintf(fid,'\n');//thermal bc type
fprintf(fid,'\n');//use profile heat flux
fprintf(fid,string(Vz(cnt)*10/Bx/Bz)+'\n');//heat flux
fprintf(fid,'\n');//shell conduction
fprintf(fid,'\n');//wall motion
fprintf(fid,'\n');//shear boundary condition

//      fprintf(fid,'/solve/initialize/compute-defaults\n');
//      fprintf(fid,'all-zones\n');
//      fprintf(fid,'/solve/initialize/initialize-flow\n');

////////////////////////////////////

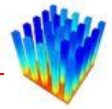
fprintf(fid,'/file/read-data\n');//read data file
fprintf(fid,filelist(k)+'\n');//data file name
fprintf(fid,'yes\n');//in case of something

fprintf(fid,'q\n');
fprintf(fid,'q\n');
fprintf(fid,'it\n');
fprintf(fid,'500\n');

fprintf(fid,'/file/start-transcript\n');

fprintf(fid, strsubst(casname, '.cas.gz', '_Vz_' + strsubst(string(Vz(cnt)), '.', '_') + '.tra\
n'));
fprintf(fid,'it\n');
fprintf(fid,'1\n');
// print temperature and heat flux data
// heat fluxes
fprintf(fid,'/report/surface-avg\n');
for i = 1 : Nz,
    fprintf(fid,'hs_xclip_'+string(i)+'_'+string(1)+'l\n');
    for j = 2 : Nx-1,
        fprintf(fid,'hs_xclip_'+string(i)+'_'+string(j)+'r\n');
        fprintf(fid,'hs_xclip_'+string(i)+'_'+string(j)+'l\n');
    end
    fprintf(fid,'hs_xclip_'+string(i)+'_'+string(Nx)+'r\n');
end
fprintf(fid,'()\n');
fprintf(fid,'heat-flux\n');
// temperatures
fprintf(fid,'/report/surface-avg\n');
for i = 1 : Nz,
    fprintf(fid,'hs_xclip_'+string(i)+'_'+string(1)+'l\n');
    for j = 2 : Nx-1,
        fprintf(fid,'hs_xclip_'+string(i)+'_'+string(j)+'r\n');

```



```

        fprintf(fid,'hs_xclip_'+string(i)+'_'+string(j)+'\n');
    end
    fprintf(fid,'hs_xclip_'+string(i)+'_'+string(Nx)+'r\n');
end
fprintf(fid,'opening_1-side1\n');
fprintf(fid,'()\n');
fprintf(fid,'temperature\n');
fprintf(fid,'/file/stop-transcript\n');
//

fprintf(fid,'/file/write-data\n');

fprintf(fid,'fluent/'+strsubst(casname, '.cas.gz', '_Vz_'+strsubst(string(Vz(cnt)), '.', '_')+'rke_ewt-fluent.dat.gz\n'));

////////////////////////////////////

    end
// end velocity loop
    end
end
fclose(fid);

```

Journal file created by the above script for one case file.

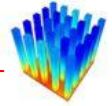
```

/file/read-case
tr_Lfin_0_004_Lgap_0_006_Wfin_0_008_Wgap_0_002.cas.gz
yes
/surface/isoclip
y-coordinate
hs_yclip
heatsink_1-side1-1
0.0045
0.0255
/surface/isoclip
z-coordinate
hs_zclip_1
hs_yclip
-0.0721
-0.0719
/surface/isoclip
x-coordinate
hs_xclip_1_1l
hs_zclip_1
-0.016001
-0.0168
/surface/isoclip
x-coordinate
hs_xclip_1_2r
hs_zclip_1
-0.013999
-0.0132
/surface/isoclip
x-coordinate
hs_xclip_1_2l
hs_zclip_1
-0.006001
-0.0068
/surface/isoclip
x-coordinate
hs_xclip_1_3r
hs_zclip_1
-0.003999
-0.0032
/surface/isoclip
x-coordinate
hs_xclip_1_3l
hs_zclip_1
0.003999

```



```
0.0032
/surface/isoclip
x-coordinate
hs_xclip_1_4r
hs_zclip_1
0.006001
0.0068
/surface/isoclip
x-coordinate
hs_xclip_1_4l
hs_zclip_1
0.013999
0.0132
/surface/isoclip
x-coordinate
hs_xclip_1_5r
hs_zclip_1
0.016001
0.0168
/surface/isoclip
z-coordinate
hs_zclip_2
hs_yclip
-0.0621
-0.0619
/surface/isoclip
x-coordinate
hs_xclip_2_1l
hs_zclip_2
-0.016001
-0.0168
/surface/isoclip
x-coordinate
hs_xclip_2_2r
hs_zclip_2
-0.013999
-0.0132
/surface/isoclip
x-coordinate
hs_xclip_2_2l
hs_zclip_2
-0.006001
-0.0068
/surface/isoclip
x-coordinate
hs_xclip_2_3r
hs_zclip_2
-0.003999
-0.0032
/surface/isoclip
x-coordinate
hs_xclip_2_3l
hs_zclip_2
0.003999
0.0032
/surface/isoclip
x-coordinate
hs_xclip_2_4r
hs_zclip_2
0.006001
0.0068
/surface/isoclip
x-coordinate
hs_xclip_2_4l
hs_zclip_2
0.013999
0.0132
/surface/isoclip
x-coordinate
hs_xclip_2_5r
hs_zclip_2
0.016001
0.0168
/surface/isoclip
z-coordinate
hs_zclip_3
hs_yclip
```



```
-0.0521
-0.0519
/surface/isoclip
x-coordinate
hs_xclip_3_1l
hs_zclip_3
-0.016001
-0.0168
/surface/isoclip
x-coordinate
hs_xclip_3_2r
hs_zclip_3
-0.013999
-0.0132
/surface/isoclip
x-coordinate
hs_xclip_3_2l
hs_zclip_3
-0.006001
-0.0068
/surface/isoclip
x-coordinate
hs_xclip_3_3r
hs_zclip_3
-0.003999
-0.0032
/surface/isoclip
x-coordinate
hs_xclip_3_3l
hs_zclip_3
0.003999
0.0032
/surface/isoclip
x-coordinate
hs_xclip_3_4r
hs_zclip_3
0.006001
0.0068
/surface/isoclip
x-coordinate
hs_xclip_3_4l
hs_zclip_3
0.013999
0.0132
/surface/isoclip
x-coordinate
hs_xclip_3_5r
hs_zclip_3
0.016001
0.0168
/surface/isoclip
z-coordinate
hs_zclip_4
hs_yclip
-0.0421
-0.0419
/surface/isoclip
x-coordinate
hs_xclip_4_1l
hs_zclip_4
-0.016001
-0.0168
/surface/isoclip
x-coordinate
hs_xclip_4_2r
hs_zclip_4
-0.013999
-0.0132
/surface/isoclip
x-coordinate
hs_xclip_4_2l
hs_zclip_4
-0.006001
-0.0068
/surface/isoclip
x-coordinate
hs_xclip_4_3r
```



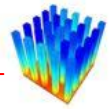
```
hs_zclip_4
-0.003999
-0.0032
/surface/isoclip
x-coordinate
hs_xclip_4_3l
hs_zclip_4
0.003999
0.0032
/surface/isoclip
x-coordinate
hs_xclip_4_4r
hs_zclip_4
0.006001
0.0068
/surface/isoclip
x-coordinate
hs_xclip_4_4l
hs_zclip_4
0.013999
0.0132
/surface/isoclip
x-coordinate
hs_xclip_4_5r
hs_zclip_4
0.016001
0.0168
/surface/isoclip
z-coordinate
hs_zclip_5
hs_yclip
-0.0321
-0.0319
/surface/isoclip
x-coordinate
hs_xclip_5_1l
hs_zclip_5
-0.016001
-0.0168
/surface/isoclip
x-coordinate
hs_xclip_5_2r
hs_zclip_5
-0.013999
-0.0132
/surface/isoclip
x-coordinate
hs_xclip_5_2l
hs_zclip_5
-0.006001
-0.0068
/surface/isoclip
x-coordinate
hs_xclip_5_3r
hs_zclip_5
-0.003999
-0.0032
/surface/isoclip
x-coordinate
hs_xclip_5_3l
hs_zclip_5
0.003999
0.0032
/surface/isoclip
x-coordinate
hs_xclip_5_4r
hs_zclip_5
0.006001
0.0068
/surface/isoclip
x-coordinate
hs_xclip_5_4l
hs_zclip_5
0.013999
0.0132
/surface/isoclip
x-coordinate
```




```
hs_xclip_5_5r
hs_zclip_5
0.016001
0.0168
/surface/isoclip
z-coordinate
hs_zclip_6
hs_yclip
-0.0221
-0.0219
/surface/isoclip
x-coordinate
hs_xclip_6_1l
hs_zclip_6
-0.016001
-0.0168
/surface/isoclip
x-coordinate
hs_xclip_6_2r
hs_zclip_6
-0.013999
-0.0132
/surface/isoclip
x-coordinate
hs_xclip_6_2l
hs_zclip_6
-0.006001
-0.0068
/surface/isoclip
x-coordinate
hs_xclip_6_3r
hs_zclip_6
-0.003999
-0.0032
/surface/isoclip
x-coordinate
hs_xclip_6_3l
hs_zclip_6
0.003999
0.0032
/surface/isoclip
x-coordinate
hs_xclip_6_4r
hs_zclip_6
0.006001
0.0068
/surface/isoclip
x-coordinate
hs_xclip_6_4l
hs_zclip_6
0.013999
0.0132
/surface/isoclip
x-coordinate
hs_xclip_6_5r
hs_zclip_6
0.016001
0.0168
/surface/isoclip
z-coordinate
hs_zclip_7
hs_yclip
-0.0121
-0.0119
/surface/isoclip
x-coordinate
hs_xclip_7_1l
hs_zclip_7
-0.016001
-0.0168
/surface/isoclip
x-coordinate
hs_xclip_7_2r
hs_zclip_7
-0.013999
-0.0132
/surface/isoclip
```



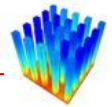
```
x-coordinate
hs_xclip_7_2l
hs_zclip_7
-0.006001
-0.0068
/surface/isoclip
x-coordinate
hs_xclip_7_3r
hs_zclip_7
-0.003999
-0.0032
/surface/isoclip
x-coordinate
hs_xclip_7_3l
hs_zclip_7
0.003999
0.0032
/surface/isoclip
x-coordinate
hs_xclip_7_4r
hs_zclip_7
0.006001
0.0068
/surface/isoclip
x-coordinate
hs_xclip_7_4l
hs_zclip_7
0.013999
0.0132
/surface/isoclip
x-coordinate
hs_xclip_7_5r
hs_zclip_7
0.016001
0.0168
/surface/isoclip
z-coordinate
hs_zclip_8
hs_yclip
-0.0021
-0.0019
/surface/isoclip
x-coordinate
hs_xclip_8_1l
hs_zclip_8
-0.016001
-0.0168
/surface/isoclip
x-coordinate
hs_xclip_8_2r
hs_zclip_8
-0.013999
-0.0132
/surface/isoclip
x-coordinate
hs_xclip_8_2l
hs_zclip_8
-0.006001
-0.0068
/surface/isoclip
x-coordinate
hs_xclip_8_3r
hs_zclip_8
-0.003999
-0.0032
/surface/isoclip
x-coordinate
hs_xclip_8_3l
hs_zclip_8
0.003999
0.0032
/surface/isoclip
x-coordinate
hs_xclip_8_4r
hs_zclip_8
0.006001
0.0068
```



```
/surface/isoclip
x-coordinate
hs_xclip_8_4l
hs_zclip_8
0.013999
0.0132
/surface/isoclip
x-coordinate
hs_xclip_8_5r
hs_zclip_8
0.016001
0.0168
/surface/isoclip
z-coordinate
hs_zclip_9
hs_yclip
0.0079
0.0081
/surface/isoclip
x-coordinate
hs_xclip_9_1l
hs_zclip_9
-0.016001
-0.0168
/surface/isoclip
x-coordinate
hs_xclip_9_2r
hs_zclip_9
-0.013999
-0.0132
/surface/isoclip
x-coordinate
hs_xclip_9_2l
hs_zclip_9
-0.006001
-0.0068
/surface/isoclip
x-coordinate
hs_xclip_9_3r
hs_zclip_9
-0.003999
-0.0032
/surface/isoclip
x-coordinate
hs_xclip_9_3l
hs_zclip_9
0.003999
0.0032
/surface/isoclip
x-coordinate
hs_xclip_9_4r
hs_zclip_9
0.006001
0.0068
/surface/isoclip
x-coordinate
hs_xclip_9_4l
hs_zclip_9
0.013999
0.0132
/surface/isoclip
x-coordinate
hs_xclip_9_5r
hs_zclip_9
0.016001
0.0168
/surface/isoclip
z-coordinate
hs_zclip_10
hs_yclip
0.0179
0.0181
/surface/isoclip
x-coordinate
hs_xclip_10_1l
hs_zclip_10
-0.016001
```



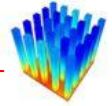
```
-0.0168
/surface/isoclip
x-coordinate
hs_xclip_10_2r
hs_zclip_10
-0.013999
-0.0132
/surface/isoclip
x-coordinate
hs_xclip_10_2l
hs_zclip_10
-0.006001
-0.0068
/surface/isoclip
x-coordinate
hs_xclip_10_3r
hs_zclip_10
-0.003999
-0.0032
/surface/isoclip
x-coordinate
hs_xclip_10_3l
hs_zclip_10
0.003999
0.0032
/surface/isoclip
x-coordinate
hs_xclip_10_4r
hs_zclip_10
0.006001
0.0068
/surface/isoclip
x-coordinate
hs_xclip_10_4l
hs_zclip_10
0.013999
0.0132
/surface/isoclip
x-coordinate
hs_xclip_10_5r
hs_zclip_10
0.016001
0.0168
/surface/isoclip
z-coordinate
hs_zclip_11
hs_yclip
0.0279
0.0281
/surface/isoclip
x-coordinate
hs_xclip_11_1l
hs_zclip_11
-0.016001
-0.0168
/surface/isoclip
x-coordinate
hs_xclip_11_2r
hs_zclip_11
-0.013999
-0.0132
/surface/isoclip
x-coordinate
hs_xclip_11_2l
hs_zclip_11
-0.006001
-0.0068
/surface/isoclip
x-coordinate
hs_xclip_11_3r
hs_zclip_11
-0.003999
-0.0032
/surface/isoclip
x-coordinate
hs_xclip_11_3l
hs_zclip_11
```



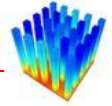
```
0.003999
0.0032
/surface/isoclip
x-coordinate
hs_xclip_11_4r
hs_zclip_11
0.006001
0.0068
/surface/isoclip
x-coordinate
hs_xclip_11_4l
hs_zclip_11
0.013999
0.0132
/surface/isoclip
x-coordinate
hs_xclip_11_5r
hs_zclip_11
0.016001
0.0168
/surface/isoclip
z-coordinate
hs_zclip_12
hs_yclip
0.0379
0.0381
/surface/isoclip
x-coordinate
hs_xclip_12_1l
hs_zclip_12
-0.016001
-0.0168
/surface/isoclip
x-coordinate
hs_xclip_12_2r
hs_zclip_12
-0.013999
-0.0132
/surface/isoclip
x-coordinate
hs_xclip_12_2l
hs_zclip_12
-0.006001
-0.0068
/surface/isoclip
x-coordinate
hs_xclip_12_3r
hs_zclip_12
-0.003999
-0.0032
/surface/isoclip
x-coordinate
hs_xclip_12_3l
hs_zclip_12
0.003999
0.0032
/surface/isoclip
x-coordinate
hs_xclip_12_4r
hs_zclip_12
0.006001
0.0068
/surface/isoclip
x-coordinate
hs_xclip_12_4l
hs_zclip_12
0.013999
0.0132
/surface/isoclip
x-coordinate
hs_xclip_12_5r
hs_zclip_12
0.016001
0.0168
/surface/isoclip
z-coordinate
hs_zclip_13
```



```
hs_yclip
0.0479
0.0481
/surface/isoclip
x-coordinate
hs_xclip_13_1l
hs_zclip_13
-0.016001
-0.0168
/surface/isoclip
x-coordinate
hs_xclip_13_2r
hs_zclip_13
-0.013999
-0.0132
/surface/isoclip
x-coordinate
hs_xclip_13_2l
hs_zclip_13
-0.006001
-0.0068
/surface/isoclip
x-coordinate
hs_xclip_13_3r
hs_zclip_13
-0.003999
-0.0032
/surface/isoclip
x-coordinate
hs_xclip_13_3l
hs_zclip_13
0.003999
0.0032
/surface/isoclip
x-coordinate
hs_xclip_13_4r
hs_zclip_13
0.006001
0.0068
/surface/isoclip
x-coordinate
hs_xclip_13_4l
hs_zclip_13
0.013999
0.0132
/surface/isoclip
x-coordinate
hs_xclip_13_5r
hs_zclip_13
0.016001
0.0168
/surface/isoclip
z-coordinate
hs_zclip_14
hs_yclip
0.0579
0.0581
/surface/isoclip
x-coordinate
hs_xclip_14_1l
hs_zclip_14
-0.016001
-0.0168
/surface/isoclip
x-coordinate
hs_xclip_14_2r
hs_zclip_14
-0.013999
-0.0132
/surface/isoclip
x-coordinate
hs_xclip_14_2l
hs_zclip_14
-0.006001
-0.0068
/surface/isoclip
x-coordinate
```



```
hs_xclip_14_3r
hs_zclip_14
-0.003999
-0.0032
/surface/isoclip
x-coordinate
hs_xclip_14_3l
hs_zclip_14
0.003999
0.0032
/surface/isoclip
x-coordinate
hs_xclip_14_4r
hs_zclip_14
0.006001
0.0068
/surface/isoclip
x-coordinate
hs_xclip_14_4l
hs_zclip_14
0.013999
0.0132
/surface/isoclip
x-coordinate
hs_xclip_14_5r
hs_zclip_14
0.016001
0.0168
/surface/isoclip
z-coordinate
hs_zclip_15
hs_yclip
0.0679
0.0681
/surface/isoclip
x-coordinate
hs_xclip_15_1l
hs_zclip_15
-0.016001
-0.0168
/surface/isoclip
x-coordinate
hs_xclip_15_2r
hs_zclip_15
-0.013999
-0.0132
/surface/isoclip
x-coordinate
hs_xclip_15_2l
hs_zclip_15
-0.006001
-0.0068
/surface/isoclip
x-coordinate
hs_xclip_15_3r
hs_zclip_15
-0.003999
-0.0032
/surface/isoclip
x-coordinate
hs_xclip_15_3l
hs_zclip_15
0.003999
0.0032
/surface/isoclip
x-coordinate
hs_xclip_15_4r
hs_zclip_15
0.006001
0.0068
/surface/isoclip
x-coordinate
hs_xclip_15_4l
hs_zclip_15
0.013999
0.0132
/surface/isoclip
```



```
x-coordinate
hs_xclip_15_5r
hs_zclip_15
0.016001
0.0168
/solve/monitors/residual/convergence-criteria
0.001
0.001
0.001
0.001
3e-8
/define/models/viscous/ke-realizable
yes
/define/models/viscous/near-wall-treatment/enhanced-wall-treatment
yes
/solve/set/discretization-scheme/epsilon
1
/solve/set/discretization-scheme/k
1
/solve/set/discretization-scheme/mom
1
/solve/set/discretization-scheme/temperature
1
/solve/set/discretization-scheme/pressure
10
/define/boundary-conditions/velocity-inlet
fan_1-sidel
yes
yes
no
2
yes
no
0
no
0
no
1
no
293.15
no
no
no
yes
5
0.0325926
/define/boundary-conditions/wall
source_1-sidel

3472.2222

/file/read-data
tr_Lfin_0_004_Lgap_0_006_Wfin_0_008_Wgap_0_002_Vz_2rke_ewt-fluent.dat.gz
yes
q
q
it
500
/file/start-transcript
tr_Lfin_0_004_Lgap_0_006_Wfin_0_008_Wgap_0_002_Vz_2.tra
it
1
/report/surface-avg
hs_xclip_1_1l
hs_xclip_1_2r
hs_xclip_1_2l
hs_xclip_1_3r
hs_xclip_1_3l
hs_xclip_1_4r
hs_xclip_1_4l
```



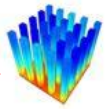

hs_xclip_1_5r
hs_xclip_2_1l
hs_xclip_2_2r
hs_xclip_2_2l
hs_xclip_2_3r
hs_xclip_2_3l
hs_xclip_2_4r
hs_xclip_2_4l
hs_xclip_2_5r
hs_xclip_3_1l
hs_xclip_3_2r
hs_xclip_3_2l
hs_xclip_3_3r
hs_xclip_3_3l
hs_xclip_3_4r
hs_xclip_3_4l
hs_xclip_3_5r
hs_xclip_4_1l
hs_xclip_4_2r
hs_xclip_4_2l
hs_xclip_4_3r
hs_xclip_4_3l
hs_xclip_4_4r
hs_xclip_4_4l
hs_xclip_4_5r
hs_xclip_5_1l
hs_xclip_5_2r
hs_xclip_5_2l
hs_xclip_5_3r
hs_xclip_5_3l
hs_xclip_5_4r
hs_xclip_5_4l
hs_xclip_5_5r
hs_xclip_6_1l
hs_xclip_6_2r
hs_xclip_6_2l
hs_xclip_6_3r
hs_xclip_6_3l
hs_xclip_6_4r
hs_xclip_6_4l
hs_xclip_6_5r
hs_xclip_7_1l
hs_xclip_7_2r
hs_xclip_7_2l
hs_xclip_7_3r
hs_xclip_7_3l
hs_xclip_7_4r
hs_xclip_7_4l
hs_xclip_7_5r
hs_xclip_8_1l
hs_xclip_8_2r
hs_xclip_8_2l
hs_xclip_8_3r
hs_xclip_8_3l
hs_xclip_8_4r
hs_xclip_8_4l
hs_xclip_8_5r
hs_xclip_9_1l
hs_xclip_9_2r
hs_xclip_9_2l
hs_xclip_9_3r
hs_xclip_9_3l
hs_xclip_9_4r
hs_xclip_9_4l
hs_xclip_9_5r
hs_xclip_10_1l
hs_xclip_10_2r
hs_xclip_10_2l
hs_xclip_10_3r
hs_xclip_10_3l
hs_xclip_10_4r
hs_xclip_10_4l
hs_xclip_10_5r
hs_xclip_11_1l
hs_xclip_11_2r
hs_xclip_11_2l
hs_xclip_11_3r



```
hs_xclip_11_3l
hs_xclip_11_4r
hs_xclip_11_4l
hs_xclip_11_5r
hs_xclip_12_1l
hs_xclip_12_2r
hs_xclip_12_2l
hs_xclip_12_3r
hs_xclip_12_3l
hs_xclip_12_4r
hs_xclip_12_4l
hs_xclip_12_5r
hs_xclip_13_1l
hs_xclip_13_2r
hs_xclip_13_2l
hs_xclip_13_3r
hs_xclip_13_3l
hs_xclip_13_4r
hs_xclip_13_4l
hs_xclip_13_5r
hs_xclip_14_1l
hs_xclip_14_2r
hs_xclip_14_2l
hs_xclip_14_3r
hs_xclip_14_3l
hs_xclip_14_4r
hs_xclip_14_4l
hs_xclip_14_5r
hs_xclip_15_1l
hs_xclip_15_2r
hs_xclip_15_2l
hs_xclip_15_3r
hs_xclip_15_3l
hs_xclip_15_4r
hs_xclip_15_4l
hs_xclip_15_5r
()
heat-flux
/report/surface-avg
hs_xclip_1_1l
hs_xclip_1_2r
hs_xclip_1_2l
hs_xclip_1_3r
hs_xclip_1_3l
hs_xclip_1_4r
hs_xclip_1_4l
hs_xclip_1_5r
hs_xclip_2_1l
hs_xclip_2_2r
hs_xclip_2_2l
hs_xclip_2_3r
hs_xclip_2_3l
hs_xclip_2_4r
hs_xclip_2_4l
hs_xclip_2_5r
hs_xclip_3_1l
hs_xclip_3_2r
hs_xclip_3_2l
hs_xclip_3_3r
hs_xclip_3_3l
hs_xclip_3_4r
hs_xclip_3_4l
hs_xclip_3_5r
hs_xclip_4_1l
hs_xclip_4_2r
hs_xclip_4_2l
hs_xclip_4_3r
hs_xclip_4_3l
hs_xclip_4_4r
hs_xclip_4_4l
hs_xclip_4_5r
hs_xclip_5_1l
hs_xclip_5_2r
hs_xclip_5_2l
hs_xclip_5_3r
hs_xclip_5_3l
hs_xclip_5_4r
```



hs_xclip_5_4l
hs_xclip_5_5r
hs_xclip_6_1l
hs_xclip_6_2r
hs_xclip_6_2l
hs_xclip_6_3r
hs_xclip_6_3l
hs_xclip_6_4r
hs_xclip_6_4l
hs_xclip_6_5r
hs_xclip_7_1l
hs_xclip_7_2r
hs_xclip_7_2l
hs_xclip_7_3r
hs_xclip_7_3l
hs_xclip_7_4r
hs_xclip_7_4l
hs_xclip_7_5r
hs_xclip_8_1l
hs_xclip_8_2r
hs_xclip_8_2l
hs_xclip_8_3r
hs_xclip_8_3l
hs_xclip_8_4r
hs_xclip_8_4l
hs_xclip_8_5r
hs_xclip_9_1l
hs_xclip_9_2r
hs_xclip_9_2l
hs_xclip_9_3r
hs_xclip_9_3l
hs_xclip_9_4r
hs_xclip_9_4l
hs_xclip_9_5r
hs_xclip_10_1l
hs_xclip_10_2r
hs_xclip_10_2l
hs_xclip_10_3r
hs_xclip_10_3l
hs_xclip_10_4r
hs_xclip_10_4l
hs_xclip_10_5r
hs_xclip_11_1l
hs_xclip_11_2r
hs_xclip_11_2l
hs_xclip_11_3r
hs_xclip_11_3l
hs_xclip_11_4r
hs_xclip_11_4l
hs_xclip_11_5r
hs_xclip_12_1l
hs_xclip_12_2r
hs_xclip_12_2l
hs_xclip_12_3r
hs_xclip_12_3l
hs_xclip_12_4r
hs_xclip_12_4l
hs_xclip_12_5r
hs_xclip_13_1l
hs_xclip_13_2r
hs_xclip_13_2l
hs_xclip_13_3r
hs_xclip_13_3l
hs_xclip_13_4r
hs_xclip_13_4l
hs_xclip_13_5r
hs_xclip_14_1l
hs_xclip_14_2r
hs_xclip_14_2l
hs_xclip_14_3r
hs_xclip_14_3l
hs_xclip_14_4r
hs_xclip_14_4l
hs_xclip_14_5r
hs_xclip_15_1l
hs_xclip_15_2r
hs_xclip_15_2l



```

hs_xclip_15_3r
hs_xclip_15_3l
hs_xclip_15_4r
hs_xclip_15_4l
hs_xclip_15_5r
opening_1-side1
()
temperature
/file/stop-transcript
/file/write-data
fluent/tr_Lfin_0_004_Lgap_0_006_Wfin_0_008_Wgap_0_002_Vz_2rke_ewt-fluent.dat.gz

```

Transcript file created by the above journal for one case file.

```

> it
Number of iterations [500] 1
  iter continuity x-velocity y-velocity z-velocity      energy          k      epsilon
time/iter
! 291 solution is converged
  291 9.8764e-04 2.1301e-06 5.7496e-06 1.1464e-04 2.2134e-08 6.8960e-04 8.2041e-04
0:00:48      1
! 292 solution is converged
  292 9.7800e-04 2.1033e-06 5.7050e-06 1.1387e-04 2.2133e-08 6.8608e-04 8.1123e-04
0:00:00      0

> /report/surface-avg
()
surface id(1) [()] hs_xclip_1_1l
surface id(2) [()] hs_xclip_1_2r
surface id(3) [()] hs_xclip_1_2l
surface id(4) [()] hs_xclip_1_3r
surface id(5) [()] hs_xclip_1_3l
surface id(6) [()] hs_xclip_1_4r
surface id(7) [()] hs_xclip_1_4l
surface id(8) [()] hs_xclip_1_5r
surface id(9) [()] hs_xclip_2_1l
surface id(10) [()] hs_xclip_2_2r
surface id(11) [()] hs_xclip_2_2l
surface id(12) [()] hs_xclip_2_3r
surface id(13) [()] hs_xclip_2_3l
surface id(14) [()] hs_xclip_2_4r
surface id(15) [()] hs_xclip_2_4l
surface id(16) [()] hs_xclip_2_5r
surface id(17) [()] hs_xclip_3_1l
surface id(18) [()] hs_xclip_3_2r
surface id(19) [()] hs_xclip_3_2l
surface id(20) [()] hs_xclip_3_3r
surface id(21) [()] hs_xclip_3_3l
surface id(22) [()] hs_xclip_3_4r
surface id(23) [()] hs_xclip_3_4l
surface id(24) [()] hs_xclip_3_5r
surface id(25) [()] hs_xclip_4_1l
surface id(26) [()] hs_xclip_4_2r
surface id(27) [()] hs_xclip_4_2l
surface id(28) [()] hs_xclip_4_3r
surface id(29) [()] hs_xclip_4_3l
surface id(30) [()] hs_xclip_4_4r
surface id(31) [()] hs_xclip_4_4l
surface id(32) [()] hs_xclip_4_5r
surface id(33) [()] hs_xclip_5_1l
surface id(34) [()] hs_xclip_5_2r
surface id(35) [()] hs_xclip_5_2l
surface id(36) [()] hs_xclip_5_3r
surface id(37) [()] hs_xclip_5_3l
surface id(38) [()] hs_xclip_5_4r
surface id(39) [()] hs_xclip_5_4l
surface id(40) [()] hs_xclip_5_5r
surface id(41) [()] hs_xclip_6_1l
surface id(42) [()] hs_xclip_6_2r
surface id(43) [()] hs_xclip_6_2l
surface id(44) [()] hs_xclip_6_3r
surface id(45) [()] hs_xclip_6_3l
surface id(46) [()] hs_xclip_6_4r
surface id(47) [()] hs_xclip_6_4l

```

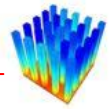


```
surface id(48) [()] hs_xclip_6_5r
surface id(49) [()] hs_xclip_7_1l
surface id(50) [()] hs_xclip_7_2r
surface id(51) [()] hs_xclip_7_2l
surface id(52) [()] hs_xclip_7_3r
surface id(53) [()] hs_xclip_7_3l
surface id(54) [()] hs_xclip_7_4r
surface id(55) [()] hs_xclip_7_4l
surface id(56) [()] hs_xclip_7_5r
surface id(57) [()] hs_xclip_8_1l
surface id(58) [()] hs_xclip_8_2r
surface id(59) [()] hs_xclip_8_2l
surface id(60) [()] hs_xclip_8_3r
surface id(61) [()] hs_xclip_8_3l
surface id(62) [()] hs_xclip_8_4r
surface id(63) [()] hs_xclip_8_4l
surface id(64) [()] hs_xclip_8_5r
surface id(65) [()] hs_xclip_9_1l
surface id(66) [()] hs_xclip_9_2r
surface id(67) [()] hs_xclip_9_2l
surface id(68) [()] hs_xclip_9_3r
surface id(69) [()] hs_xclip_9_3l
surface id(70) [()] hs_xclip_9_4r
surface id(71) [()] hs_xclip_9_4l
surface id(72) [()] hs_xclip_9_5r
surface id(73) [()] hs_xclip_10_1l
surface id(74) [()] hs_xclip_10_2r
surface id(75) [()] hs_xclip_10_2l
surface id(76) [()] hs_xclip_10_3r
surface id(77) [()] hs_xclip_10_3l
surface id(78) [()] hs_xclip_10_4r
surface id(79) [()] hs_xclip_10_4l
surface id(80) [()] hs_xclip_10_5r
surface id(81) [()] hs_xclip_11_1l
surface id(82) [()] hs_xclip_11_2r
surface id(83) [()] hs_xclip_11_2l
surface id(84) [()] hs_xclip_11_3r
surface id(85) [()] hs_xclip_11_3l
surface id(86) [()] hs_xclip_11_4r
surface id(87) [()] hs_xclip_11_4l
surface id(88) [()] hs_xclip_11_5r
surface id(89) [()] hs_xclip_12_1l
surface id(90) [()] hs_xclip_12_2r
surface id(91) [()] hs_xclip_12_2l
surface id(92) [()] hs_xclip_12_3r
surface id(93) [()] hs_xclip_12_3l
surface id(94) [()] hs_xclip_12_4r
surface id(95) [()] hs_xclip_12_4l
surface id(96) [()] hs_xclip_12_5r
surface id(97) [()] hs_xclip_13_1l
surface id(98) [()] hs_xclip_13_2r
surface id(99) [()] hs_xclip_13_2l
surface id(100) [()] hs_xclip_13_3r
surface id(101) [()] hs_xclip_13_3l
surface id(102) [()] hs_xclip_13_4r
surface id(103) [()] hs_xclip_13_4l
surface id(104) [()] hs_xclip_13_5r
surface id(105) [()] hs_xclip_14_1l
surface id(106) [()] hs_xclip_14_2r
surface id(107) [()] hs_xclip_14_2l
surface id(108) [()] hs_xclip_14_3r
surface id(109) [()] hs_xclip_14_3l
surface id(110) [()] hs_xclip_14_4r
surface id(111) [()] hs_xclip_14_4l
surface id(112) [()] hs_xclip_14_5r
surface id(113) [()] hs_xclip_15_1l
surface id(114) [()] hs_xclip_15_2r
surface id(115) [()] hs_xclip_15_2l
surface id(116) [()] hs_xclip_15_3r
surface id(117) [()] hs_xclip_15_3l
surface id(118) [()] hs_xclip_15_4r
surface id(119) [()] hs_xclip_15_4l
surface id(120) [()] hs_xclip_15_5r
surface id(121) [()] ()
average of> heat-flux
```

Area-Weighted Average



Total Surface Heat Flux	(w/m ²)
hs_xclip_1_1l	3917.911
hs_xclip_1_2r	3957.6361
hs_xclip_1_2l	3935.2916
hs_xclip_1_3r	3964.8827
hs_xclip_1_3l	3966.601
hs_xclip_1_4r	3919.2796
hs_xclip_1_4l	3958.3389
hs_xclip_1_5r	3915.5424
hs_xclip_2_1l	5461.47
hs_xclip_2_2r	4206.1661
hs_xclip_2_2l	5978.9213
hs_xclip_2_3r	5496.2956
hs_xclip_2_3l	5752.062
hs_xclip_2_4r	5972.1398
hs_xclip_2_4l	4702.4541
hs_xclip_2_5r	5465.571
hs_xclip_3_1l	4415.6299
hs_xclip_3_2r	4108.8336
hs_xclip_3_2l	4499.3127
hs_xclip_3_3r	4464.5529
hs_xclip_3_3l	4444.4516
hs_xclip_3_4r	4502.7249
hs_xclip_3_4l	4349.3661
hs_xclip_3_5r	4404.9998
hs_xclip_4_1l	4151.5945
hs_xclip_4_2r	3870.6527
hs_xclip_4_2l	4251.7191
hs_xclip_4_3r	4202.0368
hs_xclip_4_3l	4152.8874
hs_xclip_4_4r	4232.0016
hs_xclip_4_4l	4190.6332
hs_xclip_4_5r	4133.3161
hs_xclip_5_1l	3988.4066
hs_xclip_5_2r	3717.1453
hs_xclip_5_2l	4079.3889
hs_xclip_5_3r	4033.5483
hs_xclip_5_3l	3983.1668
hs_xclip_5_4r	4054.1447
hs_xclip_5_4l	4057.9267
hs_xclip_5_5r	3958.7474
hs_xclip_6_1l	3833.7192
hs_xclip_6_2r	3588.3434
hs_xclip_6_2l	3939.7617
hs_xclip_6_3r	3902.9009
hs_xclip_6_3l	3852.703
hs_xclip_6_4r	3900.6791
hs_xclip_6_4l	3927.1856
hs_xclip_6_5r	3806.652
hs_xclip_7_1l	3707.8055
hs_xclip_7_2r	3476.7235
hs_xclip_7_2l	3816.7913
hs_xclip_7_3r	3787.2348
hs_xclip_7_3l	3734.2784
hs_xclip_7_4r	3782.7108
hs_xclip_7_4l	3810.6056
hs_xclip_7_5r	3694.1291
hs_xclip_8_1l	3604.0276
hs_xclip_8_2r	3364.5496
hs_xclip_8_2l	3693.2169
hs_xclip_8_3r	3670.7341
hs_xclip_8_3l	3623.0148
hs_xclip_8_4r	3673.7787
hs_xclip_8_4l	3707.1303
hs_xclip_8_5r	3591.6062
hs_xclip_9_1l	3472.4453
hs_xclip_9_2r	3260.5302
hs_xclip_9_2l	3575.521
hs_xclip_9_3r	3547.1873
hs_xclip_9_3l	3504.7621
hs_xclip_9_4r	3549.6532
hs_xclip_9_4l	3589.362
hs_xclip_9_5r	3473.4888
hs_xclip_10_1l	3339.6647
hs_xclip_10_2r	3144.7642
hs_xclip_10_2l	3447.2625



hs_xclip_10_3r	3426.075
hs_xclip_10_3l	3389.4171
hs_xclip_10_4r	3432.4654
hs_xclip_10_4l	3477.5305
hs_xclip_10_5r	3362.4292
hs_xclip_11_1l	3233.4338
hs_xclip_11_2r	3025.8874
hs_xclip_11_2l	3317.5281
hs_xclip_11_3r	3284.4801
hs_xclip_11_3l	3252.4832
hs_xclip_11_4r	3296.3263
hs_xclip_11_4l	3346.3331
hs_xclip_11_5r	3238.2682
hs_xclip_12_1l	3084.8278
hs_xclip_12_2r	2891.8327
hs_xclip_12_2l	3172.596
hs_xclip_12_3r	3142.583
hs_xclip_12_3l	3113.7837
hs_xclip_12_4r	3155.465
hs_xclip_12_4l	3209.1795
hs_xclip_12_5r	3108.7592
hs_xclip_13_1l	2921.2364
hs_xclip_13_2r	2743.9541
hs_xclip_13_2l	3013.0344
hs_xclip_13_3r	2981.4485
hs_xclip_13_3l	2954.7919
hs_xclip_13_4r	2997.3318
hs_xclip_13_4l	3053.7931
hs_xclip_13_5r	2941.1386
hs_xclip_14_1l	2760.8019
hs_xclip_14_2r	2580.02
hs_xclip_14_2l	2839.0105
hs_xclip_14_3r	2804.0693
hs_xclip_14_3l	2779.0842
hs_xclip_14_4r	2825.7252
hs_xclip_14_4l	2879.7232
hs_xclip_14_5r	2786.9767
hs_xclip_15_1l	2527.5972
hs_xclip_15_2r	2322.0297
hs_xclip_15_2l	2630.1701
hs_xclip_15_3r	2567.7236
hs_xclip_15_3l	2545.0968
hs_xclip_15_4r	2606.1851
hs_xclip_15_4l	2591.151
hs_xclip_15_5r	2539.6186
Net	3636.3839

```

> /report/surface-avg
(21 22 23 24 25 26 27 28 30 31 32 33 34 35 36 37 39 40 41 42 43 44 45 46 48 49 50 51
52 53 54 55 57 58 59 60 61 62 63 64 66 67 68 69 70 71 72 73 75 76 77 78 79 80 81 82 84
85 86 87 88 89 90 91 93 94 95 96 97 98 99 100 102 103 104 105 106 107 108 109 111 112
113 114 115 116 117 118 120 121 122 123 124 125 126 127 129 130 131 132 133 134 135
136 138 139 140 141 142 143 144 145 147 148 149 150 151 152 153 154)
surface id(1) [21] hs_xclip_1_1l
surface id(2) [22] hs_xclip_1_2r
surface id(3) [23] hs_xclip_1_2l
surface id(4) [24] hs_xclip_1_3r
surface id(5) [25] hs_xclip_1_3l
surface id(6) [26] hs_xclip_1_4r
surface id(7) [27] hs_xclip_1_4l
surface id(8) [28] hs_xclip_1_5r
surface id(9) [30] hs_xclip_2_1l
surface id(10) [31] hs_xclip_2_2r
surface id(11) [32] hs_xclip_2_2l
surface id(12) [33] hs_xclip_2_3r
surface id(13) [34] hs_xclip_2_3l
surface id(14) [35] hs_xclip_2_4r
surface id(15) [36] hs_xclip_2_4l
surface id(16) [37] hs_xclip_2_5r
surface id(17) [39] hs_xclip_3_1l
surface id(18) [40] hs_xclip_3_2r
surface id(19) [41] hs_xclip_3_2l
surface id(20) [42] hs_xclip_3_3r
surface id(21) [43] hs_xclip_3_3l
surface id(22) [44] hs_xclip_3_4r
surface id(23) [45] hs_xclip_3_4l
surface id(24) [46] hs_xclip_3_5r

```



```
surface id(25) [48] hs_xclip_4_1l
surface id(26) [49] hs_xclip_4_2r
surface id(27) [50] hs_xclip_4_2l
surface id(28) [51] hs_xclip_4_3r
surface id(29) [52] hs_xclip_4_3l
surface id(30) [53] hs_xclip_4_4r
surface id(31) [54] hs_xclip_4_4l
surface id(32) [55] hs_xclip_4_5r
surface id(33) [57] hs_xclip_5_1l
surface id(34) [58] hs_xclip_5_2r
surface id(35) [59] hs_xclip_5_2l
surface id(36) [60] hs_xclip_5_3r
surface id(37) [61] hs_xclip_5_3l
surface id(38) [62] hs_xclip_5_4r
surface id(39) [63] hs_xclip_5_4l
surface id(40) [64] hs_xclip_5_5r
surface id(41) [66] hs_xclip_6_1l
surface id(42) [67] hs_xclip_6_2r
surface id(43) [68] hs_xclip_6_2l
surface id(44) [69] hs_xclip_6_3r
surface id(45) [70] hs_xclip_6_3l
surface id(46) [71] hs_xclip_6_4r
surface id(47) [72] hs_xclip_6_4l
surface id(48) [73] hs_xclip_6_5r
surface id(49) [75] hs_xclip_7_1l
surface id(50) [76] hs_xclip_7_2r
surface id(51) [77] hs_xclip_7_2l
surface id(52) [78] hs_xclip_7_3r
surface id(53) [79] hs_xclip_7_3l
surface id(54) [80] hs_xclip_7_4r
surface id(55) [81] hs_xclip_7_4l
surface id(56) [82] hs_xclip_7_5r
surface id(57) [84] hs_xclip_8_1l
surface id(58) [85] hs_xclip_8_2r
surface id(59) [86] hs_xclip_8_2l
surface id(60) [87] hs_xclip_8_3r
surface id(61) [88] hs_xclip_8_3l
surface id(62) [89] hs_xclip_8_4r
surface id(63) [90] hs_xclip_8_4l
surface id(64) [91] hs_xclip_8_5r
surface id(65) [93] hs_xclip_9_1l
surface id(66) [94] hs_xclip_9_2r
surface id(67) [95] hs_xclip_9_2l
surface id(68) [96] hs_xclip_9_3r
surface id(69) [97] hs_xclip_9_3l
surface id(70) [98] hs_xclip_9_4r
surface id(71) [99] hs_xclip_9_4l
surface id(72) [100] hs_xclip_9_5r
surface id(73) [102] hs_xclip_10_1l
surface id(74) [103] hs_xclip_10_2r
surface id(75) [104] hs_xclip_10_2l
surface id(76) [105] hs_xclip_10_3r
surface id(77) [106] hs_xclip_10_3l
surface id(78) [107] hs_xclip_10_4r
surface id(79) [108] hs_xclip_10_4l
surface id(80) [109] hs_xclip_10_5r
surface id(81) [111] hs_xclip_11_1l
surface id(82) [112] hs_xclip_11_2r
surface id(83) [113] hs_xclip_11_2l
surface id(84) [114] hs_xclip_11_3r
surface id(85) [115] hs_xclip_11_3l
surface id(86) [116] hs_xclip_11_4r
surface id(87) [117] hs_xclip_11_4l
surface id(88) [118] hs_xclip_11_5r
surface id(89) [120] hs_xclip_12_1l
surface id(90) [121] hs_xclip_12_2r
surface id(91) [122] hs_xclip_12_2l
surface id(92) [123] hs_xclip_12_3r
surface id(93) [124] hs_xclip_12_3l
surface id(94) [125] hs_xclip_12_4r
surface id(95) [126] hs_xclip_12_4l
surface id(96) [127] hs_xclip_12_5r
surface id(97) [129] hs_xclip_13_1l
surface id(98) [130] hs_xclip_13_2r
surface id(99) [131] hs_xclip_13_2l
surface id(100) [132] hs_xclip_13_3r
surface id(101) [133] hs_xclip_13_3l
```




```

surface id(102) [134] hs_xclip_13_4r
surface id(103) [135] hs_xclip_13_4l
surface id(104) [136] hs_xclip_13_5r
surface id(105) [138] hs_xclip_14_1l
surface id(106) [139] hs_xclip_14_2r
surface id(107) [140] hs_xclip_14_2l
surface id(108) [141] hs_xclip_14_3r
surface id(109) [142] hs_xclip_14_3l
surface id(110) [143] hs_xclip_14_4r
surface id(111) [144] hs_xclip_14_4l
surface id(112) [145] hs_xclip_14_5r
surface id(113) [147] hs_xclip_15_1l
surface id(114) [148] hs_xclip_15_2r
surface id(115) [149] hs_xclip_15_2l
surface id(116) [150] hs_xclip_15_3r
surface id(117) [151] hs_xclip_15_3l
surface id(118) [152] hs_xclip_15_4r
surface id(119) [153] hs_xclip_15_4l
surface id(120) [154] hs_xclip_15_5r
surface id(121) [()] opening_1-side1
surface id(122) [()] ()

```

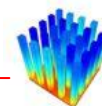
average of> temperature

Area-Weighted Average
Static Temperature (k)

```

-----
hs_xclip_1_1l 296.10246
hs_xclip_1_2r 295.95439
hs_xclip_1_2l 295.95089
hs_xclip_1_3r 295.97675
hs_xclip_1_3l 295.99467
hs_xclip_1_4r 295.93189
hs_xclip_1_4l 295.98778
hs_xclip_1_5r 296.1369
hs_xclip_2_1l 308.54806
hs_xclip_2_2r 310.91517
hs_xclip_2_2l 307.41522
hs_xclip_2_3r 308.31979
hs_xclip_2_3l 307.81387
hs_xclip_2_4r 307.57587
hs_xclip_2_4l 310.07195
hs_xclip_2_5r 308.50815
hs_xclip_3_1l 310.19271
hs_xclip_3_2r 310.80608
hs_xclip_3_2l 309.91241
hs_xclip_3_3r 310.01821
hs_xclip_3_3l 310.06046
hs_xclip_3_4r 310.01891
hs_xclip_3_4l 310.35545
hs_xclip_3_5r 310.21062
hs_xclip_4_1l 311.80569
hs_xclip_4_2r 312.37523
hs_xclip_4_2l 311.50059
hs_xclip_4_3r 311.65089
hs_xclip_4_3l 311.75951
hs_xclip_4_4r 311.62028
hs_xclip_4_4l 311.70052
hs_xclip_4_5r 311.86141
hs_xclip_5_1l 313.21804
hs_xclip_5_2r 313.7237
hs_xclip_5_2l 312.89106
hs_xclip_5_3r 313.03175
hs_xclip_5_3l 313.1447
hs_xclip_5_4r 313.01796
hs_xclip_5_4l 312.99846
hs_xclip_5_5r 313.26398
hs_xclip_6_1l 314.53724
hs_xclip_6_2r 315.00646
hs_xclip_6_2l 314.19659
hs_xclip_6_3r 314.32348
hs_xclip_6_3l 314.43469
hs_xclip_6_4r 314.31034
hs_xclip_6_4l 314.24078
hs_xclip_6_5r 314.55585
hs_xclip_7_1l 315.7889
hs_xclip_7_2r 316.23737

```



hs_xclip_7_2l	315.45294
hs_xclip_7_3r	315.55233
hs_xclip_7_3l	315.67026
hs_xclip_7_4r	315.53695
hs_xclip_7_4l	315.4645
hs_xclip_7_5r	315.79284
hs_xclip_8_1l	317.00774
hs_xclip_8_2r	317.41931
hs_xclip_8_2l	316.66047
hs_xclip_8_3r	316.76083
hs_xclip_8_3l	316.86757
hs_xclip_8_4r	316.74926
hs_xclip_8_4l	316.66506
hs_xclip_8_5r	316.99671
hs_xclip_9_1l	318.1595
hs_xclip_9_2r	318.56651
hs_xclip_9_2l	317.83926
hs_xclip_9_3r	317.9324
hs_xclip_9_3l	318.02767
hs_xclip_9_4r	317.91718
hs_xclip_9_4l	317.81803
hs_xclip_9_5r	318.14223
hs_xclip_10_1l	319.24355
hs_xclip_10_2r	319.66459
hs_xclip_10_2l	318.96647
hs_xclip_10_3r	319.06804
hs_xclip_10_3l	319.15007
hs_xclip_10_4r	319.04801
hs_xclip_10_4l	318.93659
hs_xclip_10_5r	319.2432
hs_xclip_11_1l	320.30833
hs_xclip_11_2r	320.70858
hs_xclip_11_2l	320.036
hs_xclip_11_3r	320.13044
hs_xclip_11_3l	320.20153
hs_xclip_11_4r	320.11139
hs_xclip_11_4l	319.98863
hs_xclip_11_5r	320.28506
hs_xclip_12_1l	321.28873
hs_xclip_12_2r	321.67564
hs_xclip_12_2l	321.02833
hs_xclip_12_3r	321.11976
hs_xclip_12_3l	321.18324
hs_xclip_12_4r	321.10233
hs_xclip_12_4l	320.9715
hs_xclip_12_5r	321.26204
hs_xclip_13_1l	322.16378
hs_xclip_13_2r	322.54975
hs_xclip_13_2l	321.92887
hs_xclip_13_3r	322.01557
hs_xclip_13_3l	322.07387
hs_xclip_13_4r	322.00326
hs_xclip_13_4l	321.86672
hs_xclip_13_5r	322.1255
hs_xclip_14_1l	322.95795
hs_xclip_14_2r	323.32493
hs_xclip_14_2l	322.72668
hs_xclip_14_3r	322.80571
hs_xclip_14_3l	322.86024
hs_xclip_14_4r	322.80035
hs_xclip_14_4l	322.67005
hs_xclip_14_5r	322.91041
hs_xclip_15_1l	323.58396
hs_xclip_15_2r	324.01456
hs_xclip_15_2l	323.3033
hs_xclip_15_3r	323.44213
hs_xclip_15_3l	323.49164
hs_xclip_15_4r	323.35375
hs_xclip_15_4l	323.3823
hs_xclip_15_5r	323.50191
opening_1-side1	317.12905
Net	316.2458

```
> /file/stop-transcript
```